MECHANISMS OF POLYDISPERSITY AND CLIENT-INDUCED CO-AGGREGATION OF SMALL HEAT SHOCK PROTEINS

By

Adam P. Miller

A DISSERTATION

Presented to the Department of Chemical Physiology and Biochemistry

And the Oregon Health and Science University

School of Medicine

In partial fulfillment for the degree of

Doctor of Philosophy

July 2024

Table of Contents

Chapter 1: The structure and function of small heat shock proteins 1

Overview of small heat shock proteins 1

The α-crystallins role in lens transparency and cataract 5

The structure of small heat shock proteins 10

Client recognition and co-aggregation of small heat shock proteins 15

Single-particle approaches of electron microscopy to characterize the dynamic structure of small heat shock proteins 18

Chapter 2: The α-crystallin chaperones undergo a quasi-ordered co-aggregation process in response to saturating client interaction 23

Introduction 26

Results 28

Single-particle analysis reveals full extent of αA- and αB-crystallin Polydispersity 28

αA- and αB-crystallin display different degrees of susceptibility to client-induced co-aggregation 32

Saturating client conditions induce structural transitions toward light-Scattering α-crystallin/lysozyme co-aggregates 37

Single-particle analysis by EM reveals an expansion, elongation, and amorphous collapse chaperone mechanism 38

Client-induced expansion, elongation, and amorphous collapse is preserved with an alternative client 42

Native heteromeric lens α-crystallins exhibit a similar chaperone mechanism, with diminished activity toward the model client lysozyme 45

Discussion 49

Limitations of the study 55

Methods 57

Expression and purification of recombinant αA- and αB-crystallin 57

Isolation of native α-crystallins from ovine lenses 58

Chaperone aggregation suppression assays 59

Dynamic light-scattering measurements 60

Native stain electron microscopy 61

Single-particle EM image analysis 62

Sequence alignment of α-crystallin homologs 63

Statistical analysis and data representation 64

Chapter 3: Structural mechanisms of small heat shock protein client sequestration and induced polydispersity and induced polydispersity 73

Introduction 75

Results 78

N-terminal domain mediates plasticity of mjHSP16.5 cages 78

A conserved phenylalanine-rich region mediates oligomer stability 83

Client-induced polydispersity of mjHSP16.5 85

CryoEM of mjHSP16.5/lysozyme chaperone complexes 87

Flexible C-terminal domain enables client-induced polydispersity 88

Polarization/elongation drives “holdase” activity 91

Discussion 93

Methods 98

Construction of wildtype and mutant mjHSP16.5 plasmids 98

Expression and purification of mjHSP16.5 wildtype and mutants 98

Aggregation assays of reduced lysozyme at 37° C 100

Heat induced binding assays with lysozyme at 75° C 100

Size-exclusion chromatography of mjHSP16.5 wildtype, mutants, and mjHSP16.5/lysozyme complexes 101

Negative stain EM imaging and single-particle size analysis 101

Cryo-EM data collection 103

CryoEM image processing of apo-state mjHSP16.5 (37° C) 103

Single-particle CryoEM image processing of apo-state mjHSP16.5 (75° C) 104

Single-particle CryoEM image processing of mjHSP16.5 complexes With lysozyme (12:1 ratio) 105
Atomic model building apo-states and client bound mjHSP16.5 108

Chapter 4: Conclusion: Endless forms most beautiful: Determining structural mechanism of small heat shock protein polydispersity and client binding 119

Appendix Chapter 1: Single-particle CryoEM datasets of αA- and αB-crystallin demonstrate high levels of oligomeric heterogeneity 126

Methods 134

Appendix Chapter 2: Conserved and divergent features of neuronal CaMKII holoenzyme structure, function, and high-order assembly 136

Introduction 138

Results 139

The dodecameric CaMKIIβ holoenzyme adopts an extended kinase radius 140

Autophosphorylation of pT286 in CaMKIIα versus pT287 in CaMKIIβ 142

CaMKIIβ forms multimeric assemblies of 12 – 16-mers 143

Resolution of kinase domain dimers within intact CaMKIIβ holoenzymes 145

CaMKIIα and CaMKIIβ differ in CaM activation constants but not In activation cooperativity 147

CaMKIIα and β form higher-order holoenzyme clusters both *in vitro* and in neurons 148

Homomeric CaMKIIβ holoenzymes show less propensity for higher-order clustering 149

Discussion 152

Holoenzyme expansion and autophosphorylation kinetics 153

Higher-order assemblies and subcellular CaMKII targeting 155

Multivalent interactions within the holoenzymes and cooperative CaMKII regulation 156

Beyond the 12-mer: Outlook for future studies 159

Limitations of study 161

Acknowledgements 161

Star⋆Methods 163

Resource availability 164

Experimental model and subject details 165

Methods 166

DNA constructs 166

CaMKII and CaM purification 166

Electron microscopy 166

Single-particle measurements and statistical analysis 167

Pseudo-atomic modeling of the CaMKII 16-meric hub assembly and back-projection analysis 168

Live imaging of hippocampal cultured neurons 169

CaMKII *in vitro* reactions 169

SDS-PAGE and immunoblot 170

Quantification and statistical analysis 171

Supplemental Figures and Legends 173

References 179

Table of figures

Chapter 1

Figure 1: Diversity of small heat shock proteins and relation to age-related diseases 2

Figure 2: Age related changes to the lens proteome 6

Figure 3: Structure of small heat shock proteins 11

Figure 4: Oligomeric diversity of small heat shock proteins supported by conserved regions of N- and C-terminal domains 12

Figure 5: Generalized schematic representing sHSP "holdase" function 15

Chapter 2

Figure 1:Structural analysis of polydispersed apo-states of αA- and αB-crystallin 29

Figure 2: Chaperone activity and structural characterization of α-crystallin/lysozyme complexes and co-aggregates 33

Table 1: Summary of chaperone aggregation suppression assay results for α-crystallin/client complexes 34

Figure 3: Quantitative structural analysis of αAc and αBc/lysozyme complex formation and co-aggregation by single-particle EM 39

Table 2: Summary of single particle morphology analysis extracted from NS-EM micrographs for α-crystallin/client complexes 40

Figure 4: Quantitative structural characterization of α-crystallin/insulin complexes and co-aggregates by single-particle EM 42

Figure 5: Chaperone activity and structural characterization of native lens α-crystallin/lysozyme complexes and co-aggregates 47

Supplemental figures

Supp. Figure 1: Biochemical isolation and structural assessment of recombinant apo-state α-crystallins 65

Supp. Figure 2: Image processing workflow applied to NS-EM micrographs for the morphological analysis of individual sHSP complexes and co-aggregates applied using the software FIJI 66

Supp. Figure 3: Dynamic light scattering measurements of α-crystallin/lysozyme reactions and micrograph of aggregated lysozyme 67

Supp. Figure 4: Half-maximal ratio analysis for α-crystallin/lysozyme chaperone assays 68

Supp. Figure 5: Representative micrographs and single-particle shape analysis for αAc/lysozyme complexes 69

Supp. Figure 6: Representative micrographs and single-particle shape analysis for αBc/lysozyme complexes 70

Supp. Figure 7: Representative micrographs and single-particle shape analysis for αAc and αBc/lysozyme complexes 71

Supp. Figure 8: Representative micrographs and single-particle shape analysis for αLc/lysozyme complexes 72

Chapter 3

Figure 1: Single-particle Cryo-EM analysis of mjHSP16.5 in the absence and presence of destabilized client 79

Figure 2: Conserved Phe residues within the NTD are critical to sHSP assembly, stability, and chaperone function 82

Figure 3: Flexible CTD interactions facilitate multiple oligomeric states that correlate with weakened inter-protomer contacts 89

Figure 4: Local resolution analysis of mjHSP16.5/lysozyme complexes reveal polarized stability across each oligomeric state 92

Supplemental Information

Supp. Figure 1: Purified mjHSP16.5 constructs used in this study 110

Supp. Figure 2: Single-particle Cryo-EM processing workflow for mjHSP16.5 apo-37 and apo-75 datasets 111

Supp. Figure 3: Resolution assessment and 3D variability analysis of the apo-37 Cryo-EM dataset 112

Supp. Figure 4: Resolution assessment and 3D variability analysis of the apo-75 Cryo-EM dataset 113

Supp. Figure 5: Chaperone-client binding assays for mjHSP16.5 wildtype (mj-wt) and NTD variants (mj1x: F15A, mj-3x: F15/18/19A) 114

Supp. Figure 6: Single-particle Cryo-EM processing workflow for the mjHSP16.5/lysozyme dataset 115

Supp. Figure 7: Resolution assessment and non-canonical ACD/CTD interactions obtained from the mjHSP16.5/lysozyme dataset 116

Supp. Table 1 117

Supp. Table 2 118

Appendix Chapter 1

Figure 1: Single-particle Cryo-EM analysis of αB-crystallin (dataset #1) 128

Figure 2: Single-particle Cryo-EM analysis of αB-crystallin (dataset #2) 129

Table 1 131

Appendix Chapter 2

Figure 1: Comparative structural analysis of CaMKII holoenzymes resolved by single-particle EM 140

Figure 2: Comparative analysis of CaMKII holoenzyme stoichiometries resolved by single-particle EM 143

Figure 3: CaMKIIα and CaMKIIβ kinase domains form dimers within the holoenzyme 146

Figure 4: Clustering of CaMKIIα and CaMKIIβ induced by prolonged glutamate in wild-type neurons 149

Figure 5: CaMKIIβ self-aggregates in vitro*, but less than CaMKIIα* 150

Figure 6: Clustering of CaMKIIα and CaMKIIβ induced by prolonged glutamate in CaMKIIα knockout (KO) neurons 151

Figure 7: Overview of structural states supported by CaMKII holoenzymes under basal and ischemic conditions 153

Key Resources Table 163

Supplemental Information 173

Figure S1: Effect of local kinase domain concentration on pT286-CaMKIIα and pT287-CaMKIIβ in vitro *kinetics. Related to Figure 1.* 173

Figure S2: CaMKIIα and CaMKIIβ activation by CaM: individual experiments. Related to Figure 3. 174

Figure S3: EM analysis of CaMKII holoenzyme clustering under basal conditions. Related to Figure 4. 175

Figure S4: CaMKIIβ does not move to inhibitory synapses following prolonged glutamate. Related to Figure 4. 176

Figure S5: Aggregation of heteromeric CaMKIIα/b holoenzyme. Related to Figure 5. _____ *177*

Figure S6: CaMKII movement normalized and compared by genotype. Related to Figures 4 and 6. _____ *178*

Acknowledgments

To my parents for stressing the importance of college so I don't "end up like them" and to my partner, Kassondra Watson, who continually inspires me to become a better person and scientist.

Special acknowledgment to Dr. Steve Reichow for guidance throughout my PhD program and to the family that is the Reichow Lab for all the inspiration, teaching, and laughs.

Abstract

The family of small heat shock proteins (sHSPs) are molecular chaperones that function in preventing protein aggregation induced by various cellular stresses (e.g., temperature, pH, oxidative stress). The sHSPs utilize an ATP-independent “holdase” function to sequester aggregation prone “clients” in soluble complexes where the client can later be released for refolding by ATP-dependent chaperones (e.g., HSP70/100 systems). Humans encode ten sHSPs with varying tissue expression patterns and functional demands. In addition to their roles in aggregation prevention, sHSPs help regulate a variety of other cellular processes, such as apoptosis, cytoskeletal dynamics, and cellular development. Because of these central roles, many human sHSPs are associated with human disease, in particular aggregation-related and age-related diseases, such as Alzheimer’s and Parkinson’s diseases, cataracts, and cardiovascular diseases. Despite decades of research, there remain major gaps in understanding the mechanisms of sHSP client sequestration and how these chaperone systems respond to saturating conditions of clientele.

Unique and dynamic features of sHSP structure and function are exemplified in all kingdoms of life, where this family of chaperones exhibits diverse cellular roles with equally varied structural morphologies and characteristics. Through dynamic multi-domain interactions, many sHSPs form large and polydispersed oligomeric assemblies which respond to environmental conditions (e.g., temperature and pH) and client characteristics (e.g., size and destabilization). These dynamic assemblies are supported by an underlying propensity to rapidly exchange subunits between oligomers, with subunit exchange dynamics being a necessity for the chaperone function of many sHSPs. The high-degree of structural heterogeneity of sHSPs – via intrinsically disordered regions, polydisperse assemblies, subunit exchange dynamics, and heterogeneous client-binding interactions –

have delivered a challenge to defining mechanisms that enable these features and elucidating their “holdase” function.

The research presented in this dissertation set out to define mechanistic details of sHSP assembly and client-induced polydispersity/co-aggregation by leveraging single-particle methods employed by electron (cryo-)microscopy. I developed a semi-automated approach to extract single-particle measurements of sHSP/client complexes imaged directly by electron microscopy, enabling the quantitative characterization of client induced co-aggregation of the eye lens sHSP α-crystallin (αAc and αBc). These studies describe a conserved mechanism of quasi-ordered expansion and elongation of the sHSP scaffold that is induced upon increasing client saturation – providing novel mechanistic insight into the titration model of age-related cataract formation (Chapter 2). Then, using the archaeal sHSP (mjHSP16.5) as a model system, I harnessed the high-resolution capabilities of cryo-electron microscopy (Cryo-EM) to define, for the first time, an atomic-level description of sHSP client sequestration and induced polydispersity. These studies unveiled features of the elusive sHSP N-terminal domain that enable chaperone plasticity, and uncovered a process of client induced polarization of sHSP stability that facilitates directional elongation of sHSP/client complexes (Chapter 3). Together these results provide important structural details on how sHSPs assemble and respond to unfolding clientele and deliver long-sought high-resolution details of sHSP chaperone function.

CHAPTER 1: Structure & Function of small heat shock proteins

Sub-section 1: Overview of small heat shock proteins

The family of small heat shock proteins (sHSPs) has evolved for stress response and plays supportive roles in cellular proteostasis across all domains of life[1–4]. (Figure 1a). sHSPs were first discovered through their upregulation during heat stress in *Drosophila* and later shown to provide chaperone activity during stress conditions *in vitro*[5–7]. sHSPs prevent irreversible aggregation of partially denatured proteins (clients) through an ATP independent "holdase" function that responds rapidly to many types of stress events (*e.g.,* heat shock, pH stress, oxidative stress)[5,8–13]. Additionally, sHSPs are present under basal conditions with function pertaining to regulation of apoptosis and autophagy, cell cycle and development, mitochondrial proteostasis, and cytoskeletal structure[14–25]. The sHSPs are regulated at the transcriptional and translational levels to provide basal level pools of available chaperone and fast response mechanisms during cellular stress events[26,27]. Many sHSPs are additionally regulated through post-translational modification (e.g., phosphorylation, glycation) and hetero-oligomerization with other sHSPs which alter oligomer size and specificity of interactions toward clients[14,28–34]. The sHSPs have high selectivity to unfolding clientele and interact with an array of partially unfolded proteins when executing their chaperone function[35–37]. Importantly, sHSPs can maintain clientele in refolding competent states for downstream processing by ATP-dependent refolding machinery after stress conditions have subsided[38–40]. This prevention of aggregation and maintenance of client proteins by sHSPs is described as a 'hold-ase' function and provides a valuable mechanism for cells to respond to and recover from a myriad of stress events.

Small heat shock proteins perform diverse roles throughout the body with numerous implications in health and disease. Humans encode ten sHSPs (HSPB1-10) that vary in their function and expression throughout the body (Figure 1b) and are referred to by

a

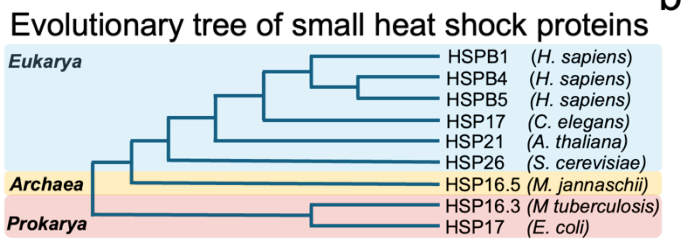

b

Human sHSP	Location	Disease
HSPB1	Ubiquitous	
HSPB2	Muscle/brain	
HSPB3	Muscle/brain	
HSPB4	Eye lens	
HSPB5	Ubiquitous	
HSPB6	Ubiquitous	
HSPB7	Heart/muscle	
HSPB8	Ubiquitous	
HSPB9	Testes	
HSPB10	Testes	

cardiac, neurological, cancer, skeletal muscle, eye lens, blood, reproductive

c

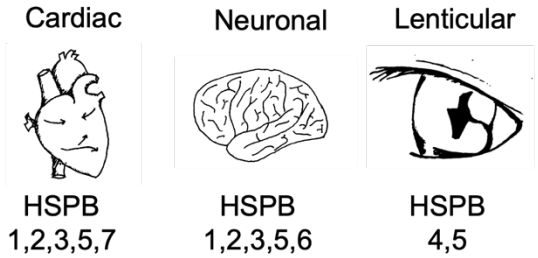

Figure 1: Overview of small heat shock protein diversity and association with human disease **(a)** Schematic overview of evolutionarily distant small heat shock proteins from all domains of life covering Vertebrates (HSPB1, HSPB4, and HSPB5, human), invertebrates (HSP17, *C. elegans*), plants (HSP21, *A thaliana*), fungus (HSP26, *S. cerevisiae*), Archaea (HSP16.5, *M. jannaschii*), bacteria (HSP16.3, *M. tuberculosis* and HSP17, *E. coli*) **(b)** Table describing the expression location and disease association for human HSPB1-10 (pictographic key below table) **(c)** Depiction of human sHSPs associated with cardiac (HSPB1,2,3,5,7), neuronal (HSPB1,2,3,5,6), and lenticular (HSPB4,5) age-related diseases in long lived tissues.

various names: HSPB1 (HSP27), HSPB2 (myotonic dystrophy kinase binding protein, MKBP), HSPB3 (HSP17), HSPB4 (αA-crystallin, αAc), HSPB5 (αB-crystallin, αBc), HSPB6 (HSP20), HSPB7 (cardiovascular Hsp, cvHsp), HSPB8 (HSP22), HSPB9 (cancer/testis antigen 51, CT51), HSPB10 (outer dense fiber protein 1, ODFP1)[41]. Among these various isoforms, the α-crystallins (αAc and αBc) of the eye lens were among the first sHSPs to be identified with aggregation prevention properties and have been perhaps the most well studied[5,42–44].

Some sHSPs exhibit wide expression and interaction with many cellular clients/substrates such as HSP27, αBc, HSPB6, and HSPB8. Other human sHSPs display more selective expression and distinct roles such as αAc in the eye lens, HSPB7 in cardiac tissue, and HSPB9-10 in testes. The sHSPs are of small size (12-43 kDa), although many form large oligomeric structures[1]. Overlapping expression of sHSPs can allow for hetero-

oligomerization with modulatory effects on function and client preference[14,28,45]. Due to the pleiotropic function of human sHSPs, mutation and dysregulation are associated with many diseases and their association with age-related diseases will likely become more relevant as the aged population rises and lifespans increases (Figure 1c)[46–49].

The wide distribution of sHSPs in the body is accompanied by a range of functional roles with some sHSPs being constitutively expressed in long-lived cells and tissues and playing multiple roles in cellular physiology and pathophysiology[50]. There are five sHSPs (HSPB1,5,6,7,8) expressed in cardiac and skeletal muscle through which mutation and dysregulation are linked to various disease[51]. For instance, αBc shows high levels of expression in cardiac tissue and the αBc-R120G mutant is directly related to desmin-related cardiomyopthy[16,52–56]. Other abundantly expressed sHSPs in cardiac and smooth muscle are HSP27 and HSPB6 where they protect against ischemic and oxidative stress[51,55,57,58].

There is growing evidence for the role of sHSPs in development and protection throughout the central nervous system were a breakdown of proteostasis is a hallmark feature of many neurodegenerative diseases[59]. Multiple mutations in HSPB1 are directly associated with Charcot-Marie-Tooth disease type 2F – a degenerative nerve disease which impairs muscle size and strength[23,60]. Multiple *in vitro* studies have shown effective chaperone response by HSP27 and αBc toward amyloid aggregating proteins related to neurodegenerative diseases such as tau and amyloid-β (Alzheimer's disease, AD), polyglutamine (polyQ, Huntington's disease), and α-synuclein (Parkinson's disease)[61–68]. Further *in vivo* studies have shown roles for neuroprotection in mouse models and synaptogenesis in *Drosophila*[69–72]. HSP27 can efficiently modulate tau filament dynamics and rescues long-term potentiation in mouse models of tauopathy[29]. Recently, it was shown in human AD brain that HSP27 is secreted by astrocytes to the extracellular space during inflammatory response – showcasing an extracellular "non-cell-autonomous" role

in neuroprotection[73]. The diverse roles that sHSPs play in neuroprotection throughout life – from development through aging – highlight the importance of understanding these ubiquitous chaperones in disease.

Perhaps the most well-known example of sHSP function is in the eye lens where high concentrations of αAc and αBc (~3:1 ratio) make up ~30-40% of soluble protein content, support lens transparency for vision, and help prevent cataract disease[45,49,74–78]. The lens α-crystallins have served as a model system for studying sHSP structure due to the seemingly simplified metabolism and proteome complexity of this system. Nevertheless, cataract is an incredibly diverse and complicated disease, with significant variation in location, heredity, age of onset, and environmental factors – leaving the full etiology of this disease left to be completely understood. There are diverse disruptions and age-related challenges to α-crystallin lenticular chaperone function that result in the formation of large protein aggregates and subsequent disruption of vision, leading to cataract - the leading cause of blindness worldwide[48,49,79–83]. While αAc resides in other tissues and ocular regions at low levels, expression is by far the most abundant in the lens[84]. In contrast, αBc is one of the most widely expressed human sHSPs with abundance in the lens, heart/muscle, and brain[70,75,85]. Multiple mutations of αAc (e.g., R49C) and αBc (e.g., R120G) are associated with congenital cataract, resulting in early onset of the disease, and are listed in the online global cataract database Cat-Map[86–88].

In addition to displaying diverse roles in human health and disease, some sHSPs have shown intriguing connections to cancer biology for their roles in cancer proliferation and treatment resistance, making these proteins intriguing therapeutic targets[89–92]. Currently there are no drugs targeting sHSPs, due to challenges in gaining molecular level insight of their chaperone function. Many sHSPs exhibit extreme structural heterogeneity which has stymied a mechanistic understanding of their anti-aggregation properties and

how they interact with refolding and degradation pathways. Additional difficulties in targeting sHSPs arise from their importance in multiple cellular processes and the diverse array of clientele/substrates they bind. Overcoming these gaps in knowledge will require a detailed understanding of how sHSPs interact with clients and rigorous investigation into their function/misfunction in various disease states.

Sub-section 2: The α-crystallins: role in lens transparency and cataract

The eye lens exhibits unique adaptions and challenges to maintaining proteostasis required for transparency and vision. The primary function of the lens is to focus light onto the retina with minimal aberration, providing clarity (or acuity) of vision (Figure 2). To achieve this role the lens must maintain both transparency and a high refractive index, utilizing unique physiological adaptations to accomplish this task. To reduce light scattering, lenticular tissue is avascular. Furthermore, the highly-elongated mature lens fiber cells shed their large cellular organelles, resulting in minimal metabolic function[93–96]. The cytosol of lens fiber cells also contain a high concentration of crystallin proteins – up to 450 mg/mL – which form a liquid crystalline state with unique structure and packing features that provide a high refractive index and yet also prevention complete crystallization at such high concentrations[74,75,97]. The lens crystallins are comprised of two protein families – the aforementioned α-crystallins and the β/γ-crystallins – which are distinct in their structure and function[78,98,99]. In addition to these major cytosolic components, lens fiber membranes host an abundance of aquaporins, gap junctions, adherins, and other integral membrane proteins to facilitate the lens micro-circulatory system within this avascular organ and contribute to formation of tight cell-to-cell junctional interactions that serve to further reduce light scattering[100,101].

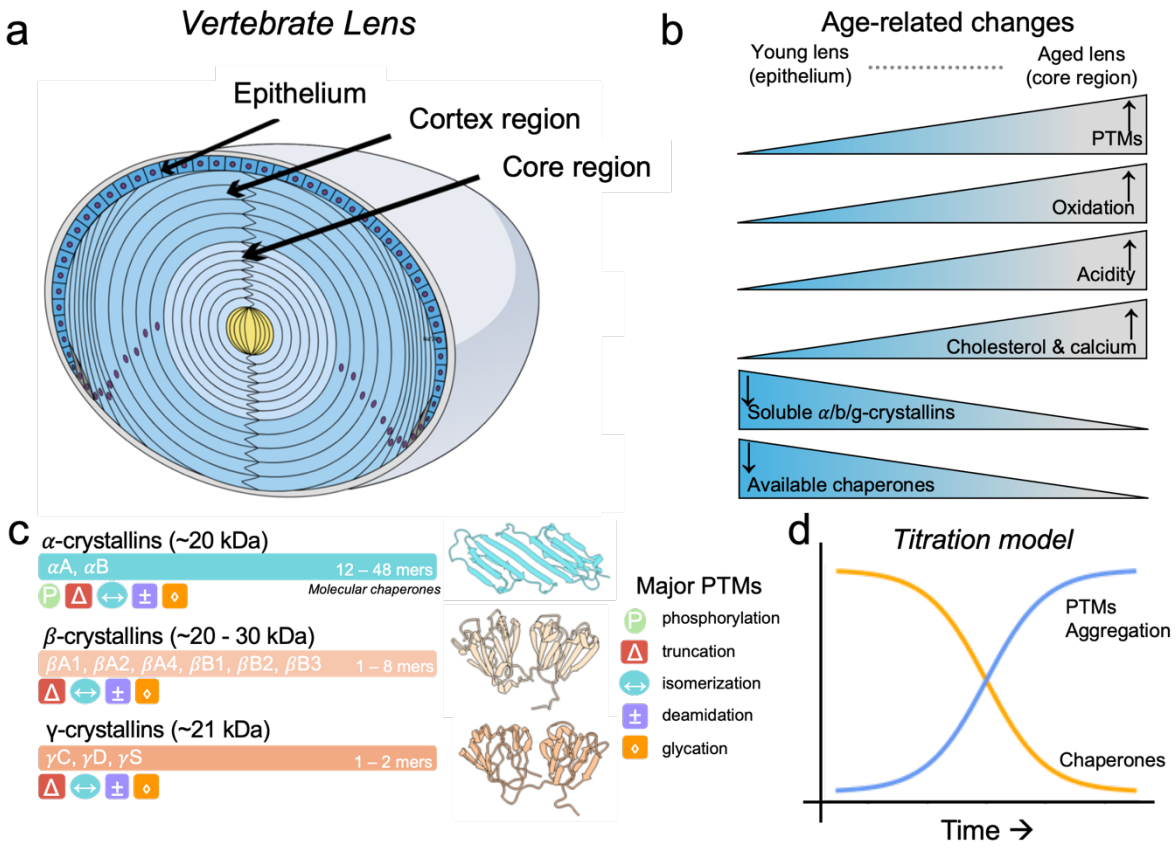

Figure 2: Age-related changes to the eye lens cellular structure and proteome modifications **(a)** Cartoon depiction of vertebrate lens highlighting the epithelial (youngest), cortex, and core (oldest) regions and loss of nuclei (black circles) from elongated lens fiber cells with age **(b)** Selected age-related changes to lens covering increases in crystallin post-translational modification (PTM), oxidation, acidity, cholesterol, and calcium accompanied by decreases in soluble lens crystallins and available α-crystallin chaperones. **(c)** Graphical representation of $\alpha/\beta/\gamma$-crystallins showing approximate molecular weight, oligomerization states, major PTMs, and structure (dimer: α-crystallin PDB 2n0k: , monomer: β-crystallins PDB 3lwk, γ-crystallin PDB 2m3t) **(d)** Generalized schematic of the ”titration model” of age-related cataracts relating an increase in post-translational modifications and aggregation associated with decrease in chaperone capacity of lens α-crystallins.

Lens fiber cells, once formed, continue to age throughout the organism’s lifetime. In the developing lens, there is a single layer of epithelial cells that divide and differentiate to form fiber cells (cortex region) which continuously envelop older fully mature fiber cells (core region)[102] (Figure 2a). As a result, the most mature fiber cells within the lens core are as old as the organism and must remain functional throughout life to support vision. Because of the minimal metabolic function within mature fiber cells there is little reliance

on protein synthesis, degradation, and refolding pathways. By the time lens fiber cells – and their constituent proteins – reach decades in age they have been faced with a variety of endogenous and exogenous stresses with potential impacts on protein stability and aggregation[103]. Age-related cellular changes – including increase in oxidation and acidity – chemically alter the lens crystallins which can decrease structural stability and alter surface charge properties[49,80,82,104] (Figure 2b,c). Chemical damage to the lens proteome can therefore accumulate throughout a person's lifetime, and multiple age-related modifications of lens crystallins have been identified in cataractous lenses including truncation, phosphorylation, deamidation, oxidation, isomerization, and glycation[80,82,105–108] (Figure 2c). Surprisingly, *in vitro* studies characterizing such modifications in $\alpha/\beta/\gamma$-crystallins often reveal minimal disruption to the overall protein fold, yet still induce alterations in stability and aggregation propensity[105,109–114].

To overcome the challenges to long-term protein stability the lens has evolved the α-crystallin (αAc/HSPB4 and αBc/HSPB5) sHSP chaperone system, representing ~30-40% of soluble lens protein[78,115]. As previously discussed, (*see Sub-section 1)*, sHSPs are a class of molecular chaperones important in preventing aggregation of destabilized proteins (clients) through an ATP-independent "holdase" mechanism. First isolated from the lens in the late 1800s and later recognized as heat shock proteins, the function of α-crystallins remained obscure until a hallmark paper by Horwitz in 1992 that showed the molecular chaperone function of the lens α-crystallins to prevent aggregation[5,116]. Since then the α-crystallins have been shown to prevent the chemical- or heat-induced aggregation of many native and non-native client proteins[35,111,117–120].

The "holdase" function of α-crystallins is thought to protect against age-related aggregation in the lens through the formation of soluble sHSP/client co-aggregates that delay large-scale aggregation events leading to cataract[77,121]. There is evidence from

mouse models that α-crystallins support lens transparency, especially the more abundant αAc[122,123]. Additionally, the polydisperse oligomeric structure of α-crystallins appears to be important for holdase function and may support lens transparency through structural and anti-crystallization properties[49,124,125]. Despite this importance to the physical properties of the lens and homeostasis, the polydisperse assemblies of α-crystallins and their interactions with native clients remain poorly understood, limiting mechanistic insights into the lens chaperone system.

Based on prevailing evidence, the so-called 'titration model' of age-related cataract has been developed which describes the accumulation of destabilized lens proteins throughout life that eventually overwhelms the α-crystallin system, leading to irreversible chaperone-client co-aggregates capable of scattering light and progressively reducing vision[77,108] (Figure 2d). This model is supported by multiple proteomics studies which identified an enrichment of modified α/β/γ-crystallins in the insoluble fractions of cataractous lenses[80,82,105,126–128]. Additional *in vitro* investigations of sHSP function (including α-crystallins) show diminished chaperone efficiency with increasing amounts of client and a concentration dependent chaperone activity[5,35,117,118]. Recombinant mutations mimicking congenital cataract in β/γ-crystallins and age-related PTMs (with incorporation of multiple PTMs) have proven useful in understanding the types of clients prone to aggregation in the lens[110–114]. For example, mutation mimicking UV-damage of a γ-crystallin (gD-W130E) interacts with α-crystallins at physiological temperature and pH[129–131]. Notably, co-aggregates of α-crystallins with clients formed *in vitro* and isolated high-molecular weight aggregates from aged lenses share morphological similarities and are notably distinct from apo-state α-crystallins (homomeric αAc and αBc) and αL-crystallin (heteromeric αAc and αBc) from younger lens tissue, respectively. These morphological differences include increased size, heterogeneity, and hydrophobicity as the α-crystallin

becomes saturated with client[35,115,118]. In addition, it is possible that morphological changes induced by saturation of α-crystallin chaperones would disrupt the relative abundance or nature of short-range interactions between soluble crystallins and promote their aggregation under the saturating conditions of the lens.

Although other pathways to cataract are likely present, the titration model has become widely accepted for describing a major avenue toward age-related cataract. There has yet to be a treatment targeting the titration model for cataractogenesis and there are significant limitations in understanding the multiple pathways likely responsible for cataracts. For instance, the multitude of post-translational modifications identified in the lens make it difficult to discern those contributing to aggregation from those that may be adaptive toward preventing aggregation . Additionally, it remains difficult to study α-crystallin interactions with β/γ-crystallins at physiological temperature, pH, and concentrations relevant to the lens due to their high-stability and evolved structures that limit stable interactions.

Despite effective surgical treatment, much of the world remains susceptible to the impacts of cataract and associated blindness – demanding more accessible treatment options. Current animal models and *in situ* methods to investigate age-related cataract are limited in their applicability to human-age scales and spatiotemporal resolution, respectively. Developing treatments to prevent cataract will likely entail an understanding of α-crystallin chaperone function, client destabilization effects, and how these relate inside of the tightly packed and regulated environment of the lens. Newly developed models of cataract based on lens organoid culturing is a promising avenue for studying protein stability in the tightly packed lens, however the long-time scales associated with cataract formation may still impose limitations in their physiological relevance[132,133]. Cataract therapies to either prevent client destabilizing modifications or slow the co-aggregation rate of α-crystallin/client complexes may provide promising avenues for

treating this widespread disease. Of note, the full etiology of cataract is likely diverse involving additional modes toward aggregation that involve disruption to the lens fiber membrane and the membrane protein-mediated micro-circulatory system of the lens.

Sub-section 3: The structure of sHSPs

The sHSPs are an intriguing class of proteins from a structural biology point-of-view, as many are capable of displaying a wide array of polymorphic states. All sHSPs share a conserved tripartite domain organization comprised of a ~70 residue central α-crystallin domain (ACD), flanked by a dynamic N-terminal domain (NTD) and flexible C-terminal domain (CTD) (Figure 3a,c)[1,134]. Multiple structural studies of the core ACD reveal 8-9 β-strands, arranged in an antiparallel immunoglobulin-like fold with one face of the β-sandwich comprised of β4, β5, and β6/β7 and the other face with β2, β3, β8, and β9[135–140]. Many sHSPs readily dimerize and the dimer constitutes a basic structural unit that establishes larger oligomeric structures observed in many sHSPs (Figure 3b,c). Notably, the foundational ACD dimer is distinct between identified metazoan and non-metazoan sHSPs. This is due to variation in the number and arrangement of β-sheets in the ACD leading to dimerization along the extended β6+7 strand of metazoans (β7-interface dimer), while non-metazoan dimerization occurs via swapping extended β5-7 loops (β6-swapped dimer) with a neighboring ACD (Fig3b, yellow β-strands). Functionally, the ACD is shown to contribute directly to chaperone function through interaction with amorphous and amyloid aggregating clients[62–64,141]. The ACD of αAc contains a 19 residue segment that displays effective aggregation prevention deemed the “mini-chaperone”[63,68,142,143].

In contrast to the highly conserved ACD, the flanking CTD and NTD are much more variable in sequence, length and complexity[1]. The CTD is diverse among sHSPs, shown to play a role in maintaining structural flexibility and contains a high density of charged

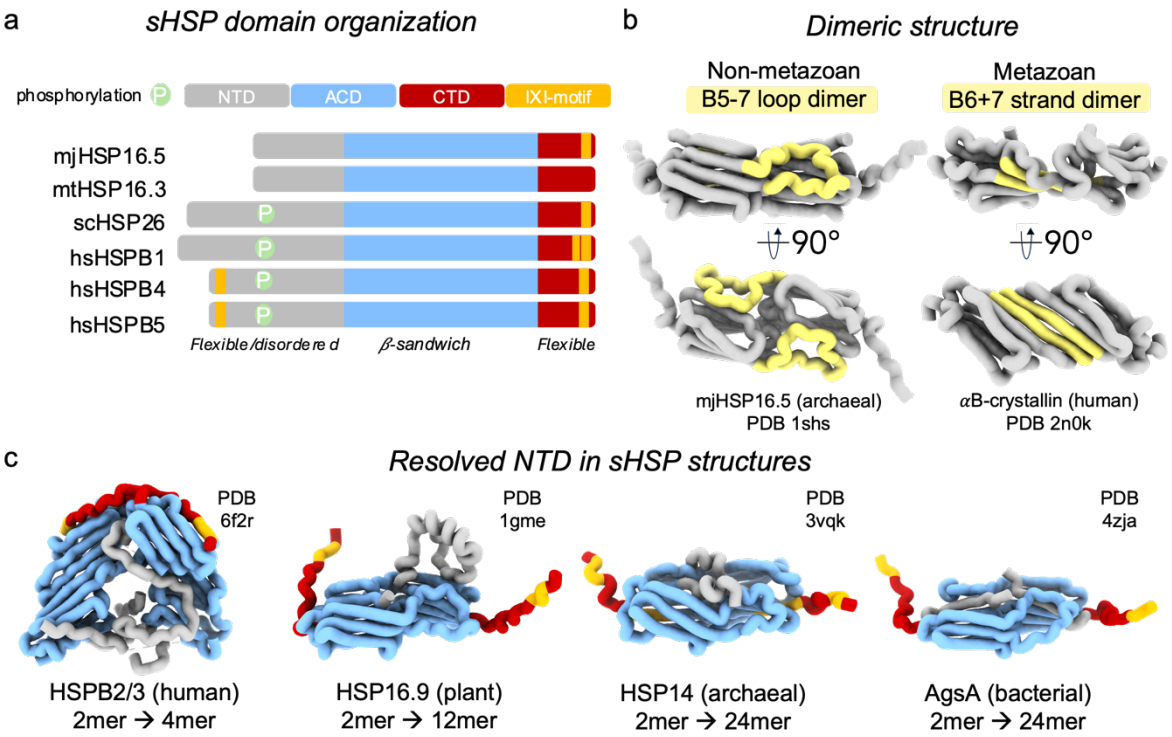

Figure 3: Small heat shock proteins share conserved and divergent features across all domains of life **(a)** Schematic representation of sHSP tripartite domain organization showing the N-terminal domain (NTD, gray), α-crystallin domain (ACD, blue), C-terminal domain (CTD, red), IXI-motifs (yellow), and phosphorylation prone NTDs (green). Bar lengths for each sHSP indicate relative primary sequence length. **(b)** Dimeric structure of non-metazoan (β5-7 loop exchange) and metazoan (β6+7 strand exchange) sHSPs. The exchanging loop and β-strand are highlighted yellow for HSP16.5 (PDB 1shs, non-metazoan) and αB-crystallin (PDB 2n0k, metazoan), respectively. **(c)** Selected sHSPs revealing partial N-terminal domain structure for human HSPB2/3 (4mer), pea HSP16.9 (2mer from 12mer complex), archaeal HSP14 (2mer from 24mer complex), and bacterial AgsA (2mer from 24mer complex). Coloring scheme is the same used in panel (a) NTD:gray, ACD:blue, CTD:red, and IXI-motif:yellow.

residues that helps facilitate solubility. Additionally, a highly conserved IXI motif has been identified in the CTD of most sHSPs, which binds to a hydrophobic groove in the ACD of another protomer, contributing to high-order assembly (Figure 4a,c)[4,125,144–146].

The most diverse region of sHSP structure is the NTD, which a has variable length and is notably less conserved across species/isoforms[1]. Truncation of the NTD disrupts high-order oligomer formation and alters chaperone activity, showcasing the importance to structure and function of this domain[125,146,147]. Multiple human sHSPs have been isolated with phosphorylation of serine residues in the NTD. Mimicking phosphorylation *in*

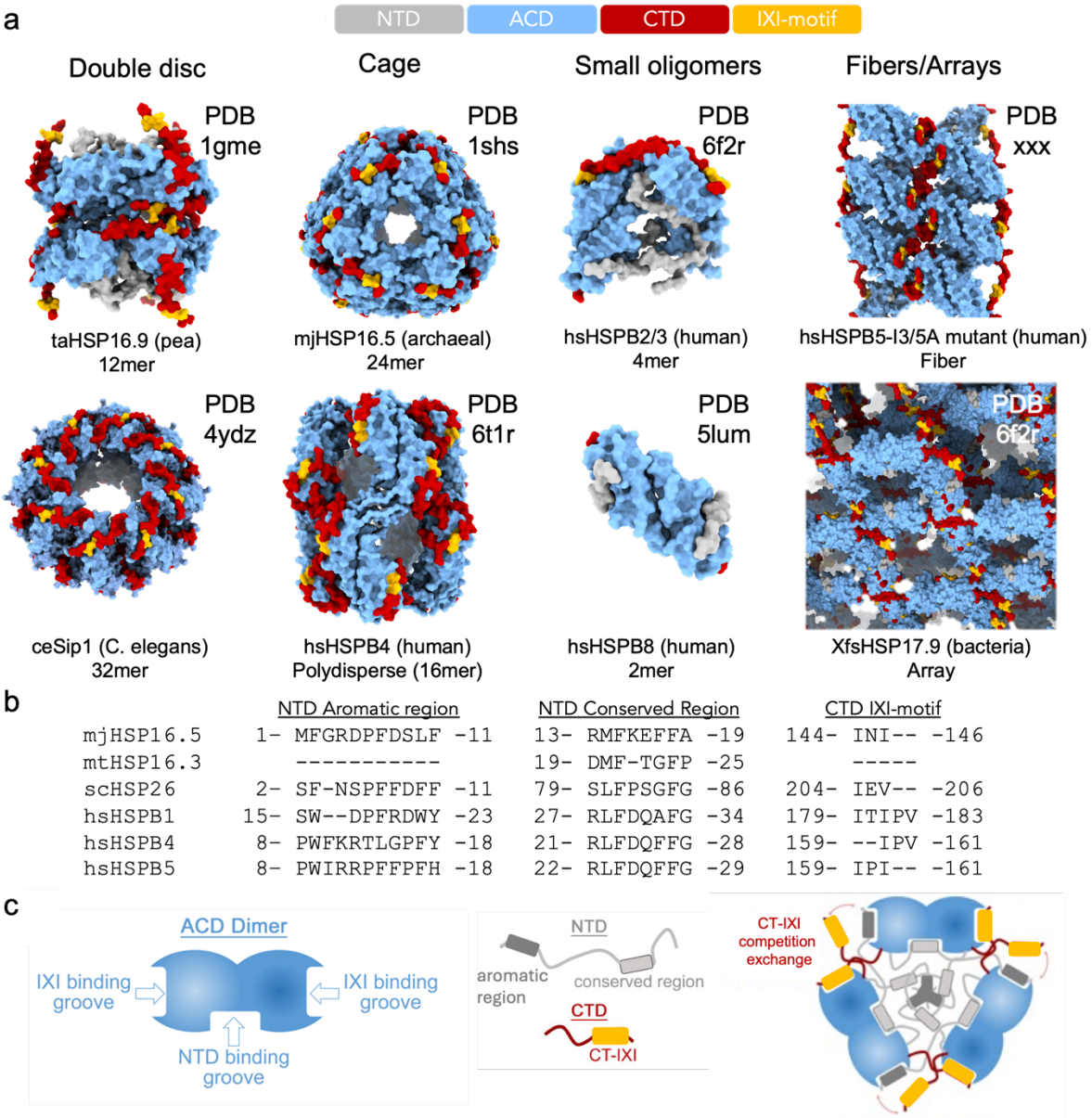

Figure 4: Diverse oligomeric morphologies of sHSPs are supported by competing interactions of NTD, ACD, and CTD **(a)** Various oligomeric states of sHSPs covering double-discs (HSP16.9 and Sip1), cages (HSP16.5 and αA-crystallin), small oligomers (HSPB2/3 and HSPB8), and fiber/array formations (αB-crystallin I3/5A and HSP17.9). Color scheme shown on top (NTD:gray, ACD:blue, CTD:red, IXI-motif:yellow) **(b)** Sequence alignment of the "Aromatic" and "Conserved" regions of the NTD and the CTD IXI-motif of archaeal HSP16.5 *(M. jannaschii),* bacterial HSP16.3 (*M. tuberculosis*), yeast HSP26 (*S. cerevisiae*), and human HSPB1, HSPB4, and HSPB5. **(c)** Schematic representation of binding donor (IXI and ACD grooves) and acceptor (NTD-aromatic region (dark gray), NTD-conserved region (gray), and CTD IXI-motif (yellow)) regions of sHSPs that facilitate oligomerization. The dimer is represented in blue.

vitro induced a shift toward smaller oligomer sizes, increased surface hydrophobicity, and modulated sHSP function in cells[29–32,68]. Despite the high-degree of variation within the NT

there are some conserved aspects, including what have been deemed the “aromatic region” and “conserved region” (Figure 4b)[148,149]. Multiple studies point to these regions as being important for the oligomeric structure and chaperone activity of sHSPs, likely through condensing subunits through hydrophobic interactions and facilitating polydispersity, respectively[148–152]. Mutation of an arginine in the conserved region altered the structure and function of multiple human sHSPs[149–152]. Intriguingly, albeit rare, an additional IXI-motif can be found in the NTD of some sHSPs, and shows importance for client interactions and modulation of oligomeric structure[63,153]. Remarkably, an αBc-I3/5A mutant has been show to assemble reversibly into helical filaments with diminished chaperone activity[145]. The few studies revealing NTD structure uncover helical regions and multivalent interactions with the ACD[137,140,145,154–156]. Solved oligomeric structures suggest the NTD is less solvent exposed and likely clustered within cavities formed by caged/fiber assemblies or closely associated with other regions of the oligomer[4,137,138,157].

The sHSPs form diverse oligomeric assemblies existing as flat/disc-like (HSP16.9, HSPB2/3, ceSip1), cage-like (αAc, αBc, mjHSP16.5, hsHSPB1, ceHSP17, *E. coli* IbpA/IbpB, scHSP26), and array/fibrillar (ehHSP18.5, salmonella AgsA) (Figure 4a) [4,10,32,117,137,138,144,154,155,157–161]. While some sHSP oligomers are mono-dispersed (mjHSP16.5, wheat HSP16.9), most others – including the aforementioned α-crystallins – form a polydisperse ensemble of oligomers. The quaternary assemblies of polydispersed sHSPs are fluid with subunit exchange and quaternary dynamics being an important aspect of chaperone function[30,162–166]. Subunit exchange is thought to expose hydrophobic regions to facilitate client interactions although some sHSPs exhibit chaperone activity regardless of modifications that limit subunit exchange (crosslinking, mutation/truncation)[125,150,162,162,167]. However, experiments on sHSP subunit exchange often involve fluorescent labeling which may alter polydispersity and oligomer assembly/disassembly and may not faithfully reflect the wildtype structure/function[168].

Regulation by phosphorylation and/or pH can alter the size, subunit exchange kinetics, and stability of some sHSPs with associated effects on chaperone function[30,32,139,169–171]. Additional complexity in quaternary structure, exchange dynamics, and function arises via hetero-oligomerization[14].

The molecular level details of sHSP/client interactions are limited by the dynamic and heterogeneous nature of sHSPs, and evolutionary diversity has limited a universally applicable mechanistic understanding of their chaperone function. Despite these limitations, there have been multiple sHSP/client interactions observed that showcase the diverse morphological response of sHSPs during stress events and highlight some conserved features. For example, all three structural domains of sHSPs (NTD, ACD, and CTD) play some role in chaperone function, either through direct interactions with clients or through contribution to the dynamic assembly of sHSPs. Crosslinking mass-spectrometric studies of the yeast sHSP HSP26 show diverse and widespread interactions with clientele, involving the NTD, ACD, and CTD[172]. Furthermore, it's been reported that a 10-residue segment in the middle of the NTD of αAc and αBc is responsible for differential chaperone activity between the two isoforms[149].

Despite inherent difficulties in studying heterogeneous protein structures there has been some progress in understanding how competing interactions across structural domains drives plasticity and polydispersity in mammalian sHSPs (Figure 4c). Human HSP27 and αBc show prominent inter- and intra-molecular interactions between the NTD, ACD, and CTD in oligomer assembly and polydispersity[65,148,149]. Using structural restraints from mass spectrometry and nuclear magnetic resonance, a model has been proposed for polydispersity of αBc oligomers through interconverting polyhedrons composed of monomer/dimer building blocks[173]. Polydispersity of the monodisperse mjHSP16.5 can be induced through insertion of an NTD peptide from human HSP27 and alteration of the sequence within this insert modulated the resulting oligomeric species[174,175]. The

polydispersity of α-crystallins has been well documented through various electron microscopy studies, and mass spectrometry has defined the range of the oligomeric ensemble of αB-crystallin (24 - 33mers)[118,124]. Despite what has been revealed about polydispersity in sHSPs there remains an incomplete mosaic view of how multiple interactions contribute to forming/interconverting oligomers. Characterizing polydispersity of sHSPs – in the absence and presence of clientele – will help develop a framework for how these diverse chaperones support proteostasis.

Sub-section 4: Client recognition and co-aggregation of sHSPs

As mentioned in S*ub-section 3*, many sHSPs display diverse interactions with clients – utilizing the NTD, ACD, and CTD to maintain structural plasticity and prevent aggregation (Figure 5). While structural plasticity of sHSPs has been a major hurdle in mechanistically characterizing their chaperone mechanism, multiple clues to this process have been gleaned – with some general themes emerging related to client recognition and co-aggregation.

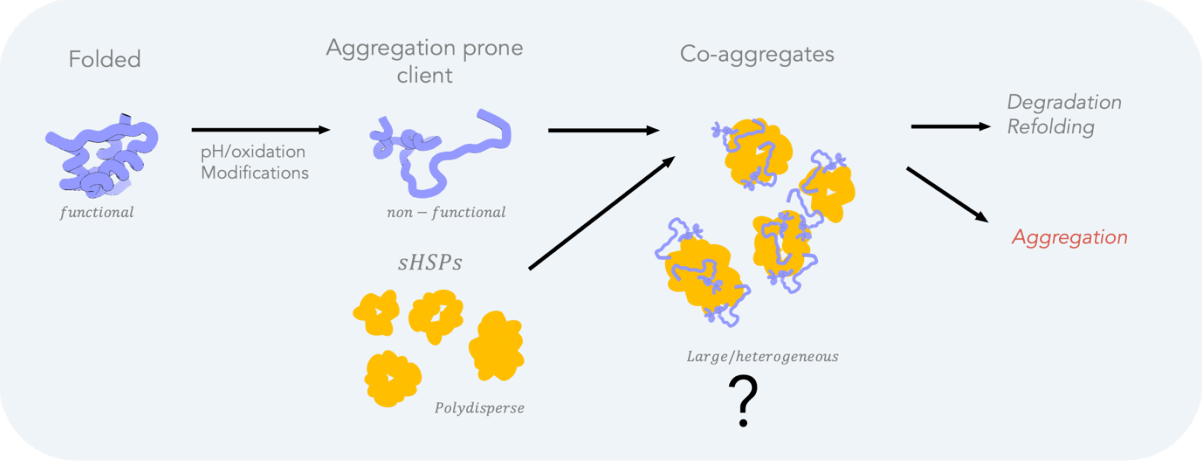

Figure 5: Generalized schematic representing sHSP "holdase" function in response to stress-induced client unfolding. Cellular stress events and modifications disrupt functional protein folds which lead to partial unfolding of a prospective client (purple). sHSPs (yellow) recognize and bind partially unfolded clients, forming soluble co-aggregates which can transfer the client to ATP-dependent refolding and degradation pathways. Conversely, in the eye lens sHSP/client co-aggregation can lead to lens opacification and disrupted vision, known as cataract.

During cellular stress events, prospective destabilized clients emerge which are recognizable by the resulting exposure of multiple hydrophobic binding sites recognized by the sHSP[172,176–178]. The sHSPs show very little specificity, capable of acting on a wide range of cellular clients and form soluble sHSP/client co-aggregates *in vivo*[36,37]. When bound by sHSP, clients remain in a refolding competent state for downstream recovery by the HSP70 stress response system[11,40,179]. *In vitro* studies have shown multimodal binding and an increased affinity toward more energetically destabilized clients, possibly reflecting an adaptive trait for stress response. In a series of papers, Mchaourab, et al. propose a chaperone mechanism based on two-modes of client binding that trade-off binding affinity and capacity based on the level of client destabilization and chaperone saturation[119,180–182]. Using a series of bimane-labeled T4-Lysozyme (T4L) mutants with known differences in $\Delta G_{unfolding}$, the researchers demonstrated under equilibrium conditions that α-crystallins can bind two distinct unfolded states of T4L – using the low-affinity/high-capacity binding mode for the more destabilized T4L state. In a follow-up study this was also demonstrated with the archaeal HSP16.5 – highlighting possible conserved features of sHSPs through distant domains of life[183].

sHSP/client co-aggregates play both physiological and pathophysiological roles within the cell (*see Sub-section 2)*. While the structural complexity and heterogeneity of induced co-aggregates has hindered structural characterization at high resolution, several studies aimed at elucidating these formations have shed light on the client-induced co-aggregation process. Mass spectrometric studies of pea HSP18.1 with the client firefly luciferase revealed over 300 sHSP/client complexes with varying stoichiometries that exhibit separate binding and augmentation stages of co-aggregation[184]. *Chapter 2* of this dissertation describes a mechanism of expansion and elongation of αAc, αBc, and natively extracted ovine αLc with the clients lysozyme and insulin to produce a continuum of co-aggregate states, ranging from ~14 nm cages to 100 nm long fiber-like complexes and

large (>300 nm) amorphous co-aggregates[118]. The co-aggregates identified in this work show striking resemblance to high-molecular weight aggregates isolated from the aged lens[115]. Client size and the compound binding of multiple clients influence the morphological rearrangements of sHSPs when confronted with unfolding client[157,185,186]. Recently, a novel method for studying sHSP co-aggregation was developed using single-molecule fluorescence and TIRF-microscopy/photobleaching to uncover the stoichiometries of multiple αBc/client complexes that support a two-mode co-aggregation process whereby an initial binding step is followed by recruitment of more sHSP subunits[168]. In a follow up study, Benesch, et al. show a similar mechanism with HSP27 and that recruitment of additional sHSP subunits may be both chaperone and client dependent[187]. Together these studies convey inherent plasticity of sHSPs and sHSP/client complexes as an important and conserved feature of these chaperones.

In addition to their canonical “holdase” function, some sHSPs further possess an “aggregase” function that promotes sHSP/client co-aggregation and cellular localization during stress events. Holdase and aggregase function HSP26 and HSP42 in *S. cerevisiae* are shown to provide different modes of client interaction, where HSP42 promotes the formation of larger co-aggregates under stress conditions[188]. HSP17 from *C. elegans* showed multifunctionality toward various clients with differential aggregation propensity and interaction with refoldases – providing further evidence of client influence on sHSP function[189]. The ability of sHSPs to form dynamic aggregates is also showcased in sHSP contributions to regulating phase separation inside of the cell. Human HSPB3 regulates the phase separation properties of HSPB2 in cells. Mutations in HSPB3 are associated with myopathy, and may be a consequence of disrupted HSPB2/3 hetero-oligomerization and subsequent formation of aberrant phase separation of HSPB2[190,191]. Human HSP27 and HSPB8 are involved in the maintenance of stress granules – large membrane-less/phase-separated organelles containing large amounts of untranslated mRNA and

RNA binding proteins – and are related to stress response and aging[192,193]. Deciphering the myriad sHSP/client interactions within cells and influence of client on co-aggregation will be crucial for understanding how sHSPs support proteostasis and facilitate robust stress protection and other diverse physiological roles.

Despite decades of effort, there are still many open questions regarding fundamental aspects of sHSP chaperone function. Characterizing the structural transitions which accommodate client binding has remained challenging largely due to the heterogeneous nature of these interactions. For instance, previous EM studies indicate bound client resides on the inside of mjHSP16.5 oligomeric cage, effectively forming a steric border from the environment[183]. In contrast, a high-resolution structure of a monomeric plant sHSP bound to a native client highlights the diversity in holdase schemes among this diverse family of chaperones[176]. Moreover, the consequences of hetero-oligomerization, co-aggregation, and client-binding promiscuity are all still not well understood. Understanding these processes will help drive translational studies to harness sHSPs as therapeutic targets/agents and as potential biomarkers for disease and aging. A major aim of this dissertation is to extend the current understanding of sHSP/client co-aggregation and define pathways of co-aggregation relevant to cataract and other protein aggregation related diseases.

Sub-section 5: Single-particle approaches of electron microscopy to characterize the dynamic structure and function of sHSPs

The aims of my dissertation research attempt to fill gaps in knowledge on the pathway from initial client binding by a sHSP to the ultimate formation of large sHSP/client co-aggregates relevant to light-scattering structures associated with cataract. The lens α-crystallins are a model system for studying polydisperse sHSPs and their direct roles in supporting vision make them attractive therapeutic targets. The α-crystallins offer an interesting comparison of isoform and hetero-oligomeric modulation, while also utilizing

common sHSP mechanisms such as subunit exchange and polydispersity for chaperone function. Additional interest in this system lies in developing a foundational understanding for the molecular basis of aging and mechanisms that drive pathophysiological protein aggregation-related disease.

My dissertation project started with a characterization of the client-induced co-aggregation of α-crystallins (αAc and αBc) with the model clients, lysozyme and insulin. These clients were chosen for their historical use in the field, and that they are relatively small in size (similar to β/γ-crystallins) and display similar aggregation kinetics upon disulfide reduction-induced unfolding at physiological temperature (37° C) and pH range (~ pH 7). Upon incubation with client under reducing conditions there was a noticeable shift in size and polydispersity of αA/client and αB/client complexes and a concentration dependent reduction in client aggregation/co-aggregation, similar to previous studies with other sHSPs. To overcome the obstacle of quantitatively characterizing the complex range of morphologies induced under these varying conditions and characterize the aggregation pathway of these sHSP/client systems, I developed an approach to analyze the size of individual sHSP/client particles visualized directly by electron microscopy (EM). The co-aggregates formed by αAc and αBc displayed features indicative of a conserved mechanism of client-induced expansion and elongation, whereby chaperone/client co-aggregates reached lengths up to 100 nm while maintaining widths of ~15-20 nm (similar to the initial apo-state). Further study of the αL-crystallin hetero-oligomer isolated from sheep lenses showed the client-induced elongation and expansion mechanism is preserved by these native assemblies. Overall, this work defines a conserved pathway of client-induced co-aggregation for α-crystallins with lysozyme and insulin and present a novel single-particle approach for characterizing the heterogeneous sHSP/client structures. This work is presented in *Chapter 2: "The α-crystallin chaperones undergo a*

quasi-ordered co-aggregation process in response to saturating client interaction" in the form published by the Journal of Molecular Biology[118].

High-resolution CryoEM is a potentially powerful tool for characterizing the structural heterogeneity presented by sHSPs to uncover molecular mechanism of their chaperone function. I attempted to resolve the structures of various oligomeric states of apo-state αBc by CryoEM. After multiple datasets and sample optimizations, I ultimately faced challenges from the continuum of compositional/conformational heterogeneity that could not be overcome by current methods (discussed further in *Appendix Chapter I*). Realizing these intractable difficulties and understanding the conserved features of distantly related sHSPs, I pivoted my focus to the monodispersed archaeal sHSP (mjHSP16.5) as a simplified system to address questions concerning the role of the NTD in facilitating high-order oligomerization and client-induced co-aggregation (Chapter 3). The structure of mjHSP16.5 was first published in 1998 and further published EM structures demonstrate the formation of a similar cage structure and two-mode binding to that of the α-crystallins[138,183,194]. Therefore, it was expected that principles of oligomer formation facilitated by the NTD and induced polydispersity present in mjHSP16.5/client complexes would provide relevant insight to how other oligomeric sHSPs assemble & function.

In previously determined high-resolution structures of mjHSP16.5, details of the NTD have been limited or completely unresolved[138,194]. I was able to obtain a CryoEM dataset of the apo-state of mjHSP16.5, and resolved the structure to 2.3-2.5Å resolution, which revealed helical density in the cavity of the cage and lining the inside of the ACD dimer interface belonging to the NTD – providing the first insights into the role of this domain in facilitating high-order oligomerization. Furthermore, I showed the apo-state caged-assembly adopts multiple conformational states that vary in size through various modes of stretching and expansion that are accompanied by NTD rearrangements. The

newly recognized features were of sufficient quality for atomic modeling and uncovered a putative “Phenylalanine-shuffling” mechanism proposed to stabilize oligomerization and conformational plasticity. Further structure-guided mutational studies of these conserved regions provide further evidence for their role in stabilizing oligomers and guiding co-aggregate formation.

CryoEM analysis was performed on mjHSP16.5 incubated with lysozyme at 75° C – functionally relevant temperatures to mjHSP16.5 and where lysozyme (Tm ~80C) is destabilized, but not fully unfolded. Single-particle analysis of this specimen unveiled multiple chaperone/client oligomeric states (26mer, 32mer, 34mer, and 36mer) that could be fully resolved. These are the first high-resolution structures for client-bound sHSP complexes and highlight mechanisms of dimer capture/insertion, CTD dynamics/client-binding, and maintenance of a cage-like structure in sequestering destabilized lysozyme client(s) to prevent aggregation. Comparative analysis of the multiple client-bound states provided evidence for an induced polarization of oligomeric stability (stable->unstable), yielding key insight into a mechanism for client-induced elongation. This work is described in *Chapter 3: Structural mechanisms of small heat shock protein client sequestration and induced polydispersity”* and presented in the form that is planned for submission for publication.

In addition to these primary works, my interest in the functional role of protein dynamics and polydispersity was applied to a collaboration with Professor Ulli Bayer’s laboratory (University Colorado, Anschutz), applying single-particle methods in EM to characterize the structure of the Calcium-calmodulin dependent protein kinase II (CaMKII). CaMKII is the most abundant protein in neurons and plays an intriguing role in synaptic plasticity, long-term potentiation/depression, and memory formation[195]. I applied EM imaging and single-particle analysis methods to characterize the dynamic CaMKIIβ structure, building on my previous characterization of CaMKIIα and provided a statistical

representation of CaMKII structural dynamics. This work revealed a novel 16mer oligomeric state of CaMKIIβ and inter-holoenzyme and intra-holoenzyme dimerization between regulatory domains with implications into high-order CaMKII clustering observed under ischemic conditions. This work showcased the ability of single-particle EM approaches to study dynamic protein assemblies and supported functional experiments from the Bayer laboratory to both validate and extend their findings on the activation mechanisms of CaMKII. The structural characterization and comparison of CaMKII alpha and beta isoforms is presented in *Appendix Chapter 2* as the manuscript *"Conserved and divergent features of neuronal CaMKII holoenzyme structure, function, and high-order assembly"* as published in Cell Reports[196].

Chapter 2: The α-crystallin chaperones undergo a quasi-ordered co-aggregation process in response to saturating client interaction

Authors: Adam P. Miller[1,2,3], Susan E. O'Neill[3], Kirsten J. Lampi[4], Steve L. Reichow[1,2,3,*]

Affiliations:

[1] Department of Chemical Physiology and Biochemistry, Oregon Health & Science University, Portland, Oregon 97239, USA

[2] Vollum Institute, Oregon Health & Science University, Portland, Oregon 97239, USA

[3] Department of Chemistry, Portland State University, Portland, Oregon 97201, USA

[4] Biomaterial and Biomedical Sciences, Oregon Health & Science University, Portland, Oregon 97239, USA

* Correspondence: reichow@pdx.edu

Published in the Journal of Molecular Biology:

DOI: 10.1016/j.jmb.2024.168499

PMID: 38401625

PMCID: PMC11001518

Keywords:

α-crystallin, small heat shock protein (sHSP), HSPB4, HSPB5, chaperone, cataract, eye lens, aggregation, proteostasis, electron microscopy, single particle analysis, light scattering

ABSTRACT

Small heat shock proteins (sHSPs) are ATP-independent chaperones vital to cellular proteostasis, preventing protein aggregation events linked to various human diseases including cataract. The α-crystallins, αA-crystallin (αAc) and αB-crystallin (αBc), represent archetypal sHSPs that exhibit complex polydispersed oligomeric assemblies and rapid subunit exchange dynamics. Yet, our understanding of how this plasticity contributes to chaperone function remains poorly understood. Using biochemical and biophysical analyses combined with single-particle electron microscopy (EM), we examined structural changes in αAc, αBc and native heteromeric lens α-crystallins (αLc) in their apo-states and at varying degree of chaperone saturation leading to co-aggregation, using lysozyme and insulin as model clients. Quantitative single-particle analysis unveiled a continuous spectrum of oligomeric states formed during the co-aggregation process, marked by significant client-triggered expansion and quasi-ordered elongation of the sHSP oligomeric scaffold, whereby the native cage-like sHSP assembly displays a directional growth to accommodate saturating conditions of client sequestration. These structural modifications culminated in an apparent amorphous collapse of chaperone-client complexes, resulting in the creation of co-aggregates capable of scattering visible light. Intriguingly, these co-aggregates maintain internal morphological features of highly elongated sHSP oligomers with striking resemblance to polymeric α-crystallin species isolated from aged lens tissue. This mechanism appears consistent across αAc, αBc and αLc, albeit with varying degrees of susceptibility to client-induced co-aggregation. Importantly, our findings suggest that client-induced co-aggregation follows a distinctive mechanistic and quasi-ordered trajectory, distinct from a purely amorphous process. These insights reshape our understanding of the physiological and pathophysiological co-aggregation processes of α-crystallins, carrying potential implications for a pathway toward cataract formation.

INTRODUCTION

The α-crystallins (αA- and αB-isoforms) are prototypical members of the small heat shock protein (sHSP) family of ATP-independent chaperones, with key roles in cellular proteostasis[5,197] sHSPs counteract detrimental protein aggregation events implicated in various human diseases, including cataract formation[198]. Humans have ten sHSP proteins (HSPB1-10) that are differentially expressed throughout the body, functioning as holdases and serving as initial responders to diverse forms of cellular stress[199]. αA-crystallin (αAc; aka HSPB4, 19.8 kDa) and αB-crystallin (αBc; aka HSPB5, 20.2 kDa) are abundantly expressed in the eye lens, where they form heteromeric co-assemblies that ensure transparency for vision[5,76,98]. While αAc is primarily found in the lens, αBc exhibits ubiquitous expression, with high levels in cardiac and neuronal tissues[200]. Consequently, αBc is associated with a number of diseases, including cataract, myopathies, neuropathies, protein folding disorders (*e.g.,* Parkinson's and Alzheimer's), and some cancers[201,202]. Despite their significance, our mechanistic understanding of how these sHSPs function as chaperones remains limited, due in part to their complex structural dynamics and molecular organization.

Some sHSPs, including the α-crystallins, exhibit polydispersed high-order oligomeric assemblies, marked by dynamic subunit interactions that are pivotal for their biological roles[124,203–207]. The core domain shared among sHSP subunits, the α-crystallin domain (ACD), is flanked by a variable N-terminal domain (NTD) and a flexible C-terminal domain (CTD) (**Fig. 1A**). These domains orchestrate multivalent interactions, facilitating the formation of high-order oligomers[117,148,149,158,160,208–211]. αAc and αBc oligomers consist of approximately 12 to 48 subunits and exhibit rapid subunit exchange dynamics[117,124,205,212–216]. This dynamic behavior underpins a high degree of structural plasticity among these sHSPs that is thought to enable the recognition and sequestration

of a wide spectrum of destabilized client proteins. It is hypothesized that smaller assemblies or exchanging subunits are the more active states that recognize destabilized clients, while high-order oligomers are involved in sequestering and storing misfolded (or destabilized) clients[168,182,217,218]. In this stored form, the client is maintained in a refolding-competent state that may be recovered by ATP-dependent chaperones like HSP70/HSP40[38,219–221].

Notably, sHSP sequestration of destabilized proteins does not preclude formation of insoluble aggregates. Saturating binding conditions can lead to chaperone-client co-aggregates, while still enabling functional recovery of the client, in contrast to misfolding client aggregates formed without sHSPs[11,222,223]. Multiple factors influence sHSP/client co-aggregation, including stress conditions (*i.e.,* temperature, oxidation, pH), sHSP:client ratio, and the identity of the client leading to distinct morphologies of varying sizes[35,157,224]. The extreme degree of structural heterogeneity associated with this co-aggregation process has posed significant challenges to structural analysis and extraction of mechanistic principles associated with sHSP client sequestration and co-aggregation. In the context of the eye lens, which lacks protein turnover and ATP-dependent refolding pathways[49], the α-crystallin system can become overwhelmed in old age and result in formation of both soluble and insoluble light-scattering sHSP/client co-aggregates (*i.e.,* cataract), the leading cause of global vision loss[83]. While this phenomenon has been studied *in vitro* and presumed to be amorphous in nature, the structural morphology of the light-scattering aggregates has not been systematically analyzed[110,111,225].

Here, our objective was to quantitatively delineate the structural and morphological transformations of α-crystallins (αAc and αBc) during client-induced co-aggregation. We systematically compared αAc, αBc and native heteromeric lens α-crystallins (αLc) in their apo-states and across various stages of client-induced aggregation, employing the model clients lysozyme and insulin. These model clients allowed for the determination of the

induced morphological changes to the chaperone without the complicating factor of stress-inducing conditions (*e.g.,* elevated temperature, low pH, oxidation, etc.) known to influence sHSP conformational states[160,205,216,226]. To surmount the complexities arising from structural heterogeneity, we devised a single-particle electron microscopy (EM) image analysis workflow, enabling quantification of sHSP morphologies at the individual particle level. Through a combination of light-scattering methods, biochemical analysis, and direct visualization through single-particle EM, we unveiled a continuous spectrum of oligomeric states, whereby the basal-state sHSP caged-like assemblies undergo a remarkable degree of oligomeric reorganization that appear as both expansion and elongation, or directional growth of the sHSP oligomer, in response to unfolding client. These changes culminated in the amorphous collapse of chaperone-client co-aggregates, which had the capacity to scatter light. The co-aggregates that are formed share striking similarity to polymeric species of α-crystallin isolated from aged lens tissue[115]. Importantly, these observations imply a mechanistic foundation that is shared between homomeric αAc and αBc, as well as native heteromeric αLc chaperones, and characterized by a quasi-ordered co-aggregation pathway that is clearly distinct from a purely amorphous process. Our findings provide new insights into the morphological transitions of α-crystallins during client-induced aggregation, shedding light on processes crucial for cellular proteostasis and age-related cataract formation.

RESULTS

Single-particle analysis reveals full extent of αA- and αB-crystallin polydispersity

To establish a baseline for our comparative study, we examined αAc and αBc under conditions resembling their basal apo-state. We employed size-exclusion chromatography (SEC), dynamic light scattering (DLS), and single-particle analysis using negative stain

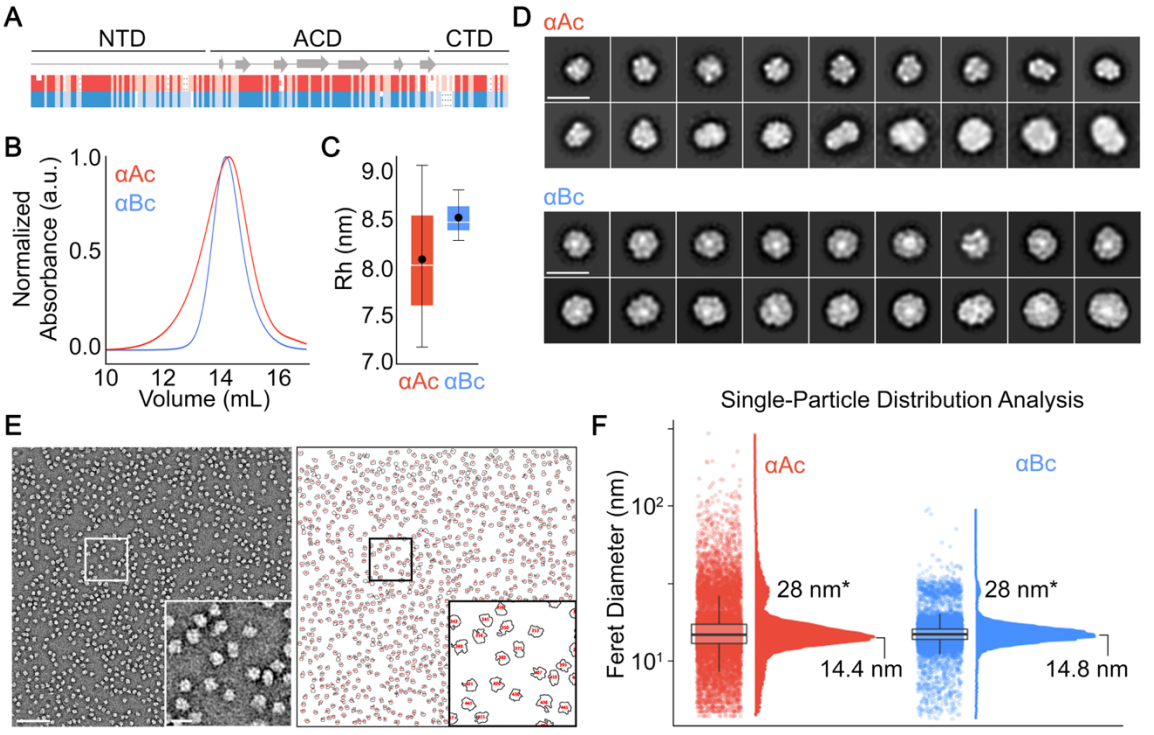

Fig. 1: Structural analysis of polydispersed apo-states of αA- and αB-crystallin. A. Comparison of primary sequence homology between various mammalian αA- (αAc, red) and αB-crystallins (αBc, blue) (see **Methods**). Coloring indicates positions that are conserved in both αAc and αBc (dark shading), within αAc or αBc (light shading), and non-conserved (white). Gaps are indicated with a dash. Annotations for secondary structure and domain organization are indicated. **B.** Overlay of representative size exclusion chromatography (SEC) elution profiles for αAc (red) and αBc (blue). **C.** Boxplots displaying hydrodynamic radii (R_H) of αAc (red) and αBc (blue) determined by dynamic light scattering (n = 3). **D.** Representative 2D class averages of negatively stained αAc (top) and αBc (bottom) oligomeric assemblies (scale bar = 20 nm). **E.** Left: Representative micrograph of αBc oligomers (scale bar = 100 nm, zoom scale bar = 20 nm). Right: Representative image showing isolated particles from the same micrograph following single-particle distribution analysis using the developed FIJI workflow (see also **Supplemental Fig. 2**). **F.** Raincloud plot showing the distributions of Feret diameters of αAc (red) and αBc (blue) oligomers extracted from NS-EM images using our single-particle distribution analysis workflow shown in panel E. Feret diameters for major population modes centered around 14 nm and 28 nm are indicated.

electron microscopy (NS-EM). Full-length human αAc and αBc were expressed in *E. coli* and isolated biochemically without engineered purification tags (**Supplemental Fig. 1** and **Methods**). To ensure consistency and account for environmental factors known to affect sHSP structure, we prepared purified samples in buffer at pH 7.4 supplemented with chelators (EDTA and EGTA) to remove trace amounts of divalent cations[226]. Prior to analysis, the samples were equilibrated overnight (~16 hours) at 37° C to equilibrate exchange dynamics[205,216]. Human αAc contains two cysteine residues (C131 and C142),

which readily form disulfide bridges under oxidative conditions *in vitro* and produce larger oligomers that can transfer disulfides to clientele to assist chaperone function[160]. To limit such complications, αAc was kept under reducing conditions during purification using DTT and during functional assays and structural analyses using TCEP.

Using solution-state analysis by SEC, we observed that αAc forms slightly smaller and more polydispersed assemblies compared to αBc. The apparent molecular weights (m.w) of αAc and αBc, as determined by SEC, were approximately 440 kDa and 470 kDa, respectively. This finding is in line with the radius of hydration (R_H) values obtained from dynamic light scattering (DLS), which measured 8.1 ± 1.0 nm for αAc and 8.5 ± 0.3 nm for αBc (mean ± sd; p = 0.5, t-test) (**Fig. 1 B-C** and **Supplemental Fig. 1**).

To further characterize their structural properties, we employed NS-EM and 2D classification methods for single-particle analysis (**Fig. 1D** and **Supplemental Fig. 1**). The resulting 2D classes revealed that both αAc and αBc adopt a range of polydispersed oligomeric assemblies, exhibiting expected caged-like morphologies. Notably, αAc displayed a broader range of diameters (12.6 – 21.3 nm) within the resolved 2D classes compared to αBc (~14.3 – 21.3 nm), although this difference was not statistically significant. While many of the assemblies observed in the NS-EM images appeared approximately spherical in projection, some 2D classes depicted complexes with oblique or irregular shapes. Although some of the variation can be attributed to different viewing angles of the complexes; overall, these results are consistent with the ability of both αAc and αBc to adopt diverse oligomeric states, as described in previous EM studies[158,160,227].

The high degree of polydispersity and structural heterogeneity exhibited by sHSPs poses practical limitations on commonly applied single-particle 2D image classification and averaging methods. The outputs of these methods discretize continuum ensembles, which is not ideal for analyzing such systems[196,228,229]. To overcome these limitations, we employed a relatively simple and accessible workflow using available image processing

tools in FIJI[230]. This approach enabled the extraction of structural descriptors from individual complexes (*e.g.,* diameter, circumference, surface area, etc.), without employing signal averaging methods, and allowed for quantitatively describing the polydispersity of sHSPs at the individual particle level (see **Fig. 1E**, **Supplemental Fig. 2** and **Methods**). While various structural descriptors could be obtained using this method, we focused on utilizing Feret diameter (*i.e.,* maximal particle diameter) as the primary descriptor of particle morphology in this study.

Feret diameters of individual particles were extracted from NS-EM micrographs of both αAc and αBc (**Fig. 1F**). To statistically compare the distribution of particle diameters, we employed a two-sample Kolmogorov-Smirnov test (K-S test). The population distributions of both αAc and αBc were found to be bimodal. The most populated mode for αAc was centered at 14.4 nm, slightly smaller than the primary mode of 14.8 nm observed for αBc. Both datasets exhibited a second mode centered at approximately 28 nm. While the population of αBc particles appeared as Boltzmann-like distributions, those of αAc displayed noticeable tails weighted toward smaller species and a prevalence of larger species compared to αBc. This dispersion is indicative of a greater degree of polydispersity in αAc. Consequently, the mean and standard deviation of particle diameters for αAc (17.4 ± 11.7 nm; mean ± sd) were larger than those for αBc (15.3 ± 3.5 nm), with a significant difference ($p < 0.0001$, K-S test). Importantly, the single-particle measurements and the extent of variation (*i.e.,* polydispersity) observed in αAc and αBc were consistent with our 2D classification results and DLS measurements obtained under solution-state conditions.

This single-particle distribution analysis offers a valuable advantage by providing quantitative information about rare states that were not well captured by 2D-class averaging or other ensemble measurements (SEC, DLS). This analysis revealed the presence of both very small and very large assemblies sampled by both αAc and αBc

isoforms, with diameters ranging from approximately 5 nm to over 90 nm for αBc and over 250 nm for αAc (**Fig. 1F**). As noted, both αAc and αBc exhibited an additional minor, yet significant, population with Feret diameters of approximately 28 nm, which is roughly twice the diameter of the most populated modes. Upon closer examination of the raw micrographs, it became apparent that this population resulted from two oligomers positioned in close contact, which were unresolved by our segmentation approach. This observation suggests the possibility of a true population of "kissing oligomers" or it could be attributed to particle crowding on the EM grid (**Fig. 1F**, *asterisk*, see **Discussion**).

Based on these results, we concluded that our approach to single-particle distribution analysis of NS-EM images was effective at quantitatively describing and discriminating nuanced differences in sHSP structure and degree of polydispersity. With this development, we aimed to apply this constellation of methods to investigate the structural changes and dynamics of αAc and αBc in response to client interactions.

αA- and αB-crystallin display different degrees of susceptibility to client-induced co-aggregation

For comparative functional analysis, αAc and αBc were assessed using aggregation suppression assays, monitored by light-scattering (turbidity) at 360 nm. Following the functional assays, the chaperone-client complexes were then directly subjected to structural characterization by SEC and DLS, without prior filtering or centrifugation (**Fig. 2**). We utilized lysozyme (lyso) as a model client due to its molecular weight (14.4 kDa), which is similar to the clients found in the eye lens, such as β/γ-crystallins. Unlike native clients, lysozyme readily unfolds at physiological pH (7.4) and temperature (37° C) in the presence of a reducing agent (TCEP), allowing for a controlled analysis of the structural effects induced on the chaperone complexes. This allowed us to determine the basal mechanism of action of the chaperone without the complication of altering environmental

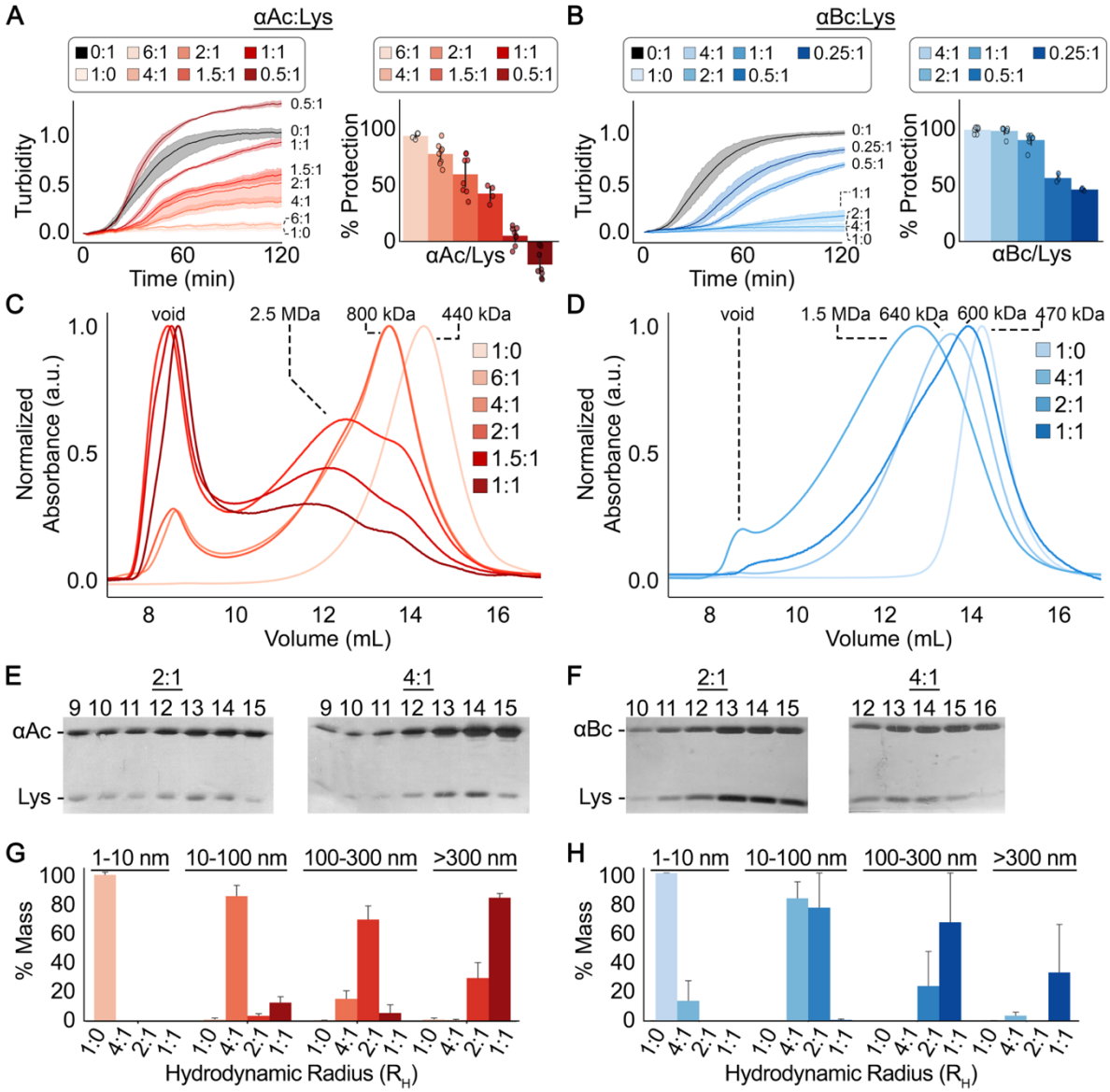

Fig. 2. Chaperone activity and structural characterization of α-crystallin/lysozyme complexes and co-aggregates. A,B. Aggregation suppression assays against unfolding lysozyme (Lys) client conducted with varying molar ratios of αAc (red traces, panel A) and αBc (blue traces, panel B). Turbidity measurements at 360 nm were used to monitor aggregation. Lysozyme-only conditions (0:1 ratio) are shown in black. *Left:* Raw turbidity traces with mean ± std displayed. *Right:* Histograms showing overall percent protection (relative reduction of turbidity compared to lysozyme only) with error bars representing ± std (n = 4 – 7). **C,D.** Overlay of size exclusion chromatography (SEC) elution profiles for αAc (red, panel C) and αBc (blue, panel D) chaperone/client complexes formed after aggregation suppression assays. The apparent molecular weights (m.w.) of major elution peaks are indicated. **E,F.** SDS-PAGE analysis of elution fractions from SEC for the 2:1 and 4:1 ratios of αAc (panel e) and αBc (panel f). Protein bands corresponding to the presence of αAc or αBc chaperone and lysozyme (Lys) are marked. **G,H.** Size distribution analysis from dynamic light scattering (DLS) measurements of chaperone/client co-aggregates formed between αAc/lysozyme (panel G) and αBc/lysozyme (panel H) at varying chaperone:client ratios of 4:1, 2:1, 1:1, and 1:0 (negative control). The measurements were taken after 2 hours of initiating aggregation suppression assays, as shown in Fig. 2A,B. Particle size measurements were binned at 1-10 nm, 10-100 nm, 100-300 nm, and >300 nm. Bar plots show mean ± sem (n = 3).

conditions (such as heat or pH) that are known to affect sHSP structure[226]. It should be

noted that the ratios of chaperone to client used in these experiments do not directly correlate with the stoichiometry of the formed chaperone/client complexes, as the aggregation suppression assays are conducted under non-equilibrium conditions. However, the observed dose-dependent response of chaperone concentrations suggests that at lower chaperone-client ratios, the chaperone is relatively more saturated by the binding of unfolding (or destabilized) client.

Under control conditions with 10 μM lysozyme alone (0:1 ratio of chaperone:client), we observed consistent aggregation kinetics of the client, with a $t_{1/2}$ of 33 ± 2 minutes (mean ± sem) for the αAc assay and 35 ± 3 minutes for the αBc assay (**Fig. 2A, B**; grey lines). In contrast, when αAc and αBc (pre-equilibrated at 37° C for ~16 hours) were prepared alone and in the presence of TCEP (*i.e.,* apo-state conditions, or 1:0 ratio), no aggregation was observed under the same conditions (**Fig. 2A, B**). Furthermore, incubating αAc or αBc with lysozyme but without reducing agent also did not result in aggregation under these conditions (data not shown).

Table 1: Summary of chaperone aggregation suppression assay results for α-crystallin/client complexes. Chaperone activity of αAc, αBc, and αLc toward the aggregation of reduced lysozyme (10 μM) and reduced insulin (40 μM) at 37° C at various chaperone:client ratios, showing percent protection as a measure of the chaperone's ability to suppress turbidity, number of technical replicates (n) for each ratio, and the time (minutes) of half aggregation ($t_{1/2}$). Percent protection was calculated as the average ± sem turbidity of each ratio compared to the average turbidity obtained for client-only conditions for each biological replicate. Values for $t_{1/2}$ were determined as the average ± sem time at which turbidity reached half the maximal value for each technical replicate.

αAc/lysozyme		
ratio	% protection (n)	$t_{1/2}$ (min)
lysozyme	-- (8)	33 ± 2
6:1	91 ± 1 (4)	--
4:1	76 ± 3 (8)	46 ± 3
2:1	58 ± 6 (8)	54 ± 2
1.5:1	42 ± 4 (4)	48 ± 2
1:1	5 ± 3 (8)	48 ± 3
0.5:1	-20 ± 4 (8)	37 ± 3
αBc/lysozyme		
ratio	% protection (n)	$t_{1/2}$ (min)
lysozyme	-- (8)	35 ± 3
4:1	98.8 ± 0.2 (7)	--
2:1	96 ± 1 (7)	--
1:1	87 ± 2 (7)	65 ± 2
0.5:1	32 ± 2 (7)	65 ± 2
0.25:1	17 ± 3 (7)	60 ± 1
αLc/lysozyme		
ratio	% protection (n)	$t_{1/2}$ (min)
lysozyme	-- (4)	37 ± 1
4:1	91.4 ± 0.3 (4)	45 ± 6
2:1	54 ± 4 (4)	65 ± 4
1:1	1 ± 5 (4)	55.5 ± 0.3
Insulin aggregation		
ratio	% protection (n)	$t_{1/2}$ (min)
insulin	-- (8)	23 ± 4
αAc:insulin (0.5:1)	41.7 ± 0.1 (7)	25 ± 3
αBc:insulin (0.2:1)	46.7 ± 0.1 (7)	15 ± 1

When lysozyme was treated with a reducing agent in the presence of pre-equilibrated αAc, nearly complete aggregation suppression (~92% protection) was achieved at a molar ratio of 6:1 (chaperone:client), with a decreasing degree of protection at lower ratios (**Fig. 2A,B** and **Table 1**). At a ratio of 1:1, αAc showed only ~5% protection, but there was still a significant delay in the aggregation kinetics compared to lysozyme alone ($t_{1/2}$ = 48 ± 3 min, $p < 0.0001$). Notably, at even more saturating levels of the client (0.5:1), turbidity was enhanced beyond the lysozyme-only conditions, indicated by negative protection values of approximately -20%. This negative protection (*i.e.,* scattering beyond lysozyme alone) is interpreted to reflect the increased scattering caused by the formation of large co-aggregates between αAc and lysozyme in addition to free lysozyme aggregates that escaped chaperone capture (see below).

In comparison, αBc exhibited ~99% protection at a ratio of only 4:1 (chaperone:client) and ~96% protection at a 2:1 ratio (**Fig. 2B**). At a ratio of 1:1 (where αAc showed 5% protection), αBc displayed ~87% protection and still exhibited ~17% protection even at a sub-stoichiometric ratio of 0.25:1, along with a significant delay in aggregation kinetics compared to lysozyme only conditions ($t_{1/2}$ = 40 ± 1 min, $p < 0.0001$). Fitting of these data provide a half-maximal protection ratio for αAc of 1.8 versus the substantially lower value of 0.7 for αBc, representative of the higher chaperone efficacy against lysozyme (**Supplemental Fig. 4**).

Representative conditions from the completed chaperone assays were then subjected to SEC to demonstrate binding and characterize changes in structure and/or polydispersity at different chaperone-client ratios. When αAc was present at higher chaperone ratios (6:1 and 4:1), the major SEC peak was shifted to a higher apparent molecular weight of ~800 kDa compared to the apo-state (~430 kDa). Additionally, a small left-hand shoulder peak appeared at approximately 2.5 MDa appeared, as well as a minor void peak that is indicative of high-molecular weight species (**Fig. 2C**). At lower chaperone

ratios, there was a progressive increase in peak broadening, indicating higher polydispersity, accompanied by the loss of the ~430 kDa peak and a shift towards the ~2.5 MDa and void peaks (**Fig. 2C**).

Under conditions where αBc provided complete protection against reduced lysozyme (4:1 ratio), the SEC profile exhibited a relatively Gaussian shape, but with a shift towards higher molecular weight of ~640 kDa compared to ~470 kDa for the apo-state. There was also an overall increase in peak broadening, indicating increased polydispersity (**Fig. 2D**). No significant void peak was observed under these conditions, which is consistent with the complete suppression of light-scattering at 360 nm. At the lower ratio of 2:1, the major SEC peak shifted further to an average m.w. ~1.5 MDa, accompanied by even greater peak broadening. Additionally, a small void peak was observed, consistent with minor contribution to scattering at 360 nm under these conditions. These observations are very similar to what we have previously observed between αAc and native lens client protein, βB2-crystallin[111].

When αBc was applied to SEC at the lowest ratio (1:1), a major peak centered at an apparent m.w. ~600 kDa was observed, accompanied by a noticeable left-hand shoulder at m.w. ~1.7 MDa. However, no significant void peak was observed under this condition. Initially, this result seemed unexpected, as larger molecular weight species were anticipated under more saturating client conditions. Nevertheless, this consistent observation suggests that larger aggregates formed under these conditions were not entering the SEC column. This notion is supported by the lack of SEC elution profiles for samples prepared at lower chaperone:client ratios for both αAc (*e.g.,* 0.5:1) and αBc (*e.g.,* 0.5:1 or 0.25:1), as well as by the subsequent detection of high molecular weight species by DLS and NS-EM discussed below. Analysis of the elution fractions by SDS-PAGE confirmed the presence of both lysozyme and αAc or αBc in the resolved SEC peaks

(shown for the 2:1 and 4:1 ratios in **Fig. 2E,F**), indicating the formation of relatively stable and long-lived complexes under these conditions.

Saturating client conditions induce structural transitions toward light-scattering α-crystallin/lysozyme co-aggregates.

To further evaluate the structural effects of client binding, we analyzed apo-αAc, apo-αBc, and their complexes with lysozyme at representative chaperone:client ratios using DLS. The data were binned into four size ranges based on the radius of hydration (R_H): 1-10 nm, 10-100 nm, 100-300 nm, and >300 nm (**Fig. 2G,H** and **Supplemental Fig. 3**). Under control conditions (1:0 ratios), apo-αAc and apo-αBc were predominantly within the 1-10 nm R_H bin (97.4 ± 1.9% and 99.8 ± 0.2%, respectively; mean ± sem). At a 4:1 chaperone:client ratio, both αAc and αBc showed the emergence of larger species and increased polydispersity, as indicated by populations in multiple R_H bins compared to the apo-states. The R_H distribution of αAc/lysozyme complexes under these conditions was 82.3 ± 8.6% (10-100 nm), 14.9 ± 8.3% (100-300 nm), and 0.7 ± 0.7% (>300 nm). Similarly, for αBc, there was a major population in the 10-100 nm bin, but also a persistence of species in the 1-10 nm bin, with populations represented by R_H values of 13.7 ± 13.7% (1-10 nm), 82.8 ± 13.0% (10-100 nm), and 3.6 ± 2.8% (>300 nm) under the same conditions.

At a 2:1 ratio, αAc and αBc populations are both shifted to larger species. The majority of αAc/lysozyme complexes are found in the 100-300 nm bin (67.7 ± 15.3%), with a significant population in the >300 nm bin (28.8 ± 16.9%). Under these conditions, αBc/lysozyme complexes are predominantly in the 10-100 nm bin (76.5 ± 23.5%), but with a notable population in the 100-300 nm category (23.5 ± 23.5%). At a 1:1 ratio, the majority of αAc/lysozyme complexes have an R_H >300 nm (82.3 ± 3.7%), consistent with significant light scattering at 360 nm. Only small populations are observed in the 10-100 nm (12.3 ± 6.0%) and 100-300 nm bins (5.5 ± 5.5%). For αBc/lysozyme complexes under these same

conditions, significant populations are also found at >300 nm (32.6 ± 32.6%), but the most populated states fall into the 100-300 nm bin (66.7 ± 33.3%). The presence of >300 nm species in αBc is consistent with the light scattering observed at 360 nm in the turbidity assays. These findings support the idea that the SEC profile obtained under this condition is anomalous, likely due to the selective removal of larger species by the column filter.

Single-particle analysis by EM reveals an expansion, elongation and amorphous collapse chaperone mechanism

We next proceeded to apply our single-particle EM analysis workflow, as described above, to obtain a more detailed and quantitative morphological characterization of the client-induced aggregation states of αAc and αBc (**Fig. 3** and **Table 2**). To statistically compare the cumulative Feret diameter distributions between different chaperone:client ratios, we employed the Kolmogorov-Smirnov test (K-S test, two-sample).

NS-EM datasets were analyzed for αAc/lysozyme complexes formed at 4:1, 2:1, and 1:1 chaperone:client ratios (**Fig. 3A-D** and **Supplemental Fig. 5**). At the higher chaperone ratio of 4:1 (representing the least saturating client conditions imaged by NS-EM), it was evident that the sequestration of lysozyme led to a variety of polymorphic structures. These structures appeared as enlarged spherical-like complexes with diameters ranging from approximately 20 to 50 nm, with average Feret diameter of 21.2 ± 0.2 nm (mean ± sem) being significantly larger than the apo-αAc structures (17.4 ± 0.1, $p < 0.0001$; K-S test) (**Fig. 3A,D**). In addition, an emergence of elongated structures, measuring as much as 100 nm long and ~15 to 20 nm wide, were also observed. Morphologically, these largest complexes appeared consistent with the formation of highly elongated and/or daisy-chained (*i.e.,* interlinked) chaperone complexes (see **Fig 3A**, *insets*), covering a continuous range of lengths ~30 to 100 nm. The degree of morphological changes observed suggest a client-induced reorganization of the sHSP

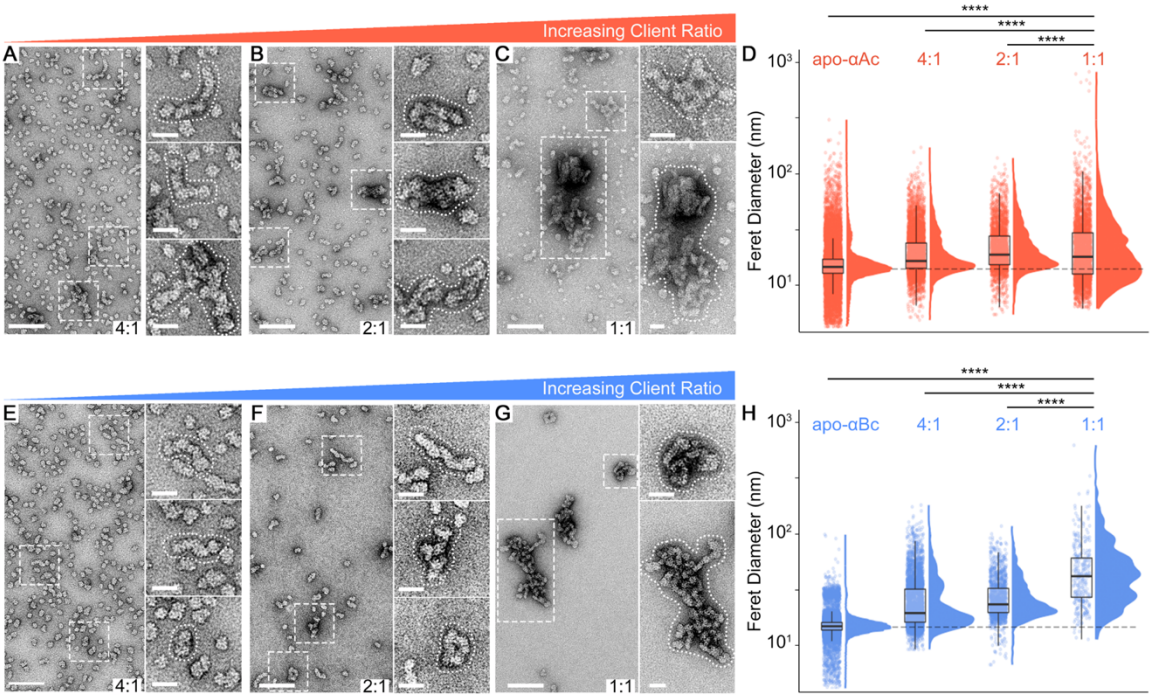

Figure 3: Quantitative structural analysis of αAc and αBc/Lysozyme complex formation and co-aggregation by single-particle EM. A-C. Representative micrographs of negatively stained αAc/lysozyme complexes and co-aggregates formed at varying chaperone:client ratios of 40 μM:10 μM (panel A, 4:1), 20 μM:10 μM (panel B, 2:1), and 10 μM:10 μM (panel C, 1:1), scale bar = 100 nm. Example co-aggregates from each condition are boxed and zoomed (insets, scale bar = 25 nm). **D.** Raincloud plot showing single-particle distributions of Feret diameters extracted for apo-αAc (control) and various chaperone/client complexes and co-aggregates isolated from NS-EM datasets for the 40 μM:10 μM, 20 μM:10 μM, and 10 μM:10 μM chaperone:client ratios. **E-G.** Representative micrographs of negatively stained αBc/lysozyme complexes and co-aggregates formed at varying chaperone:client ratios of 40 μM:10 μM (panel E, 4:1), 20 μM:10 μM (panel F, 2:1), and 10 μM:10 μM (panel G, 1:1), scale bar = 100 nm. Example co-aggregates from each condition are boxed and zoomed (insets, scale bar = 25 nm). **H.** Raincloud plot showing single-particle distributions of Feret diameters extracted for apo-αAc (control) and various chaperone/client complexes and co-aggregates isolated from NS-EM datasets for the 4:1, 2:1, and 1:1 chaperone:client ratios. Measurements were taken after 2 hours of initiating aggregation suppression assays, as shown in Fig. 2A,B. KS test, **** $p < 0.0001$

oligomeric state(s) may be used to accommodate varying degrees of client sequestration (see Discussion).

At the more saturating 2:1 chaperone:client ratio, the formation of expanded and elongated αAc/lysozyme complexes was even more pronounced (**Fig. 3B,D**). These complexes exhibited an average Feret diameter of 24.0 ± 0.3 nm, which was significantly larger than both the apo-state and the 4:1 condition ($p < 0.0001$; KS test) (**Fig. 3D**). Morphologically, the most elongated complexes reached lengths of approximately 125 nm

Table 2: Summary of single particle morphology analysis extracted from NS-EM micrographs for α-crystallin/client complexes. Feret diameter and Area values represent the mean ± sem obtained from measurements for individual apo-state α-crystallin oligomers (1:0) and α-crystallin/client complexes and co-aggregates obtained at chaperone:client ratios indicated. Values were obtained using the single-particle distribution analysis workflow described in **Methods** and **Supplemental Fig. 2**.

	Feret (nm)	Feret range (nm)	Area (nm^2)	Area range (nm^2)	$N_{particles\ (images)}$
			αAc/lysozyme		
1:0 (apo)	17.4 ± 0.1	4 - 299	181.4 ± 2.8	10 - 14390	13889 (30)
4:1	21.2 ± 0.2	5 - 170	248.2 ± 3.3	12 - 6642	5846 (8)
2:1	24.0 ± 0.3	6 - 137	302.8 ± 6.2	16 - 3498	2757 (8)
1:1	25.0 ± 0.4	6 - 235	367.0 ± 13.7	25 - 15490	3381 (10)
			αBc/lysozyme		
1:0 (apo)	15.3 ± 0.02	4 - 97	140.5 ± 0.4	10 - 2607	17192 (43)
4:1	26.5 ± 0.3	9 - 177	349.8 ± 7.2	44 - 6068	3793 (8)
2:1	28.0 ± 0.4	7 - 115	398.8 ± 8.7	23 - 2748	1421 (8)
1:1	50.7 ± 2.0	11 - 320	1324.5 ± 108.2	32 - 1129	342 (22)
			αLc/lysozyme		
1:0 (apo)	20.7 ± 0.2	4 - 108	254.8 ± 3.7	10 - 3610	3691 (9)
4:1	29.5 ± 0.5	5 - 269	451.7 ± 16.0	10 - 12659	2574 (6)
2:1	23.5 ± 0.3	4 - 429	318.7 ± 12.2	10 - 41904	4566 (10)
1:1	29.5 ± 0.9	4 - 544	614.6 ± 69.6	11 - 64539	1191 (7)
			αAc/insulin		
0.5:1	16.5 ± 0.1	5 - 144	157.9 ± 2.4	10 - 3747	5750 (9)
			αBc/insulin		
0.2:1	24.0 ± 0.2	12 - 290	277.1 ± 5.8	90 - 13711	6659 (9)

before they appeared to undergo a collapse, resulting in the formation of larger and seemingly more amorphous aggregates (see **Fig. 3B**, *insets*).

At a chaperone-client ratio of 1:1, where αAc's chaperone activity is significantly diminished, large amorphous aggregates become predominant, reaching sizes exceeding hundreds of nanometers and approaching 1 μm (**Fig. 3C,D**). The formation of these large complexes correlates with the significant light scattering observed at 360 nm under these conditions, surpassing the scattering observed for lysozyme alone (see **Fig. 2A**). Morphologically, these structures retain the elongated (or daisy-chained) features observed at higher chaperone-client ratios, indicating the collapse of highly elongated chaperone/client complexes (compare **Fig. 3B** and **3C**, *insets*). These co-aggregates

exhibit distinct morphology from the plaque-like aggregates formed by lysozyme alone (refer to **Supplemental Fig. 3**). Additionally, smaller irregularly shaped species with diameters of approximately 7-12 nm are prevalent under these conditions (**Fig. 3C,D**). These smaller species resemble previously described aggregates of reduced lysozyme[231] and likely represent unbound lysozyme aggregates or also possibly unsaturated αAc/lysozyme complexes (compare to **Supplemental Fig. 3**). Notably, since αAc is no longer efficient in chaperoning at these saturated levels of client, the presence of unbound lysozyme and aggregates that evade chaperone sequestration is expected. The significant population of these smaller species contributes to a mean Feret diameter of 25.0 ± 0.4 nm in this dataset, which is comparable to the 2:1 condition. However, the increased polydispersity in this data leads to a significant difference in the distribution of Feret diameters between these two conditions ($p < 0.0001$; KS test).

Qualitatively, the morphological appearance of αBc/lysozyme complexes observed under different client conditions closely resembles those obtained for αAc at varying client ratios, indicating a conserved mechanism of client sequestration (**Fig. 3E-H** and **Supplemental Fig. 6**). However, quantitative comparisons reveal distinct differences that likely reflect the variations in chaperone efficacy towards the model client, lysozyme. At a 4:1 chaperone-client ratio, Feret diameter measurements demonstrate a significant increase in the polydispersity of particle size distribution compared to apo-αBc conditions (26.5 ± 0.3 nm vs. 15.3 ± 0.02 nm, respectively, $p < 0.0001$; K-S test) (**Fig. 3H**). Morphologically, the most prevalent structures formed under these conditions are characterized by roughly spherical oligomers similar to apo-αBc (**Fig. 3E**), with the emergence of some elongated (or daisy-chained) complexes (**Fig. 3E**, *insets*).

At a ratio of 2:1, morphological differences compared to apo-αBc become more apparent. The size and polydispersity of complexes, as indicated by distribution of Feret diameters, increases significantly compared to the 4:1 condition (28.0 ± 0.4 nm vs. 26.5 ±

0.3 nm; $p < 0.0001$; K-S test). In contrast to the 4:1 condition, oligomers most similar in size to apo-state appear to no longer be significantly populated (**Fig. 3H**, dotted line), consistent with our solution-state DLS data. Similar to αAc, highly elongated complexes become prevalent and are readily observed in the raw micrographs, including examples where elongated complexes appear collapsed on themselves to form more amorphous-like aggregates (**Fig. 3F**, *insets*).

Finally, when αBc was imaged under the most saturating conditions (1:1 ratio) using NS-EM, we observed the prevalence of very large aggregates with diameters reaching 100's of nanometers (**Fig. 3G**). These co-aggregates also appeared as highly elongated or daisy-chained chaperones that had collapsed onto themselves, forming more amorphous-like structures. However, in contrast to αAc under the same conditions, there was a notable absence of smaller oligomers. Additionally, the size distribution of αBc/lysozyme complexes at this ratio appear multimodal with distinct peaks in the 50 – 100 nm diameter range. The comparative absence of smaller species contributed to an increased Feret diameter of 50.7 ± 37.7 nm as compared to αAc/lysozyme complexes at the same 1:1 ratio (25.0 ± 21.1 nm, $p < 0.0001$; K-S test). These findings are consistent with the enhanced efficacy of chaperone activity exhibited by αBc and the high degree of protection against light-scattering under these conditions (~87% protection, **Fig. 2B**).

Client-induced expansion, elongation and amorphous collapse is preserved with an alternative client.

The aggregation protection and co-assembly of sHSPs with client vary depending on stress conditions and the unfolding client[35,224]. To extend our analysis, we aimed to discern if the client-induced structural alterations observed in αAc and αBc were preserved when employing an alternative client protein. We utilized bovine insulin as a model client in these experiments, due to its smaller molecular weight compared to lysozyme (5.7 kDa versus

14.4 kDa). Importantly to this study, insulin can be comparably induced to unfold under reducing conditions, thus permitting the consistency of all other experimental parameters, including pH, salt concentrations, and temperature, to those employed in the lysozyme experiments. Under these established conditions, insulin (40 μM) displayed reproducible aggregation kinetics, with $t_{1/2}$ values of 23 ± 4 minutes (**Table 1**).

For structural examination, we conducted chaperone protection assays under conditions that induced approximately half-maximal protection by αAc (0.5:1 chaperone:client ratio, yielding ~42% protection) and αBc (0.2:1 chaperone:client ratio, yielding ~47% protection), as depicted in **Fig. 4A,B**. Notably, αAc produced a statistically non-significant reduction in aggregation kinetics, with $t_{1/2}$ values of 25 ± 3 min ($p = 0.7$) (**Table 1**). Conversely, while αBc demonstrated a delayed initiation of aggregation (as evidenced by a right-shifted turbidity trace in **Fig. 4B**), the overall aggregation kinetics were mildly enhanced compared to insulin alone, with $t_{1/2}$ values of 15 ± 1 min, however this difference was not statistically significant ($p = 0.13$). Consistent with observations from lysozyme assays, αBc exhibited higher chaperone efficacy relative to αAc against insulin aggregation. However, both αAc and αBc demonstrated an enhanced capacity for insulin compared to lysozyme, indicated by the relative differences in half maximal protection ratios, potentially reflecting the reduced size of the client protein. However, it is noted that this propensity may also be modulated by other factors, such as the differential aggregation kinetics characteristic of the clients.

Under these effective conditions, both αAc and αBc exhibited similar client-induced structural transformations, as assessed by SEC and NS-EM. By SEC analysis, both αAc and αBc conditions yielded nearly indistinguishable elution profiles, typified by a predominant major peak centered at an apparent m.w. of 595 kDa, with a pronounced left-handed tail that extended toward the void (**Fig. 4C,D**). Both conditions also generated a substantial void peak, signaling the formation of high molecular weight co-aggregates.

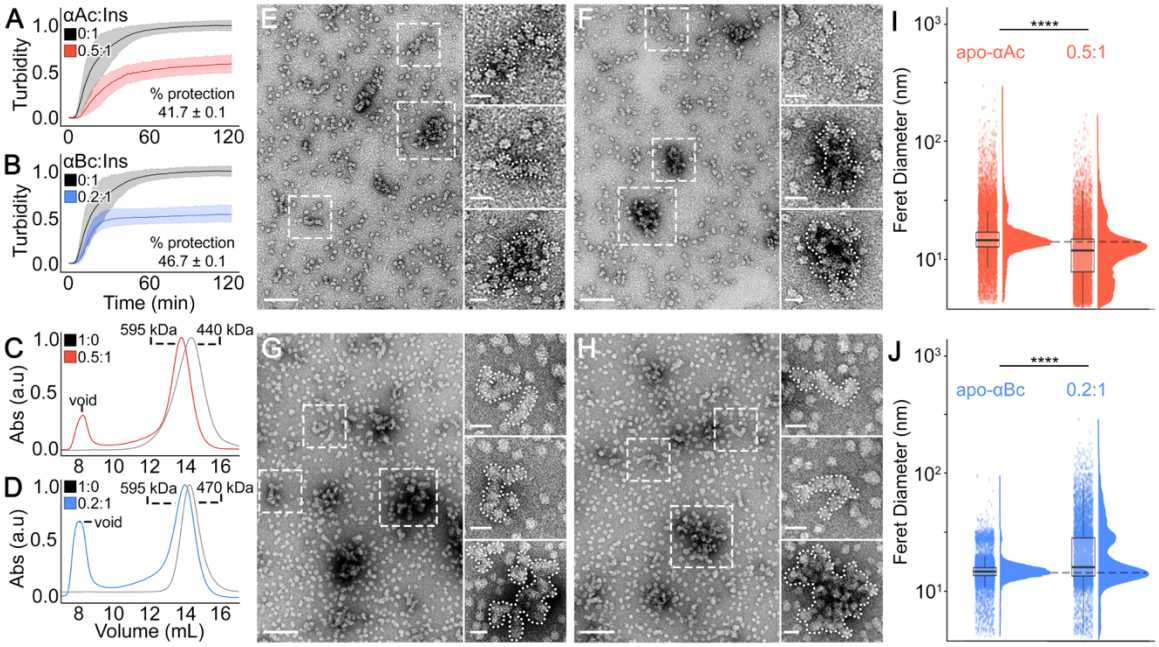

Figure 4: Quantitative structural characterization of α-crystallin/insulin complexes and co-aggregates by single-particle EM. A,B. Aggregation suppression assays against unfolding insulin (Ins, 40 μM, n = 8) client conducted under conditions providing approximately half-maximal protection with αAc (0.5:1 chaperone:client ratio, red traces) and αBc (0.2:1 chaperone:client ratio, blue traces), respectively. Insulin-only conditions (0:1 ratio) are shown in black. Raw turbidity traces with mean ± std displayed (n = 7). **C,D.** Overlay of size exclusion chromatography (SEC) elution profiles for αAc/Insulin (red) and αBc/Insulin (blue), respectively, formed after aggregation suppression assays. αAc and αBc only conditions overlayed for comparison (gray). The apparent molecular weights (m.w.) of major elution peaks are indicated. **E-H.** Representative micrographs of negatively stained αAc/insulin complexes (panels E and F) and αBc/insulin complexes (panels G and H) formed after aggregation suppression assays, scale bar = 100 nm. Example co-aggregates from each condition are boxed and zoomed (*insets*, scale bar = 25 nm). **I,J.** Raincloud plots showing single-particle distributions of Feret diameters extracted from the NS-EM datasets and compared to apo-αAc and apo-αBc, respectively. KS test, **** $p < 0.0001$.

Morphological evaluations by NS-EM corroborated these SEC data, with a major population of complexes exhibiting Feret diameters and spherical morphologies that resemble their respective apo-states (**Fig. 4E-J, Supplemental Fig. 7** and **Table 2**). Moreover, the induction of polydispersed populations of higher molecular weight species was also observed. These larger complexes adopted morphologies that appear as expanded spherical structures, highly elongated complexes, as well as larger more amorphous co-aggregates measuring more than 100 nm in diameter (**Fig. 4E-H**, *insets*). These larger structures displayed internal features that were consistent with the collapse of highly elongated sHSP/client morphologies. Collectively, the array of induced

assemblies appeared qualitatively comparable to the polymorphic structures induced by lysozyme when subjected to analogous levels of unfolding client saturation (see also, **Supplemental Fig. 5-7**).

The population of complexes exceeding 100 nm in diameter was notably more abundant in the αBc-treated sample, aligning with a more substantial void fraction detected by SEC. Quantitatively, this was reflected in an overall mean Feret diameter for αBc/insulin complexes, which was significantly larger compared to the apo-state ($p < 0.0001$; K-S test) (**Fig. 4J**). In contrast, the mean Feret diameter for αAc/insulin complexes was significantly smaller compared to the apo-state ($p < 0.0001$; K-S test) (**Fig. 4I**). This observation is attributable to the considerable population of smaller complexes identified in these conditions, measuring less than 10 nm in diameter. This pattern mirrors the behavior noted for αAc in the presence of lysozyme under saturating conditions and might similarly signify a composite of smaller chaperone complexes and/or aggregated insulin that escaped chaperone protection.

Native heteromeric lens α-crystallins exhibit a similar chaperone mechanism, with diminished activity toward the model client lysozyme.

In the mammalian lens, αAc and αBc co-assemble with an approximate 3:1 stoichiometry (αAc:αBc)[5,76]. Previous studies suggest heteromeric assembly of α-crystallins may augment the overall structure, dynamics, and chaperone activity, compared to the homomeric counterparts[45,232,233]. Thus, we aimed to ascertain whether native lens α-crystallin complexes (αLc) exhibit a similar type of elongation and expansion chaperone mechanism that was characterized for the homomeric sHSPs. For these investigations, αLc was purified to homogeneity from lens cortical fiber cells (*ovine*) using methods adapted from previously described protocols and verified to contain a mixture of both αAc and αBc (see **Methods** and **Supplemental Fig. 1**). For all functional and structural

analyses, αLc was prepared in our standard reaction buffer (20 mM HEPES, pH 7.4, 100 mM NaCl, and 1 mM EDTA) and pre-equilibrated at 37° C for approximately 16 hours. Under control conditions, αLc alone (*i.e.,* apo-state conditions, or a 1:0 ratio), exhibited no aggregation over a 120-minute observation period in the presence of TCEP. Moreover, incubating αLc with lysozyme at 37° C, in the absence of a reducing agent, did not result in aggregation (data not shown).

In the presence of reduced lysozyme (10 μM), αLc exhibited characteristic concentration-dependent suppression of light-scattering at 1:1, 2:1, and 4:1 molar ratios of chaperone to client (**Fig. 5A,B** and **Table 1**). At a 4:1 ratio, αLc achieved nearly complete aggregation suppression (~91% protection). Moderate suppression was observed at a 2:1 ratio (~54% protection), and at a 1:1 ratio, αLc offered minimal protection after 120 minutes (~1% protection). Notably, even at a 1:1 ratio, αLc significantly delayed the aggregation kinetics compared to lysozyme alone ($t_{1/2}$ = 55.5 ± 0.3 min versus 37.0 ± 1.1 min; $p < 0.001$). The fitting of these data yields a half-maximal protection ratio of 1.9 (**Supplemental Fig. 4**), which was higher than that of either αAc or αBc, suggesting αLc has a reduced chaperone efficacy toward lysozyme compared to the recombinant isoforms.

Structural analysis by SEC revealed that apo-αLc assemblies were substantially larger than both apo-αAc and apo-αBc, with an apparent m.w. of approximately 1 MDa. When completed chaperone activity reactions were analyzed by SEC, the elution profiles displayed characteristics most similar to αAc (compare **Fig. 5C** and **Fig. 2C**). SDS-PAGE analysis of the major SEC elution peaks at the 4:1 and 2:1 chaperone:client stoichiometries confirmed the presence of αLc (αAc and αBc) and lysozyme, indicative of stable complex formation (**Fig. 5D**). At the highest chaperone:client ratio (4:1), there was a primary elution peak that was shifted slightly towards a higher molecular weight as compared to apo-αLc (apparent m.w. ~1.2 MDa). This peak overlapped with a broad peak

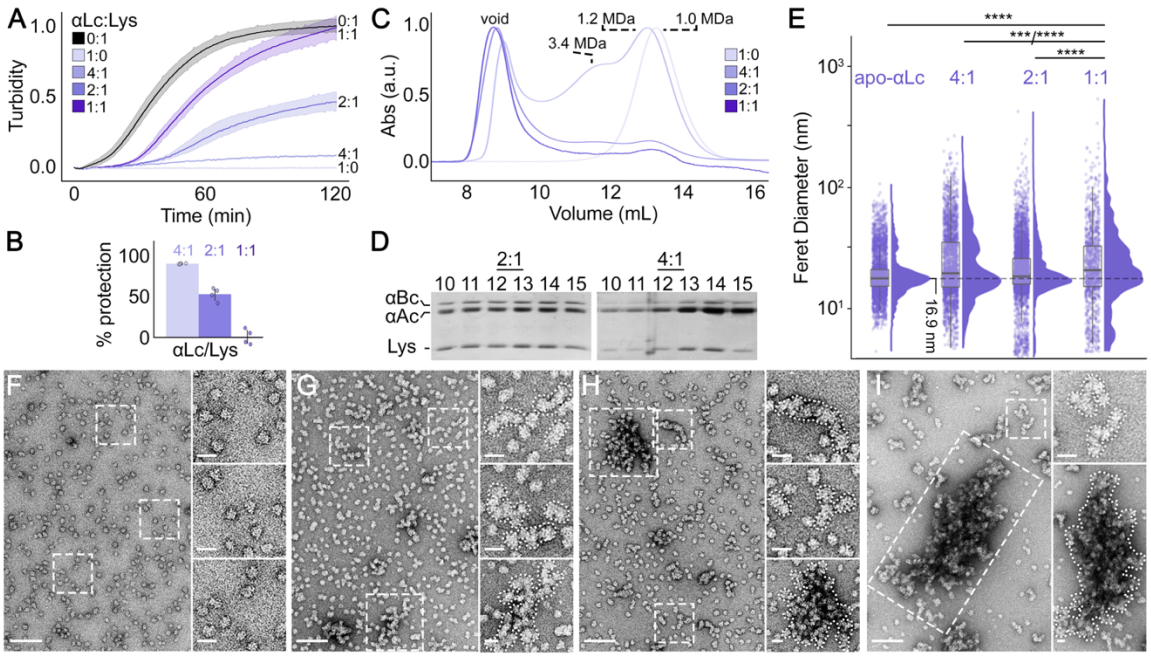

Figure 5: Chaperone activity and structural characterization of native lens α-crystallin/lysozyme complexes and co-aggregates. A. Aggregation suppression assays against unfolding lysozyme (Lys, 10 μM) client conducted with varying chaperone:client molar ratios of native lens α-crystallin (αLc) (purple traces). Turbidity measurements at 360 nm were used to monitor aggregation. Lysozyme-only conditions (0:1 ratio) shown in black. Raw turbidity traces with mean ± std displayed. **B.** Histogram showing overall percent protection with error bars representing ± std (n = 4). **C.** Overlay of size exclusion chromatography (SEC) elution profiles for αLc (purple) chaperone/client complexes formed after aggregation suppression assays. The apparent molecular weights (m.w.) of major elution peaks are indicated. **D.** SDS-PAGE analysis of purified αLc (left), and elution fractions from SEC for the 2:1 (middle) and 4:1 (right) chaperone:client ratios. Protein bands corresponding to the presence of αAc and αBc chaperone and lysozyme (Lys) are marked. **E.** Raincloud plot showing a summary of single-particle distributions of Feret diameters extracted from NS-EM datasets for αLc (control) and various chaperone/client complexes and co-aggregates for the 4:1, 2:1, and 1:1 chaperone:client ratios. KS test, **** $p < 0.0001$; *** $p < 0.001$ (4:1 and 2:1 comparison). **F-I.** Representative micrographs of negatively stained αLc chaperone (panel F) and αLc/lysozyme complexes and co-aggregates formed at varying chaperone:client ratios of 4:1 (panel G), 2:1 (panel H), and 1:1 (panel I), scale bar = 100 nm. Insets in panel F, showing zoomed views of apo-state αLc chaperones. Insets in panels G-I, showing zoomed views of example co-aggregates from each condition (*insets*, scale bar = 25 nm).

centered at an apparent m.w. of ~3.4 MDa as well as a prominent void peak. At the 2:1 and 1:1 chaperone:client ratios, the SEC elution profiles appeared similar, with a broad plateau peak starting at an apparent m.w. of ~1 MDa extending to the void volume, alongside a prominent void peak, indicative of significant polydispersity and formation of high molecular weight species.

Morphological analysis by NS-EM confirmed αLc adopts a similar structure and follows a client-induced mechanism of expansion, elongation, and amorphous collapse, akin to what was observed for the homomeric sHSPs (**Fig. 5E-I**, **Supplemental Fig. 8** and **Table 2**). Single-particle distribution analysis of the apo-αLc complexes exhibited a bimodal distribution consistent with the apo-states of αAc and αBc (**Fig. 5E** and **F**, *insets*). The major population of particles displayed a slightly larger Feret diameter of 16.9 nm as compared to apo-αAc and apo-αBc, aligning with the SEC data. Moreover, the second mode in this population exhibited a Feret diameter of ~ 31 nm, approximately twice the diameter of single chaperone complexes. NS-EM images captured at the highest chaperone:client ratio (4:1) revealed that the majority of particles maintained a spherical morphology similar to the apo-state. Additionally, a multimodal population of larger complexes emerged, characterized by morphologies that appeared expanded and/or highly elongated states with dimensions of up to 100 nm in length while maintaining a width of ~15 to 20 nm. Under these conditions, there was also the appearance of larger aggregates, reaching over 100 nm in diameter, which exhibited a more amorphous or collapsed morphology (**Fig 5E** and **G**, *insets*).

At the 2:1 chaperone:client ratio, the detected morphologies appeared somewhat similar to those in the 4:1 conditions, comprising a significant population of apo-like structures as well as elongated and high molecular weight co-aggregates (**Fig 5E** and **H**, *insets*). However, under the most saturating conditions (1:1 ratio), the spherical apo-like structures become less prevalent, with most complexes manifesting as highly elongated structures and large amorphous co-aggregates (**Fig 5E** and **H**, *insets*). Co-aggregates in these conditions were observed exceeding 400 nm in diameter, aligning with the substantial light-scattering detected. The larger co-aggregates maintained internal morphological features indicative of an amorphous collapse (or clustering) of highly elongated sHSP/client complexes, similar to those observed for αAc and αBc. Notably,

under these saturating conditions, there was also an emergence of a significant population of smaller complexes, measuring less than 10 nm in diameter. Again, likely attributed to a composite of smaller chaperone complexes and/or aggregated lysozyme that escaped chaperone protection.

DISCUSSION

In this study, we demonstrated that the α-crystallins utilize an "expansion and elongation mechanism" to accommodate increasing levels of client sequestration. This mechanism involves the formation of highly elongated chaperone/client co-assemblies that can reach lengths of up to ~125 nm that maintain a relatively constant width of ~15 to 20 nm, followed by an ultimate collapse or folding onto themselves, resulting in the formation of larger amorphous co-aggregates reaching 1 μm in size. The degree of morphological changes suggest client-sequestration is capable of inducing high-order reorganization of the sHSP oligomeric assembly, resulting in formation of both larger cage-like assemblies and highly elongated oligomeric formations (discussed in detail below). This expansion and elongation process is shared by both αAc and αBc, indicating a conserved mechanism, and found to be preserved when these isoforms are co-assembled as hetero-oligomers isolated from native lens fiber cells. However, we also observed isoform-specific features that correlated with differences in chaperone activities of these two isoforms towards the chemically-induced unfolding of model clients, lysozyme and insulin. Importantly, the quasi-ordered structural transitions observed along the client-induced co-aggregation pathway suggests that this process is mechanistically controlled and distinct from uncontrolled, purely amorphous protein aggregation. Further investigation of this mechanism could have broad implications for understanding the physiological response of α-crystallin sHSPs to extreme cell stress and the pathophysiology of cataract-associated light-scattering aggregate formations.

Under our experimental conditions, αAc, αBc and αLc exhibited distinct morphological variability in their apo-states, with Feret diameters in the range of approximately ~10 to ~20 nm. Notably, αAc displayed a higher degree of polydispersity, with a wider range of smaller and larger assemblies compared to αBc. αLc exhibited distinct structural features, but most comparable to aAc, consistent with the predominance of this isoform in our native preparations. These findings align with previous structural studies by electron microscopy[76,117,158,160,203,209,227] and solution-state methods[234,235], and underscores the notion that α-crystallins can adopt a continuum of stoichiometric and quaternary structural arrangements contributing to the challenges in defining their high-resolution structures that have long eluded investigators despite decades of effort[203,236].

The polydispersity of sHSPs is believed to be facilitated by rapid subunit or dimer exchange dynamics[205,213–215,236], which have led to a "traveling subunit" model to explain this mechanism. Structures corresponding to individual subunits or dimers are expected to have maximal diameters of approximately 5 – 7 nm[237–239]. While such species were not detected by SEC or DLS, our single-particle EM data did isolate a small but significant population of structures in this size range for the apo-state datasets (~4%, ~1% and 0.4% for αAc, αBc, and αLc respectively). This observation further supports the strength of this single-particle approach and is consistent with the notion that isolated monomer or dimer species are not long-lived and represent only a minor population at equilibrium under the tested conditions[205]. Alternatively, or in addition, subunit or dimer exchange may occur through direct engagement between oligomers, at least under certain conditions. In this context, we also observed a significant population of apo-state αAc, αBc and αLc species with a diameter of approximately 28 nm (31 nm for αLc) using single-particle EM. Upon closer examination of raw micrographs, these species appeared consistent with the presence of "kissing oligomers". Although it is possible that this observation is influenced by the sample preparation conditions for NS-EM that might produce random placement of

particles in close-proximity, it is also a possibility that such direct interactions between oligomers could effectively facilitate subunit exchange. Further exploration into the mechanism(s) of subunit exchange is still needed to fully resolve these possibilities.

The most notable distinction between the two α-crystallin isoforms was their differential chaperone activities towards both lysozyme and insulin, in agreement with previous studies that αBc displays a significantly higher efficacy compared to αAc toward many clients at 37° C[35,149,240]. Morphologically, these functional differences are reflected in the greater polydispersity and larger chaperone/client complex formation by αAc under comparable client saturation conditions, as evidenced by SEC, light-scattering, and NS-EM analyses. Analysis of αAc at the highest conditions of client saturation resulted in light-scattering behavior that surpassed lysozyme alone. Based on our morphological analysis by NS-EM, this behavior was attributed to the combination of aggregating lysozyme and the presence of large chaperone/client co-aggregates. A similar phenomenon has also observed with native lens clients but had not been fully explained[110,111,225,241].

Despite differences in their chaperone activities shown here, αAc, αBc and αLc all exhibited similar response mechanisms when confronted with unfolded (or destabilized) client proteins. Indeed, understanding of these differences in chaperone efficacy contributes to a more comprehensive understanding of the chaperone-response mechanism revealed by the structural characterizations in this study. Under conditions of high chaperone protection, such as the 4:1 chaperone-client ratio for αBc, chaperone complexes exhibit a morphology resembling the spherical cage-like apo-state oligomer, with slightly expanded spherical/oblique cage-like structures and the emergence of some elongated assemblies. This suggests only minor perturbation to the basal-state sHSP assembly is induced under minimal conditions of client sequestration. Shape analysis suggests that an overall spherical expansion of the chaperone in response to client persists up to a Feret diameter of approximately 20-30 nm, while significantly larger

species take on an elongated morphology. Under intermediate conditions of client challenge (both lysozyme and insulin), highly elongated structures become predominant, and beyond an extension of approximately 125 nm, these structures appear to collapse onto themselves, forming amorphous-like structures that can reach sizes exceeding hundreds of nanometers in diameter. Ultimately, under conditions of overwhelming client interaction, such as the 1:1 ratio condition for αAc and αLc using lysozyme, large chaperone-client co-aggregates exceeding 1 μm in size are formed. In addition, NS-EM images obtained under these conditions show a prevalence of small aggregates that are expected to be un-bound lysozyme aggregates. This assertion is based on comparison to lysozyme-only controls (**Supplemental Fig. 3**) and the expectation that the chaperone's capacity has been fully depleted under these conditions. However, we also cannot exclude the possibility of the presence of smaller unbound (or inactive) chaperone assemblies under these conditions.

Overall, these observations are consistent with the general notion that many sHSPs form large heterogenous complexes with unfolding clients that are morphologically distinct from apo-state sHSPs and from aggregated clients formed in the absence of sHSP. The influence of clientele on aggregation protection and the co-aggregation process has been previously described for other sHSPs using various clients[35,157,186,224]. For instance, the sHSPs yeast HSP26 and murine HSP25 formed co-aggregates with distinct morphological features in response to different unfolding clients (citrate synthase, rhodanese, α-glucosidase, and insulin)[224] [41]. Despite variation across clients, the morphological features of co-aggregates where qualitatively similar between HSP26 and HSP25 with each client. Notably, co-aggregates of HSP26/insulin and HSP25/insulin were described as "fibrous, network-like structures with diameters ~15 – 20 nm". In this current study we describe co-aggregates of αAc/insulin and αBc/insulin with similar morphologies, demonstrating that identity of unfolding client may have similar influences on the co-

aggregation process of different sHSPs. Surprisingly, our results show a very similar morphological co-aggregation processes for αAc and αBc when challenged with either lysozyme or insulin. One explanation for this conservation may be due to the similar small size of these clients (~14 kDa for lysozyme and ~6 kDa for insulin). Indeed, client size was shown to influence the polydispersity of complexes formed by other stress induced proteins (*e.g.,* HSP18.1, DegP)[186,242]. Future studies aimed at characterizing the influence of client size on the co-aggregation of α-crystallins could provide valuable insights to understanding the potential diversity of their chaperone response mechanism(s).

The mechanistic details underlying the elongation of the chaperone/client co-assemblies observed in this study remain unclear due to limitations of resolution inherent to NS-EM methods and the possibility for multiple potential pathways that could contribute to the formation of the observed structures. One possibility is the formation of elongated chaperone complexes through a daisy-chain type mechanism, where associated chaperone complexes may be interconnected by binding to common client proteins. Indeed, many of the elongated morphologies observed in our NS-EM analysis appeared as polymeric spherical (caged) assemblies interlinked in a directional manner. Under this proposed scenario, a portion of the client may be trapped between chaperone cages or on the periphery of the cage, and thus remain more exposed than a client completely internalized by the sHSP cage. Such exposure may support more efficient recovery by refolding chaperones[243,244]. While the relevance of this scenario to lens biology is limited since fiber cells lack refolding machinery, it may reflect a more general feature of these sHSPs. Another proposed possibility is that the chaperone undergoes oligomeric remodeling to accommodate client sequestration, involving subunit exchange to facilitate oligomeric growth in a directional fashion[184,218]. Under this scenario, the sHSP architecture may function as a scaffold that can continuously adapt to the entrapped cargo in order to facilitate high-capacity binding under increasingly saturating conditions. It is also

conceivable that elongated chaperone complexes are formed through a combination of these mechanisms. Notably, remarkably similar elongated morphologies for αAc and αBc have been observed upon heating[245], suggesting this structural transition is innate to these sHSP assemblies. However, a comprehensive understanding of these possibilities will require further investigation.

Overall, the findings in this study provide valuable insights into the sequestration of destabilized client proteins by the dynamic α-crystallin system and the formation of chaperone-client co-aggregates under conditions of overwhelming client challenge. In the context of the eye lens, the chaperone to client ratio will ultimately determine the efficiency of the sHSP system. In old age, as destabilized clients become more prevalent and α-crystallins become depleted, the balance will ultimately be pushed toward co-aggregation and formation of light-scattering opacities responsible for cataract and vision loss. Alternatively, the induced changes in sHSP structure may significantly alter the delicate balance of short-range interactions within the super-saturated environment of the lens leading to loss of transparency[75,128]. Therapeutic approaches targeting the preservation of intact chaperone in the lens may therefore be beneficial in preventing this global vision problem. Moreover, the results here suggest a definable mechanistic basis for client-induced co-aggregation, which might ultimately be inhibited by pharmacological intervention. Further exploration into the universality of the expansion-elongation mechanism across different client types, sHSP systems, and stress conditions such as temperature and oxidation will undoubtedly provide a more robust understanding of the sHSP co-aggregation mechanism. The single-particle analysis methods presented in this study offer an accessible and effective approach to structurally characterize and quantitatively compare such conditions.

Limitations of the study

While addressing the limitations of this work, it is important to note several aspects of the NS-EM analysis that could potentially impact interpretation. Specimens prepared for NS-EM are necessarily prepared under dilute concentrations, placed on a solid carbon support and undergo dehydration before imaging, which might influence the formation and morphology of the observed amorphous aggregates. Additionally, the single-particle distribution analysis workflow utilized has certain selection criteria and segmentation limitations in our experience, making it difficult to analyze extremely large aggregates (*e.g.,* greater than ~1 μm), potentially leading to an underestimation of such species formed under highly saturated client conditions. Furthermore, this approach cannot distinguish between chaperone/client complexes and unbound client aggregates, which may be present in the most saturated conditions observed for αAc. Despite these limitations, the substantial agreement of results obtained by this approach with solution-state DLS measurements and previous studies supports its utility.

ACKNOWLEDGEMENTS

We thank Dr. Russell McFarland for helpful discussions and the staff at the OHSU Multiscale Microscopy Core for EM instrumentation access and training. The research was funded by National Institutes of Health grants R01EY030987 and R35GM124779 (to S.L.R.), R01EY027012 (to K.J.L.), and T32EY23211 and F31EY033226 (to A.P.M.).

AUTHOR CONTRIBUTIONS

A.P.M. and S.E.O. performed experiments; S.L.R. and K.J.L. conceived this study, with contribution from all authors; A.P.M. and S.L.R. wrote the original draft and all authors contributed to the final manuscript.

CONFLICT OF INTERESTS

Authors declare no competing interests.

DECLARATION OF GENERATIVE AI AND AI-ASSISTED TECHNOLOGIES IN THE WRITING PROCESS

During the preparation of this work the authors used ChatGPT to help revise portions of the text to improve readability. After using this tool, the authors reviewed and edited the content as needed and take full responsibility for the content of the publication.

METHODS

Expression and purification of recombinant αA- and αB-crystallin

Expression and purification of αAc and αBc was adapted from Horwitz[5]. Recombinant human αAc and αBc in the expression vector pET3d were heterologously expressed in *E. coli* BL21(DE3) cells. Cells were grown at 37° C in LB media supplemented with ampicillin until reaching OD_{600} of 0.7 – 1.0. For αAc, expression was induced with 1 mM isopropyl β-D-1-thiogalactopyranoside (IPTG) followed by overnight expression at 18° C. For αBc, expression was induced with 1 mM IPTG for four hours at 37° C. Cells were harvested by centrifugation at 15,000 x g for 15 min at 4° C and resuspended in lysis buffer, containing: 20 mM Tris-HCl (pH 7.4 for αAc and pH 8.0 for αBc) aliquoted and frozen at -20° C.

For purification, a freshly thawed cell suspension was supplemented with 0.5 mM 1,4-dithiothreitol (DTT) and 0.1 mM PMSF, lysed by sonication, and cleared by ultracentrifugation at 165,000 r.c.f. for 30 min at 4° C to remove cellular debris. The supernatant was treated with DNase I (~400 units, Thermo Scientific) for 30 min on ice and passed through a 0.22 μm filter. The clarified lysate was loaded onto a gel filtration column packed with sephacryl 300 resin (S-300; Pharmacia) equilibrated in 20 mM Tris-HCl and 1 mM EDTA (pH 7.4 for αAc and pH 8.0 for αBc). Gel filtration fractions were assessed by SDS-PAGE and fractions containing αAc or αBc were pooled and supplemented with 0.5 mM DTT. The pooled fractions were further purified by anion exchange chromatography (MonoQ; GE Healthcare) equilibrated in buffer containing: 20 mM Tris-HCl, 1 mM EGTA and 0.16 mM EDTA (pH 7.4 for αAc and pH 8.0 for αBc) and eluted with a 1 M NaCl gradient. Fractions pertaining to the elution peak for αAc or αBc were pooled, concentrated to 2 mL using a centrifugal device (Vivaspin, 100,000 kDa m.w.c.o.), and loaded onto a Superose 6 size exclusion chromatography (SEC) column (GE Healthcare) equilibrated in 20 mM HEPES (pH 7.4), 100 mM NaCl, and 2 mM EDTA. Fractions containing αAc or αBc were pooled and concentrated to ~60 – 100 mM with a

100,000 m.w.c.o. spin concentrator (Vivaspin), aliquoted, flash frozen in liquid nitrogen, and stored at -80° C. Protein purity was assessed by SDS-PAGE and concentrations were determined by UV absorbance at 280 nm using the extinction coefficients 16,507 $M^{-1}cm^{-1}$ (αAc) and 19,000 $M^{-1}cm^{-1}$ (αBc). Due to the tendency of α-crystallin to co-purify with nucleic acids the ratio of A280/A260 was determined as >1.5 on purified samples. To maintain αAc in a reduced state, 0.5 mM DTT was added to the purified protein. Protein specimens were flash frozen and stored at -80°C for later use or incubated at 37° C for immediate use.

Isolation of native α-crystallins from ovine lenses

Whole lamb eyes were purchased from Wolverine Packing Co. (Detroit, MI) and Nebraska Scientific (Omaha, NE) and whole lenses were extracted immediately using a dissection scalpel and stored at -80° C. Cortical lens fiber cells were separated from core lens fiber cells with a dissection scalpel. Cortical lens fiber tissue was suspended in lysis buffer (10 mM Tris, 5 mM EDTA, 5 mM EGTA, pH 8.0) at a 1:1 ratio (v/v) and lysed with a glass dounce homogenizer. The cell lysate was centrifuged at 165,000 x *g* for 20 minutes at 4°C and the supernatant was collected for further purification. Supernatant was loaded onto a SEC column packed with sephacryl 300 resin (S-300; Pharmacia) equilibrated with 20 mM Tris-HCl, 1 mM EDTA, pH 7.4. The central fraction of the sizing peak containing native αLc (containing a mixture of αAc and αBc, as determined by SDS-PAGE) was loaded onto a Superose 6 SEC column (GE Healthcare) equilibrated with 20 mM HEPES, 100 mM NaCl, 2 mM EDTA (pH 7.4). Purified αLc was quantified using the extinction coefficient 17,125 $M^{-1}cm^{-1}$ (assuming a 3:1 ratio of αA:αB). Fractions containing αLc were pooled and supplemented with DTT (0.5 mM) to maintain a reducing environment. Freshly purified αLc was then flash frozen and stored at -80°C for later use or incubated at 37° C for immediate use.

Chaperone aggregation suppression assays

Aggregation assays were performed in a Nunc clear bottom 384 well plate (ThermoScientific) in 20 mM HEPES, 100 mM NaCl, 2 mM EDTA (pH 7.4) and 2mM tris(2-carboxyethyl)phosphine (TCEP). Lysozyme (Fisher, MS grade) and insulin (Sigma Aldrich, bovine pancreas) were used as an unfolding client and held at a constant concentration of 10 μM (lysozyme) and 40 μM (insulin) for all reactions. Freshly purified (or freshly thawed) samples of αAc, αBc, or αLc were incubated at 37° C overnight to equilibrate quaternary structure prior to performing the aggregation assays. The reduction induced aggregation of 10 μM lysozyme was monitored in the absence and presence of varying chaperone concentrations between 60 – 5 μM for αAc (*i.e.,* chaperone:client ratios of 6:1, 4:1, 2:1, 1.5:1, 1:1, and 0.5:1); 40 – 2.5 μM for αBc (*i.e.,* chaperone:client ratios of 4:1, 2:1, 1:1, 0.5:1, and 0.25:1); and 40 – 10 μM for native αLc (*i.e.,* chaperone:client ratios of 4:1, 2:1, and 1:1). The reduction induced aggregation of 40 μM insulin was monitored in the absence and presence of varying ratios of αAc and αBc at chaperone:client ratios corresponding to approximately half-maximal protection based on turbidity readings (0.5:1 for αAc and 0.2:1 for αBc).

Chaperone/client mixtures were incubated at 37° C for 15 min followed by the addition of TCEP (2mM final concentration) to initiate lysozyme and insulin unfolding. Turbidity at 360 nm was measured on a Tecan Infinite M200 Pro with a constant temperature of 37° C for 120 minutes. Aliquots of pooled aggregation reactions were set aside for SDS-PAGE and negative stain EM (NS-EM). The remainder of the pooled reactions were loaded onto a Superose 6 SEC column (GE Healthcare) equilibrated with 20 mM HEPES, 100 mM NaCl, and 2 mM EDTA (pH 7.4) to assess the size of soluble chaperone/client co-aggregates. The pooled reactions were not filtered or centrifuged prior to SEC analysis. The Superose 6 column (24 mL bed volume) was calibrated using a

commercial calibration kit (Biorad) containing thyroglobulin (670 kDa), g-globulin (158 kDa), Ovalbumin (44 kDa), myoglobin (17 kDa), vitamin B12 (1.35 kDa). The Superose 6 void volume was determined using dextran blue 2000. Aliquots of each size exclusion fraction were taken for SDS-PAGE to determine the co-elution profile of the chaperone and client.

Statistical analysis comparing αAc, αBc, and αL chaperone activity assays was performed in excel and all visual interpretation of the data was done using matplotlib based libraries in python. Raw turbidity data was processed by subtracting the baseline of each replicate and normalizing to the average turbidity of reduced client-only replicates. Turbidity assays were replicated with 1-3 biological replicates and 4-8 technical replicates for each ratio. An F-test was performed comparing isoforms at each ratio, followed by a two-sample t-test. Aggregation half-times ($t_{1/2}$) were determined as the time point corresponding to half maximal absorbance for each replicate. Statistical comparison of $t_{1/2}$ values between chaperone:client ratios were done with a two-sample t-test. The half-maximal ratio for aggregation suppression for the lysozyme assays was determined by fitting a sigmoidal curve (Scikit learn) of percent protection against chaperone:client ratio.

Dynamic light scattering measurements

All DLS measurements were performed at 37° C in an Aurora 384 well plate on a Wyatt DynaPro plate reader III (Wyatt Technology, Santa Barbara, USA) equipped with an 830 nm laser and 150º DLS detector angle. Light scattering measurements were acquired over 10 seconds and processed in Dynamics software v7.10.1 (Wyatt). Protein samples were mixed and incubated at 37° C for 15 minutes before the addition of TCEP (2 mM final concentration) to initiate lysozyme unfolding. The aggregation of 10 μM lysozyme in the presence of αAc or αBc (40 μM, 20 μM, and 10 μM) was monitored by DLS for 120 minutes (n=3). These concentrations were the same used in turbidity analysis. Additionally, it was

shown that the aggregation of 10 μM lysozyme alone was below the limit of detection on the DLS instrument and ensured that DLS measurements were monitoring the apo-state αAc and αBc oligomers and/or their co-aggregates formed with lysozyme. Due to the small size of lysozyme, control DLS measurements of reduced and oxidized lysozyme in the absence of αAc or αBc were performed at 100 μM with 20 mM TCEP to provide reliable measurement of the hydrodynamic radii within the instrument's limit of detection.

Three technical replicates were carried out for each reaction. Hydrodynamic radii and percent mass were calculated using the Dynamics software regularization fitting algorithm for polydisperse samples. For comparative analysis, hydrodynamic radii and their corresponding percent mass were binned into one of four bins: 1-10 nm, 10-100 nm, 100-300 nm, and 300+ nm. The average and standard error of the mean were calculated for each bin of each reaction.

Negative stain electron microscopy

For NS-EM performed on the apo-state chaperones, samples containing only purified αAc, αBc, or αLc were pooled from SEC and diluted to ~2 – 3 μM in 20 mM HEPES (pH 7.4), 100 mM NaCl, and 2 mM EDTA (αAc and αLc samples also contained 1 mM DTT). Sample grids of chaperone/client mixtures at or below 2:1 ratio were prepared directly from the aggregation reactions without dilution, while the 4:1 reactions were diluted 2x with dilution buffer. For each sample, a 3 μL drop was applied to carbon coated 400 mesh copper grids (Ted Pella) that were glow discharged at 15 mA for 1 min. Excess protein was blotted with filter paper, washed twice with ultra-pure water, stained with freshly prepared (0.75% wt vol^{-1}) uranyl formate (SPI-Chem), blotted, and dried with laminar air flow.

Negatively stained EM specimens were imaged on a 120 kV TEM (Tecnai T12, FEI) and micrographs were collected on a 2K x 2K CCD camera (Eagle, FEI) at a nominal magnification of 49,000 x at the specimen level. All micrographs were collected with a

defocus range of ~1.5 – 2.5 μm and calibrated pixel sizes of 4.37 Å/pixel for apo-state αBc (n = 43) and 4.401 Å per pixel for apo-state αAc (n = 30), apo-state aLc (n=9), αAc:lysozyme 4:1/2:1/1:1 (n = 8/8/10), αBc:lysozyme 4:1/2:1/1:1 (n = 8/8/22), aL:lysozyme 4:1/2:1/1:1 (n=6/10/7), aAc:insulin 0.5:1 (n=9), and aBc:insulin 0.2:1 (n=9) reactions.

Single particle EM image analysis

Two-dimensional (2D) class averages were obtained as follows. Micrographs for apo-state αAc and αBc (equilibrated at 37° C for ~16 hours) were pre-processed in EMAN 2.91[246] by screening for astigmatism and drift based on Thon rings of Fourier transforms following manual CTF fitting. Particles were picked with EMAN's interactive particle picker and extracted with box sizes of 72 x 72 pixels for apo-state αAc (10405 particles) and αBc (14502 particles). The phase flipped particle stack from EMAN2.91 was normalized using relion_image_handler and imported into RELION3.0[247]. Reference-free 2D classification was performed on the CTF-corrected images in RELION3.0 using a mask size of 200 – 250 Å.

Single-particle morphological analysis developed for this work was performed in FIJI[230] using full micrographs of the apo-state αAc, αBc, and αLc, 4:1, 2:1, and 1:1 reactions of αAc, αBc, and αLc with lysozyme, 0.5:1 reaction of αAc and insulin, and 0.2:1 reaction of αBc and insulin. An FFT bandpass filter was applied to each image stack using the default filter settings in FIJI (filter large structures at 40 pixels, filter small structures at 3 pixels, 5% tolerance, auto scale after filtering, saturate image when autoscaling). Next, the maximum filter was used with a default radius of 2 pixels followed by background subtraction (rolling ball radius of 25 - 50 pixels) was used on each micrograph stack. The filtered and background subtracted micrographs were subsequently binarized (with dark background). Background noise removal with the Remove Outliers tool and

erosion/dilation of binarized segments were tuned to optimize segmentation results (see **Supplemental Figs. 2, 5-8**).

The FIJI Analyze Particles tool was used to collect Feret diameter measurements. Images of numbered particle outlines were generated along with a table of particle analysis measurements. The number of particles analyzed for each sample were: 13889 for apo-αAc, 5846 for αAc:lysozyme 4:1, 2757 for αAc:lysozyme 2:1, 3381 for αA:lysozyme 1:1, 17192 for apo-αBc, 3793 for 4:1 αBc:lysozyme, 1421 for αBc:lysozyme 2:1, and 342 for αB:lysozyme 1:1, 3401 for apo-αLc, 2271 for 4:1 αLc/lysozyme, 4187 for 2:1 αLc:lysozyme, 1224 for 1:1 αLc:lysozyme, 5750 for 0.5:1 aAc:insulin, and 6018 for 0.2:1 αBc:insulin. A two-sample Kolmogorov-Smirnov test (K-S test) was performed in python (Scipy.stats) used to statistically compare the distributions of Feret diameter measurements between isoforms and at sHSP:lysozyme ratios and between αAc or αBc with and without insulin.

Sequence alignment of α-crystallin homologs

Amino acid sequences of αA-crystallin and αB-crystallin (human (P02489 and P02511), bovine (P02470 and P02510), and canine (P68280 and A0A8C0JXJ4)) were aligned using ClustalW in Jalview 2.11.2.7[248] and shaded to indicate positions that are conserved in both αAc and αBc (dark shading), within αAc or αBc (light shading), and non-conserved (white). Gaps are indicated with a dash. Annotation of secondary structure (β-sheets) displays the consensus of three X-ray crystallographic structures of αB-crystallin (PDB 2WJ7[237], PDB 2Y1Y[238], and PDB 3L1G[239], using MODELLER[249] in ChimeraX1.15[250].

Statistical analysis and data representation

All statistical descriptors (mean, standard deviation, standard error of the mean, mode) were calculated using the python based open-source software SciPy[251]. The presented

ranges for Area and Feret diameter (Table 2) were calculated by truncating the bottom 2.5% and top 2.5% of the distribution to remove potential outliers. Two-sample Kolmogorov-Smirnov tests (K-S test) were done in SciPy. F-tests and T-tests for turbidity data were done either in Microsoft Excel or SciPy. Curve fitting to determine half-maximal protection ratios against lysozyme was done by using the scipy.optimize.curve_fit program (method='lm') to fit data to the equation $y = \frac{L}{1+e^{-k(x-x_0)}} + b$. All data plots were generated using libraries in python3, except the raincloud plots made in R Studio.

Data Availability

Raw data used for structural analysis, electron micrographs and processed image files, are provided on zenodo doi: 10.5281/zenodo.8240041.

SUPPLEMENTAL FIGURES & LEGENDS

Supplemental Figure 1

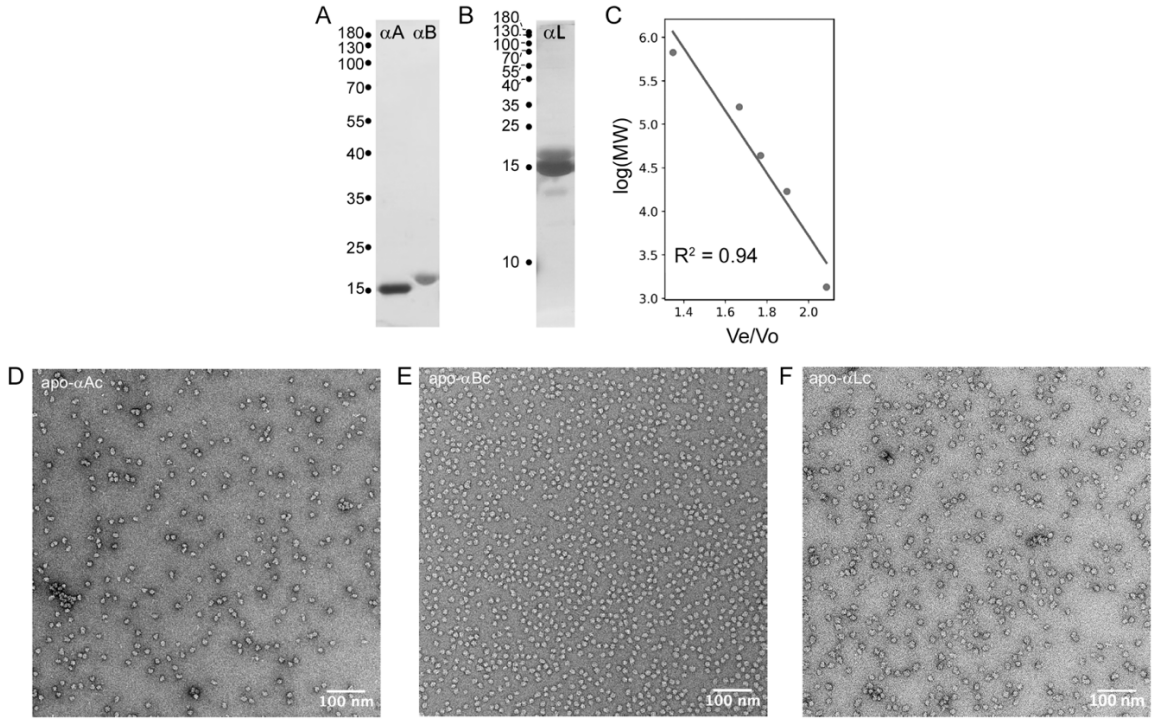

Supplemental Figure 1. Biochemical isolation and structural assessment of apo-state α-crystallins. **A,B.** SDS-PAGE gels of purified αA- and αB-crystallin (panel A, 15% gel) and native αL-crystallin (panel B, 17.5% gel) with molecular weight (MW) positions annotated (kDa). Note, the gel in panel B was run at higher percent acrylamide to resolve the αA and αB bands present in the native heteromeric assembly. **C.** Standard calibration curve of Sepharose-6 size exclusion column using calibration standards (Biorad # 1511901; MW range of 1.35 – 670 kDa) and Dextran Blue (DB2000) for void volume (Vo) determination, plotted as log (MW) versus ratio of elution volume (Ve) over Vo. **D-F.** Representative NS-EM micrographs of purified apo-αAc, apo-αBc and apo-αLc (scale bar = 100 nm).

Supplemental Figure 2

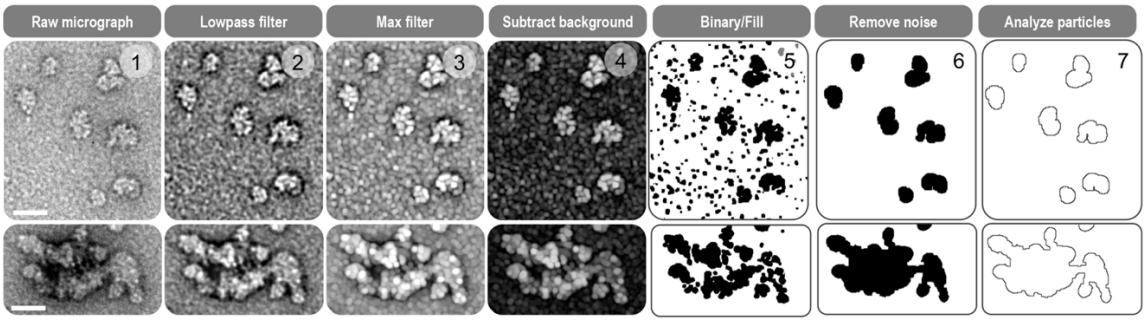

Supplemental Figure 2. Image processing workflow applied to NS-EM micrographs for the morphological analysis of individual sHSP complexes and co-aggregates applied using the software FIJI. Example workflow shows representative co-aggregates of αAc/lysozyme at a 2:1 chaperone:client ratio. Top row of images include examples of cage-like morphologies and the bottom row shows an example of a larger co-aggregate (scale bar = 20 nm). Step 1, shows original raw micrograph with an effective pixel size of 4.40 Å/pixel. Step 2, shows result of FFT band-pass filter with applied settings: (filter large structures at 40 pixels, filter small structures at 3 pixels, 5% tolerance, auto scale after filtering, saturate image when autoscaling). Step 3, shows result of applied maximum filter set to a default radius of 2 pixels. Step 4, shows result of background subtraction (rolling ball radius of 25 - 50 pixels). Step 5, shows the result of binarization (with dark background). Step 6, shows the result of removing background noise by tuning of the radius parameter in the Remove Outliers tool, and erosion/dilation of binarized segments. Step 7, shows the final result of particle contours used for morphology analysis using the FIJI Analyze Particles tool.

Supplemental Figure 3

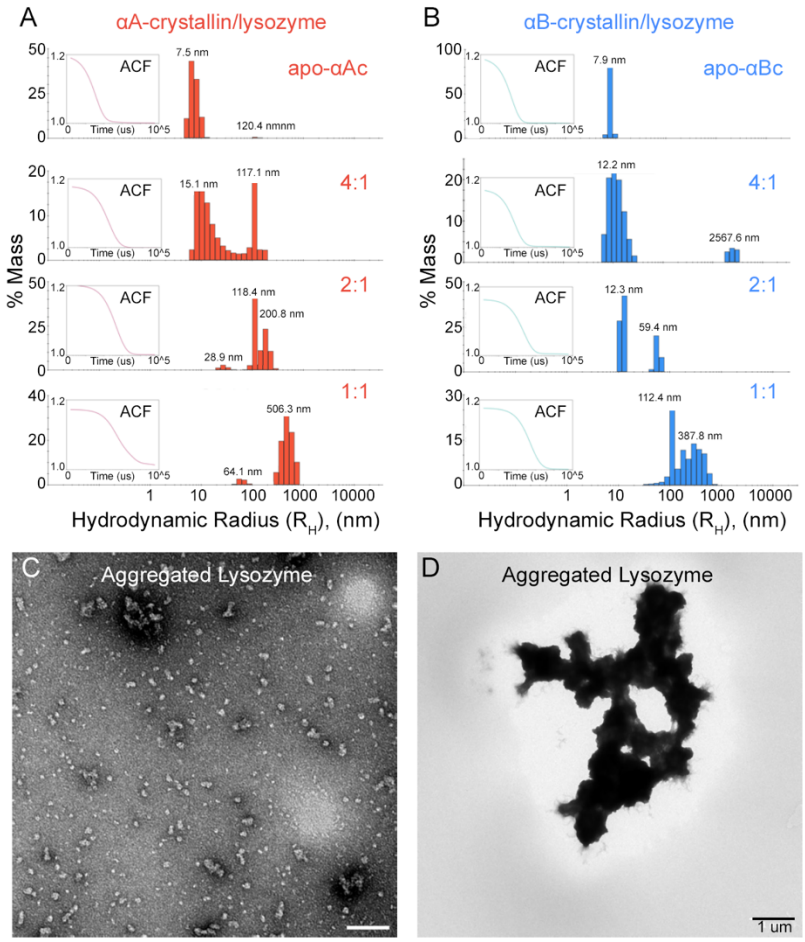

Supplemental Figure 3. Dynamic light scattering measurements of α-crystallin/lysozyme reactions and micrograph of aggregated lysozyme. **A,B.** Mass % histogram of hydrodynamic radii (R_H) obtained by dynamic light scattering (DLS) with autocorrelation function (ACF) for a single technical replicate shown for each experiment (inset). Representative data for αAc (panel A) and αBc (panel B) and results of aggregation suppression assays using reduced lysozyme at varying chaperone:client ratios are shown. **C,D.** Representative NS-EM micrograph of reduced lysozyme showing examples of smaller aggregates (panel C, scale bar = 100 nm) and large plaque-like aggregates (panel D, scale bar = 1 μm).

Supplemental Figure 4

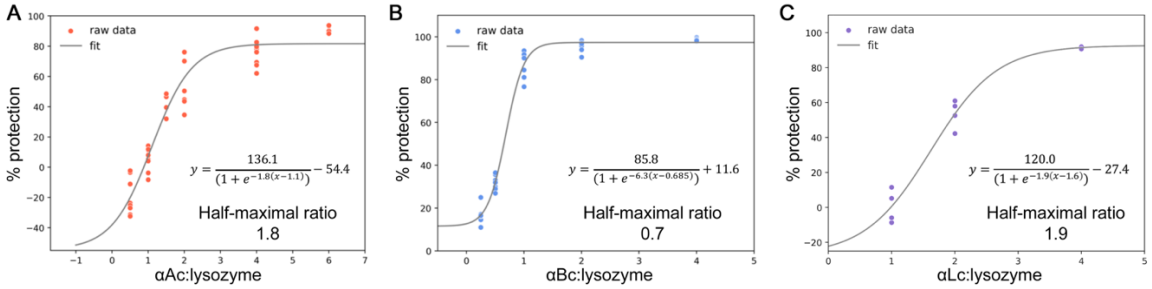

Supplemental Figure 4. Half-maximal ratio analysis for α-crystallin/lysozyme chaperone assays. A-C. Raw percent protection values were plotted and fit to a sigmoidal curve to determine the half-maximal % protection ratios for αAc/lysozyme (panel A), αBc/lysozyme (panel B), and αLc/lysozyme (panel C).

Supplemental Figure 5

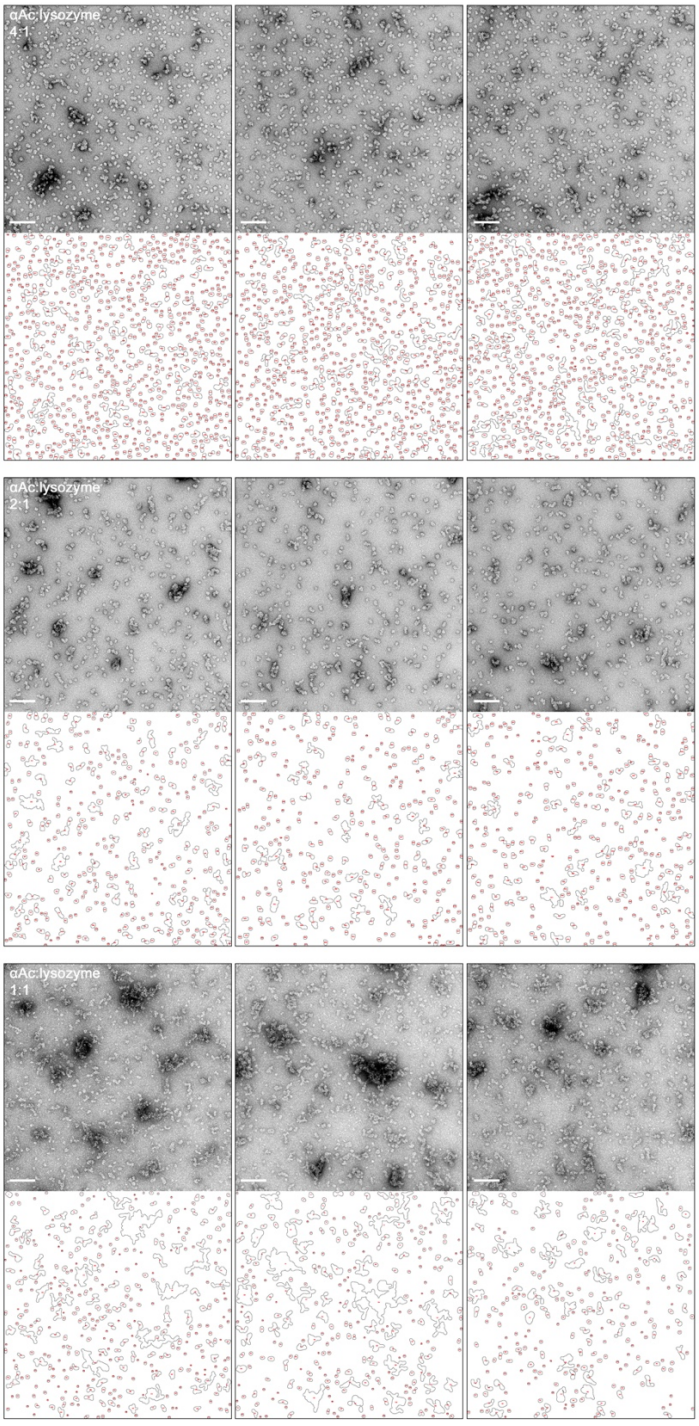

Supplemental Figure 5. Representative micrographs and single-particle shape analysis for αAc/lysozyme complexes. Representative micrographs of negatively stained αAc/lysozyme complexes and co-aggregates formed at varying chaperone:client ratios of 4:1, 2:1, and 1:1, scale bar = 100 nm (top), and resulting single-particle morphology profiles obtained from FIJI analysis (bottom).

Supplemental Figure 6

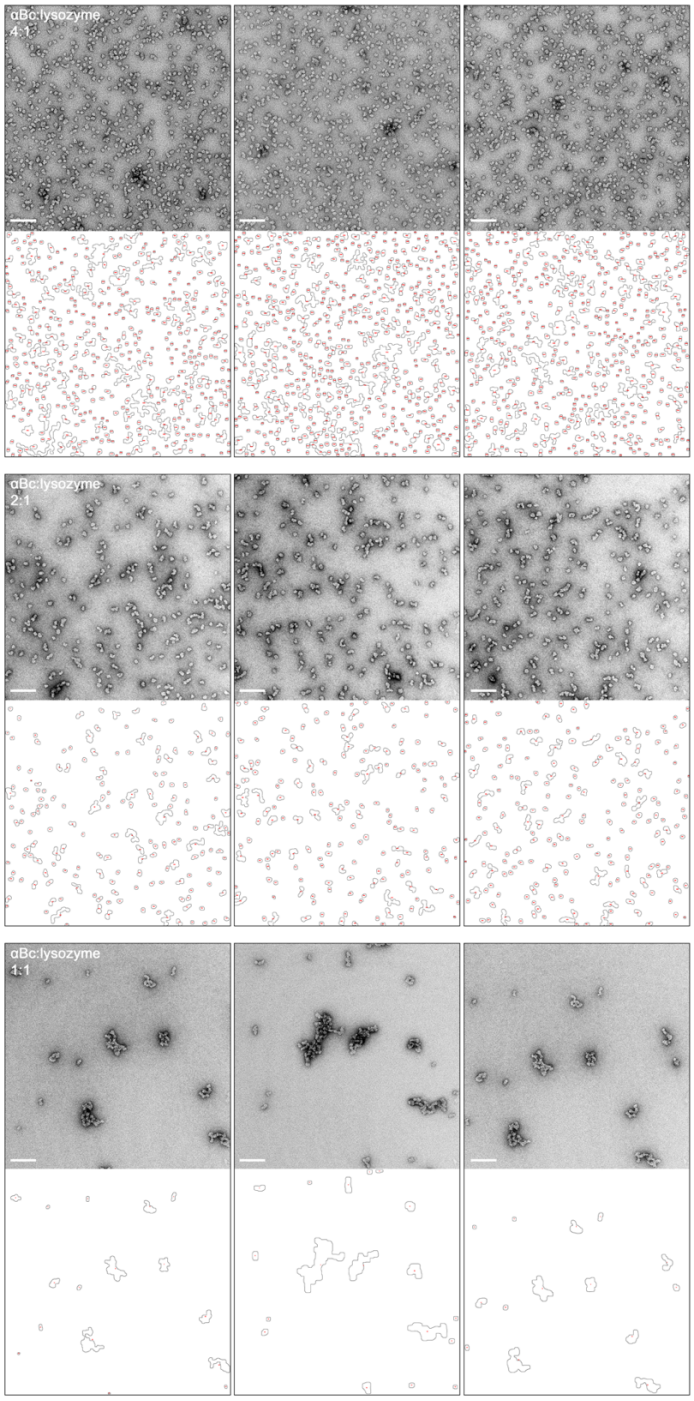

Supplemental Figure 6. Representative micrographs and single-particle shape analysis for αBc/lysozyme complexes. Representative micrographs of negatively stained αBc/lysozyme complexes and co-aggregates formed at varying chaperone:client ratios of 4:1, 2:1, and 1:1, scale bar = 100 nm (top), and resulting single-particle morphology profiles obtained from FIJI analysis (bottom).

Supplemental Figure 7

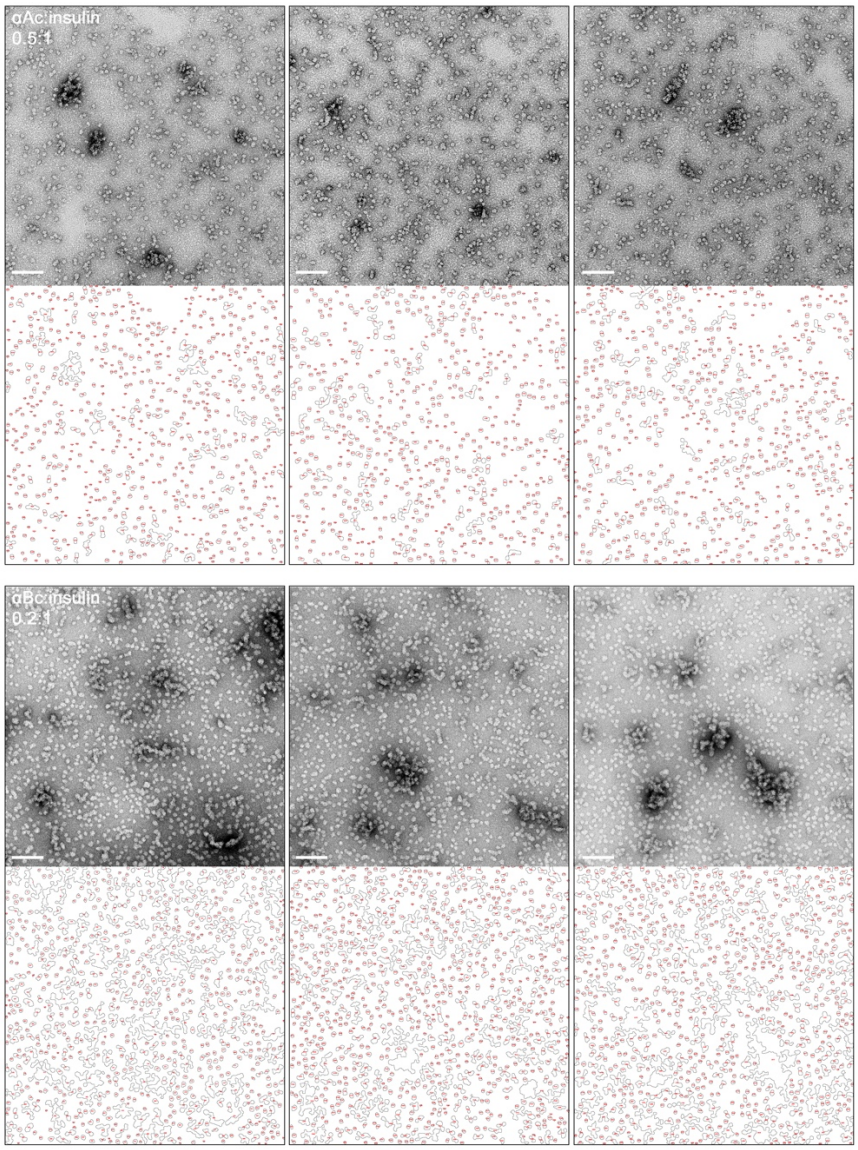

Supplemental Figure 7. Representative micrographs and single-particle shape analysis for αAc and αBc/insulin complexes. Representative micrographs of negatively stained αAc and αBc/lysozyme complexes and co-aggregates formed at varying chaperone:client ratios of 0.5:1 and 0.2:1, respectively (scale bar = 100 nm) (top), and resulting single-particle morphology profiles obtained from FIJI analysis (bottom).

Supplemental Figure 8

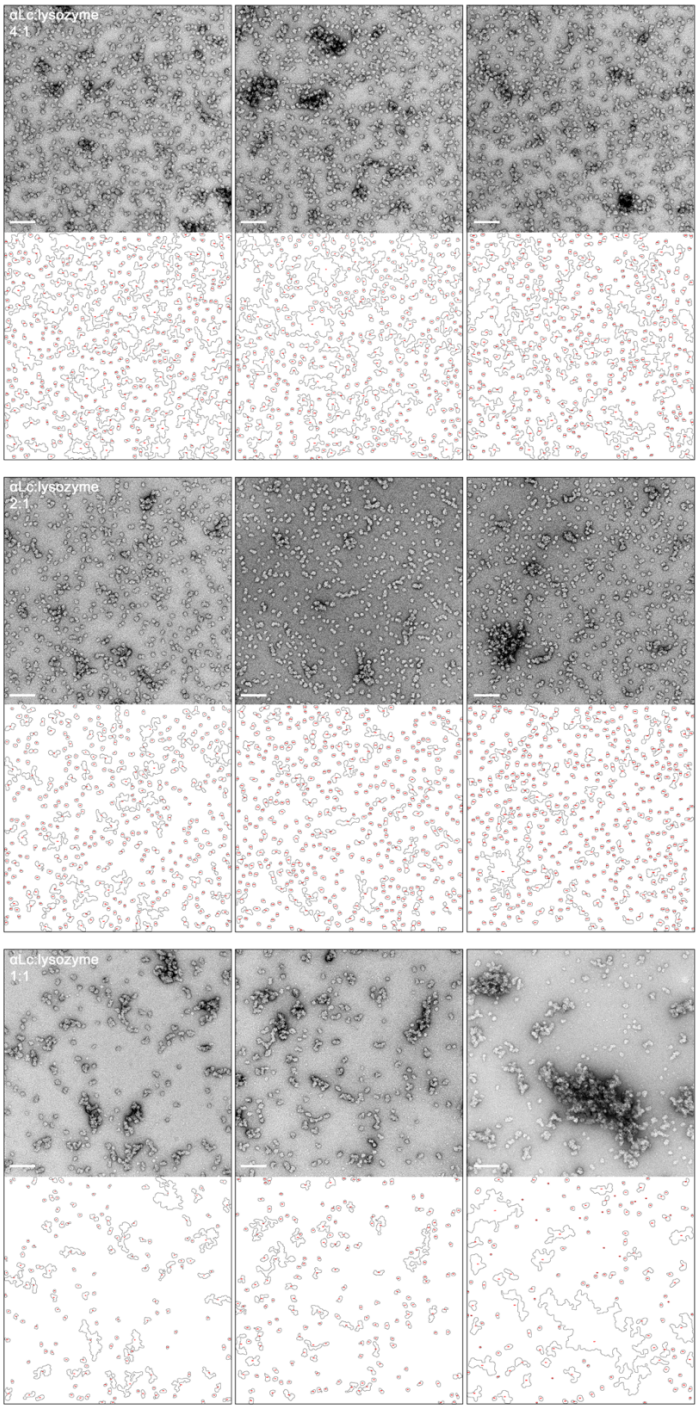

Supplemental Figure 8. Representative micrographs and single-particle shape analysis for αLc/lysozyme complexes. Representative micrographs of negatively stained αLc/lysozyme complexes and co-aggregates formed at varying chaperone:client ratios of 4:1, 2:1, and 1:1, scale bar = 100 nm (top), and resulting single-particle morphology profiles obtained from FIJI analysis (bottom).

Chapter 3: Structural mechanisms of small heat shock protein client sequestration and induced polydispersity

Authors: Adam P. Miller[1,2] and Steve L. Reichow[1,2]

[1] Department of Chemical Physiology and Biochemistry, Oregon Health and Science University, Portland OR 97239, U.S.A.

[2] Vollum Institute, Oregon Health and Science University, Portland OR 97239, U.S.A.

ABSTRACT

Small heat shock proteins (sHSPs) are ATP-independent molecular chaperones that support proteostasis during cellular stress events that promote protein unfolding and aggregation. Mechanistic insights into how sHSPs dynamically assemble and sequester destabilized client proteins have been limited, due to client-induced polydispersity of sHSP/client complexes and heterogeneous protein-protein interactions that guide sHSP assembly. Here, we present Cryo-EM structures of a model sHSP (mjHSP16.5) in the absence and presence of a destabilized client at sufficient resolution for atomic model building of multiple oligomeric states. Interrogation of structural details coupled with functional mutation studies suggest the dynamic mjHSP16.5 N-terminal domain – in particular conserved hydrophobic regions – play a critical role in chaperone assembly, plasticity, and client sequestration. Engagement and sequestration of destabilized client under equilibrium conditions induced an ensemble of higher-order sHSP/client states, facilitated by the intrinsic plasticity of multiple sHSP subunit interactions also resolved in the apo-state. Client engagement results in polarization of stability across the mjHSP16.5 scaffold, proposed to facilitate a directional elongation mechanism to enhance client-capacity. While formation of some higher-order sHSP/client states appear to form through simple addition of dimeric subunits into newly formed geometrical features, other states suggest the existence of multiple sHSP/client assembly pathways. Together, these results provide long-sought insight into the chaperone function of sHSPs and showcase the relationship between polydispersity and client-sequestration under stress conditions.

INTRODUCTION

The small heat shock proteins (sHSPs) are a diverse family of ATP-independent molecular chaperones that play a major role in proteostasis and aggregation prevention across all domains of life[252,253]. Many sHSPs act as first responders to cellular stress and utilize a “holdase” chaperone function by forming soluble chaperone/client complexes[5,203]. sHSPs preferentially bind destabilized states of a wide range of clientele through recognition of non-native protein folds and retain clients in partially unfolded or refolding competent states[12,35,40,179]. Additionally, sHSPs maintain other important cellular functions including regulation of apoptosis and cellular life cycle, cytoskeletal protection, and vertebrate vision[15,49,57,254]. Activation of sHSP function occurs in response to various cellular stress including high/low temperatures, pH changes, and oxidative stress. Mutation, upregulation, and dysregulation of human sHSPs (e.g., HSPB1/HSP27, HSPB5/αB-crystallin, and HSPB6) are associated with diverse disease states including various myopathies, cardiac diseases, and aggregopathies (Alzheimer’s disease, Parkinson’s disease, cataract)[46,54,55,87,255]. The association of sHSPs with human diseases make them intriguing pharmacological targets, however major difficulties in understanding heterogeneous sHSP assemblies and diverse client interactions have limited molecular level insights into their chaperone mechanism.

The sHSPs are relatively small (12-43 kDa) and many form large oligomeric structures from 200-800+ kDa. sHSPs share a tripartite domain architecture of a central α-crystallin domain (ACD) flanked by a largely disordered N-terminal domain (NTD) and a flexible C-terminal domain (CTD)[252]. The monomeric structure of most sHSPs consists of two anti-parallel β-sheets of ~7-9 β-strands with evolutionary divergence in β-strand arrangement that give rise to distinct dimeric structures between metazoan (β6+7-strand exchange) and non-metazoan (β5+6 loop/β7-strand exchange) lineages. sHSPs representing all domains of life have exhibited dimer tethering to produce high-order

oligomeric states through interactions of a conserved Ile-X-Ile (IXI) motif in the CTD binding to a hydrophobic pocket (β4/β8-groove) of a neighboring protomer's ACD[137,138,154]. The NTD of sHSPs exhibits lower sequence conservation and extreme structural flexibility while supporting structure and function through high-order oligomerization and client interactions[1,63,256–258]. Characterization of the sHSP NTD is missing or incomplete from many structural studies due to flexibility and the mechanism(s) by which it supports oligomerization and chaperone function are not fully known.

The first high-resolution structure of a fully assembled oligomeric sHSP was HSP16.5 from the thermophilic archaeon *Methanocaldococcus jannaschii* (mjHSP16.5), which formed an octahedrally symmetric cage with a diameter of ~12 nm comprised of 12 ACD dimers tethered by canonical ACD/CTD interactions[138]. The NTDs (residues 1-32) where unresolved and attributed to flexibility of this region, however the structure supports the notion of the NTD residing inside of the cage. Subsequent studies have described the NTD of mjHSP16.5 to adopt multiple conformations (residues 24-33) within the cage and possible α-helical segments (residues 13-24)[194,259]. Previously characterized structural aspects of NTD inter-/intra-molecular interactions among various sHSP assemblies include interaction with the ACD, short helical segments, and binding to client proteins[63,137,154,260,261]. Cage-like structures are conserved in archaeal, bacterial, viral, and eukaryotic sHSPs, along with other morphologies (e.g., disc-like, fibrillar), as well as low-order dimer/tetramers – showcasing the diversity of the sHSP structural landscape[4,10,137,138,144,153–155,158,160,161,260,261]. Many sHSPs exhibit a polydisperse ensemble of oligomeric states with subunit exchange dynamics that are enhanced under stress conditions or as a constituent aspect of oligomerization under non-stress conditions, depending on the sHSP[125,158,186]. Polydispersity has delivered a challenge to structural characterization of many sHSPs, often yielding low-resolution depictions of limited

interpretability, yet this level of plasticity is an essential characteristic of sHSP holdase function.

The role of sHSPs in preventing client aggregation involves mechanisms to recognize aggregation prone clients and facilitate a means of sequestering the bound client from other destabilized proteins, thus preventing aggregation. The chaperone function of mjHSP16.5 provides a well-studied example of how structural plasticity is needed for efficient response to stress-induced client unfolding. Subunit exchange of mjHSP16.5 is not detected below temperatures of 60° C (well below the physiological temperature for this thermophilic species) and results in a greatly depleted chaperone efficiency, requiring 20- to 80-fold excess of mjHSP16.5 to prevent the aggregation of client[262,263]. At higher temperatures, above 60° C, mjHSP16.5 exhibited subunit exchange kinetics (0.067 min^{-1} at 68° C) and proficient client aggregation protection[262]. Many sHSPs display similar relationships between subunit exchange kinetics and temperature, likely reflecting coupled structure/function dynamics during stress events[8,165,264]. High-resolution mechanistic details of sHSP/client co-aggregation remain largely unknown and are limited by heterogeneity and structural complexity of sHSP/client complexes and the influence of clientele (size, destabilization) on co-aggregation.

Here we utilized single-particle Cryo-EM to uncover structural details of the mjHSP16.5 in the apo-state and various client-induced oligomeric states contributing to the sequestration of a model client, lysozyme. Characterization of the apo-state 24-mer demonstrated a dynamic behavior (modes of stretching and expansion) that had not been captured previously. Significant regions of the NTD could be resolved in the apo-state and describe a putative mechanism involving a conserved Phe-rich region supporting oligomer assembly and plasticity, as well as a role in client-induced polydispersity that is supported by mutagenesis studies. Cryo-EM analysis of mjHSP16.5/lysozyme complexes formed under equilibrium-state conditions of heat-induced client destabilization (i.e., at ~75° C,

just below the melting temperature of lysozyme) revealed an ensemble of induced oligomeric states of the sHSP scaffold (24 – 36mers), whereas similar transformations were not observed in the absence of client. These structures describe a polarization/elongation mechanism, suggesting directional recruitment of dimer/client units and stability of the sHSP/client complex amidst increasing clientele. Together, these findings provide long-sought structural insights into the mechanistic coupling of sHSP polydispersity and chaperone function.

RESULTS

NTD mediates plasticity of mjHSP16.5 cages

For structural and functional characterization, mjHSP16.5 was recombinantly expressed in *E. coli* and purified to homogeneity without tags (Supplementary Fig. 1). Purified mjHSP16.5 in the apo-state was incubated at 37° C (apo-37) for ~16 hours and 75° C for 2 hours (apo-75) before vitrification for Cryo-EM data collection, resulting in 16,214 movies for single-particle analysis for apo-37 and 6,460 micrographs for apo-75. These temperatures correspond to inactive and chaperone-competent states of mjHSP16.5, respectively.

For the apo-37 dataset, 2D classification (Supplementary Fig. 2, 3a) showed monodisperse cage-like complexes of uniform diameter (~12 nm). A non-symmetric consensus refinement yielded a 3.01 Å reconstruction exhibiting the cage-like structure of a mjHSP16.5 24-mer agreeing with previous structural studies[138,194]. The twelve dimeric building blocks display canonical β5+6 loop exchange architecture of non-metazoan sHSPs and ACD-groove/CTD-IXI tethering interactions between neighboring dimers. The asymmetric reconstruction also showed a mix of disordered and helical density within the cage cavity, with density lining the inner-ACD surface attributed to the NTD. Throughout multi-class ab initio generation and subsequent heterogeneous classification, it became

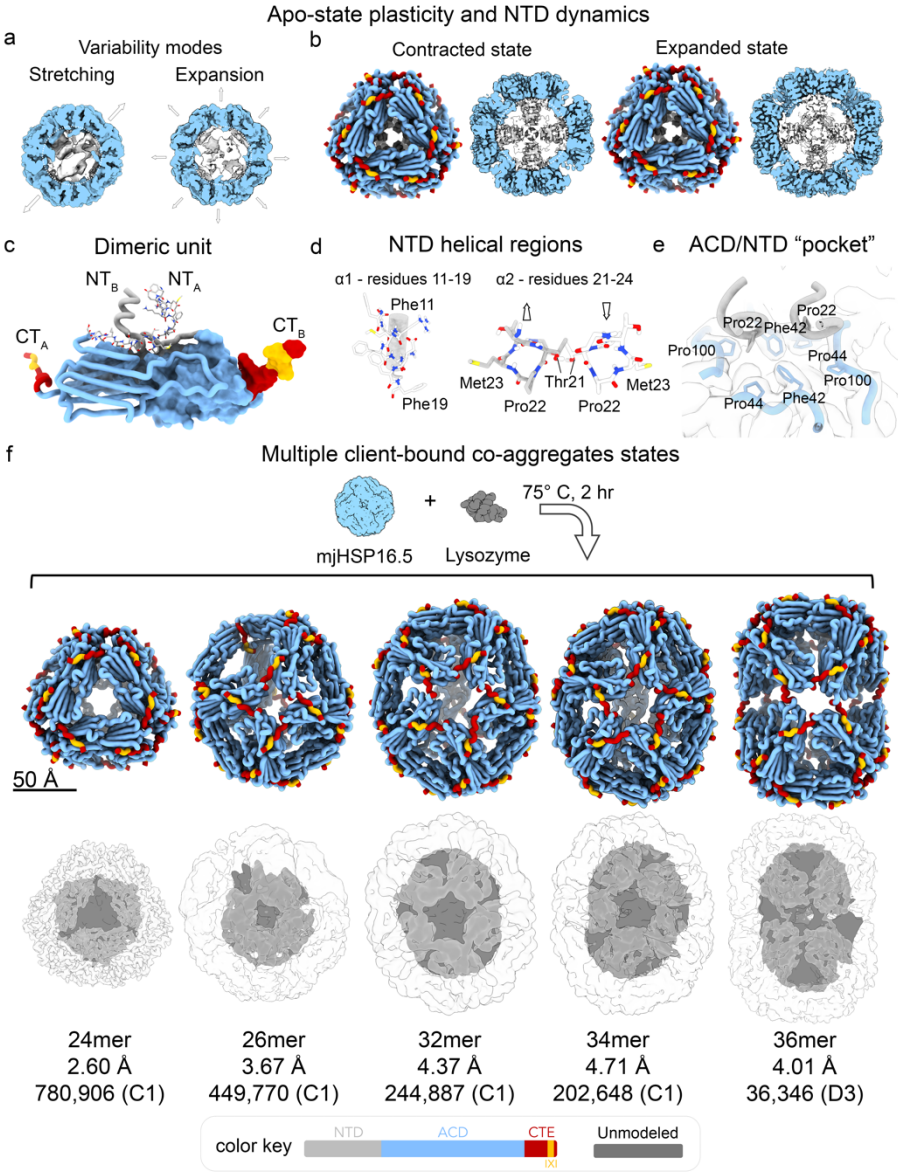

Figure 1: Single-particle Cryo-EM analysis of mjHSP16.5 in the absence and presence of destabilized client (a) mjHSP16.5 apo-state displayed conformational dynamics, described by modes of stretching and expansion that were identified by Cryo-EM 3D variability analysis. Asymmetric Cryo-EM density maps displayed in slice view to show the central cavity, with ACDs colored in blue and internal density belonging to the NTD colored in gray (b) Resolved contracted (left) and expanded (right) states of mjHSP16.5 apo-state (37° C). (left) Atomic models depicted in cartoon representation (ACD:blue, CTD:red, IXI-motif:yellow). (right) Central slice of the corresponding Cryo-EM density map with the NTD density colored in gray and ACD colored in blue (c) sHSP dimeric unit of the expanded state with NTD region colored the same as in (b) and throughout Fig.1 (see color key) (d) Atomic models of NTD helical regions α1 (residues 11-19, left) and α2 (residues 21-24, right) with various residues labeled for orientation purposes (e) Atomic model and Cryo-EM map (semi-transparent) showing the ACD/NTD pocket pertaining to ACD residues (Phe42, Pro44, and Pro100) and Pro22 region of the NTD that fits into the ACD "pocket" (f) Atomic models (top) and Cryo-EM density maps (bottom) of the 24mer, 26mer, 32mer, 34mer, and 36mer states obtained in the presence of destabilized lysozyme (75° C incubation for 2 hours). The resolutions and particles count for each oligomeric state indicated (bottom). Color key: NTD in light gray, ACD in blue, CTD in red, IXI-motif in yellow, and unmodeled density in dark gray.

apparent that there were two similar, yet distinct, cage sizes present in the dataset.

Principal component modes of 3D variability uncovered cage stretching and expansion modes of dynamics accompanied by rearrangement of NTD density within the cage (Figure 1a and Supplementary Fig. 3d). Further classification and refinement with octahedral symmetry yielded a contracted state refined at 2.50 Å resolution and an expanded state at 2.35 Å resolution (Supplementary Fig. 3b,c). Both of the octahedral reconstructions show strong helical density inside the cage along with NTD density lining the inner-ACD surface (Figure 1b, internal slice views). The apo-75 dataset resulted in a similar octahedral 24mer cage reconstruction at 2.86 Å resolution with 24 helical densities within the cage and similar stretching/expansion modes (Supplementary Fig. 4).

The high-resolution reconstructions of the contracted and expanded states allowed for model building of the complete ACD, CTD and NTD residues 11-32 for each state/condition (Figure 1b-e). The expanded state of apo-37 is used for discussion and visualization in figures, selected for its higher resolution and particle count within the dataset. While some differences in the NTDs are uncovered between each of the apo-state models, the overall topology of the NTD is shared, consisting of a helix-turn-helix-turn-βsheet (where secondary elements are denoted: α1 (residues 11-19), α2 (residues 21-24), and β0 (residues 30-32). The dimeric building blocks shows domain-swapped interactions between α1s with potential stabilizing interactions provided by charged residues (Glu12 and Lys16, Figure 1c,d). The semi-helical α2 region displays intra-dimer hydrogen bonding potential between Thr21 of one chain and Thr21 of the opposing chain (Cβ distance 3.1 Å, apo-37 expanded state) (Figure 1d). Additionally, within this region Pro22 abuts (<5 Å distances) the inner surface of the ACD forming an “inner ACD pocket” with Phe42, Pro44, and Pro100 from each chain in the dimer (Figure 1e). Additional intra-

dimer Van der Waals contacts occur between Met28 (chain A) and Phe19 (chain B) with Cγ(Met28)-Cγ(Phe19) distance of 4.5 Å (apo-37, expanded state).

To better understand the structural differences leading to expansion/contraction of the mjHSP16.5 cage, a Cα root-means-square-deviation (RMSD) comparison was performed between monomers of each state (contracted/expanded) in the apo-37 dataset (Figure 2a). There is high agreement between superimposed dimer ACDs of the contracted and expanded states (overall RMSD 0.326 Å), with much of the variation localized to NTD residues reaching up to 1.5 Å deviation. The helical conformation of NTD α1 remains nearly constant, with overall distance of 13.5 Å and 13.7 Å in the contracted and expanded states, respectively (intra-subunit Cα distances of Phe11-Ala20) (Figure 2b, yellow lines). However, the NTD segments within a dimer reside closer together in the contracted versus expanded state, where the inter-subunit Lys16-Lys16 Cα distances between dimer chains is 9.5Å in the contracted state and extends to 10.3 Å in the expanded state (0.8 Å displacement) (Figure 2b, red lines). The apo-75 model shows distinct a NTD arrangement from the apo-37 models, with Phe11-Ala20 Cα distance of 11.0 Å and helical separation at Met14 Cα of 6.6 Å (Supplemental Fig. 4f). The use of Met 14 (vs. Lys16) provided the closest approach in both cases, corresponding to helical rotation with interdimer helix distance tightening. Additionally, density for NTD α1 – specifically density corresponding to Phe18 and Phe19 – was weaker in the apo-75 model (Supplemental Fig 4b,h). This may reflect intra-dimer competition of Phe18 and Phe19 (chain A) with Met28 (chain B) (Supplemental Fig. 4f), disrupting the Phe19/Met28 interaction observed in the apo-37 contracted and expanded states (Supplementary Fig. 3h).

In addition to these NTD interactions resolved in the octahedral reconstructions, the non-symmetric consensus reconstruction retained the “inner ACD pocket” interactions

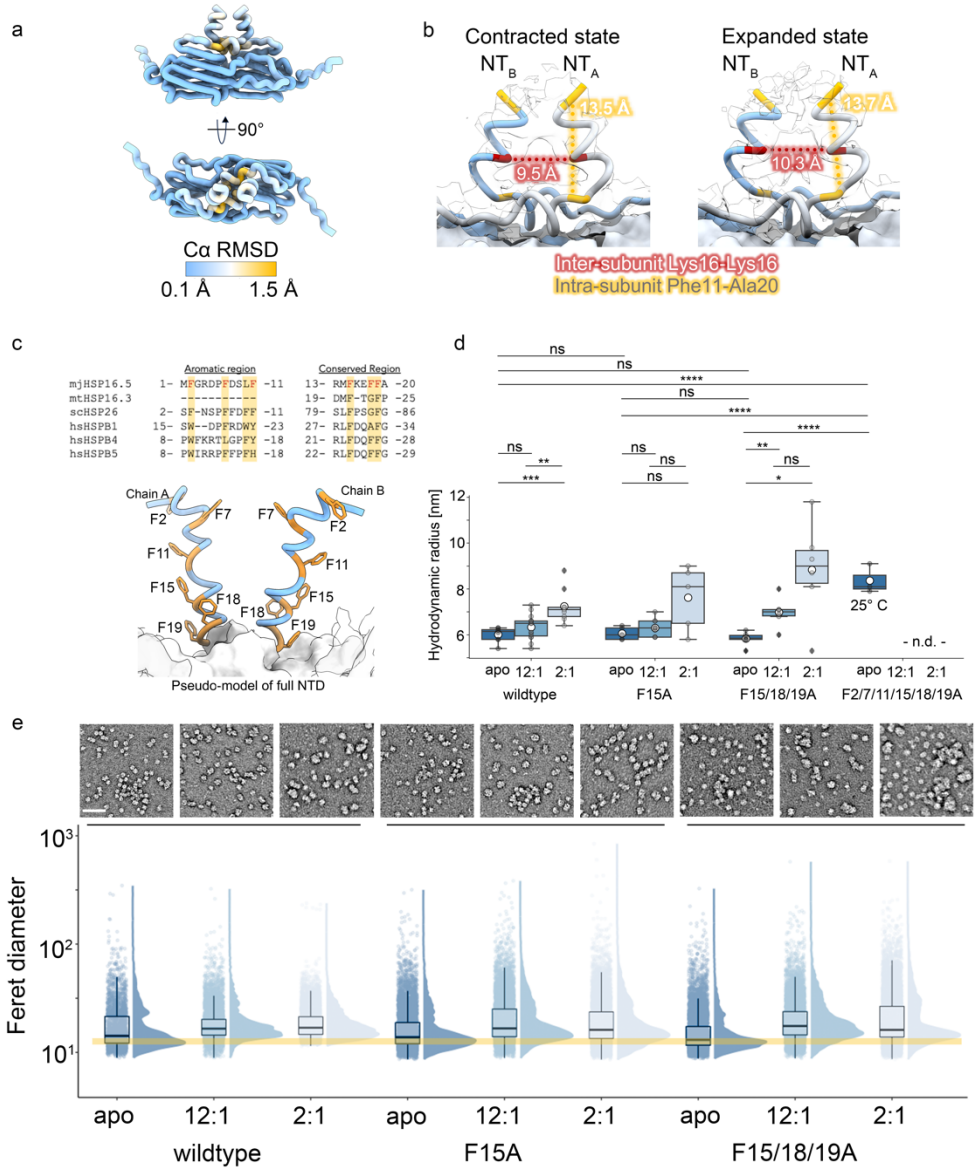

Figure 2: Conserved Phe residues within the NTD are critical to sHSP assembly, stability and chaperone function (a) Cα root-mean square standard deviation (RMSD, colored) comparison between the contracted and expanded states of the apo-37 dataset. (b) Distance measurements between NTDs from neighboring chains within a dimer (NT_A and NT_B) for the contracted and expanded states. Measurements were made between Cα atoms of Lys16 of each chain, and between Phe11 with Ala20 within a chain (c) Sequence alignment (top) of "aromatic" and "conserved" regions within the NTD of various small heat shock proteins (mjHSP16.5, *M. tuberculosis* HSP16.3, *S. cerevisiae* HSP26, and human hsHSPB1 (HSP27), hsHSPB4 (αA-crystallin), and hsHSPB5 (αB-crystallin). Phe residues of mjHSP16.5 mutated in this study are highlighted. Pseudo-atomic model (bottom) of full NTDs within a dimer (chains A and B) with each Phe residue labeled (d) Hydrodynamic radii of major populations detected by DLS for mjHSP16.5 wildtype and NTD variants (F15A, F15/18/19A) in the absence (apo) or presence of lysozyme (12:1 and 2:1, chaperone:client ratios) after incubation at 75° C for 2 hours. The F2/7/11/15/18/19A mutant experiment was performed at 25° C, and only for the apo-state (e) Electron micrographs of negatively stained specimens and associated Feret diameters obtained from single-particle measurements for mjHSP16.5 wildtype and mutants (F15A and F15/18/19A) in the presence (12:1 and 2:1) and absence (apo) of lysozyme after incubation at 75°C for 2 hours. Scale bar is 50 nm.

throughout the oligomer as determined by the prevalence of density corresponding to

Pro22. The cavity density is heterogeneous, with some density connecting opposite sides of the cage. Intermediate reconstructions from variability analysis display NTD interactions that dynamically move through the inner cavity, suggesting multiple transient interactions between NTDs (Supplementary Fig. 2d). Together, these novel NTD interactions support both dimer stability and high-order oligomer assembly – and further support the notion that sHSP NTDs are highly dynamic and facilitate sHSP oligomer plasticity.

Conserved phenylalanine-rich regions mediate oligomeric stability

In mjHSP16.5, each NTD contains six phenylalanine (Phe) residues (F2/7/11/15/18/19) for a total of 144 Phe residues, providing a rich environment for non-specific transient interactions within the 24mer cage cavity. The α1 motif corresponds to the sHSP NTD "conserved region" where Phe residues spaced 3-4 residues (Phe11/15/18/19) apart are found highly conserved throughout species (including human, Figure 2c). Multiple Phe-based pi-pi/cation-pi interactions would be favorable for heat stability in the native high-temperature environment of this sHSP (up to 120° C) while providing non-specific interactions to support plasticity/dynamics necessary for chaperone function[265,266].

To interrogate the role of these conserved Phe residues, we generated three variants that replace Phe with Ala within the NTD: F15A (mj-1x), F15/18/19A (mj-3x), and F2/7/11/15/18/19A (mj-6x) to assess the role of these residues in structure and function. Deletion constructs of the NTD at positions 20 and 32 (mj-NTDΔ20 and mj-NTDΔ32) did not yield soluble protein during expression and purification and were not used for structural/functional characterization. The F15A variant (mj-1x) resides in the middle of the NTD α1 helical region between prospective pi-stacking partners F11, F18, and F19, while the mj-3x and mj-6x variants would eliminate Phe residues throughout the "conserved" region and all NTD Phe residues (including both the unresolved "aromatic" region and α1

“conserved” region), respectively. The mj-1x and mj-3x variants provided high yields of purified protein sufficient to perform experiments, however the diminished solubility of the mj-6x variant lead to low yields following purification, limiting some of the analysis on this variant. The purified mj-1x and mj-3x variants had approximately the same size as wildtype, as determined by dynamic light scattering (75° C) with hydrodynamic radii (average ± sem) of 6.1 ± 0.1 nm (n=5) and 5.8 ± 0.1 nm (n=6), respectively, versus 6.0 ± 0.1 nm for wildtype (n=8, Figure 2d). The hydrodynamic radius of mj-6x at 25° C was 8.3 ± 0.3 nm (n=3), significantly larger than mj-wt, mj-1x, and mj-3x ($p < 0.0005$, Figure 2d). mj-6x had greatly diminished heat stability, requiring a lower temperature for DLS measurements, with a determined aggregation temperature around 60° C (n=2, Supplemental Fig. 1f) while mj-1x and mj-3x maintained solubility up to 85° C (highest temperature tested, Supplemental Fig. 1f) at 75° C for over two hours. The mj-3x variant exhibited a slight decrease in radius leading to a full decrease of ~1 nm between 75-85° C These results suggest a minimal number of Phe residues needed for the canonical 24mer assembly and that the intrinsically disordered “aromatic” region is especially important for 24mer stability.

Single-particle size analysis by negative stain EM (NS-EM) provides a means to statistically characterize and compare sHSP morphology at a per-particle level, by analyzing single-particles directly from raw NS-EM micrographs and automated measurement of each particle’s longest axis (i.e., Feret diameter). The main modes of Feret diameter were similar for wt-apo (11.9 nm), mj-1x (12.2 nm), and mj-3x (10.7 nm), while the overall distributions were significantly different ($p < 0.0005$, K-S test, Figure 2e). These measurements agree with the hydrodynamic radii measured by DLS while allowing visualization of additional high-order assemblies (clusters) of mjHSP16.5. The mj-1x and mj-3x particles exhibit the canonical spherical cage-like morphology of mjHSP16.5 (wt-apo) while existing as both isolated particles and in clusters with other spherical oligomers.

Surprisingly, clusters formed by wt-apo and mj-1x can reach >100 nm in size while the constituent oligomers retain the same size/morphology as the isolated particles – suggesting minimal disruption to the cage-like structure upon clustering. Larger clusters of mj-3x appear more amorphous and irregular compared to wt-apo and mj-1x particles. Intriguingly, mj-6x displayed ring like structures of ~20 nm in diameter in addition to smaller spherical particles, as well as thin filamentous structures ~2 nm across that formed extensive networks (Supplementary Fig. 1d,e). Due to background interference from the filamentous structures, the mj-6x micrographs could not be assessed by the single-particle size analysis workflow. Hand measurements of 100 particles gave an average (± sem) diameter of 21.3 ± 2.3 nm, indicating substantial impact to the native quaternary structure.

Client-induced polydispersity of mjHSP16.5

To investigate mjHSP16.5 chaperone function, we sought to establish equilibrium binding conditions where the client is not yet unfolded – but has increased sampling of partially unfolded states – as this is most reproducible and best represents early stress conditions expected in the cell. Hen egg lysozyme (14.3 kDa) was chosen as a suitable binding partner of mjHSP16.5 under these conditions as it has a reported melting temperature (Tm ~75° C), well above temperatures necessary for subunit exchange and chaperone function of mjHSP16.5 (~60° C)[262,267]. mjHSP16.5 was shown to have no protection against the reduction-induced aggregation of lysozyme at 37° C and that lysozyme can maintain solubility (no aggregation) up to ~80° C (Supplemental Fig. 5a,b). Binding assays were performed at 12:1 and 2:1 chaperone:client ratios, with mjHSP16.5 at either 120 μM or 20 μM, respectively, and lysozyme constant at 10 μM. Components were incubated at 75° C for 2 hours, and hydrodynamic radii monitored by DLS. For comparison, complexes were also formed with mjHSP16.5 variants and lysozyme at 75° C for 2hr at a 12:1 sHSP:client ratio. The mj-1x/lyso 12:1 reaction yielded complexes of

similar size to mj-wt/lyso at this same ratio, measuring 6.3 ± 0.1 nm, 99.5 mass% (n=10) for mj-wt/lyso and 6.3 ± 0.1 nm, 99.4 mass% (n=6) for mj-1x/lyso. In contrast, mj-3x/lyso complexes were significantly different from wildtype (7.0 ± 0.3 nm, 92.4 mass%, $p > 0.05$, n=6) (Figure 2d and Supplementary Fig. 5c). Incubation of mjHSP16.5 variants with lysozyme at 2:1 ratio (20 μM sHSP:10 μM lysozyme) resulted in complexes with larger hydrodynamic radii for mj-1x/lyso (7.6 ± 0.6 nm, 99.7 mass%, n=5) and mj-3x/lyso (8.8 ± 0.9 nm, 67.1 mass%, n=6) compared to mj-wt/lyso complexes (7.2 ± 0.2, 97.2 mass%), although these differences were not significantly different. Stable complex formation was confirmed for all reactions by size-exclusion chromatography (SEC) and SDS-PAGE, which also showed increased size and polydispersity following incubation with client (Supplemental Fig. 5 d-j).

Single-particle size analysis by NS-EM of mjHSP16.5 with lysozyme displayed increased size and polydispersity of co-aggregates compared to the apo-states for mj-wt, mj-1x, and mj-3x – in agreement with hydrodynamic radii measured by DLS (Figure 2e). For mj-wt the primary Feret diameter mode increased from 11.9 nm (wt-apo) to 13.9 nm and 14.4 nm for the 12:1 and 2:1 ratios, respectively. The mj-1x and mj-3x variants showed similar responses to lysozyme binding at 12:1 and 2:1 ratios, with primary Feret diameter mode increases to 14.5 nm (12:1 and 2:1 mj-1x), 14.0 nm (12:1 mj-3x) and 14.5 (2:1 mj-3x). The size distribution of apo-state oligomers and lysozyme-bound states formed by mj-1x and mj-3x are significantly different from mj-wt apo-state and client-bound states ($p < 0.0005$, KS test). Morphologically, client-bound states formed by mj-wt, mj-1x, and mj-3x exhibit morphological expansion, elongation, and clustering. Similar to the apo-states, clustered co-aggregates of mj-wt and mj-1x with lysozyme retain morphological appearance of apo-like spherical assemblies (~10-15 nm diameter) while closely packed together. The clusters formed by mj-3x appear more amorphous, lacking the apo-like spherical cage morphologies, potentially reflecting the loss of stable NTD interactions. In

summary, mutation of one (mj-1x) or three (mj-3x) NTD “conserved region” Phe residues resulted in increased size and polydispersity of mjHSP16.5 client-bound states, while mutations of all NTD Phe residues (mj-6x) increased the apo-state size while diminishing the temperature stability of this thermophilic sHSP.

Cryo-EM of mjHSP16.5/lysozyme chaperone complexes

We next sought to determine high-resolution structures of the client-bound state(s) for wildtype mjHSP16.5 formed with lysozyme at the 12:1 ratio (sHSP:client) as this gave similar sizes (hydrodynamic radius and Feret diameter) to the apo-state, suggesting a more tractable target for high-resolution analysis. Furthermore, the binding temperature and low client saturation conditions attempted to mimic possible client binding events under early stress conditions, where partially unfolded transitions states of a client are recognized and sequestered by the chaperone. The 12:1 reaction was vitrified following complex formation at 75° C for 2 hours and Cryo-EM data collection resulted in 13,276 movies for single-particle analysis (Supplementary Fig. 6). 2D classification and multi-class *ab initio* model generation made it apparent there was a range of induced mjHSP16.5 oligomeric states present under these conditions (Supplementary Fig. 6, 7a). Ultimately, five different structures were resolved corresponding to a mjHSP16.5 24mer (2.60 Å), 26mer (3.65 Å), 32mer (4.37 Å), 34mer (4.71 Å), and 36mer (4.01 Å) at sufficient resolution for model building of the ACD and CTD regions (Figure 1f and Supplementary Fig. 7b). These models showcase new structural features (windows and axes) compared to the canonical 24mer and the dynamic ability to assemble into diverse morphologies using fundamental building blocks (ACD dimers coupled through flexible CTD tethering). The volume of internal density of each oligomeric state increases from 24mer to 36mer, presumably reflecting an increased client sequestration capacity of the higher oligomeric states. However, this internal region in all of the maps remained at lower resolution – likely

reflecting extensive heterogeneity/disorder of the NTD/client and/or non-specific binding of the client lysozyme (Figure 1f). The resolved 24mer was very similar to the apo-states described for apo-37 and apo-75 with comparable NTD densities as well as stretching/expansion variability modes – possibly representing an unbound oligomeric state for mjHSP16.5 (Supplementary Fig 6). This notion is further supported by the minimal vacant volume within the apo-state that would limit capacity for the ~14 kDa client.

A Flexible CTD enables client-induced sHSP polydispersity

Cα RMSD of the component subunits was measured to assess the flexibility of the CTD in tethering ACD dimers into various cage assemblies. Due to CTD dynamics and limited resolvability, the 26mer, 32mer, and 34mer Cα RMSD measurements only include 22, 31, and 33 subunits, respectively (Figure 3a). For comparison, RMSD analysis showed minimal Cα deviation within the core ACD region in all cases, similar to the apo-state (Figure 2a). In contrast, the CTD appears to adopt a continuum of states within the various assemblies, with two primary modes of CTD extension that are most clearly separated in the symmetric 36-mer resulting in ~10 Å Cα deviation of the CTD IXI-motif (Figure 3a, far left). In addition to the canonical 24mer 3-fold windows (~530 Å^2) and 4-fold axes (Figure 3b), the flexible interactions of the CTD support a novel 4-fold window (~3000 Å^2) and 3-fold axis in the 26mer; 4-fold windows (~2700 Å^2) and new 5-fold axes in the 32mer and 34mer; and elongated 4-fold windows (~2000 Å^2) and 4-fold axes in the 36mer (Figure 3b). The conformations of the CTD influence canonical 3-fold windows and newly identified 5-fold axes (CTD downward mode, as shown in Figure 3a) in addition to the new 4-fold windows present in the higher-order states (CTD upward modes, as shown in Figure 3a). Newly inserted dimers resulted in multiple non-canonical CTD interactions, including evidence of diffuse CTD/β4-β8 groove binding and CTDs oriented inward toward the

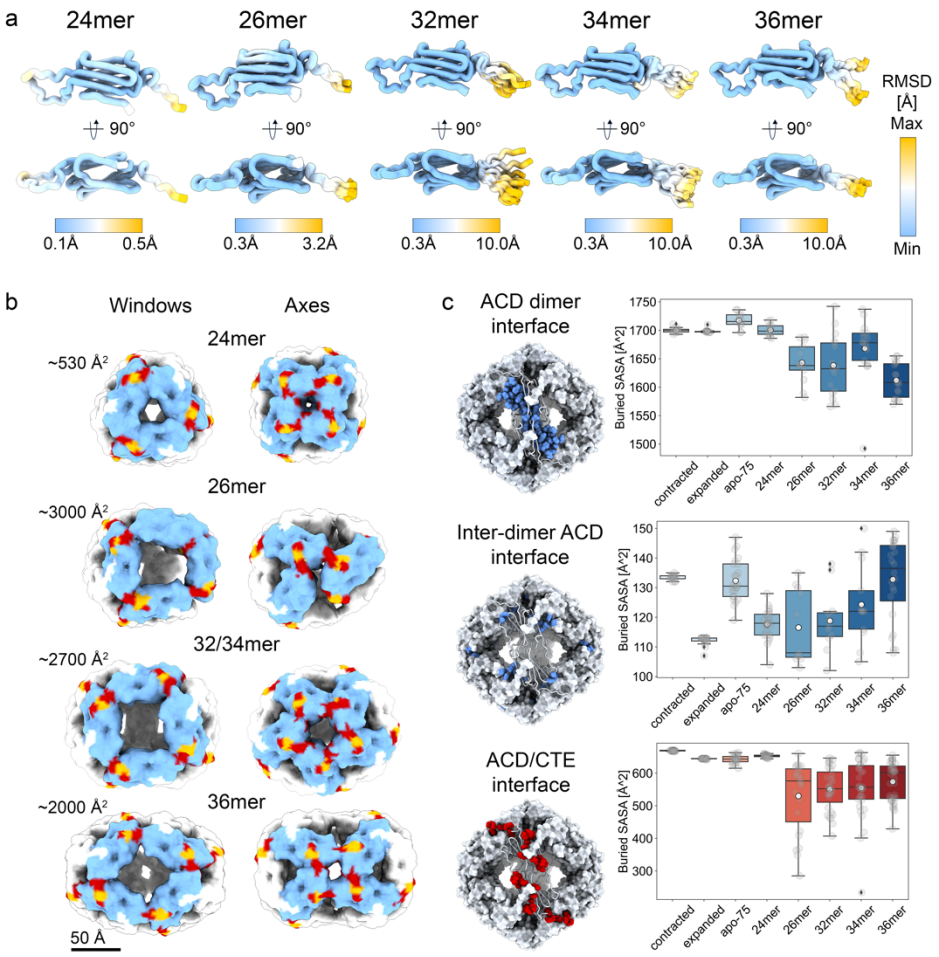

Figure 3: Flexible CTD interactions facilitate multiple oligomeric states that correlate with weakened inter-protomer contacts (a) Comparison of Cα RMSDs of protomers within each oligomer state obtained in the presence of lysozyme (24mer, 26mer, 32mer, 34mer, and 36mer). RMSD values indicated by color (bottom). (b) Windows and axes adopted by the 24mer (canonical 3-fold window/4-fold axis), and non-canonical states formed by the 26mer (4-fold window/3-fold axis), 32 and 34mer (4-fold window/5-fold axis), and 36mer (4-fold window/4-fold axis). sHSP depicted as density generated from the atomic models (corresponding to 10 Å resolution) and colored to highlight the specified features. (c) Box and whisker plots showing measurements of the buried solvent accessible surface areas (SASA, interfaces) of protomers for atomic models of apo-37 (contracted and expanded), apo-75, and each oligomeric state from the mjHSP16.5/lysozyme dataset. Interfaces corresponding to the ACD intra-/inter-dimer interface and ACD/CTD interaction. Inlays, depict residues buried in the interface (blue for ACD dimer interface and Inter-dimer interface, red for ACD/CTD interface).

internal density of the cage, and thus possibly interacting with client (Supplementary Fig. 7c).

Oligomers of mjHSP16.5 are supported by contacts within the ACD dimer (intra-dimer), between ACD dimers (inter-dimer), and through canonical ACD/CTD (β4/β8-

groove) tethering interactions. To assess the extent of these interactions, the buried solvent-accessible surface area (SASA) was calculated for residues 33-147 for comparison across all oligomeric states (Figure 3c). The apo-state models showed an average (± s.e.m.) buried surface area involving intra-dimer interactions (along the ACD/ACD interface) of 1700 ± 1.4 $Å^2$, 1699 ± 1.1 $Å^2$, and 1717 ± 3.9 for the contracted (apo-37), expanded (apo-37), and apo-75 models, respectively. The average (± s.e.m.) ACD dimer buried surface area of the 24mer from the dataset with lysozyme is similar to apo-37, measuring 1701 ± 3.1 $Å^2$, while the 26mer, 32mer, 34mer, and 36mer showed decreased ACD buried surface areas, measuring 1643 ± 9.6 $Å^2$, 1638 ± 13.4 $Å^2$, 1668 ± 13 $Å^2$, and 1612 ± 7.0 $Å^2$, respectively. The inter-dimer interface is smaller and reflects contacts between β5 and β7 strands of one dimeric protomer with the β5+6 loop of a neighboring dimeric protomer (Figure 3c, middle). The contracted and expanded states of apo-37 had inter-dimer interfaces of 133 ± 0.2 $Å^2$ and 112 ± 0.3 $Å^2$, respectively, while the apo-75 inter-dimer interface was 132 ± 1.4 $Å^2$. In the presence of lysozyme, the 24mer, 26mer, 32mer, and 34mer had a general decrease in the inter-dimeric interface (188 ± 1.0 $Å^2$, 117 ± 3.7 $Å^2$, 119 ± 13.4 $Å^2$, and 124 ± 3.6 $Å^2$, respectively). The 36mer inter-dimer interface was 133 ± 2.8 $Å^2$, similar to the apo-37 contracted state and apo-75. Oligomers from the dataset with lysozyme show a general decrease in intra-dimer interactions with increases in oligomeric size, while the inter-dimer interactions initially decrease (24mer to 25mer) before increasing in the 32mer, 34mer, and 36mer. CTD-IXI tethering interactions with a neighboring ACD β4/8 groove had an average (± s.e.m.) buried surface area of 669 ± 0.1 $Å^2$ and 644 ± 0.2 $Å^2$ for the apo-37 contracted and expanded models, respectively, while the apo-75 and 24mer in the presence of lysozyme were 642 ± 2.4 $Å^2$ and 653 ± 0.8 $Å^2$, respectively. This same buried surface area of the 26mer, 32mer, 34mer, and 36mer exhibited a marked decrease compared to the 24mer states, measuring 530 ± 23 $Å^2$, 551 ± 11.7 $Å^2$, 555 ± 15.6 $Å^2$, and 574 ± 10.0 $Å^2$, respectively. This observation is attributed to

alternative CTD conformations in these higher-order assemblies. Overall, comparing the 24mer models to the 26 – 36mer models in the client-bound dataset there was a decrease in the average buried surface area of ~2 - 5% for the intra-dimer interface, ~13% increase of the inter-dimer interface, and ~12 - 17% decrease for the ACD/CTE tethering interface.

sHSP polarization/elongation drives "holdase" activity

Local resolution Cryo-EM maps were generated from asymmetric reconstructions of each oligomeric state in the mjHSP16.5/lysozyme dataset for assessment of regional stability and comparative analysis across the various assembly states (Figure 4). The 24mer reconstruction obtained in the presence of lysozyme showed limited variation in resolution over the ACD/CTD regions, with local resolution variance < 3 Å , while the internal NTD/client density measured lower resolution (< 4.5 Å), however the internal density was uninterpretable. The 26mer, 32mer, and 34mer show extensive resolution variation across the ACD/CTD cage scaffold, resulting in a high resolution (~3-4 Å) region (i.e., most well defined) localized around a single canonical 4-fold axis accompanied by a continuous decrease in resolution moving across the elongated cage morphologies, reaching ~9-10 Å resolution. The asymmetric 36mer reconstruction is of overall lower resolution, due to limited number of particles in this class, but shows a more uniform resolution distribution across the elongated scaffold (~7-8 Å). By aligning the most structured side of each cage, it is possible to make some inference as to which dimers are likely inserted based on the arrangement of windows and axes between the complexes. Of note, there was no evidence of monomer insertion, suggesting the dimer as the primary exchanging subunit.

Based on these observations, it is suggested that initial events of client sequestration (producing a 26mer) effectively polarize the stability of the cage across the long axis and may provide a means for further directional elongation and non-stochastic

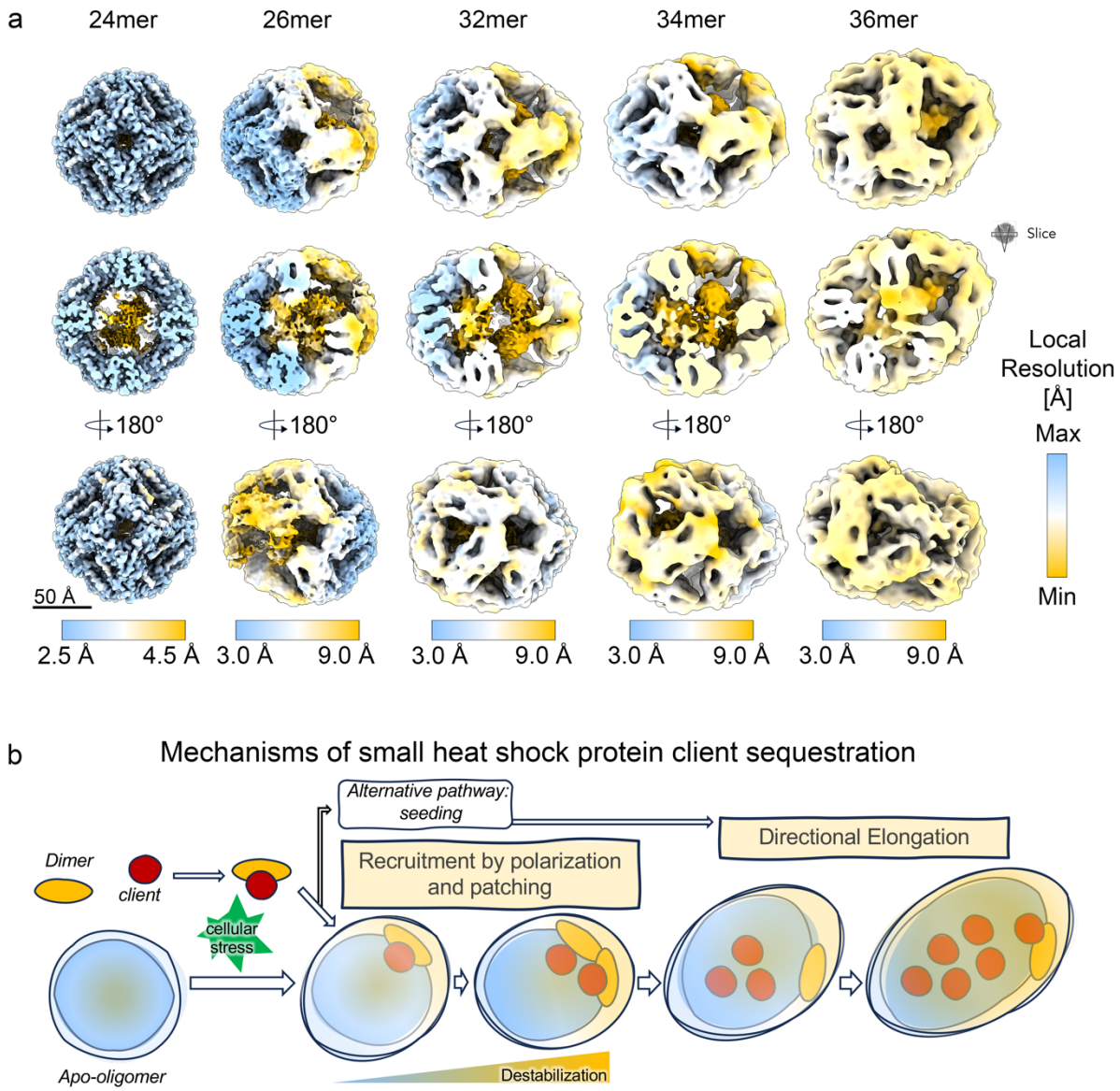

Figure 4: Local resolution analysis of mjHSP16.5/lysozyme complexes reveal polarized stability across each oligomeric state. (a) The Cryo-EM density map of each oligomeric state is depicted along a 4-fold axis (top), an internal slice view (middle), and a 180° rotation (bottom), with map density colored according to the resolution range (indicated). Scale bar is 50 Å. (b) Cartoon representation of proposed mechanisms of sHSP client sequestration by seeding, patching (dimer/client insertion), and directional elongation.

client-induced formation of higher-order oligomers. The transition from 24mer to 26mer involves insertion of a dimer through disassembly of a canonical 4-fold axis in the 24mer to produce 2 larger 4-fold windows and two unstable 3-fold axes. Variability analysis of the 26mer uncovered extensive dynamics of the newly inserted dimer with high flexibility

between the two new 3-fold axes. No bona fide 28mer or 30mer populations could be classified out of the Cryo-EM dataset. It is possible that additional dimer/clients needed to stably occupy the large 4-fold windows assembled in the 26mer (effectively removing the unstable 3-fold axes) to form a more stable 32mer and is either highly cooperative or that a pre-formed hexamer is required to assemble the 32mer from the 26mer. A plausible transition from a 32mer to a 34mer was directly uncovered by 3D variability analysis and would involve insertion of a dimer into a large 4-fold window of the 32mer to produce two 3-fold windows and another 5-fold axis. Intriguingly, there does not appear to be a simple or direct dimer insertion path to go from the 34mer to the 36mer. This transition would involve disassembly of two 5-fold axes and rearrangement of multiple dimers to accommodate another dimer/client unit. It is possible that the 36mer assembled through an alternative pathway (discussed below) than that suggested to be followed by the 26mer, 32mer, and 34mer. Interestingly, with the potential existence of multiple pathways of client-sequestration, ultimately formation of elongated caged-assemblies where one dimension is longer than the perpendicular dimension appears to be favored.

DISCUSSION

Insights into the apo-state dynamics of HSP16.5

Here we describe previously unresolved portions of the client-interacting NTD of mjHSP16.5 and provide multiple high-resolution structures of client-bound sHSP oligomers, providing unprecedented insight into the mechanism of sHSP structural plasticity and client sequestration of this archetypal chaperone. In mjHSP16.5 the NTD provides additional inter-dimer stabilizing interactions through helices α1 (“conserved region”) and α2, with conserved Phe residues stabilizing the amphipathic α1 interactions. Variability analysis of mjHSP16.5 in the apo-state proposes conformational dynamics of

the caged-assembly that involve order-to-disorder transitions of α1 within the NTD associated with expansion and stretching modes of motion – facilitating conformational plasticity within the 24mer apo-state. In addition, our Cryo-EM results show the distal region of the NTD (residues 1-10 containing the “aromatic region”) remains disordered with observed features that suggest a role in facilitating long-range interactions between NTDs across the internal cavity of the oligomeric cage. The crystal structure of the eukaryotic (plant) sHSP HSP16.9 resolved 6/12 NTDs where Phe pi-pi stacking potential is present within and between NTD helices of protomers across the dodecameric (12mer) disc – providing long-range stabilization across the oligomeric structure[137].

We show that progressive ablation of conserved NTD Phe residues in mjHSP16.5 promoted the formation of larger and more amorphous complexes formed with lysozyme (F15/18/19A, mj-3x variant) and attenuated the stability of the oligomer (F2/7/11/15/18/19A, mj-6x variant) leading to a mixture of larger spherical oligomers and thin filamentous aggregates. The “aromatic” and “conserved” regions in the NTD of sHSPs may support oligomerization and dynamics by providing multiple hydrophobic and non-specific interacting sequences that effectively condense subunits into a larger assembly while facilitating oligomeric plasticity. Previous studies show the “aromatic region” of mjHSP16.5 to play a role in oligomerization and client interaction, where truncation of the first 12 residues resulted in smaller oligomers (hexamers) with diminished chaperone protection[257]. The “conserved region” of human α-crystallins (αA and αB isoforms) has been predicted to adopt an amphipathic helix, while deletion or mutation of conserved residues in this region alter oligomeric size, thermal stability, and chaperone activity[150,212]. Similar results were reported for human HSPB6 where targeted disruption of the conserved region enhanced chaperone activity and altered the dimeric structure of HSPB6[153]. Other sHSP structures have identified inter-subunit aromatic-aromatic and cation-pi interactions with structure guided mutagenic studies, supporting a role for Phe

residues in structure/function[137,261]. Overall, hydrophobic interactions provided by conserved regions within the NTD of evolutionarily distant sHSPs appears to play a pivotal role in structure and function of these chaperones, likely in combination with other inter-subunit interactions (e.g., ACD/ACD and ACD/CTD-IXI tethering).

Mechanisms of client sequestration and induced polydispersity

The array of sHSP/client states uncovered in this study suggest the primary building block for mjHSP16.5 is a dimer, which are tethered together by flexible CTDs to form a caged scaffolding that can accommodate sequestered clientele through the addition of dimeric subunits that increase capacity of the internal cavity and promote formation of new cage features (windows and axes). The induced sHSP polydispersity is coupled to a polarization of cage stability and increased solvent exposure of the internal cavity. The internal cavity of the 24mer is nearly filled with density belonging to the NTD, and thus appears incapable of sequestering clients as large as lysozyme (14 kDa). However, even a modest transition to a 26mer induces an increase of the internal non-NTD volume by ~100% (50 nm^3 in the 24mer and 100 nm^3 in the 26mer), sufficient to sequester the client. The concomitant increase in the cavity volume established by the formation of higher-order assemblies (34, 36mers) would facilitate higher capacity client binding, enabling a single sHSP complex to sequester multiple clients or clients of variable size.

The unresolved nature of the client density in this work is consistent with either extensive client unfolding in the sHSP-bound state or multiple transient binding interactions that prevented alignment for 3D reconstruction. An unforeseen impact of client-sequestration was the induced polarization of stability in the sHSP scaffold (shown by local resolution and analysis of binding interfaces). Phosphorylation of HSP26 was suggested to activate chaperone function and induce a polarity in the overall cage-like

structure[32]. This localized destabilization may be critical for the chaperone mechanism, for example, by providing “hot spots” for additional client insertion or enabling the access and reversible release of clients to downstream refolding machinery[268].

While these results provide many new insights into how client-induced sHSP polydispersity is achieved, many mechanistic details are still unclear. Binding of a model client by mjHSP16.5 required high-temperature, consistent with requirement for subunit exchange dynamics[262]. Therefore, it is possible that dimer subunits leave the apo-state, recognize destabilized client, and return the client cargo to the caged-assembly; effectively building higher-order states in a sequential and directional (polarized) manner – deemed “elongation” of the sHSP scaffold. Once initial client binding occurs (forming the 26mer) there are large 4-fold windows in which new dimers could be inserted, or “patched”, onto the complex. This was supported through 3D variability analysis, suggesting a simple transition from the 32mer to the 34mer that could occur via dimer “patching” onto a large 4-fold window. Increased exposure of the internal cavity along these 4-fold windows may enable hydrophobic interactions between NTDs within the cage and with exchanging or unbound NTDs/clients. Indeed, previous studies have proposed that larger complexes formed by mjHSP16.5 exhibit increased affinity toward clientele that was attributed to increased hydrophobic surface area[174,175].

It is also conceivable that newly formed complexes between clients and exchanging sHSP dimers could seed *de novo* assembly, by recruiting other exchanging subunits or subunit/client complexes, and the most energetically favorable sHSP scaffold architecture would be determined by client characteristics (aggregation state/size and degree of unfolding) that seeded the interaction. Our structural data are also consistent with this “seeding” model. For example, it remains unclear how transition from the 34mer to the 36mer may be achieved by simple addition of a dimer into the 4-fold window without substantial rearrangements of the 34mer scaffold (disrupting two 5-fold axes). This seeded

assembly model is supported by recent single-molecule fluorescence experiments on αB-crystallin and HSP27 where initial client binding is followed by additional subunit recruitment, with differences between the two sHSPs indicating chaperone specific variation in this mechanism[168,269]. Additionally, the only previous high-resolution structure of a sHSP/client complex depicted a monomeric subunit of plant HSP21 binding a native client to form a soluble complex[176]. Of note, these mechanistic models (elongation, patching, and seeding) are not mutually exclusive and could all contribute to the overall complexity of sHSP sequestration mechanisms. Future studies targeted at trapping the transition states involved in client-sequestration will be needed to fully resolve these mechanistic details.

Concluding remarks

A major hurdle in understanding sHSP chaperone mechanisms has been the heterogeneous and polydisperse nature of sHSP/client complexes. We show that mjHSP16.5 is a model system for studying polydispersity in relation to chaperone function and may potentially be harnessed in guiding future studies addressing structure/function of other sHSPs. Structural characterization of mjHSP16.5 under varying amounts of client saturation and with different client types will help decipher the molecular determinants of client binding and the diversity of sHSP sequestration mechanisms. Future efforts to explore sHSP/client complexation in the cellular context may yield insight for targeting the co-aggregation pathway in sHSP-related diseases (i.e., cataract, Alzheimer's disease, cardiac diseases, myopathies) and cancer treatment resistance[87,90,270].

Methods

Construction of expression plasmids

The gene sequence of wildtype mjHSP16.5 (GENID: 1451140) was codon-optimized for bacterial expression and encoded into a pET23a(+) expression vector and sequences encoding variants within the N-terminal domain of mjHSP16.5: F15A (mj-1x), F15/18/19A (mj-3x), F2/5/11/15/18/19 (mj-6x), deletion of residues 1-32 (mj-Δ32, introduces Met1 at position 32), and deletion of residues 1-20 (mj-Δ20, introduces Met1 at position 20) were encoded into the pET21a(+) vector (Genscript). Protein expression constructs used in this study did not contain solubility or purification tags. Full plasmid sequencing (Plasmidsaurus, Eugene, OR) confirmed the correct gene sequence, insertion site, and placement of mutations/truncations.

Expression and purification of mjHSP16.5 wildtype and variants

Wildtype (mj-wt) and variant constructs (mj-1x, mj-3x, mj-6x, mj-Δ32, and mj-Δ20) of mjHSP16.5 were expressed in bacteria and purified using the same protocols (modified from Quinlan, *at al.*[271]). Briefly, *E. coli* BL21(DE3) was used as an expression host for all constructs and the growth media (LB) was supplemented with ampicillin (0.5 mM). Cells were grown at 37° C to an optical density (A.U. at 600 nm) of 0.6 – 1.0 and expression was induced with 1 mM isopropyl β-D-1-thiogalactosidase (IPTG). Cells were harvested by centrifugation (4,000 r.c.f for 15 min at 4° C) after 3-4 hours post-induction at 37° C. Pelleted cells were resuspended in 20 mM Tris-HCl (pH 8.0), aliquoted, and frozen at -80° C for further use.

For purification of each protein construct, cell suspensions were thawed and supplemented with 1,4-dithioreitol (DTT, 0.5 mM final concentration) and phenylmethylsulfonyl fluoride (PMSF, 0.1 mM final concentration), lysed by sonication on ice (70% amplitude, 6 rounds of 30s on/off), supplemented with additional PMSF (0.2 mM final concentration), and cellular debris cleared by ultracentrifugation at 165,000 r.c.f for 30 minutes at 4° C. The supernatant was supplemented with NaCl (1M final concentration) and 20 mM Tris-HCl (pH 8.0) and incubated in an 80° C water bath for 30 minutes (V = 20 mL). The heated lysate was recovered on ice for 5 minutes and denatured protein was pelleted by ultracentrifugation at 165,000 r.c.f for 30 minutes at 4° C. The supernatant was collected, DNase I (~400 units, Thermo Scientific) was added and incubated for 30 minutes on ice before being filter at 0.22 μm prior to chromatography. The clarified lysate was applied to a gel filtration chromatography column (S300 resin; Pharmacia) equilibrated with 20 mM Tris-HCl (pH 8.0), 1 mM EDTA and 0.5 mM DTT. Fractions from gel filtration were assessed via SDS-PAGE and fractions containing mjHSP16.5 (wildtype or mutants) were pooled and supplemented with DTT (0.5 mM final concentration). The pooled fractions were loaded onto a MonoQ anion exchange column (GE Healthcare) equilibrated with buffer A (20 mM Tris-HCl (pH 8.0), 0.16 mM EDTA, and 1 mM EGTA) and eluted with a NaCl gradient (buffer A with 1 M NaCl). Eluted fractions containing the target mjHSP16.5 construct were pooled, concentrated to a volume of ~2 mL with a 100,000 kDa cutoff spin concentrator (Vivaspin), and loaded onto a Superose 6 size-exclusion chromatography (SEC) column equilibrated with 20 mM HEPES (pH 7.4), 2 mM EDTA, 2 mM EGTA, and 100 mM NaCl. Fractions containing purified mjHSP16.5 constructs were pooled, aliquoted and either flash frozen in liquid nitrogen and stored at -80° C for later use or incubated at 37° C (wildtype) or 4° C (mutants) for immediate use. Nucleic acid contamination was assessed by monitoring UV absorbance ratio of 280/260 nm with all purified protein having ratios >1.5, indicating minimal co-purification of nucleic acids. The

concentration of purified protein was determined by UV absorbance at 280 nm using the extinction coefficient 8,257 $M^{-1}cm^{-1}$ [143]. The variants mj-Δ20 and mj-Δ32 resulted in insoluble protein and was not purified for downstream analyses.

Aggregation assays of reduced lysozyme at 37° C

All aggregation assays were performed in reaction buffer containing 20 mM HEPES (pH 7.4), 2 mM EDTA, 2 mM EGTA, and 100 mM NaCl. Aggregation of hen egg-white lysozyme (Fisher, MS grade) was induced with the addition of 2 mM tris(2-carboxyethyl)phosphine (TCEP) at 37° C. Lysozyme (10 μM) aggregation by TCEP was monitored in the presence of 120 μM (12:1 ratio) and 20 μM (2:1 ratio)) or absence of mj-wt. Chaperone/client mixtures were allowed to equilibrate at 37° C for 15 minutes prior to the addition of TCEP (2 mM final concentration). Turbidity measurements were monitored by absorption at 360 nm, collected in 384-well plates (Nucleon, flat black, clear bottom) on a Tecan Infinite M NANO+ for 2 hours at 37° C.

Heat induced aggregation and binding assays with lysozyme at 75° C

Dynamic light scattering (DLS) measurements were performed in an Aurora 384 well plate on a Wyatt DynaPro plate reader III (Wyatt Technology, Santa Barabara, USA) operating with an 830 nm laser and 150° DLS detector angle. All measurements were acquired with five reads and 10s acquisition time in the Dynamics software v7.10.1 (Wyatt). To determine the aggregation temperature of lysozyme, the hydrodynamic radius in solution was monitored using DLS while ramping temperature from 25° to 85° C at 0.91° C/min (n = 3). Due to the small size of lysozyme (~2 nm radius) the working concentration of 10 μM was not detectable and 100 μM was used to determine the aggregation temperature. Likewise, lysozyme at 50 and 100 μM was monitored by DLS at a constant 75° C for 2 hours to show no immediate (<1 hour) aggregation at these temperatures. For binding assays, lysozyme

(10 μM) was incubated in the presence and absence of mjHSP16.5 wildtype, mj-1x, and mj-3x at 120 μM (12:1 ratio) and 20 μM (2:1 ratio) at 75° C for 2 hours in 20 mM HEPES (pH 7.4), 2 mM EDTA, 2 mM EGTA, and 100 mM NaCl. Prior to incubation at 75° C the mixed samples were incubated at 25° C for 30 minutes. Additionally, samples of mjHSP16.5 were measured by DLS in the absence of lysozyme at 25° C (mj-6x), or 37° C, 75° C, or through a temperature ramp from 25 – 85° C at a rate of 0.49° C min^{-1} (mj-wt, mj-1x, mj-3x: 120 μM, n=3). The aggregation temperature of mj-6x was determined using a heat ramp of 0.3 °C/min from 25-85°C. Replicates of DLS readings were pooled for downstream analyses (SEC/SDS-PAGE, NS-EM, Cryo-EM). The average ± sem was calculated for the hydrodynamic radius of combined replicates across trials for each sample. Statistical significance was assessed by completing a F-test for variability followed by a Student's T-test (equal/unequal variance depending on F-test results).

Size-exclusion chromatography

Following binding assays performed at 75° C, pooled DLS replicates of wt/1x/3x-apo, wt/1x/3x-2:1, and wt/1x/3x-12:1) were loaded (125 μL injection) onto a Superose 6 SEC column equilibrated with 20 mM HEPES (pH 7.4), 2 mM EDTA, 2 mM EGTA, and 100 mM NaCl. Elution peaks were monitored by SDS-PAGE (17.5% acrylamide) and protein bands were visualized by silver staining.

Negative stain EM and single-particle morphology analysis

Purified apo-state mjHSP16.5 was incubated at 37° C for approximately 16 hr and diluted to ~3 μM in dilution buffer containing 20 mM HEPES (pH 7.4), 100 mM NaCl, 2 mM EDTA, and 2 mM EGTA. Chaperone assay reaction products of mj-wt, mj-1x, and mj-3x in the absence (apo) and presence of lysozyme (12:1 and 2:1 chaperone:client ratios) prepared at 75° C were recovered on ice and diluted to ~ 3 μM (mjHSP16.5 concentration) with

dilution buffer. Carbon coated 400 mesh copper EM grid (Ted Pella) were glow discharged at 15 mA for 1 min prior to sample application. For each sample 3 µL of sample was applied to the grid and excess protein/buffer was blotted with filter paper, washed twice with ultrapure water, stained with freshly prepared (0.75% wt vol^{-1}) uranyl formate (SPI-Chem), blotted with filter paper, and dried with laminar air flow. Grids of chaperone reactions were set within 30 minutes following ice recovery (to quench subunit exchange dynamics) following complex formation at 75° C. Negatively stained specimens were imaged on a 120 kV TEM (Tecnai T12, FEI) equipped with either a 2K x 2K CCD camera (Eagle, FEI) at a nominal magnification of 49,000 and a calibrated pixel size of 4.414 Å $pixel^{-1}$ (mj-wt apo, 12:1, 2:1) or an AMT camera (model XR16) using the AMT Image Capture Engine (v602.591j) at a nominal magnification of 30,000 with a calibrated pixel size of 3.991 Å $pixel^{-1}$. Micrographs were collected with a defocus range from 1.5 – 2.2 µm.

Single-particle morphology analysis was performed as previously described[118]. Briefly, unprocessed micrographs were imported into FIJI[230] and the scale was set based on the calibrated pixel size of the micrograph. Micrographs were filtered using the fast-Fourier transform based bandpass filter with default settings (filter large structures at 40 pixels, filter small structures at 3 pixels, 5% tolerance, auto scale after filtering, saturate image when autoscaling) followed by a maximum filter (radius of 2 pixels) and background subtraction (rolling ball radius of 25-50 pixels). The filtered and background subtracted micrographs were binarized (dark background) and segmentation was optimized using the Remove Outliers tool and erosion/dilation of binary segments tools. Processed micrographs were compared to the raw micrograph during optimization of binary segments. The Analyze Particles tool was used for automated determination of Feret diameter of each segment within a minimum particle area of 50 nm^2. Feret diameters are

presented as raincloud plots generated in R Studio (v4.0.5). Statistical analysis was done in Excel (average ± sem) and Scipy[251] (Kolmogorov-Smirnov test).

Cryo-electron microscopy data collection

Prior to vitrification, samples were incubated for >16 hr at 37° C (apo-37C) or for 2 hours at 75° C (reaction products from DLS experiments) in the absence and presence of lysozyme (apo-75C and mj:lyso-75C at a 12:1 ratio). 3 µL of each sample (~1 mg/mL) was applied to a freshly glow discharged (15mA, 1 min) holey carbon copper grid (apo-37C: Cflat (EMS) R1.2/1.3, apo-75C and mj:lyso-75C samples: Quantifoil R2/1, 400 mesh). Grids were blotted (1 – 1.5 s) at room temperature and 90% humidity and plunge froze into liquid ethane on a Vitrobot Mark IV (FEI, Thermo Fisher Scientific). Image datasets were collected at the Pacific Northwest Cryo-EM Center (NIH, Portland, OR) on a 300 kV Titan Krios equipped with a K3 detector (Gatan) using SerialEM[272]. Movies were collected in super-resolution mode at a calibrated physical/super-resolution pixel size of 0.788/0.394 Å pixel^{-1} (apo-37C sample), 1.0125/0.50625 Å pixel^{-1} (apo-75C sample), and 1.0655/0.53275 Å pixel^{-1} (mj:lyso-75C) with a total dose rate of ~40 e^{-} Å^{-2} over 70 frames for the apo-37C sample and ~50 e^{-} Å^{-2} over 50 frames for apo-75C and mj:lyso-75C. Movies were collected over a defocus range of 1.0 – 2.5 µm. The apo-75C and mj:lyso-75C samples were collected using a GIF energy filter (Gatan) with a 10 eV slit width.

Cryo-EM image processing of apo-state mjHSP16.5 (37° C)

All steps of Cryo-EM image processing were performed in CryoSPARC v3.3.1[273]. A dataset of 16,214 micrographs for mjHSP16.5 (apo-37C) was preprocessed with Patch Motion Correction (micrographs binned 2x, 0.788 Å pixel^{-1}) and Patch CTF estimation. Low quality micrographs were removed based on CTF resolution fit, A subset of 100 micrographs was subjected to blob picking (120-160 Å diameter) to yield a particle set of ~3.4 million

particles extracted with binning (2.46 Å pixel^{-1}). Noisy particles and low occupancy classes were removed by 2D classification to give a set of 1,170,772 M particles used for multi-class ab initio model generation with 4 classes and maximum resolution of 6 Å. Multi-class ab initio generation yielded 2 good classes (1,060,133 M total particles) corresponding to 24-mer caged assemblies with slightly different diameters. Further rounds of 2D yielded 968,458 particles that were again subjected multi-class ab initio reconstruction (3 classes), yielding two distinct classes of 24meric cages with 441,253 particles in class 1 (expanded state) and 421,283 particles in class 2 (contracted state). A consensus refinement of re-extracted particles (1.05 Å pixel^{-1}) of the combined classes (862,436 particles) without symmetry (C1) yielded a consensus reconstruction at 2.99 Å resolution. 2D classification and heterogeneous refinement (C1, 6 classes) and removal of low occupancy classes yielded 630,757 particles which refined with octahedral (O) symmetry to 2.44 Å.

A C1 consensus refinement of the 630,757 particle stack was used as input for 3D Variability analysis with 3 orthogonal principal modes and a filter resolution of 5 Å[274]. Additionally, this particle set was expanded with octahedral (O) symmetry (15,136,968 expanded particles) and used for 3D Variability analysis with 3 orthogonal principal modes and a filter resolution of 5 Å. These particles were subjected to heterogeneous refinement with four classes which gave two high occupancy classes at ~2.7 Å resolution (expanded state: 257,168 particles; contracted state: 205,181 particles). Separate cleanup of the two particle sets was done by 2D classification yielding final non-uniform refinements (O symmetry) of 2.35 Å for the expanded state (256,929 particles) and 2.50 Å for the contracted state (186,720 particles).

Cryo-EM image processing of apo-state mjHSP16.5 (75° C)

All steps of Cryo-EM image processing were performed in CryoSPARC 4.4.1[273]. The full dataset of 6,460 micrographs for mjHSP16.5 apo-75C was preprocessed with Patch Motion Correction (micrographs binned by 2x, 1.0125 Å pixel^{-1}) and Patch CTF estimation. The resulting micrographs were culled based on CTF estimation resolution, relative ice thickness, and average intensity to yield 6,186 micrographs carried forward for particle picking. Blob particle picking on the full micrograph stack generated ~2.4 million picks that were extracted at 2.373 Å pixel^{-1} and cleaned up by two rounds of 2D classification to yield 185,806 particles for further analysis. Results from multi-class ab initio generation (4 classes) were input into a heterogeneous refinement (C1 symmetry, 4 classes) which yielded two cage-like maps at 5.69 Å (54,739 particles, set 1) and 4.92 Å (99,715 particles, set 2) resolution. Particles from these two classes were combined and re-extracted at 1.187 Å pixel^{-1} and the pooled particle set (153,807 particles) were reconstructed with O symmetry to 2.86 Å. Results from a C1 consensus non-uniform refinement were input into a 3D Variability analysis with three orthogonal principal modes and a filter resolution of 5 Å[274].

Cryo-EM image processing of mjHSP16.5/lysozyme complexes (12:1 ratio)

All steps of Cryo-EM image processing were performed in CryoSPARC v4.2.1-4.4.1[273]. The full dataset of 13,276 movies for mj:lyso-75C was preprocessed with Patch Motion correction (micrographs binned by 2x, 1.0655 Å pixel^{-1}) and Patch CTF estimation. The micrographs were culled based on CTF estimation resolution, relative ice thickness, and average intensity to yield 12,704 micrographs carried forward for particle picking. Blob picking (120 – 220 Å diameter) on a subset of 500 micrographs to yield 197,163 particles. Particles were extracted at 2.5 Å pixel^{-1}, submitted to 2D classification, and the resulting good classes were used as 2D templates for particle picking. Inspection of template-based picks resulted in 8,446,808 particles that were subjected to two rounds of 2D classification

to yield 3,055,664 good particles which were then extracted at 3.33 Å pixel^{-1}. This particle set was used as input for a multi-class ab initio job (8 classes, initial resolution 80 Å). The resulting eight ab initio models along with the full good particle stack were input into a heterogeneous refinement job which gave six good classes (2,826,578 total particles) and two noisy classes. A second round of heterogeneous refinement was performed using the six good maps/particles and the two noisy maps (to assist removing noisy particles) which generated four good classes identified as a 24mer (985,163 particles), 26mer (450,391 particles), 32mer (653,689 particles), and a 36mer oligomeric states (242,970 particles) that were used for further analysis.

The initial particle set pertaining to the 24mer oligomeric state (985,163 particles) was cleaned up by 2D classification to produce a particle set of 960,040 that was extracted at 1.25 Å pixel^{-1} and input into 3D Variability analysis with three orthogonal principal modes and filter resolution of 5 Å[274]. Intermediate mode analysis of the first component was done with five intermediate maps and particles were used as inputs for heterogeneous refinement which produced two classes below 4 Å resolution. These two classes were pooled and refined (non-uniform refinement) without applied symmetry to 2.60 Å resolution.

The particle set associated with the 26mer oligomeric state class (450,391 particles) was extracted at ~1.2x binning (1.25 Å pixel^{-1}) followed by global CTF refinement and non-uniform refinement without symmetry (C1) to 3.65 Å. 3D variability analysis was performed with three orthogonal principal modes and intermediates analysis of the three components generated five intermediates states that refined to ~4 – 8.5 Å resolution without imposed symmetry (C1).

The 32mer oligomeric state particle set (653,689 particles) was extracted at 1.25 Å pixel^{-1} and cleaned up by 2D classification to give 645,384 particles that refined without applied symmetry to 4.80 Å resolution. 3D variability analysis was performed with three

orthogonal principal modes at a filter resolution of 5 Å, followed by intermediates analysis to generate five intermediates states that were used as input for heterogeneous refinement[274]. Heterogeneous refinement produced two classes below 7 Å resolution that corresponded to a 32mer state (244,887) and a 34mer state (202,648) that refined (non-uniform refinement) without symmetry (C1) to 4.37 Å and 4.79 Å, respectively. The 34mer particles went through global CTF refinement and a final non-uniform refinement (C1) to yield a 4.71 Å final map.

The 3x binned particle set for the 36-subunit cage class (242,970) was refined with (D3) and without (C1) symmetry and the resulting maps were used as input for a heterogeneous refinement (C1) with two classes (40 Å initial lowpass filter) and generated one class displaying D3 symmetric features at 8.27 Å resolution with 111,271 particles. Low quality particles were removed by 2D classification resulting in 85,180 particles that refined to 4.50 Å resolution with D3 symmetry. This particle set was expanded with D3 symmetry to yield 511,080 particles that were subjected to local refinement (C1) resulting in a 4.30 Å reconstruction. Output from local refinement was used as input for 3D Variability with three orthogonal principal modes and a filter resolution of 5 Å[274]. Intermediate mode analysis (five intermediates) of the principal components resulted in five intermediate maps with corresponding particle sets that where input for 3D classification without alignment (5 classes). A highly populated class containing 144,177 particles was used for local refinement (C1) resulting in a final reconstruction of the 36-subunit cage structure at 4.01 Å resolution. A reconstruction without symmetry (C1) of the expanded particles was refined to 6.39 Å and used for local resolution analysis. Local resolution estimation of the final refined maps of each oligomeric state was performed in CryoSPARC using default parameters and resolution-based coloring of each map was done in ChimeraX (v1.7)[250,275,276].

Atomic Modeling and Validation

Atomic model building into the mjHSP16.5 apo-state (37° C) in both contracted and expanded states was initiated using a dimer model from the previously published crystal structure of mjHSP16.5 (PDB ID: 1SHS[138]). Final maps (O symmetric) corresponding to the contracted and expanded cages were sharpened using Phenix AutoSharpen[277]. Dimers were initially fit as rigid bodies into each map using in ChimeraX to produce a 24meric model and model refinement was done using phenix real space refinement with secondary structure and NCS restraints[278]. Atomic model building of NTD residues 11-32 for the contracted and expanded states were built in COOT as a polyalanine chain, refined, and side chains added before further refinement and side chain adjustment. Iterative manual and automatic model refinement was done in COOT and Phenix (real space refinement) using secondary structure and NCS restraints.

The final 24mer map (C1) from the mjHSP16.5/lysozyme (75°C) dataset was sharpened using Phenix AutoSharpen and model building was initiated by rigidly fitting the expanded model from the apo-37C dataset with deletion of residues 11-26[277,278]. Real-space refinement was performed in Phenix using reference model and secondary structure restraints. The final 24mer model contained residues 27-147. All subsequent model building was initiated using a dimer model from the 24mer rigidly fit into the final 26mer, 32mer, 34mer, and 36mer maps. For each oligomeric state various deletions of NTD and CTD residues of the monomers were done to agree with resolved map density and iterative manual remodeling of CTDs to fit the map density was performed in COOT and ISOLDE along with real-space refinement in Phenix[278–280]. Model building of the 26mer state rigidly fit 13 dimers into the unsharpened 26mer map with truncations yielding 22 chains with residues 34-147 and 4 chains with residues 34-139. Sixteen dimers were refined in the sharpened (Phenix local anisotropic sharpening) 32mer map, resulting in 31 chains with residues 31-147 and one chain with residues 35-143. For the 34mer state 17

dimers refined into a Phenix auto-sharpened map, resulting in 33 chains covering residues 33-147 and one chain with residues 35-143. The 36mer state model was built with 18 refined dimers fit into a Phenix AutoSharpened map with 36 chains covering residues 31-147. For all models, validation of model refinement and map-to-model fit was done using Phenix validation and the PDB validation server[277].

For visualization of unmodeled density, final maps were low-pass filtered at 7 Å resolution and density corresponding to the atomic models of each state were generated using the molmap (7 Å) function in ChimeraX v1.17.1[250,275,276]. Density corresponding to the 7 Å molmaps were subtracted from the respective 7 Å low-pass filtered Cryo-EM maps to generate a subtracted map containing the unmodeled internal density. C_α RMSD calculations were generated in ChimeraX using only chains with full CTDs (through residue 147) resulting in 24 chains for the 24mer, 22 chains for the 26mer, 31 chains for the 32mer, 33 chains for the 34mer, and 36 chains for the 36mer. Coloring based on RMSD and local resolution was done in ChimeraX with the color by attributes and surface color utilities, respectively. Buried surface areas for the ACD-dimer interface, inter-dimer interface, and the canonical CTD/ACD-groove interface were calculated using the Interfaces function in ChimeraX with default settings except areaCutoff set to 100 $Å^2$. For visualization, modelling of NTD residues 1-10 was (Fig 2c) was done by extension of residues distally from residue 11 of the contracted model and subsequent addition of side chains in COOT[279]. Measurement of the internal volume density (at ~2σ) was performed in ChimeraX (v1.7) by subtracting cage density using molmaps generated at 7 Å and the volume subtraction tool.

Supplementary Figures

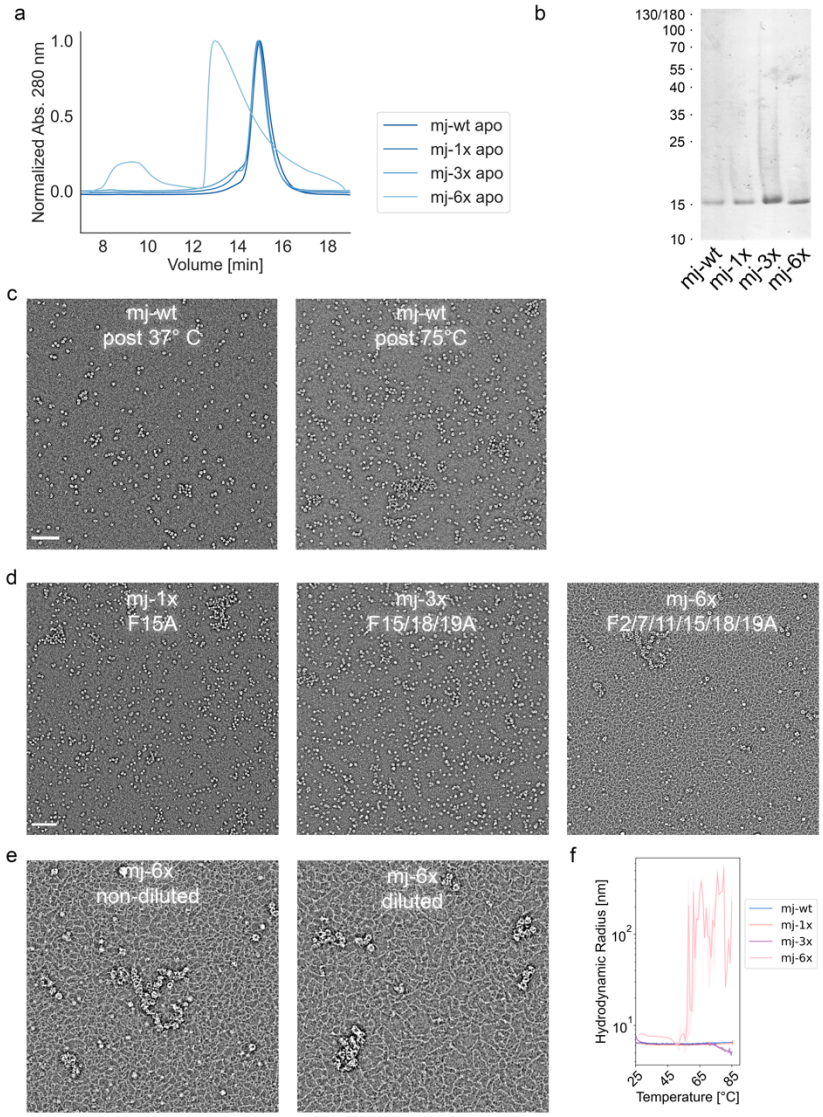

Supplementary Fig. 1: Purified mjHSP16.5 constructs used in this study. (a) Size-exclusion chromatography traces for apo-states of mjHSP16.5 wildtype (mj-wt) and NTD variants (mj-1x, mj-3x, and mj-6x) (b) SDS-PAGE visualized by silver staining of purified mj-wt, mj-1x, mj-3x, and mj-6x (c) Negative-stain electron microscopy (NS-EM) of apo-state mjHSP16.5 after heating at 37° C (~16 hours) and 75° C (2 hours) (d) NS-EM of apo-state mj-1x and mj-3x (75° C) and mj-6x (25° C) (e) NS-EM of mj-6x at two dilutions displaying the dilution of background fibers (~2 nm wide) that were prevalent in this sample. (f) Temperature ramp from 25-85° C for mj-1x, mj-3x, and mj-6x and corresponding hydrodynamic radius showing mj-6x aggregation around 55-60° C.

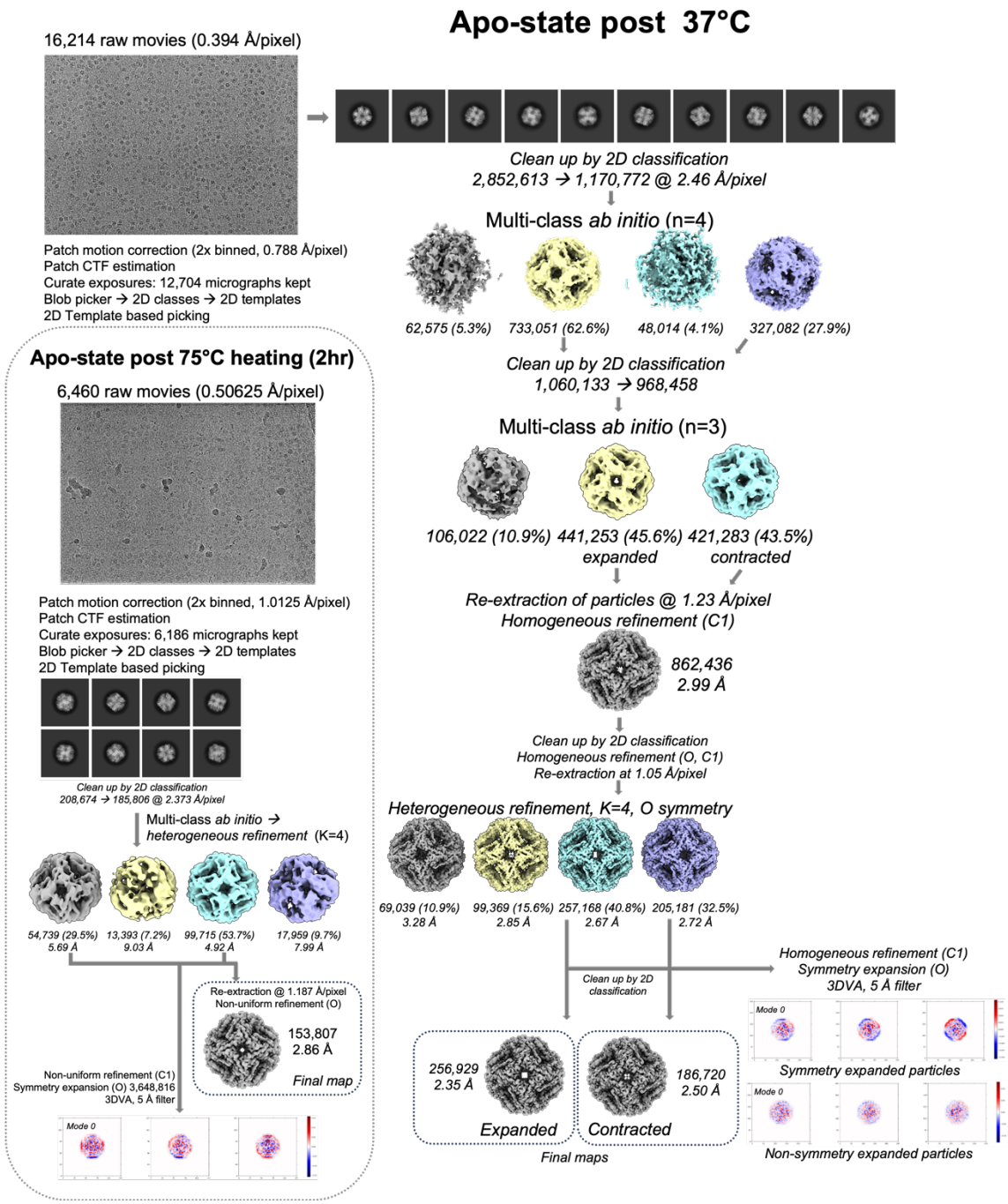

Supplementary Fig. 2: Single-particle Cryo-EM processing workflows for the mjHSP16.5 apo-37 and apo-75 datasets. Overview of preprocessing, 2D/3D classification, ab initio model generation, 3D refinement, and 3D variability analysis steps. Particle count numbers, pixel sizes, symmetries, and resolutions are noted were appropriate.

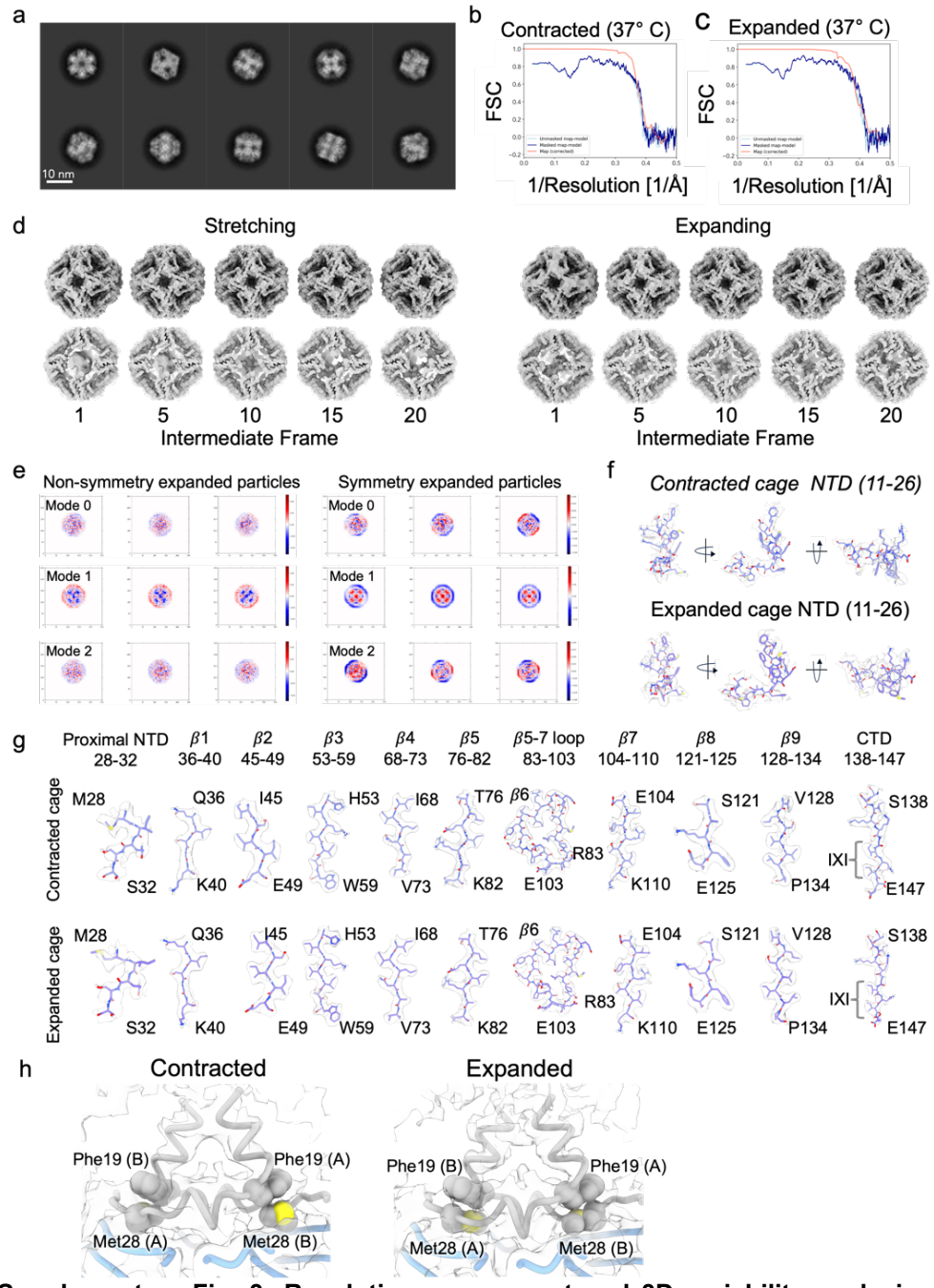

Supplementary Fig. 3: Resolution assessment and 3D variability analysis of the apo-37 Cryo-EM dataset (a) Representative 2D classes showing multiple views of the canonical 24mer caged assembly (b,c) Fourier Shell Correlation (FSC) plots of the contracted and expanded states displaying the CryoSPARC generated FSC plot of the corrected map (red), and the unmasked map to model FSC (light blue) and masked map to model FSC (dark blue) generated by Phenix. (d) Intermediate reconstructions for the stretching and expansion principal component modes identified from 3D variability analysis in CryoSPARC, shown along 4-fold axis (top) and internal slice view (bottom) (e) Principal component modes from 3D variability analysis with and without symmetry expansion of the consensus particle set, displayed as heat maps of density variability across each mode (f,g) Segmented views of the model-to-map fit for the contracted and expanded atomic models. (h) Interaction of Phe19 and Met28 (shown as space-filling model) between dimeric protomers (A and B).

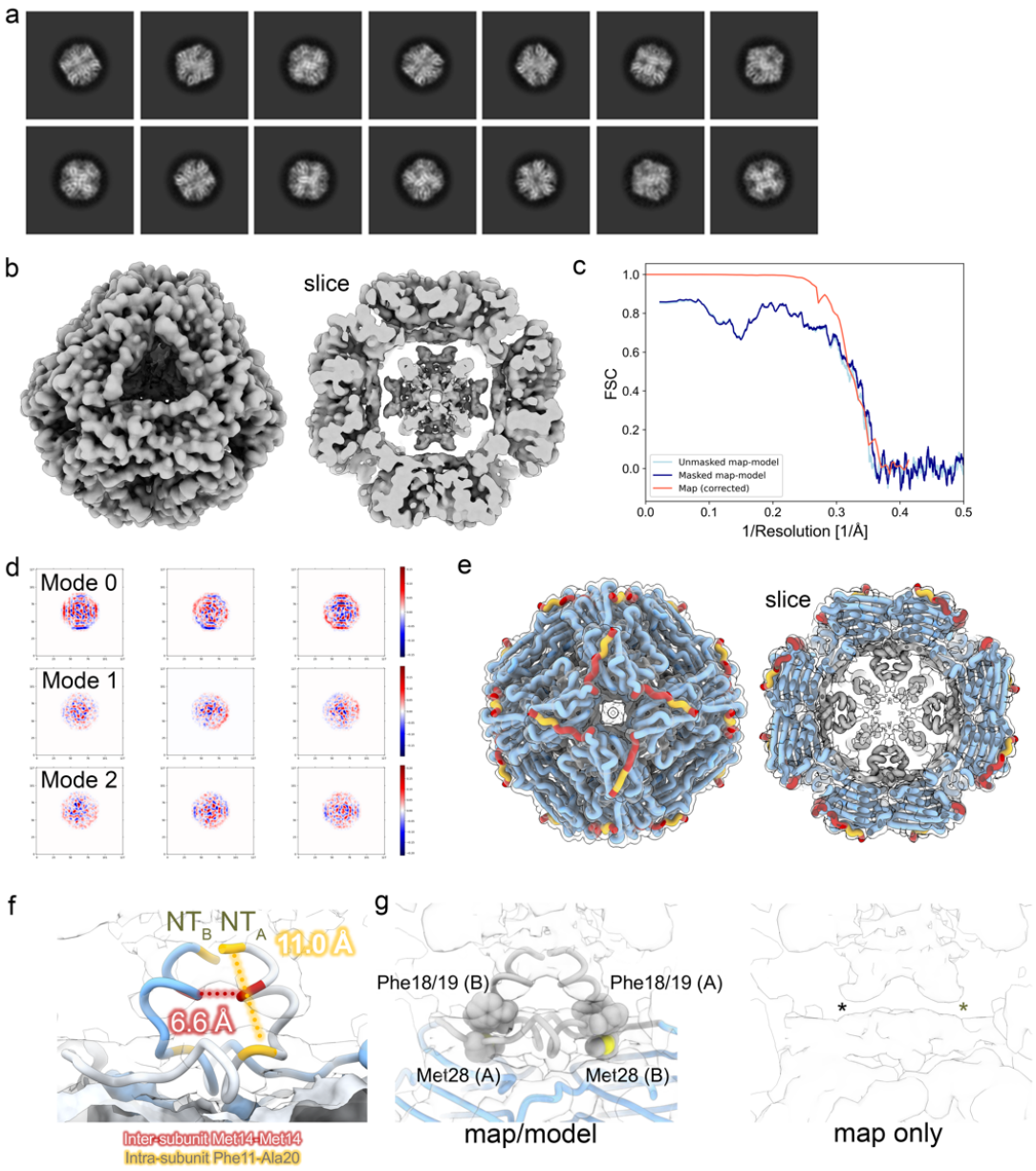

Supplementary Fig. 4: Resolution assessment and 3D variability analysis of the apo-75 Cryo-EM dataset. (a) Representative 2D classes showing multiple views of the canonical 24mer caged assembly. (b) Consensus 3D reconstruction of apo-75 with octahedral (O) symmetry imposed, shown from canonical 3-fold axis of the 24mer (left) and slice view displaying internal density (right) showing helical density from the NTD protruding toward the center of the cage. (c) Fourier shell correlation plot of apo-75 reconstruction show in (b) generated by CryoSPARC (d) Principal component modes from 3D variability analysis displayed as heat maps of density variability across each mode. (e) Atomic model for residues 11-147 fit into sharpened Cryo-EM density map. (f) Intra- (Phe11-Ala20) and Inter- (Met14-Met14) protomer measurements of NTD helix α1. (g) *Left* Map and model showing putative competition between Phe18 and Phe19 with Met28 between dimeric protomer chains (A and B). *Right* Map without model showing weak density at base of NTD helix α1.

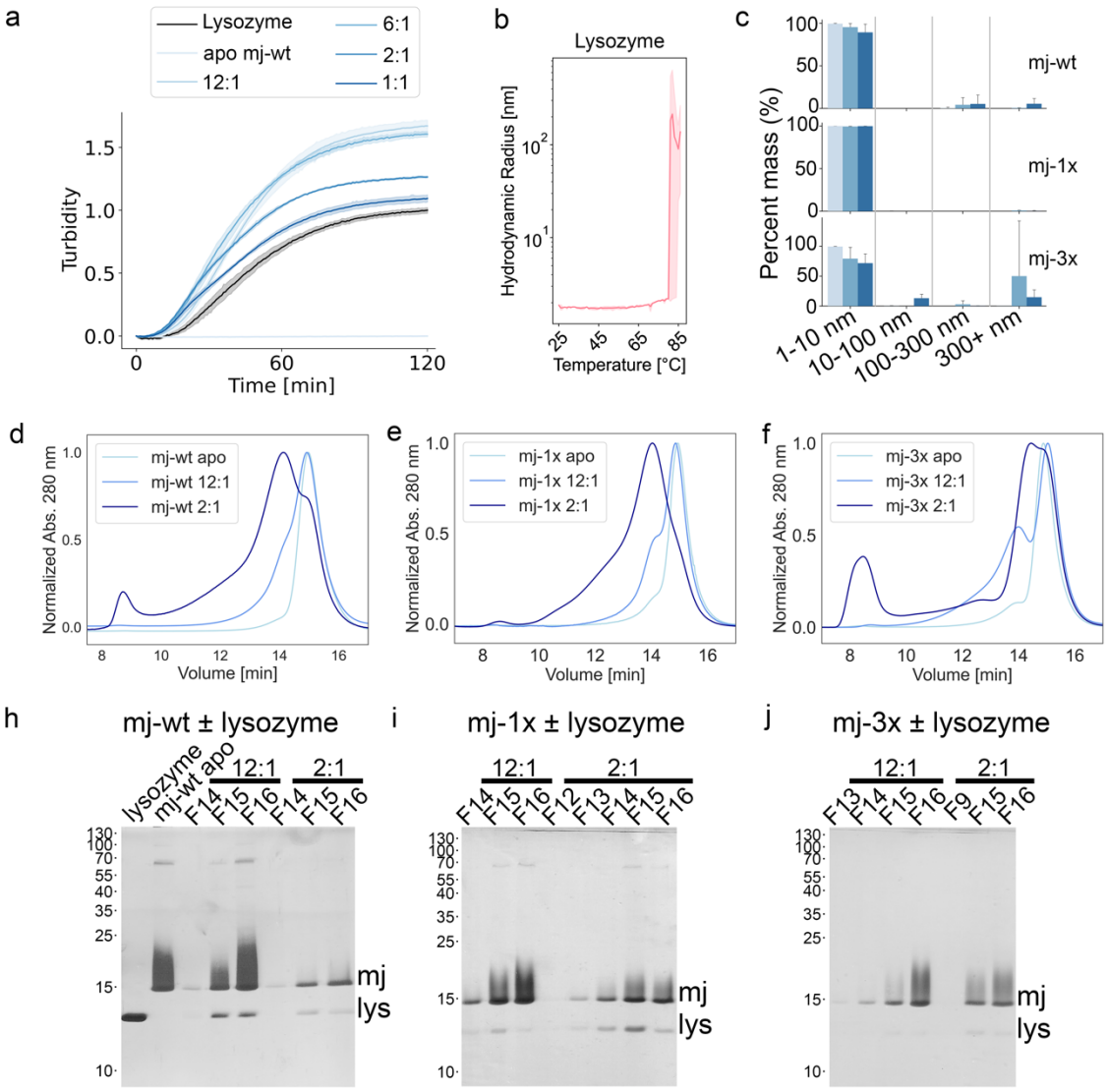

Supplementary Fig. 5: Chaperone-client binding assays for mjHSP16.5 wildtype (mj-wt) and NTD variants (mj-1x: F15A; mj-3x: F15/18/19A). (a) Overlay of turbidity traces at 37° C for ratios of mj-wt to lysozyme (12:1, 6:1, 2:1, and 1:1), mj-wt alone (light blue), and lysozyme alone (gray). For these conditions, lysozyme unfolding was initiated with reducing conditions. (b) Bulk hydrodynamic radius of lysozyme, under non-reducing conditions, measured from 25° C to 85° C by dynamic light scattering showing aggregation occurring at temperatures above ~80° C. Trace shows average and s.d. of n=3 replicates. (c) Histograms showing binned hydrodynamic radii (1-10 nm, 10-100 nm, 100-300 nm, and 300+ nm bins) and associated percent mass for mj-wt, mj-1x, and mj-3x in the presence and absence of lysozyme, under non-reducing conditions, after incubation at 75° C for two hours (d-f) Size-exclusion chromatography (SEC) traces for mj-wt (d), mj-1x (e), and mj-3x (f) with lysozyme (12:1 and 2:1 chaperone:client ratios) and in the apo-state after incubation at 75° C for two hours (h-j) SDS-PAGE analysis of fractions collected from SEC runs of mj-wt, mj-1x, and m-3x with lysozyme (12:1 and 2:1 ratios), respectively. Protein bands corresponding the mjHSP16.5 (mj) and lysozyme (lys) indicated.

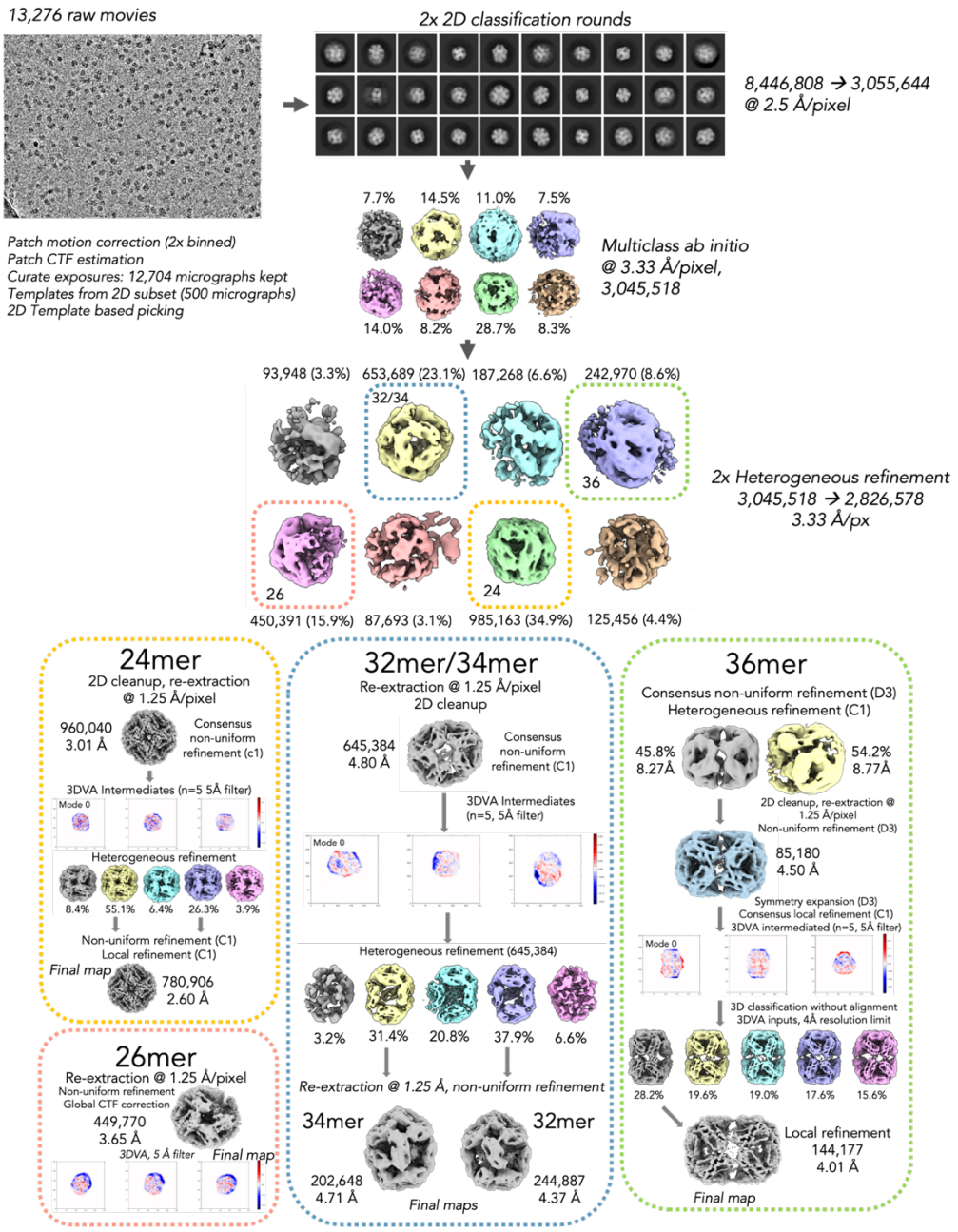

Supplementary Fig. 6: Single-particle Cryo-EM processing workflow for the mjHSP16.5/lysozyme dataset. Overview of preprocessing, 2D/3D classification, ab initio model generation, 3D refinement, and 3D variability analysis steps. Particle count numbers, pixel sizes, symmetries, and resolutions are noted were appropriate. Outlined boxes are color coded to match ab initio models and corresponding downstream processing for each oligomeric state. Final maps used for model building are noted

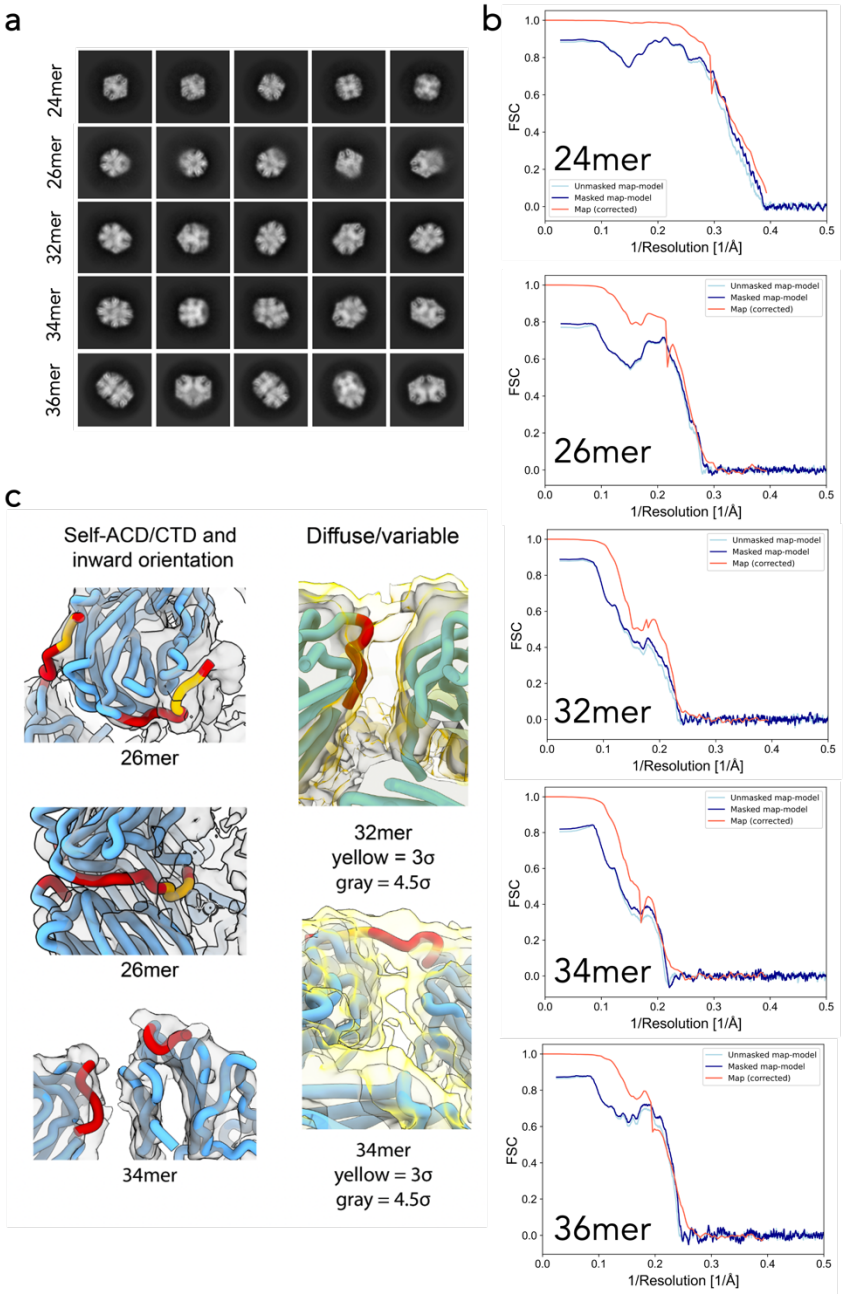

Supplementary Fig. 7: Resolution assessment and non-canonical ACD/CTD interactions obtained from mjHSP16.5/lysozyme Cryo-EM dataset. (a) Representative 2D classes of each resolved oligomeric state (24, 26, 32, 34 and 36mers) (b) Fourier Shell Correlation (FSC) plots of each oligomeric state (24, 26, 32, 34 and 36mers) displaying the CryoSPARC generated FSC plot of the corrected map (red), and unmasked map to model FSC generated (light blue) and masked map to model FSC (dark blue) generated by Phenix. (c) Non-canonical interactions of the C-terminal domain (CTD, red) and IXI-motif (yellow) from mjHSP16.5/lysozyme complexes showing association with the α-crystallin domain (ACD, blue) depicting inward orientation (left); and diffuse/variable interactions (right). Models are depicted in cartoon form and fit into the Cryo-EM density maps (semi-transparent). Diffuse/variable interactions are shown with fit into both low threshold (yellow) and high threshold (gray) map densities due to resolution variation in this region.

Supplementary Table 1

	Area (avg ± sem) [nm^2]	Area range [nm^2]	Feret (avg ± sem [nm]	Feret range [nm]	Feret mode [nm]	$N_{particles}$ (N_{mg})	DLS R_H – peak 1 [nm]	DLS % mass - peak 1
Wildtype ± lysozyme (post 75° C, 2hr)								
apo	209.3 ± 15.6	50.2 – 36634.3	18.8 ± 0.3	8.9 - 347.0	11.9	3178 (7)	6.0 ± 0.1	99.4 ± 0.6
12:1	215.5 ± 4.9	50.2 – 19224.2	19.51 ± 0.1	8.9 – 324.0	13.9	6207 (9)	6.3 ± 0.1	99.5 ± 0.2
2:1	184.1 ± 2.5	90.1 – 8270.6	19.3 ± 0.1	8.8 – 238.3	14.4	8311 (7)	7.2 ± 0.2	97.2 ± 1.3
F15A ± lysozyme (post 75° C, 2hr)								
apo	181.0 ± 5.7	50.2 – 34049.0	17.8 ± 0.1	8.6 – 317.2	12.3	7873 (6)	6.1 ± 0.1	99.9 ± 0.1
12:1	267.3 ± 8.3	50.0 – 33411.1	22.2 ± 0.2	8.9 – 384.3	14.5	8723 (6)	6.3 ± 0.1	99.4 ± 0.2
2:1	268.5 ± 18.0	50.0 – 138788.9	21.2 ± 0.2	8.6 - 844	14.5	9556 (7)	7.6 ± 0.6	99.7 ± 0.3
F15/18/19A ± lysozyme (post 75° C, 2hr)								
apo	153.5 ± 4.4	50.0 – 30767.5	16.6 ± 0.1	8.8 – 325.9	10.7	9268 (5)	5.8 ± 0.1	99.6 ± 0.3
12:1	267.4 ± 7.6	50.0 – 42640.4	21.8 ± 0.2	8.8 – 576.1	14.0	7616 (7)	7.0 ± 0.3	92.4 ± 5.6
2:1	293.8 ±	50.0 – 71722.6	23.0 ±	8.6 – 583.0	14.5	11305 (7)	8.8 ± 0.9	67.1 ± 7.6
6x-apo (25° C)*	--	--	21.3 ± 2.3	11.6 – 213.2	17.0	100 (4)	8.4 ± 0.4	100 ± 0.0

Single-particle analysis from the NS-EM datasets (Area and Fere diameter) and DLS (hydrodynamic radius and corresponding percent mass) measurements of mjHSP16.5 wildtype and NTD variants obtained in the presence and absence of client lysozyme. NS-EM grids were prepared following two hour incubation at 75° C. The exception is for 6x-apo which was done at 25° C due to reduced thermal stability and measurements obtained by hand (n=100). Measurements are presented as average ± s.e.m.

Supplementary Table 2

	Apo-state 37°C		Apo-state 75° C	+Lysozyme dataset (12:1 mj:lyso) 75°C				
	Expanded	Contracted		24mer	26mer	32mer	34mer	36mer
Data collection and processing								
Magnification	29,000	29,000	81,000	81,000	81,000	81,000	81,000	81,000
Voltage (kV)	300	300	300	300	300	300	300	300
Electron exposure (e^-/Å^2)	40	40	50	50	50	50	50	50
Defocus range (μm)	0.8 – 2.5	0.8 – 2.5	0.6 – 2.5	0.6 – 2.5	0.6 – 2.5	0.6 – 2.5	0.6 – 2.5	0.6 – 2.5
Micrographs (No.)	16,214	16,214	6,460	13,276	13,276	13,276	13,276	13,276
Pixel size (super-resolution (Å)	0.788 (0.394)	0.788 (0.394)	1.0125 (0.50625)	1.0655 (0.53275)	1.0655 (0.53275)	1.0655 (0.53275)	1.0655 (0.53275)	1.0655 (0.53275)
Symmetry imposed	O	O	O	C1	C1	C1	C1	D3 (expanded)
Initial particle images (no.)	1,170,722	1,170,722	2,444,082	3,368,583	3,368,583	3,368,583	3,368,583	3,368,583
Final particle images (No.)	256,929	187,720	153,807	780,906	449,770	244,887	202,648	36,346
Map resolution (Å)	2.35	2.50	2.86	2.60	3.67	4.37	4.71	4.01
FSC threshold	0.143	0.143	0.143	0.143	0.143	0.143	0.143	0.143
Map resolution range (Å)	2.4 – 4.8	2.4 - 21	2.7 – 24	2.9 - 30	3.0 - 55	2.7 - 30	3.0 - 30	2.7 - 52
Model Refinement								
Initial model used	1SHS (PDB)	1SHS (PDB)	apo37-expanded	apo37-expanded	24mer	24mer	24mer	24mer
Model resolution (Å)	2.35	2.50	2.86	2.60	3.67	4.37	4.71	4.01
FSC threshold	0.143	0.143	0.143	0.143	0.143	0.143	0.143	0.143
Map sharpening *B* factor (Å^2)	13.95	-5.550	-138.9	43.35	-118.2	-138.2	210.0	-112.5
Model composition								
Non-hydrogen atoms	25,752	25,752	25,728	22,488	23,062	28,563	30,351	32,610
Protein residues	3288	3288	3288	2904	2964	3674	3904	4211
Ligands	0	0	0	0	0	0	0	0
R.M.S. deviations								
Bond lengths (Å)	0.004 (0)	0.014 (0)	0.003 (0)	0.004 (0)	0.003 (0)	0.003 (0)	0.003 (0)	0.004 (0)
Bond angles (°)	0.711 (0)	0.697 (24)	0.704 (0)	0.637 (0)	0.474 (0)	0.536 (0)	0.515 (0)	0.721 (10)
Validation								
Molprobity score	1.76	1.36	1.52	1.20	1.64	1.91	1.26	1.33
Clash score	4.09	4.11	3.35	4.11	7.34	8.74	4.5	2.33
Poor rotamers (%)	1.67	0.83	0.00	0.00	0.62	0.25	0.41	0.00
Ramachandran plot								
Favored (%)	94.07	97.04	94.07	98.32	96.46	93.07	97.86	95.39
Allowed (%)	5.93	2.96	5.93	1.68	3.50	6.87	1.98	4.32
Disallowed (%)	0.00	0.00	0.00	0.00	0.03	0.06	0.16	0.29

Summary of single-particle Cryo-EM data collection, processing, model building, and validation for maps and models.

Chapter 4: Endless Forms Most Beautiful: Determining structural mechanisms of small heat shock protein polydispersity and client sequestration

A central theme in biology is that structure determines function. Small heat shock proteins (sHSPs) are a class of molecular chaperones which play out this structure/function relationship as molecular transformers capable of adopting diverse morphologies in response to various functional and physiological demands. Utilizing an ATP-independent "holdase" function, sHSPs prevent irreversible protein aggregation events potentiated by conditions of cellular stress (e.g., heat, pH change, oxidation)[5,8–13]. The ubiquitous importance of this function is highlighted by the fact that sHSPs are expressed across all domains of life – sharing a conserved domain organization consisting of a central α-crystallin domain (ACD) surrounded by relatively disordered N-terminal (NTD) and C-terminal (CTD) domains that facilitate diverse oligomerization states[1,134]. Humans encode ten sHSPs with quaternary structure ranging from dimers (HSPB6) and tetramers (HSPB2/3) to polydisperse ensembles of 12 – 48mers (HSPB1, α-crystallins)[41]. Moreover, mutation and dysregulation of human sHSPs that impact their structure/oligomerization state is associated with multiple diseases, specifically aggregation diseases (aggregopathies) such as Alzheimer's disease, Parkinson's disease, and cataract (*discussed further in Chapter 1 of this dissertation*)[77,270]. Many of these disease states are associated with older age – making sHSPs important disease-related subjects as the aged population rises with increases in life expectancy of the world's population.

This dissertation set out to define structural mechanisms driving sHSP "holdase" function in the prevention of irreversible protein aggregation events. For decades, sHSPs have provided unique challenges to structural biologists through their diverse and dynamic structures, limiting a detailed understanding of how they engage with destabilized proteins (clients) while maintaining their own structural integrity during stress events. Early gel

filtration and electron microscopy (EM) studies of the vertebrate αL-crystallin (αA- and αB-crystallin hetero-oligomers) sHSPs isolated from bovine lenses provided early indications of the heterogenous morphologies adopted by these sHSPs[76]. Later on, EM three-dimensional (3D) reconstruction studies of α-crystallin by Horwitz, et al in 1998 depicted a caged-like assembly, interpreted as a 32mer, appearing as a hollow sphere of ~11 nm in diameter resolved to ~40 Å resolution[212]. Despite advances in CryoEM since these seminal studies, 3D reconstructions of αA- and αB-crystallin have been limited to low-resolution pseudo-atomic models, limited by the high-degree of underlying structural heterogeneity and polydispersity of these proteins[158,160]. The heterogeneity of α-crystallins, and other sHSPs, further increases upon client binding, where sHSP/client complexes can reach >100 nm in diameter and produce hundreds of complexes with varying chaperone:client stoichiometries[32,118,184,186,224].

Chapter 2 of this dissertation describes work characterizing a conserved mechanism of quasi-ordered expansion and elongation of α-crystallins with the clients lysozyme and insulin[118]. To overcome difficulties in quantitively characterizing the high-degree of structural heterogeneity displayed by these sHSP/client complexes, I developed a single-particle size measurement approach to analyze thousands of individual sHSP and sHSP/client particles directly from negative stain EM micrographs. Together with other solution-state biophysical techniques (size-exclusion chromatography and dynamic light scattering) I showed how recombinantly expressed αA-crystallin and αB-crystallin can sequester increasing amounts of unfolding client proteins by forming highly elongated particles (~15 nm wide and up to 125 nm long). This elongation mechanism appeared to persist, up to a point before an amorphous collapse of the elongated particles occurred at under saturating conditions of clientele. This mechanism of client sequestration was also observed for native αL-crystallin (hetero-oligomer of αA- and αB-crystallin) isolated from

sheep lenses with the client lysozyme, showing mechanistic conservation of the native hetero-oligomeric sHSP. Through development of a new single-particle analysis approach this work provided a quantitative description of how α-crystallins morphologically adapt to unfolded client, describing mechanisms of quasi-ordered client-induced co-aggregation utilized by the lens chaperone system to prevent aggregation.

An overarching theme of this dissertation is the use of single-particle EM methods to characterize heterogeneous sHSP structures. Advances in cryoelectron microscopy (CryoEM) over the past decade, as well as NIH supported national CryoEM facilities, have provided structural biologists with an incredible tool to analyze protein structure and dynamics[281,282]. Appendix Chapter 1 describes multiple attempts to determine high-resolution structures of αA- and αB-crystallin homo-oligomers. Various approaches were taken to classify distinct oligomeric states, in attempt to define these to high-resolution, with both unbiased methods as well as approaches using enforced symmetry (tetrahedral). While the latter yielded similar results to previously proposed models of an αB-crystallin 24mer[158,256], the underlying dynamics and polydispersity of α-crystallins prevented all attempts at uncovering high-resolution structural details and the symmetric results that were obtained were deemed to likely be the result of initial model and symmetry biases applied during image processing (unpublished). Future attempts to determine the structures of α-crystallins by CryoEM may benefit from biochemical approaches to quench some of the underlying dynamics that have made this system prohibitive, such as crosslinking/fractionation techniques (GraFIX) and processing single-particle CryoEM datasets of different fractions[283].

Structural aspects of the α-crystallins (e.g., domain organization, dimerization, caged-like high-order oligomers, polydispersity, subunit exchange dynamics) are shared by evolutionarily distant sHSPs, including HSP26 from yeast, IbpA/B from *E. coli*, and HSP16.5 from the thermophilic archaeon *Methanocaldococcus jannaschii*

(mjHSP16.5)[134]. The first high-resolution structure of an oligomeric sHSP was of mjHSP16.5, depicting a hollow 24mer octahedrally symmetric cage, however, this crystallographic structure did not resolve the first 32 amino acids (the NTD), attributed to dynamic conformations of this region within the 24mer cage[138]. Indeed, many high-resolution structures of full-length sHSPs are missing (fully or partially) the NTD – leaving gaps in knowledge on how this domain supports oligomerization[137,155,260,284]. The NTD of sHSPs contains two conserved regions rich in hydrophobic residues that provide structural dynamics and client interactions, yet how these regions impart key elements of structure and function has remained unclear[149–152,285].

Given the established tractability of the mjHSP16.5 system, I set out to use modern approaches of CryoEM to determine high-resolution structural details of the NTD to better understand its role in oligomerization, polydispersity, and client-induced co-aggregation (Chapter 3). Single-particle CryoEM of the apo-state mjHSP16.5 revealed underlying structural plasticity that had not been appreciated by previous crystallographic structures and identified both stretching and expansion modes of oligomeric dynamics while also resolving key portions of the NTD involved in oligomerization, including the phenylalanine (Phe) rich “conserved” region. This domain appears to be key to the structural plasticity of mjHSP16.5, as the NTD appeared to sample multiple transient hydrophobic interactions (pi-pi/cation-pi) within the 24mer cage cavity. Structure-guided mutagenic studies targeting these NTD Phe residues supported a functional role for maintaining oligomeric stability and complex formation with the client lysozyme. These results provide long-sought structural and functional details on the role of these conserved hydrophobic regions in the NTD.

Having recognized the potential of this system, single-particle CryoEM was then used to analyze complexes of wildtype mjHSP16.5 formed with the model client lysozyme, under equilibrium-state conditions of temperature-induced client destabilization. I was able

to resolve five complexes corresponding to a 24mer, 26mer, 32mer, 34mer, and 36mer. These represent the first high-resolution structures of an oligomeric sHSP bound to an unfolded client and uncovered multiple aspects of structural mechanics used to accommodate clientele. First, the resolved 24mers likely represent unbound (apo) oligomers and allude to a mechanism by which client sequestration retains a significant population of unbound chaperones, providing an available pool for prolonged or intensified stress events. Client sequestration is enabled through dimer/client insertion, leading to polarization of the sHSP cage's stability and establishing a destabilized end primed for future client binding/subunit exchange events. This directional priming for future client binding would drive preformed sHSP/client complexes by lowering the energetic barrier to attain additional clients (selectively leaving a pool of apo-state oligomers). This mechanism of client-induced polarization leads to an elongation of the sHSP/client complex and likely utilizes multiple pathways in the formation of higher-order assemblies. This was evidenced by the unique geometry of the 36mer, suggesting this state likely arises from a different dimer/client insertion pathway than the 32-34mers.

Together, the results put forward in this dissertation support a role for morphological, directional elongation of sHSPs as a key mechanistic principle enabling high-capacity sequestration of destabilized clientele. Elongated sHSP/client co-aggregated structures described in Chapter 2 on the α-crystallins are morphologically similar to those isolated from aged lenses, supporting the physiological relevance of these morphologies[118]. Mechanisms of directional elongation uncovered for α-crystallins and mjHSP16.5 with client may provide multiple biological benefits, including concentrating/packaging multiple clientele for downstream refolding by HSP70/100 systems (for efficient recovery from stress) and/or establishing primed "hotspots" for future binding events that could allow for a pool of apo-state oligomers to be retained for future stress events. Client-induced co-aggregation of sHSPs is known to be influenced by client specific characteristics (e.g.,

size and stability) and directional elongation may be one of multiple co-aggregation processes adopted by sHSPs[176,224]. Further investigation into the influence of varying client types and how the stress induced aggregation is initiated (e.g., heat, oxidation, pH) will help shed light on the wide spectrum of sequestration mechanisms likely present among sHSP/client systems.

Expanding our understanding of the structural landscape of sHSPs will require new tools for characterizing heterogeneous protein samples and a strict adherence in the field to standardized experimental conditions in order to faithfully apply the “structure determines function” principle of biology. For instance, it is important to keep in mind both the structural sensitivities of sHSPs to experimental conditions (pH, temperature, concentration, buffer conditions, etc.) and the delicate interplay of multiple domains involved in multivalent interactions that guide oligomerization, polydispersity, and chaperone function. Terminal tags (for purification or fluorescence imaging) may disrupt these interactions with consequences on structure and function of the sHSP. The methods described throughout this dissertation can be used on other sHSP/client systems to quantitatively describe this structural landscape from nanometer (single-particles size analysis by EM) to sub-nanometer (single-particle CryoEM) scales of resolution. Additionally, *in vitro* characterizations of sHSP/client complexes can be used as a template to assist future imagining of sHSP systems at work *in situ* using emerging techniques in cryoelectron tomography (CryoET) which could give cellular context to this co-aggregation process and may uncover new sHSP-assisted pathways of aggregation mediation and stress recovery[286].

To conclude, sHSP structure seemingly provides boundless fodder for the structural biologist’s mind through their display of conformational (intrinsic disorder) and compositional (polydispersity) heterogeneity, hetero-oligomerization, and intriguing array of structural states (i.e., cages, discs, fibers, arrays). Indeed, the number of sHSP

structures I have viewed during experiments described in this dissertation likely count in the tens of thousands. Continued efforts to unravel the multifaceted nature of sHSPs – and determine ways to target sHSPs pharmacologically – will have profound consequences on aggregation-related diseases and the people effected by them.

APPENDIX CHAPTER 1: Single-particle CryoEM datasets of αA- and αB-crystallin demonstrate high levels of oligomeric heterogeneity

An initial focus of this dissertation was targeted at characterizing the structure and polydispersity of the α-crystallins by CryoEM. In their apo-states under non-stress conditions, αA- and αB-crystallin exist as an ensemble of oligomers, ranging from dimers to >40mers, with an average of ~26 and 28 subunits, respectively. Subunits can freely exchange between oligomeric states, maintaining a level of plasticity important for their function as molecular chaperones[162,287]. One of the first described models of α-crystallin structure comes from Augusteyn and Koretz in 1987 depicting a "protein micelle" model, depicting individual subunits with hydrophobic faces arranged towards to interior of the oligomeric "aggregates" and hydrophilic surfaces toward the exterior[288]. The first reported 3D structure of an α-crystallin was in 1998 by Haley, Horwitz, and Stewart of a 40 Å CryoEM reconstruction of αB-crystallin that was described as a 32mer forming a hollow cage[212]. More recently, multiple models of a 24meric αB-crystallin oligomer with tetrahedral symmetry have been proposed[117,158,211,256]. These models depict similar arrangements of 12 dimeric units tethered by canonical ACD/CTD-IXI interactions, however distinct locations of the variable NTD (surface exposed or buried) have been proposed in these structures. Indeed, the NTD of α-crystallins has evaded structural characterization and is likely a consequence of intrinsic disorder and variable competing interactions that have been described for this domain. More recently, three CryoEM structures of αA-crystallin were reported, corresponding to a 12mer (9.2 Å), 16mer (9.8 Å), and 20mer (9.0 Å) with D3, D4, and D5 symmetries, respectively, that depict hollow barrel-like structures made of ACD dimer units[160]. However, despite the imposed high-symmetry of these reconstructions, the low resolution achieved suggest underlying

structural heterogeneity that likely does not conform to a definable symmetric morphology. Regardless, these studies showcase the difficulties in defining molecular mechanisms of α-crystallin oligomerization and polydispersity.

Over the past ten years the field of CryoEM has undergone profound advances in image acquisition hardware, data collection strategies, and image analysis algorithms that have enabled routine determination of protein structures under near native conditions at high resolution (<3.5 Å), suitable for de novo atomic modeling[282,289]. Additionally, CryoEM has been effective at resolving heterogeneous and polydisperse assemblies by harnessing various classification techniques[4,290]. At the beginning of my PhD program, I set out to determine high resolution structures of heterologously expressed human αB-crystallin using modern techniques in CryoEM. Initial CryoEM datasets showed extreme heterogeneity in 2D classification (blurry and misaligned) and resulted in uninterpretable 3D reconstructions where half of the particle was low-resolution density, and the other half was noise. Despite significant efforts to improve the quality of the sample, size of the image dataset, and various methods for resolving heterogeneity by image processing, the resolution of these maps remained low, and classification attempts were not successful at isolating any definable state(s) (Figure 1a,b).

Using a published tetrahedral structure of the 24mer (PDB ID 2YGD) as an initial model, I was able to isolate a subset of particles (~27,000) that refined to ~6Å resolution with applied tetrahedral symmetry (i.e., using similar approach to previous studies) (Figure

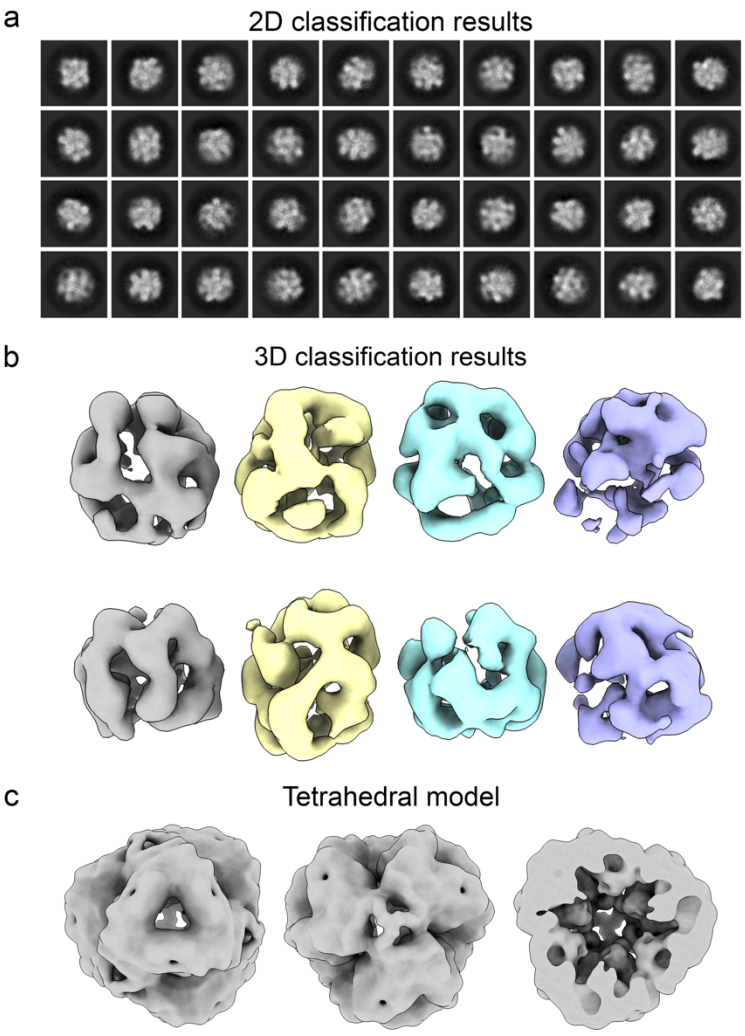

Figure 1: Single-particle CryoEM analysis of αB-crystallin (dataset #1): (a) Representative results from 2d classification of αB-crystallin (b) Four representative classes from heterogeneous refinement of αB-crystallin with 90° rotation (c) Reconstruction of αB-crystallin with imposed tetrahedral symmetry viewed from 3-fold window (left), 3-fold axis (middle) and cutaway view of central cavity (right)

1c). However, the region of the map corresponding to an ACD dimer was too small for a good fit. Overall, the results were deemed uninterpretable for pseudo-atomic modelling.

A second, larger dataset was collected in hopes that more data would help classify and align the multiple oligomeric states known to be present in the sample. Classification in 2D gave similar results to the first dataset (blurry and unaligned classes) (Figure 2a). Although 3D reconstruction results were somewhat improved compared to the first dataset with more diverse classes (Figure 2b), it was apparent that underlying heterogeneity and polydispersity of αB-crystallin was limiting image analysis, resulting in uninterpretable results. Tetrahedral symmetry was applied during 3D classification in hopes of isolating a sub-population of particles conforming to this symmetry. The resulting tetrahedral reconstructions (Figure 2c) share similar general

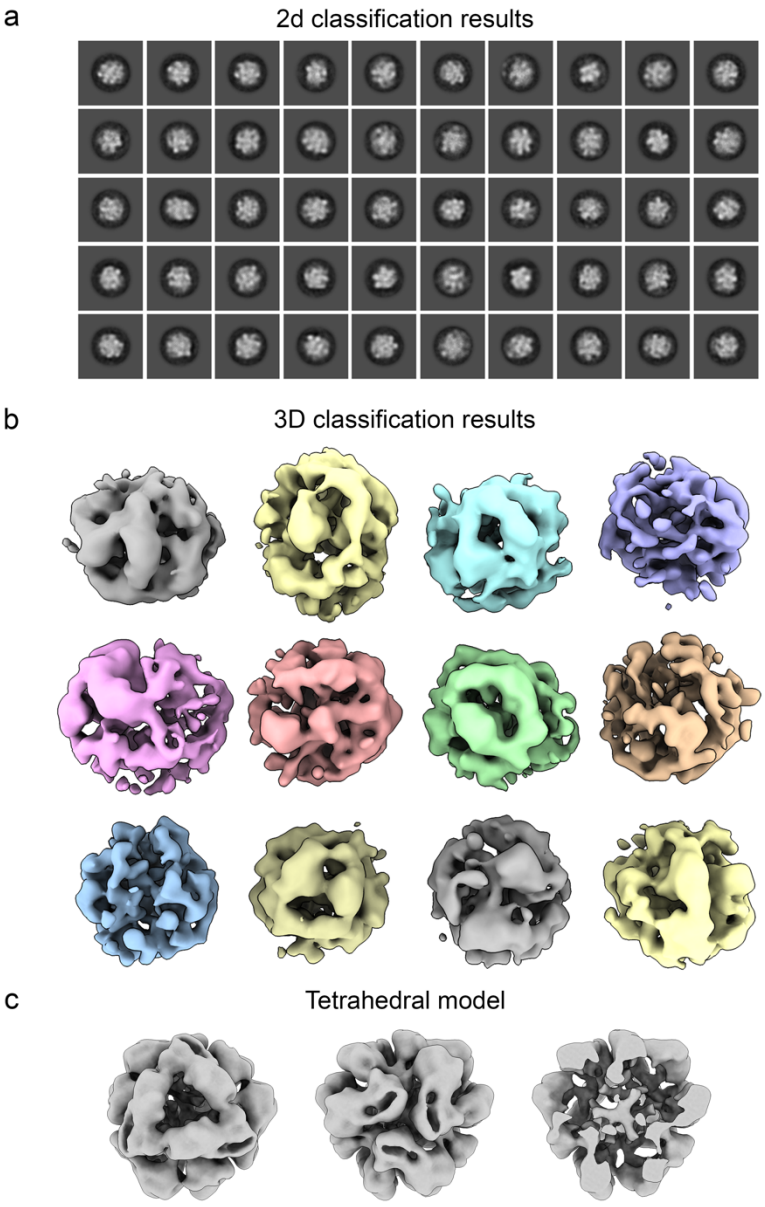

Figure 1: Single-particle CryoEM analysis of αB-crystallin (dataset #2): (a) Results from 2d classification of αB-crystallin (b) Twelve resulting classes from heterogeneous refinement of αB-crystallin (c) Reconstruction of αB-crystallin with imposed tetrahedral symmetry viewed from 3-fold window (left), 3-fold axis (middle) and cutaway view of central cavity (right)

features to previously proposed 24mer models (3-fold windows and axes). However, these reconstructions remained at low-resolution and the imposition of symmetry in attempt of "fishing out" a 24mer resulted in ambiguous and untrustworthy results that were deemed to be likely a result of overfitting and initial model bias[291,292].

A CryoEM dataset was also collected on heterologously expressed human αA-crystallin and resulted in similarly heterogeneous morphologies as judged by 2D and 3D classification results (data not shown). As performed with the αB-crystallin data, symmetries were imposed similar to those described for the published low-resolution models of αA-crystallin that were able to generate similar barrel-shaped cages at low resolution. However, again,

these results were also interpreted as potential overfitting and likely influenced by initial model bias.

For both the αA- and αB-crystallin datasets, multiple schemes of non-symmetric 3D classification and refinement were unable to uncover a sub-population of particles suitable for high-resolution characterization. For all datasets, image processing was primarily performed in both RELION and CryoSPARC with some analysis attempted in EMAN2 (2D classification) and cisTEM (2D and 3D classification)[246,273,293–295]. Results from EMAN and cisTEM are not discussed in detail, however they agree with results from RELION and CryoSPARC that extreme heterogeneity is a major limitation to analyzing these datasets.

Some details of the image processing strategies attempted in this work are briefly described below:

- 2D classification: Attempts to improve classification and alignment in 2D classification included varying the number of classes (50 – 300), adjusting alignment resolution (3 – 20 Å), and iterative sub-classification where similar sized classes were grouped and subsequently re-classified.
- 3D classification/Heterogeneous refinement and multi-class ab initio generation: Attempts to improve results in 3D classification were similar to those for 2D classification (variable number of classes, resolution limit adjustment, and sub-classification). Additional strategies included "spiking" initial classes with a tetrahedrally symmetric model to pull out a subset of symmetric particles (if they were in fact present), use of various symmetries (tetrahedral and octahedral for αBc; D3, D4, and D5 for αAc), lowpass filtering of initial models (12 – 80 Å), limiting final resolution (4 – 20 Å), adjustment of the T value in RELION processing, and including a noise map as one of the initial models to remove possible junk particles from the data.

- 3D refinement: Attempts to improve 3D refinement (symmetric and non-symmetric) included various static and dynamic masking, filtering and resolution limitations, and adjustment of T value in RELION. Additionally, I attempted various signal subtraction and local refinement strategies on sub-regions of non-symmetric maps with high density regions and the "hexameric" unit of the tetrahedral reconstructions (αBc datasets).

Table 1: Summary of data collection for single-particle CryoEM of two αB-crystallin datasets and one αA-crystallin dataset

	αBc dataset #1	αBc dataset #2	αAc dataset
Voltage	200	300	300
Electron exposure (e-/Å2)	50	50	50
Defocus range	0.8 – 2.5	0.5 – 1.8	0.5 – 1.8
Micrographs (No.)	1,717	3,015	10,332
Pixel size (Å/pixel)	1.1974	1.031	0.7984

Overall, the results of multiple CryoEM datasets of apo-state, unmodified αA- and αB-crystallin were insufficient in characterizing their polydisperse structures beyond the fact that there exists extreme structural heterogeneity in their oligomeric ensembles. These results imply the possibility of a full continuum of conformational (flexibility) and compositional heterogeneity (polydispersity) – questioning what an α-crystallin "structure" actually is!

Regardless, multiple tools exist that may improve sample homogeneity, albeit at the expense of functionally relevant structural dynamics. Some of these strategies are listed here (ordered according to increased difficulty of method) to guide future attempts at sample preparation of α-crystallins (and other polydisperse sHSPs) for single-particle

CryoEM analysis. Each of these strategies would benefit from larger datasets (5-10 million particles) to boost the signal of flexible and low-occupancy oligomeric states:

- *Incorporate novel image processing pipelines based on machine learning:* Multiple approaches to separating out heterogeneous CryoEM datasets have been put forward in recent years (CryoDRGN, e2gmm) which may prove useful in classifying α-crystallin particles[296–298]. Some limitations may arise from the need of a good initial model; however some *ab initio* methods are currently available in CryoDRGN.
- *Brute force method*: New schemes for collecting CryoEM data allow for fast acquisition and large resulting datasets. A major obstacle in CryoEM image analysis is overcoming the low signal to noise ratio of individual particle images. Collecting a sufficiently large dataset (possibly 10-20 million particles) could help by providing more raw data on the low-population states spread across the ensemble of oligomers. To overcome the large computational requirements needed for processing such a large dataset, the initial processing would need to be "chunked" into sub-groups and/or binned down to decrease raw image size. The early stages of classifying such a large dataset would benefit from binned data so the classification and alignment would focus on low resolution features defined by size and possible sub-oligomeric structures (i.e., dimers, hexamers).
- *Chemical and/or genetically encoded crosslinking*: Non-specific chemical crosslinkers of various lengths (glutaraldehyde, BS3, NHS) may help limit flexibility and improve resulting image classification and alignment of individual oligomeric states. Moreover, novel genetically encoded crosslinkers utilizing non-canonical amino acids may provide similar improvements while maintaining native-like interactions. For instance, the

photoactivatable p-benzoyl-L-phenylalanine (BPA) could be encoded in place of phenylalanine residues in the dynamic NTD to effectively capture "bound" conformations of this region and limit "transition" conformations where the NTD is transitioning between self-binding sites[299].

- *Crosslinking in combination with differential centrifugation*: There are a few modern approaches to combining chemical crosslinking (described above) with centrifugation to isolate heterogeneous morphologies suitable for high-resolution single-particle CryoEM analysis. These methods include GraFix and AgarFix which utilize a glycerol or agar gradient (respectively) centrifugation step to crosslink, separate, and isolate biomolecules[283,300]. Collecting multiple CryoEM datasets of various fractions from differential centrifugation could limit the amount of heterogeneity in each dataset to boost classification and alignment, while comparison across datasets may help characterize multiple oligomeric states.
- *Initial model generation from tomographic data*: The same sample grid used for collecting single-particle CryoEM data could be used for collection of cryoelectron tomography (CryoET) data to reconstruct low resolution initial models for single-particle analysis[301]. New strategies in CryoET data processing are capable of classifying heterogeneity of biomolecules, however there may be limitations in doing so for the α-crystallins due to the size of their complexes[286,293,302]. Additionally, this strategy would likely require a large amount of CryoET data collection and processing, which is not a minor task.

Methods

Sample preparation and data collection for single-particle CryoEM of αA-crystallin and αB-crystallin

Wildtype αA- and αB-crystallin were prepared as described in Chapter 2 of this dissertation. For CryoEM, 3 µL of sample (~1.1 mg/mL) was loaded onto freshly glow discharged (15 mA, 1 min) copper mesh EM grids (Quatifoil R1.2/1.3), blotted for 3 – 3.5 s and plunge frozen into liquid ethane. The first dataset of αBc was collected on a 200 kV Arctica (FEI/ThermoFisher) cryoelectron transmission microscope with a total dose of 50 $e^-/Å^2$ for a total of 1,717 micrographs at a pixel size of 1.1974 Å/pixel. The second dataset of αBc was collected on a 300 kV Titan Krios (FEI/ThermoFisher) cryoelectron transmission microscope with a total dose of 50 $e^-/Å^2$ for a total of 3,115 micrographs at a pixel size of 1.031 Å/pixel. The αAc dataset was collected on a 300 kV Titan Krios cryoelectron transmission microscope with a total dose of 50 $e^-/Å^2$ for a total of 10,332 micrographs at a pixel size of 0.7984 Å/pixel. All datasets were collected automatically after target picking in SerialEM[272].

Single-particle CryoEM image analysis of αAc and αBc datasets

For each dataset (αAc dataset and αBc datasets #1 and #2) image processing was primarily performed in RELION3[246,273,294,295] and CryoSPARC v2,3[273] (data shown in figures) with some 2D classification attempted and in EMAN2[246] and some 2D/3D classification attempted in cisTEM[295] (αBc dataset #1 only, data not shown). For the RELION workflow raw movies were aligned with motioncor2 and CTF estimation was done using GCTF. 2D classification, *ab initio* model generation, and 3D classification were done on binned particles (2x and 4x binning) with adjustment of the T parameter (2 – 75). For the CryoSPARC workflow movies were motion corrected and CTF estimation was done in

CryoSPARC (v2,3). All subsequent processing (2D classification, heterogeneous refinement, homogeneous/non-uniform refinement) was done on 2x or 4x binned particles. Additional processing in CryoSPARC included particle subtraction and local refinement of the tetrahedral particle stack (αBc dataset 2) and implementation of D3, D4, and D5 symmetries for the αAc dataset. Visualization of reconstructions was done in ChimeraX (v1.17)[275].

Appendix Chapter 2: Conserved and divergent features of neuronal CaMKII holoenzyme structure, function, and high-order assembly

Olivia R. Buonarati[1]*, Adam P. Miller[2]*, Steven J. Coultrap[1], K. Ulrich Bayer[1‡] and Steve L. Reichow[2‡§]

[1]Department of Pharmacology, University of Colorado Anschutz Medical Campus, Aurora, Colorado 80045; U.S.A.; [2]Department of Chemistry, Portland State University, Portland, Oregon 97201, U.S.A.

* equal contribution authors, listed in alphabetical order

[‡] Correspondence to ulli.bayer@cuanschutz.edu or reichow@pdx.edu

[§]Lead contact: Steve L. Reichow (reichow@pdx.edu)

Published in Cell Reports:

DOI: 10.1016/j.celrep.2021.110168

PMID: 34965414

PMCID: PMC8985225

SUMMARY:

Neuronal CaMKII holoenzymes (α- and β-isoforms) enable molecular signal computation underlying learning and memory, but also mediate excitotoxic neuronal death. Here, we provide a comparative analysis of these signaling devices, using single particle EM in combination with biochemical and live-cell imaging studies. In the basal state, both isoforms assembled mainly as 12-mers (but also 14-mers, and even 16-mers for the β-isoform). CaMKIIα and β-isoforms adopted an ensemble of extended activatable states (with average radius of 12.6 versus 16.8 nm, respectively), characterized by multiple transient intra- and inter-holoenzyme interactions associated with distinct functional properties. The extended state of CaMKIIβ allowed EM analysis to directly resolve intra-holoenzyme kinase-domain dimers that could enable the cooperative activation mechanism by calmodulin, which was found for both isoforms. Surprisingly, high-order CaMKII clustering mediated by inter-holoenzyme kinase-domain dimerization was reduced for the β isoform for both basal and excitotoxicity-induced clusters, both *in vitro* and in neurons.

Keywords: CaMKII; holoenzyme; structure; activation; autophosphorylation; clustering

INTRODUCTION

The Ca^{2+}/calmodulin(CaM)-dependent protein kinase II (CaMKII) is a major mediator of long-term plasticity at excitatory glutamatergic synapses in the hippocampus that is required for learning and memory[303–305]. Beyond these physiological functions, CaMKII also mediates the glutamate excitotoxicity that kills neurons during ischemia[306–308]. Both synaptic plasticity and excitotoxic cell death require the 12-meric CaMKII holoenzyme structure for at least two key regulatory functions: i) autophosphorylation at T286 (pT286)[307,309–311], which occurs between subunits within a holoenzyme[312] and enables detection of stimulation frequency[313]; and ii) binding to the NMDA-type glutamate receptor subunit GluN2B[314–316], which also requires the holoenzyme structure[317,318] and mediates CaMKII accumulation at synapses during LTP and excitotoxic insults[315,316,319]. Both pT286 and GluN2B binding require an initial stimulus by Ca^{2+}/CaM, but then maintain partial "autonomous" kinase activity even after Ca^{2+}/CaM has dissociated[303,319,320]. By contrast, the Ca^{2+}/CaM-induced clustering of multiple holoenzymes into higher order aggregates is thought to restrict kinase activity[321]. This aggregation requires ischemia-related conditions (such as low pH and higher ADP than ATP concentration) and mediates the extrasynaptic clustering in response to excitotoxic stimuli[321–324], but may contribute also to the synaptic accumulation in response to LTP stimuli[325].

Together, these holoenzyme functions are thought to provide essential mechanisms for information processing and storage[303,326,327]. Thus, elucidating the CaMKII holoenzyme structure that enables these mechanisms has been of long-standing interest, with the first electron microscopy (EM) studies performed over 30 years ago[328,329]. CaMKII holoenzymes are oligomeric assemblies, with each subunit containing an N-terminal kinase domain, followed by a variable internal linker region that connects to a C-terminal association (or hub) domain that is responsible for oligomerization. More recently, a high-resolution crystal structure showed the 12-meric holoenzyme in a compact conformation,

with the N-terminal kinase domains folding back onto the association domain that forms a central hub complex[330]. Notably, this compact conformation is not activation-competent (as the CaM binding regulatory region is buried), and transition between the compact and an extended conformation provided a potential regulatory mechanism for cooperative activation by CaM. However, subsequent studies indicated that the vast majority of kinase domains are in the activation-competent extended conformation (>95%), both *in vitro* and in intact cells[331,332], indicating that cooperativity must be mediated by a different mechanism.

To gain deeper insight into the conserved structural and functional features of CaMKII holoenzymes, we performed a comparative single-particle EM analysis to CaMKIIβ, the second most prevalent isoform in neurons[333–336]. As we have previously described for the α isoform[331], the association domains of the β isoform form a rigid central hub capable of adopting multiple stoichiometries, whereas their kinase domains where primarily extended away from the hub in an activation-competent and highly flexible manner (see Figure 1). Within the ensemble of conformational states detected by single particle analysis, our study revealed several intriguing similarities and differences between these isoforms, including formation of higher order holoenzyme clusters, which are thought to increase in response to ischemic or excitotoxic insults[323,324]. In addition, we found the first direct evidence for dimer formation between kinase domains of the same holoenzyme, a structural feature that can mediate the cooperative activation by CaM found here for both CaMKIIα and β isoforms. Thus, our analysis of CaMKIIβ revealed not only isoform-specific differences, but also generally conserved themes of CaMKII regulation that are facilitated by a dynamic ensemble of multiple transient interactions supported by the holoenzyme architecture.

RESULTS

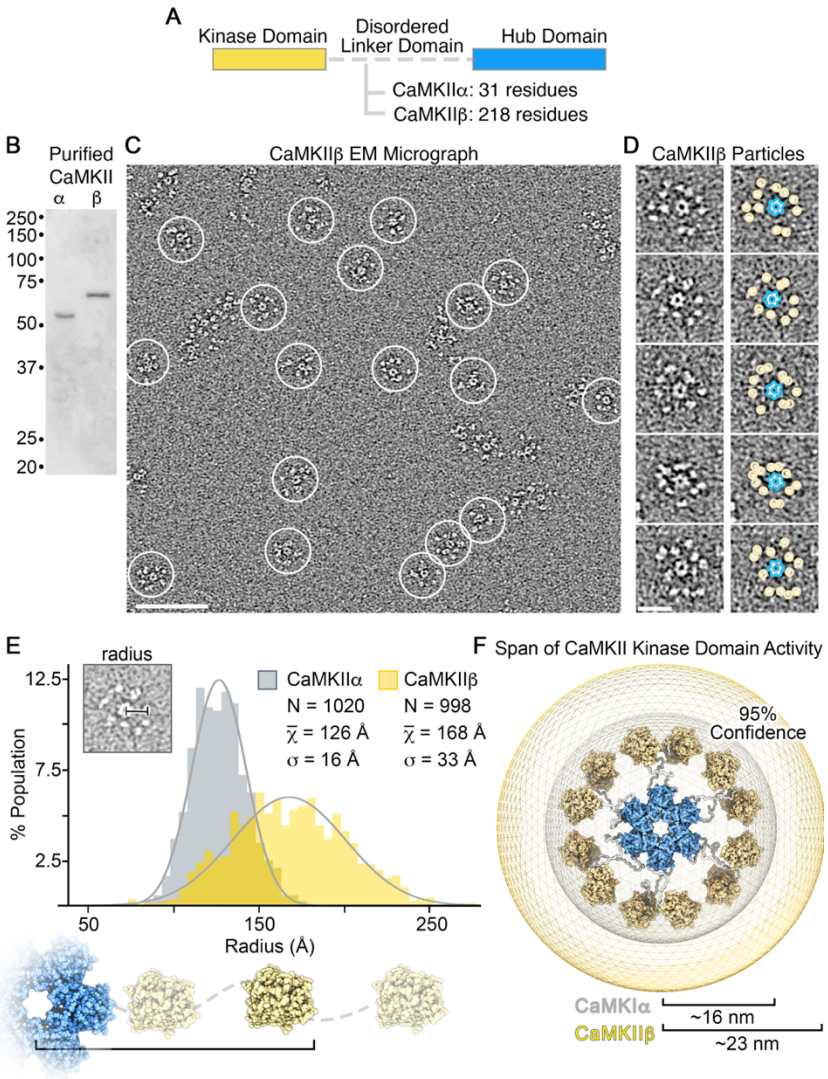

Figure 1: Comparative structural analysis of CaMKII holoenzymes resolved by single particle EM. (A) Diagram showing the major difference in CaMKIIα and CaMKIIβ domain architecture is within the length of their respective disordered linker domains. (B) SDS-PAGE gel showing full-length CaMKIIα and CaMKIIβ isoforms purified from S*f*9 cells migrate at the expected molecular weights and display no sign of proteolytic degradation. (C) Electron micrograph of negatively stained CaMKIIβ holoenzymes. Individual complexes are indicated by white

The dodecameric CaMKIIβ holoenzyme adopts an extended kinase radius

We have shown previously that the CaMKIIα holoenzyme adopts a predominant dodecameric (12-mer) assembly, with an extended and flexible activatable-state conformation as visualized by negative stain electron microscopy (NSEM)[331]. This 12-meric assembly is organized by a central and well-ordered hub domain complex, with 12 kinase domains displayed in an extended fashion via an intrinsically disordered flexible linker domain (Figure 1A). For comparative structural analysis, CaMKIIβ holoenzymes were expressed in eukaryotic cells (S*f*9), purified by chromatographic methods and prepared for NSEM using the same protocols previously described for CaMKIIα. Isolated holoenzymes show no signs of proteolytic degradation by SDS-PAGE (Figure 1B), and CaMKIIβ specimens produced

well-resolved assemblies resembling the same “flower-like” appearance of CaMKIIα holoenzyme structures observed by NSEM (Figure 1C,D). A defined central ring of density corresponding to the hub domain (~11 nm diameter) was clearly resolved, surrounded by an array of smaller densities, “the petals,” corresponding to tethered kinase domains (diameter ~5 nm) (Figure 1C,D). However, despite an overall structural similarity, the peripheral kinase domains associated with CaMKIIβ holoenzymes were qualitatively more extended and heterogeneously configured around the hub domain, as compared to CaMKIIα holoenzymes. Although the disordered linker domain is not resolvable by NSEM, these differences are consistent with the primary divergence in amino acid sequence between CaMKII isoforms, where in CaMKIIβ the linker domain is ~92 residues long (as compared to ~31 residue linker in CaMKIIα)[335,336] (Figure 1A).

For both CaMKIIα and β, the flexible linker region facilitates the formation of a variety (or continuum) of conformational states that are not directly amenable to traditional EM image classification and averaging methods. Therefore, for quantitative characterization and comparative analysis between holoenzyme structures, we took advantage of the high-contrast of NSEM imaging to conduct a series of measurements and statistical analyses conducted directly on individual holoenzyme particle images obtained from raw micrographs[331] (Figure 1D,E). In the first set of measurements, the radial extension for each kinase domain (*i.e.,* kinase radius) was obtained by measuring from the center of the hub complex to the center of each kinase domain, and this measurement was then appended by 2.25 nm to account for the approximate radius of the kinase domain (Figure 1E,F). For both isoforms, the distribution of kinase domain radii obtained from ~1000 particle measurements for each isoform appears randomly positioned with apparent gaussian distribution (Figure 1E). However, the average kinase radius of CaMKIIβ is significantly larger at ~16.8 nm (± 0.1 SEM) as compared to CaMKIIα assemblies ~12.6 nm (± 0.05 SEM) ($P < 0.001$). Since the linker domain is not directly

visible by NSEM, the edge-to-edge distance separating the kinase domain and hub domain may be used as an approximation of the linker extension of ~2.7 nm for CaMKIIα and ~6.8 nm for β. These values are consistent with random chain polymer models (traditional random walk model) based on the differences in amino acid lengths of the respective linker domains[337], and further support the idea that CaMKII kinase domains are freely tethered to the central hub domain by intrinsically disordered linker regions. Based on these measurements, a 95% confidence of kinase domain positioning can be expected to span a radius of up to ~16 nm for CaMKIIα holoenzymes and up to ~23 nm for β holoenzymes (Figure 1F).

CaMKII holoenzymes can adopt a 'compact state' involving kinase-hub domain interaction, but only a minor fraction of CaMKIIα holoenzymes was found in this conformation[330–332]. From our analysis in Figure 1E, a kinase domain radius measured less than ~10 nm would potentially place a kinase domain in steric contact with the central hub complex. Consistent with our previous analysis, CaMKIIα holoenzymes showed only a small fraction of individual subunits with kinase domain radii that fall within this category (~3% of kinase domains with radius < 10 nm[331] and Figure 1E). In comparison, CaMKIIβ displayed less than 1% of kinase domains with radius < 10 nm observed by NSEM (Figure 1E), indicating that a 'compact state' is at most only sparsely populated.

Autophosphorylation of pT286 in CaMKIIα versus pT287 in CaMKIIβ

The extended radius of the CaMKIIβ compared to the α holoenzyme would lead to a lower local concentration of kinase domains within the space occupied by a holoenzyme, based on simple geometric considerations (~1.0 mM versus ~2.3 mM; see Figure S1). Thus, we decided to directly compare CaMKIIα versus β purified holoenzymes for autophosphorylation at T286 (in α) or T287 (in β), which occurs as an inter-subunit intra-holoenzyme reaction[312,338,339]. *In vitro* kinase stimulation with Ca^{2+}/CaM resulted fast

autophosphorylation for both CaMKIIα and β, with no significant differences between T286 and T287 detected throughout the reaction time-course (Figure S1). Taken together, these results indicate that the significant difference in the proximity of kinase domains in CaMKIIβ versus CaMKIIα does not significantly affect autophosphorylation kinetics of the holoenzymes.

CaMKIIβ forms multimeric assemblies of 12 – 16-mers

Early EM studies had already indicated that CaMKIIα forms mainly 12-mers, but some studies suggested a smaller number of subunits, particularly for the β isoform[328,329]. Thus, we decided to further compare the stoichiometry of CaMKIIα versus β holoenzymes, by quantifying the symmetry of their hub domain assemblies. We performed focused 2D image classification on the NSEM datasets for both isoforms by applying a circular mask

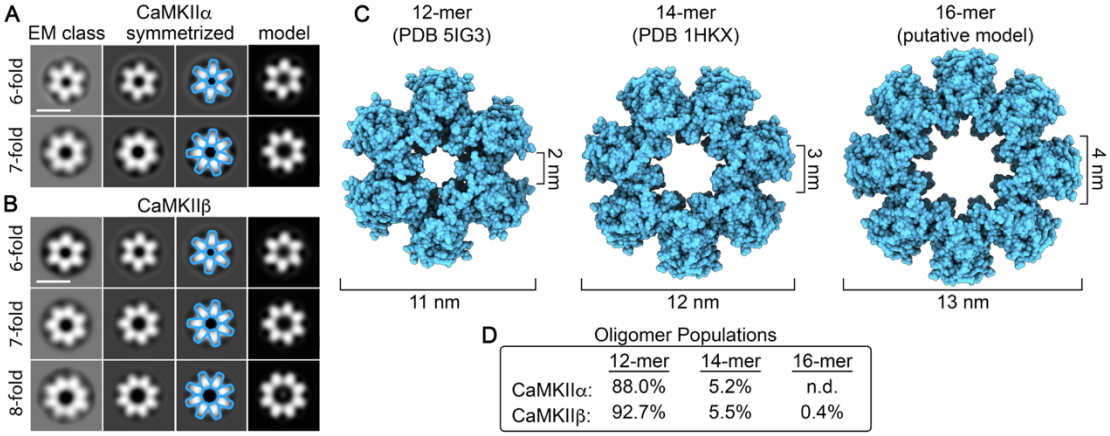

Figure 2: Comparative analysis of CaMKII holoenzyme stoichiometries resolved by single particle EM. (A and B) Single particle EM image classification and analysis of the central hub domain of CaMKIIα and CaMKIIβ holoenzymes, respectively. *Left*, Focused EM class averages obtained using an applied image mask (15 nm outer diameter) and without applied symmetry. *Middle left and right*, display symmetrized versions of the EM classes as indicated and with resolved features annotated (blue outline). *Right*, displays 2D back-projections from atomic models of hub assemblies displayed in panel (C), filtered to 30 Å. Scale bar = 10 nm. (C) *Left*, atomic model of a dodecameric (12-mer) hub domain (blue surface representation, PDBID 5IG3 (Bhattacharyya et al., 2016), *center*, heptadecameric (14-mer) hub domain (PDBID 1HKX (Hoelz et al., 2003), and *right*, pseudo-atomic model of the putative hexadecameric (16-mer) hub domain resolved in panel A. (D) Population of CaMKII holoenzyme stoichiometries resolved by single particle EM. For the CaMKIIα dataset n=10,902 and for the CaMKIIβ dataset n=17,347. The 16-mer was not detected (n.d.) in the smaller CaMKIIα image dataset.

to remove signal from the peripheral kinase domains and focus the image alignment procedures on the central hub domain (Figure 2A,B). The results of this analysis showed a predominance of particles displaying 6-fold radial symmetry, with dimensions and structural features matching 2D-projections the dodecameric (12-mer) hub assembly, representing 88% of the population for CaMKIIα and ~92.7% for β (Figure 2A–D). For both isoforms, a smaller but significant population of hub domains displaying 7-fold radial symmetry were also observed, corresponding to ~5.2% of the population for CaMKIIα and ~5.5% for β holoenzymes (Figure 2A–D). The dimensions of 7-fold symmetric hubs class averages were also consistent with 2D-projections of a previously published crystallographic model of an isolated tetradecameric (14-mer) hub assembly[340] (Figure 2A–C).

Remarkably, an additional minor population of hub domain structures was detected with clear 8-fold symmetry in the CaMKIIβ image dataset, constituting ~0.4% of the population (Figure 2B–D). The dimensions of the detected 16-mer hub are ~13 nm in outer diameter and central pore measuring ~4 nm in diameter (Figure 2B). Pseudo-atomic modeling of hub domain subunits, restricted by the dimensions of the 8-fold symmetric projection average, show a reasonable fit, with minimal steric overlap between neighboring subunits, resulting in a putative hexadecameric (16-mer) hub model (Figure 2C). This putative model produces 2D back-projections matching the experimental density (Figure 2B). 16-mer assemblies were not detected in the CaMKIIα dataset. However, given the small population of 16-mers observed for CaMKIIβ, it is possible that this species was simply not detectable by image classification due to the significantly smaller image dataset obtained for CaMKIIα. Nevertheless, inherent differences between isoforms cannot be ruled out.

It is also noteworthy that smaller assemblies (*e.g.,* 8 – 10mers) were not detected in either dataset. Given the ability of our focused image classification approach to detect

populations that represent < 1% of species present, it is likely that the CaMKII hub domain is not capable of supporting such configurations under basal-state conditions (at least to any appreciable degree).

Resolution of kinase-domain dimers within intact CaMKIIβ holoenzymes

Kinase-kinase domain pairing interactions have been proposed as a potential mechanism for CaMKII cooperative activation by Ca^{2+}/CaM. Indeed, such dimers have been observed in crystals of the kinase domain[341], however, they have not yet been directly detected in context of the intact holoenzyme. To assess for the presence of kinase domain dimerization in the context of CaMKII holoenzymes, the separation distance (center-to-center) between nearest neighbor kinase domains were measured on individual particle EM images (Figure 3A). For CaMKIIα holoenzymes, the average separation distance was 5.9 nm (± 0.05 SEM), with a near gaussian distribution (Figure 3A, grey). This value is consistent with our previous analysis and with solution-state FRET studies conducted on CaMKIIα holoenzymes[331,342], and indicates that the majority of kinase domains are non-interacting[331]. However, an appreciable fraction of kinase separation distances (~19%) measured less than 4.5 nm, the distance we had previously assigned as the cut-off for potential kinase domain pairing within the context of the holoenzyme[331]. The cut-off distance was based on the 2–3 nm radius of a kinase domain and represents a compromise in stringency: There is a potential for dimers that appear to exceed this 4.5 nm distance, but not all kinase domain pairs within this distance are likely to represent bona fide dimers. For CaMKIIβ holoenzymes, the average kinase separation distance is significantly larger 9.4 nm (± 0.2 SEM) (Figure 3A, yellow), presumably facilitated by the longer linker domain. Notably, the distribution is skewed from a random gaussian

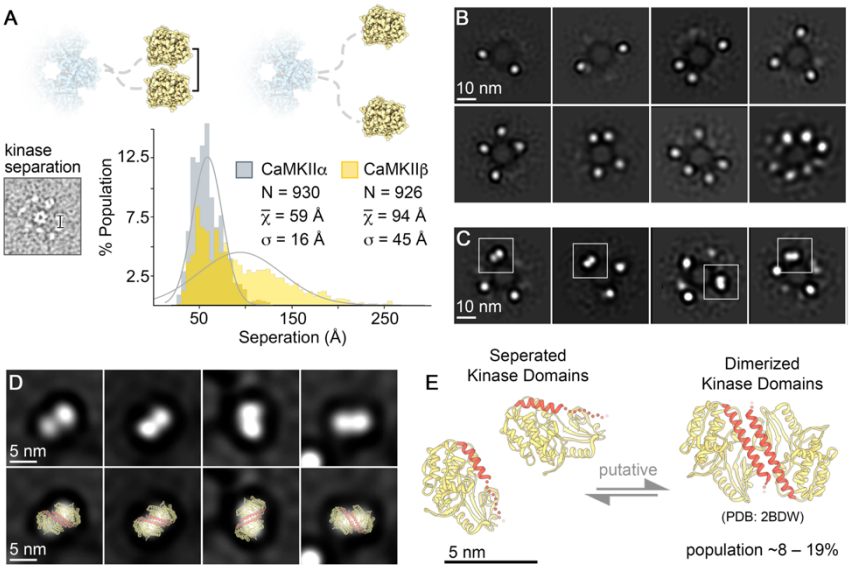

Figure 3: Kinase domain dimers resolved in the CaMKIIβ by single particle EM. (A) Histogram of measured distance separating neighboring kinase domains (center-to-center) obtained for CaMKIIα (grey, n=930) and CaMKIIβ (yellow, n=926) particles, bin = 5 Å. Grey lines represent a gaussian fit to the data. *Inset*, illustrating distances were obtained from raw particle images in EM micrographs. (B and C) Single particle EM image classification and analysis of CaMKIIβ holoenzymes with an applied mask to remove contribution of the hub domain during the alignment procedure (13.5 nm diameter). Panel (B), isolated kinase domains appear as punctate densities of ~4–5 nm in diameter. Only a subset of all 12 kinase domains could be resolved in class averages (typically 2 to ~7), due to spatial heterogeneity of kinase domain positions present within the population of CaMKIIβ holoenzymes. Panel (C), class averages displaying additionally resolve bilobed densities with approximate dimensions of ~10 x 5 nm (indicated by white squares). Scale bar = 10 nm in panels A and B. (D) *Top row,* zoom view of bilobed densities resolved in class averages in panel c, and *bottom row*, with fitted crystallographic structure of the *C. elegans* CaMKIIα kinase/regulatory domain (yellow/red ribbon; PDBID 2BDW (Rosenberg et al., 2005) previously shown to form a dimeric interface involving the regulatory domain (red). (E) Putative model depicting an equilibrium of states involving independent kinase domains (PDBID 2VZ6 (Rellos et al., 2010) and kinase domain dimer (PDBID 2BDW (Rosenberg et al., 2005)) proposed to be present in the context of the CaMKII holoenzyme. The regulatory domain (red) in the dimerized state becomes more ordered and occluded from CaM binding. Scale bar = 5 nm in panels C and D.

distribution, toward shorter separation distances, with the most populated distance bin of 4.5 – 5.0 nm (Figure 3A). The deviation from random distribution toward shorter separation distances may reflect intrinsic interactions between neighboring kinase domains. The fraction of CaMKIIβ kinase domain pairs within 5 nm distance was 15%; the fraction within the maximally possible interaction distance of 6 nm was 28%; and within our original more stringent 4.5 nm cut-off was 8%. While these data are consistent with the majority of kinase domains adopting a non-interacting configuration, a significant fraction of CaMKIIβ kinase domains are localized within the potential steric contact distance, indicating that kinase-domain pairing may represent a significant population of both CaMKIIα and β holoenzyme structures.

To further support this evaluation, we conducted focused 2D image classification on CaMKIIβ kinase domains, this time by masking away the central density of the hub domain prior to image alignment (Figure 3B,C). The results of this analysis produced two distinct groups of 2D class averages. The first group appears to resolve isolated densities of ~4–5 nm diameter, corresponding to a subset of the individual kinase domains belonging to a single holoenzyme (Figure 3B). Notably, all 12 kinase domains were not completely resolved in any of these 2D class averages obtained from CaMKIIβ holoenzymes, due to the continuum of kinase domain configurations supported by the extended linker region. In the second group of 2D class averages displayed in Figure 3C, larger elongated densities of ~10 x 5 nm are resolved in addition to the ~4–5 nm individual kinase domain densities. These larger densities have a distinct bi-lobed appearance and dimensions consistent with the crystalized kinase domain dimer structure (Figure 3D,E)[341]. For CaMKIIα, apparent kinase domain dimers were previously resolved in individual particle images[331]; however, such structures could not be resolved by 2D classification procedures. We attribute this to limitations associated with local crowding of neighboring kinase domains present in this isoform which could interfere with image classification. Taken together, these data support the notion that CaMKII kinase domains are capable of forming dimers within the context of the holoenzyme assembly in both CaMKIIα and CaMKIIβ isoforms and may represent ~8–28% of kinase domains organized by the CaMKII holoenzyme structure (Figure 3E).

CaMKIIα and β differ in CaM activation constant but not in activation cooperativity

The kinase domain dimers that were found previously in a crystal of the kinase domain[341], and potentially here in context of the holoenzyme (see Figure 3), are formed by low-affinity coiled-coil interactions between two regulatory domains; then binding of Ca^{2+}/CaM to one regulatory domain would disrupt the interaction and thereby facilitate binding also to the

other regulatory domain. This could explain the cooperative activation of CaMKII by CaM[330,331]. To directly compare CaM activation of CaMKIIα versus β purified holoenzymes, we used our established kinase activity assay that measures phosphorylation of the peptide substrate syntide-2[343,344]. Consistent with previous reports[313,345], CaMKIIβ was more sensitive to Ca^{2+}/CaM-stimulation than CaMKIIα (EC50 of 15 nM compared to 30 nM; Figure 3F, 3G and Figure S2). However, the Hill slope was indistinguishable between the isoforms and was determined to be ~1.6 for both (Figure 3H and Figure S2). Such Hill slopes between 1 and 2 are consistent with dimer formation of some but not all kinase domains within a holoenzyme, and would indicate that dimer formation is equal between α and β. Indeed, even though the dimer structure was resolved in 2D average classes only for CaMKIIβ but not α (see Figure 3 and Myers, et al.[331]), the percentage of kinase domains that are close enough for potential dimer formation are comparable for both α and β isoforms (19% and 8–28%, respectively), and arguably within the degree of uncertainty based on the limitations of our approach (see Discussion).

CaMKIIα and β form higher order holoenzyme clusters both *in vitro* and in neurons

Whereas kinase domain-dimers within a holoenzyme may contribute to cooperative CaMKII activation, an inter-holoenzyme kinase domain-dimer formation is thought to mediate higher order clustering of CaMKII holoenzymes (although the proposed dimerization mechanisms differ)[323,324]. Some clustering can occur basally in neurons and small clusters were also observed on our EM grids, with ~56–58% of holoenzymes potentially interacting to form holoenzyme pairs and/or higher-order clusters (Figure S3). However, clustering at extrasynaptic sites is majorly enhanced by ischemic conditions[322,324,325]. Additionally, clustering may contribute to the CaMKII accumulation at excitatory spine synapses during both LTP and ischemia[325], although CaMKII binding to GluN2B is at least a co-requirement for both[315,316,319]. CaMKIIβ has been described to be

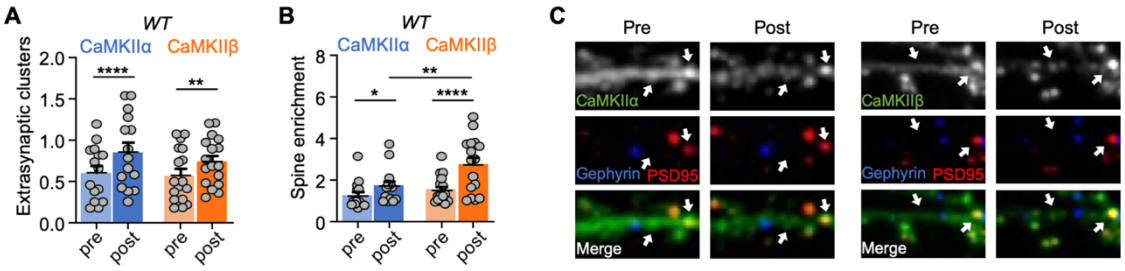

Figure 4: Clustering of CaMKIIα and CaMKIIβ induced by prolonged glutamate in wild-type neurons. Quantifications show mean + SEM. *p<0.05, **p<0.01, ****p<0.0001. (A) Quantification of extra-synaptic clusters induced by excitotoxic glutamate (100 µM glutamate, 5 min) in WT cultured hippocampal neurons (DIV 15-17) (two-way repeated-measures ANOVA, Bonferroni's test: ****p<0.0001 for CaMKIIα pre vs. post, n=15; **p=0.0049 for CaMKIIβ pre vs. post, n=17). (B) Quantification of excitatory synapse enrichment induced by excitotoxic glutamate (100 µM glutamate, 5 min) in WT cultured hippocampal neurons (DIV 15-17) (two-way repeated-measures ANOVA, Bonferroni's test: *p=0.0457 for CaMKIIα pre vs. post, n=14; **p<0.0001 for CaMKIIβ pre vs. post, n=16; **p=0.0078 for post CaMKIIα vs. post CaMKIIβ). (C) Representative confocal images show overexpressed CaMKIIα (left) or CaMKIIβ (right), endogenous PSD95 (in red) to mark excitatory synapses, and endogenous gephyrin (in blue) to mark inhibitory synapses.

incompetent for the ischemia-related clustering (at least *in vitro*[323]), but seemed to form at least some basal clusters (see Figure S3). Thus, we decided to directly compare the clustering of CaMKIIα versus β in dissociated hippocampal neurons. For live-imaging of synaptic versus extrasynaptic clustering, synapses were identified by expressing intrabodies against the synaptic marker proteins PSD95 and gephyrin, to simultaneously label excitatory and inhibitory synapses, as we have described recently[315,346]; the YFP-tagged CaMKII isoforms were expressed to visualize clustering before and after excitotoxic glutamate insults (100 µM for 5 min). CaMKII clusters were detected extrasynaptically, both basally and after stimulation (Figure 4). For both isoforms, excitotoxic stimulation significantly increased extrasynaptic clustering (Figure 4A,C) and enrichment at excitatory synapses (Figure 4B,C). As previously described for the α isoform[315], no clustering at inhibitory synapses was observed for CaMKIIβ (Figure S4).

Homomeric CaMKIIβ holoenzymes show less propensity for higher order clustering

Somewhat surprisingly, CaMKIIα and β showed the same level of extrasynaptic clustering in hippocampal neurons (Figure 4), even though CaMKIIβ has been described to be incompetent for ischemia-related clustering *in vitro*[323]. Thus, we decided to compare these isoforms also in our *in vitro* clustering assay. Ischemic conditions were mimicked by addition of Ca^{2+}/CaM and ADP at a low pH of 6.5; then cluster formation was assessed by differential centrifugation[324]. While some amount of both CaMKIIα and β was detected in the 16,000*xg* pellet under basal conditions, this amount dramatically increased under ischemic conditions only for CaMKIIα but not β (Figure 5A,B). The CaMKIIβ isoform appeared to show some minor increase in clustering, but this was not significant. By contrast, in 100,000*x g* pellets, both isoforms showed a significant increase in precipitation under ischemic conditions (Fig 5C,D). Nonetheless, the induced precipitation of CaMKIIβ was

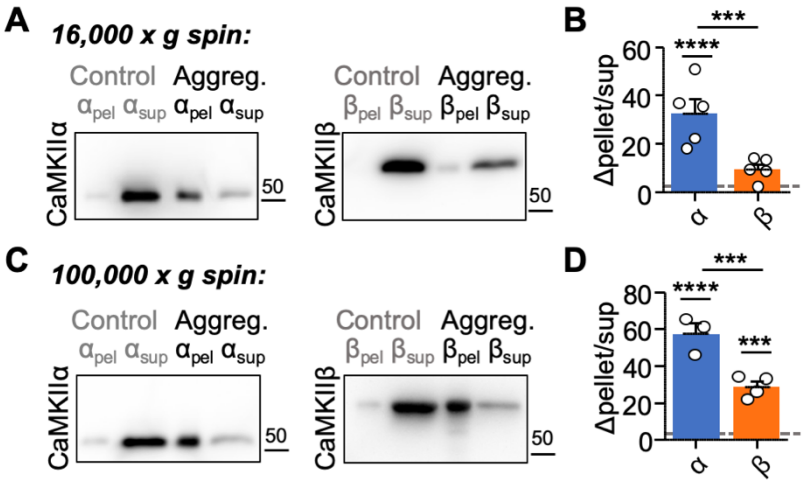

Figure 5: CaMKIIβ self-aggregates less than CaMKIIα *in vitro*. Quantifications show mean ± SEM. ***p<0.001. (A) Representative immunoblots for CaMKIIα and CaMKIIβ. Aggregates were detected in 16,000x*g* pellets following incubation in 2 mM Ca^{2+}, 1 µM CaM, and 1 mM ADP at low pH (6.4) for 5 min at room-temperature. Control samples were incubated in 50 mM EGTA at pH 7.4. (B) Quantification of change in pellet enrichment (control samples normalized to 1). Only CaMKIIα showed significant clustering under aggregation conditions, compared to control (two-way ANOVA, Bonferroni's test: ****p<0.0001 for CaMKIIα). CaMKIIβ shows significantly less self-aggregation compared to CaMKIIα (two-way ANOVA, Bonferroni's test: ***p=0.0004). (C) Representative immunoblots for CaMKIIα and CaMKIIβ. Aggregates were detected in 100,000x*g* pellets following incubation in 2 mM Ca^{2+}, 1 µM CaM, and 1 mM ADP at low pH (6.4) for 5 min at room-temperature. Control samples were incubated in 50 mM EGTA at pH 7.4. (D) Quantification of change in pellet enrichment (control samples normalized to 1). Both CaMKIIα and CaMKIIβ showed significant clustering under aggregation conditions, compared to control (two-way ANOVA, Bonferroni's test: ****p<0.0001 for CaMKIIα; ***p=0.0004 for CaMKIIβ). Furthermore, CaMKIIβ shows greater self-aggregation in 100,000x*g* pellets compared to 16,000x*g* pellets (two-way ANOVA, Bonferroni's test: ****p<0.0001). However, CaMKIIβ still shows significantly lower self-aggregation than CaMKIIα even after 100,000x*g* (two-way ANOVA; Bonferroni's test: ***p=0.0003).

significantly less than that of CaMKIIα after either centrifugation speed (Figure 5B,D). These results suggest that both isoforms can cluster *in vitro*, but that CaMKIIβ forms less and/or smaller-sized clusters than the α isoform.

Then why was clustering of CaMKIIα and β indistinguishable in WT neurons? One possibility was that CaMKIIβ might efficiently co-cluster with endogenous CaMKIIα. Thus, we decided to test if mixing CaMKIIβ with CaMKIIα can lead to detection of significant CaMKIIβ clustering even at the lower centrifugation speed. When mixed at equal amounts (0.25 μM each, to total CaMKII concentration of 0.5 μM used in the other *in vitro* experiments), no significant CaMKIIβ co-clustering was detected (Figure 5E,F). However, significant co-clustering of CaMKIIβ was detected when CaMKII concentration was increased with an excess of CaMKIIα (1.5 μM) over CaMKIIβ (0.5 μM), an isoform ratio similar as found in neurons (Figure 5G,H). Under these conditions, CaMKIIα still appeared to precipitate more than CaMKIIβ, however, this apparent difference was not statistically significant (p=0.053). When the isoforms were instead co-expressed (in order to allow

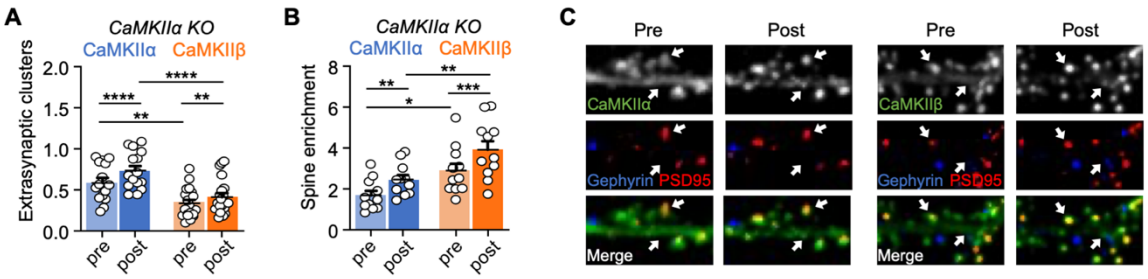

Figure 6: Clustering of CaMKIIα and CaMKIIβ induced by prolonged glutamate in CaMKIIα KO neurons. Error bars indicate SEM in all panels. **p<0.01, ****p<0.0001. (A) Quantification of extra-synaptic clusters induced by excitotoxic glutamate (100 μM glutamate, 5 min) in CaMKIIα KO cultured hippocampal neurons (DIV 15-17) (two-way repeated-measures ANOVA, Bonferroni's test: ****p<0.0001 for CaMKIIα pre vs. post, n=15; **p=0.0021 for CaMKIIβ pre vs. post, n=20; **p=0.0019 for pre CaMKIIα vs. pre CaMKIIβ; ****p<0.0001 for post CaMKIIα vs. post CaMKIIβ). (B) Quantification of excitatory synapse enrichment induced by excitotoxic glutamate (100 μM glutamate, 5 min) in CaMKIIα KO cultured hippocampal neurons (DIV 15-17) (two-way repeated-measures ANOVA, Bonferroni's test: **p=0.0025 for CaMKIIα pre vs. post, n=11; ****p<0.0001 for CaMKIIβ pre vs. post, n=11; *p=0.0242 for pre CaMKIIα vs. pre CaMKIIβ **p=0.0051 for post CaMKIIα vs. post CaMKIIβ). (C) Representative confocal images show overexpressed CaMKIIα (left) or CaMKIIβ (right), endogenous PSD95 (in red) to mark excitatory synapses, and endogenous gephyrin (in blue) to mark inhibitory synapses.

formation of heteromeric holoenzymes), both isoforms precipitated significantly and to an equal extent, as expected (Figure S5).

In order to further test the possibility that CaMKIIβ co-clusters with CaMKIIα in neurons, the clustering experiments were repeated in neurons cultured from CaMKIIα KO mice. In the absence of endogenous CaMKIIα, YFP-CaMKIIβ still clustered both basally and after excitotoxic glutamate insults, but to a significantly lesser extent than YFP-CaMKIIα (Figure 6 and Figure S6). Furthermore, the extrasynaptic CaMKIIβ clustering was significantly lower in the CaMKIIα KO neurons compared to WT neurons (Figure S6H). By contrast, in dendritic spines the basal enrichment of CaMKIIβ, but not CaMKIIα, was higher in the CaMKIIα KO neurons compared to WT neurons (see Figure S6E,F). This could be an indirect effect of the lower extrasynaptic clustering, or it might be caused more directly by the preferential interaction of CaMKIIβ with F-actin, which is enriched in dendritic spines[347–350].

Together, our *in vitro* experiments with purified protein and our imaging experiments in neurons show that CaMKIIβ can form clusters also on its own, but to a significantly lesser extent than the CaMKIIα isoform.

DISCUSSION

Our comparative structure-function analysis of the CaMKIIα and β holoenzymes revealed notable distinctions between these two major neuronal isoforms, including both expected and unexpected structural differences. Perhaps more importantly, it also revealed common structural features of CaMKII that are applicable to the regulation of both isoforms. Specifically, these include a highly dynamic activatable-state conformation, the ability to adopt several oligomeric assemblies (mainly 12-mers, but also 14- and 16-meric holoenzymes) as well as high-order clusters of holoenzymes, and the detection of kinase domain dimer interactions within CaMKIIβ holoenzymes, a mechanism that could mediate

the cooperative activation by CaM for all CaMKII isoforms (see Figure 7). As delineated below, these findings provided both answers and new questions.

Holoenzyme expansion and autophosphorylation kinetics

The most obvious difference between the CaMKIIα and β holoenzyme was in their radius of expansion, both in their average radius (12.6 vs 16.8 nm) and in their maximal radius (16 vs 23 nm). This difference appears to be also the most predictable one, based on the different lengths of their variable linker regions that tethers the kinase domains to the hub formed by the association domains. Based on the average holoenzyme radii, we calculated a local concentration of kinases domains, within the space occupied by a holoenzyme, to be 2 mM for CaMKIIα and 1 mM for β. However, there was no apparent difference in

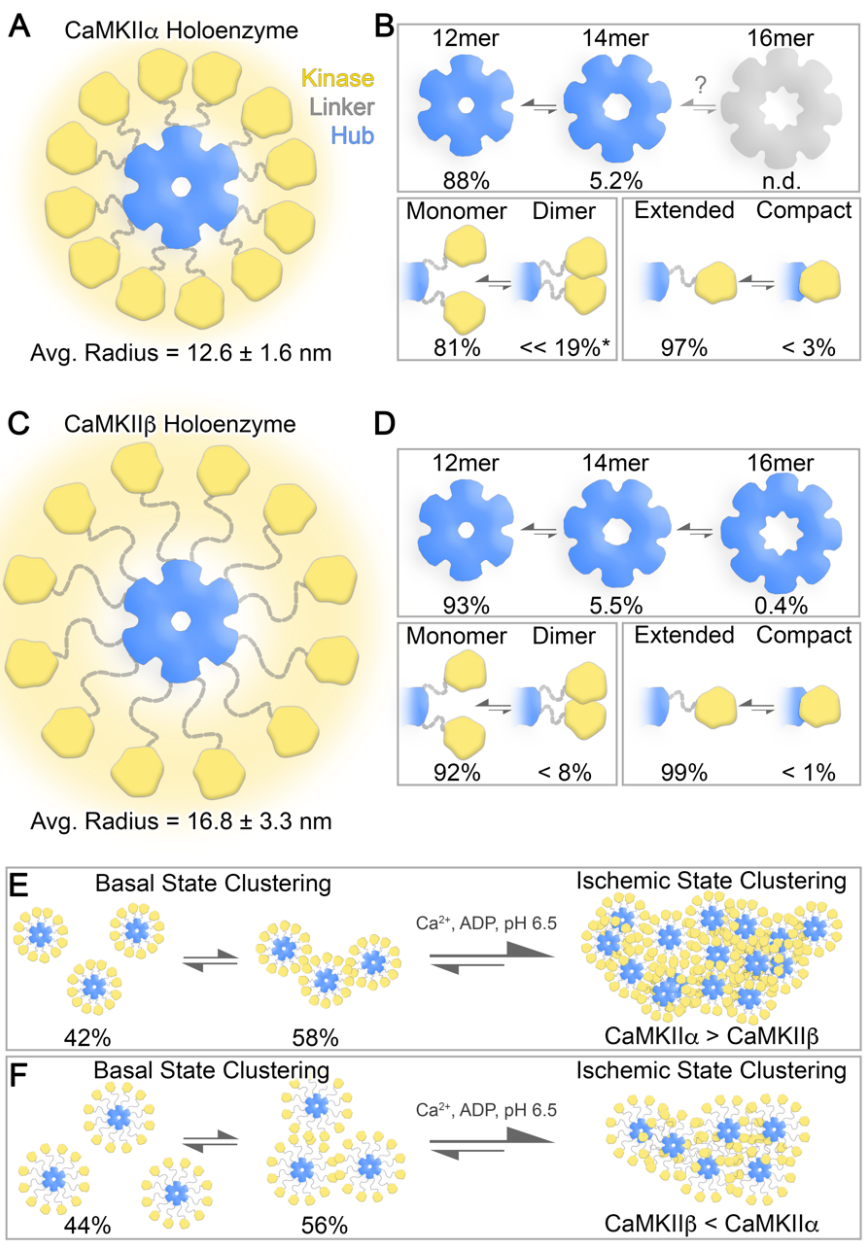

Figure 7: Overview of structural states supported by CaMKII holoenzymes under basal and ischemic conditions. (A) Illustration of the 12-meric CaMKIIα holoenzyme under basal conditions, where a flexible linker region (grey) supports a continuum of extended configurations of kinase domains (yellow) with an average radius of 12.6 ± 1.6 nm (SEM), from the center of the hub domain (blue). The halo of yellow density represents the variability in kinase domain positioning observed at the single particle level.(B) *Top,* Oligomeric states of the hub domain resolved by single particle EM, with the 12-mer most populated (88%), followed by the 14-mer (5.2%) and the 16-mer was not detected (n.d.). *Bottom Left,* Kinase domains where predominantly resolved as monomers (81%), with a significant population resolved as putative dimers (<< 19%*). Asterisk indicates that this value is likely over estimated due to artifacts associated with local crowding in the CaMKIIα isoform (see main text). *Bottom Right,* The majority of kinase domains were resolved in an extended state (97%), with a small subset of subunits were localized within contact distance of the hub domain, consistent with a compact state (< 3%). (C) The 12-meric CaMKIIβ holoenzyme, displayed as in panel A, supported a significantly larger extension of kinase domain configurations under basal conditions, as compared to CaMKIIα, with an average radius of 16.8 ± 3.3 nm (SEM) facilitated by the longer linker region. (D) *Top,* CaMKIIβ hub domains were resolved predominantly as 12-mers (93%), followed by a 14-mers (5.5%), as well as a novel 16-meric state (0.4%). *Bottom Left,* Kinase domains where also predominantly resolved as monomers (92%), with a significant population resolved as putative dimers (< 8%), (*Bottom Right)* while the compact state is consistent with only < 1% of the population of subunits. (E and F) Illustrate high-order clustering of holoenzymes detected under basal and ischemic conditions for CaMKIIα (E) and CaMKIIβ (F). Under basal conditions, both isoforms form small clusters or pairs of holoenzymes mediated by kinase domain interactions (58% for CaMKIIα and 56% for CaMKIIβ). Under ischemic conditions induced in cells or in vitro, there is a shift in the equilibrium toward higher-order clusters, where CaMKIIα clustering was found to be significantly greater than for CaMKIIβ.

the kinetics of the regulatory T286/T287 autophosphorylation that occurs between the subunits of a holoenzyme. While this result seemed counterintuitive at first glance, (i) it is predicted by simple Michaelis-Menten kinetics[351], although (ii) simple Michaelis-Menten kinetics should not necessarily be expected for this autophosphorylation reaction. When T286 is presented as an exogenous substrate on a peptide, its K_m is ~10 μM[344]; with this K_m and with 2 versus 1 mM substrate concentration, Michaelis-Menten kinetics predicts reaction speeds of 99.50% vs 99.01% of V_{max}, *i.e.* a miniscule difference that cannot be resolved in our analyses. However, within the CaMKII holoenzyme, Michaelis-Menten kinetics would break down at least after the first or second autophosphorylation reaction, due to the significant substrate depletion. Additionally, there could have been distinct steric positioning of kinase domains in the CaMKIIα versus β holoenzyme due to differences in linker length that could either facilitate or reduce the inter-subunit autophosphorylation. Indeed, the recently described differences in inhibitory

autophosphorylation at T305/306 in CaMKIIα versus T306/307 in CaMKIIβ have been attributed to the different linker lengths[352]. However, whereas T286 autophosphorylation occurs exclusively in *trans* between two subunits of a holoenzyme[312,339], the T305/306 autophosphorylation can occur both in *trans* and in *cis*[309,353]. Similarly, the different linker lengths in the CaMKIIα versus β isoforms may also affect steric accessibility to external substrate proteins, particularly when the holoenzymes are anchored at postsynaptic protein scaffolds.

Higher order assemblies and subcellular CaMKII targeting

A more surprising difference was the reduced propensity of CaMKIIβ to form higher order clusters under ischemic conditions, both *in vitro* and within neurons. While it has been previously reported that CaMKIIβ lacks excitotoxicity/ischemia-related clustering[323], the longer linker in CaMKIIβ should instead have been expected to facilitate this clustering: In the α isoform, clustering is thought to be mediated by kinase-domain pairing between holoenzymes[321,324], and a longer linker should facilitate such inter-holoenzyme pairings. The explanation might be that CaMKIIβ can form such pairings, but that the smaller CaMKIIα holoenzymes can pack into larger and/or denser clusters (see Figure 7E,F). Indeed, this notion is supported by the preferential detection of CaMKIIβ *in vitro* clustering by high- versus low-speed centrifugation (a fact that may also explain the previous failure to detect these clusters at all). Furthermore, while extra-synaptic CaMKIIβ clustering was significantly less compared to CaMKIIα, a significant level of clustering was observed also for the β isoform, even in CaMKIIα knockout neurons.

Notably, together with the decrease in extra-synaptic clusters, we observed an increase in synaptic CaMKIIβ clusters. This result appears to be in conflict with the notion that the inter-holoenzyme aggregation mediates clustering not only at extra-synaptic sites but also at synapses[325], a form of subcellular CaMKII movement that is thought to be

important in LTP[314,316,354–356]. It is well established that CaMKII movement to excitatory synapses requires CaMKII binding to the NMDA-receptor subunit GluN2B[315,316,319]. However, this does not rule out the possibility that holoenzyme aggregation contributes to this targeting. Furthermore, the reduced propensity of CaMKIIβ to cluster at extra-synaptic sites does not fully rule out the possibility that its clustering could be enhanced at synaptic sites. For instance, the larger holoenzyme radius and less dense clusters of CaMKIIβ might be favorable within the protein-concentrated environment at postsynaptic densities at excitatory synapses. Nonetheless, our results indicate that the higher-order aggregation of CaMKII holoenzymes plays a more important role in cluster formation at extra-synaptic versus synaptic sites.

The function of extra-synaptic CaMKII clustering is still unclear, but it has been proposed to provide neuro-protection by curbing the over-activation of CaMKII after excitotoxicity/ischemia[321,357]. This mechanism is clearly insufficient to completely prevent the neuronal cell death after excitotoxic/ischemic insults, but CaMKII inhibition can indeed protect neurons in mouse models of stroke or global cerebral ischemia[307,308]. Further, the CaMKII T286A mutation increases clustering[324,325] and decreases neuronal cell death[307]. However, this correlation allows only limited conclusions, as the T286A mutation also prevents generation of Ca^{2+}-independent autonomous CaMKII activity.

Multivalent interactions within the holoenzymes and cooperative CaMKII regulation

While kinase domain interactions between holoenzymes are thought to mediate the aggregation of holoenzymes into higher-order assemblies, our results here show the first direct evidence of kinase domain dimer formation also within the holoenzyme. Previous FRET studies have suggested kinase domain dimers are supported by the CaMKII holoenzyme in cells, but direct detection of dimer formation was not resolved in these studies[342,358,359]. Dimer formation was directly observed in the first crystal structure

of a CaMKII kinases domain (specifically for a *C. elegans* CaMKII that was truncated after the regulatory domain)[341]. The low affinity of this interaction (Kd > 100 μM) could be sufficient to support dimer formation based on the 1 – 2 mM concentration of kinase domains within a holoenzyme. Kinase domain dimerization has also been observed biochemically for isolated kinase domains of all four human isoforms, with similarly low-affinity (Kd's ~200 – 600 μM)[360]. However, it was entirely unclear if such dimer formation would be possible for kinase domains that are tethered to the central hub of association domains within the holoenzyme. The extended state of CaMKIIβ holoenzymes facilitated the ability to directly resolve kinase domain dimers by EM; while this did not allow detailed resolution of the dimerization surface, the defined bi-lobed densities are consistent with the crystallized CaMKII kinase domain dimer structure.

The putative population of kinase domain dimers for CaMKIIα and β were determined to be ~19% and ~8%, respectively, based on single particle distance measurements and the average center-to-center distance of ~4.5 nm separating the two subunits in the crystal structure of the kinase domain dimer (see Fig. 3E). However, when considering slightly different distance cut-offs of up to 5 – 6 Å (the difference of approximately one to three pixels in our micrographs) our data suggest dimer population in these two isoforms might be more similar than these reported values, with a likely range of ~8 – 30% kinase domain dimers for both isoforms. If CaMKIIα and β holoenzymes contain similar fractions of dimerized kinase domains, both isoforms should show a similar level of cooperative activation by CaM, as was indeed observed here. The dimers are proposed to generate cooperativity, as they are thought to be formed via interactions of the CaM-binding regulatory domains[341]. Thus, when CaM binds to one subunit, it would disrupt the dimer and thereby also facilitate binding to the other subunit. While this kinase domain dimerization predicts the observed cooperativity, it also raises some questions.

How could a relatively minor fraction of dimers (*e.g.,* ~8 – 30%) cause cooperativity with a relatively large Hill coefficient of 1.6?

An additional, or alternative, proposed mechanism for the cooperativity lies in a compact conformation in which a kinase domain folds back onto its own association domain[330]. A recent elegant cryo-EM study indeed directly demonstrated the existence of this conformation[332], whereas our previous and current studies could only set an upper limit to its prevalence[331]. However, with less than 3% of subunits in the compact state, this maximal prevalence is extremely low and consistent to all of the studies[331,332], which makes it an even less likely candidate mechanism for the observed cooperativity than the kinase domain dimers.

Then, a more likely "neighbor effect" may be that kinase domain dimerization (or disruption of the dimer) affects CaM binding not only to the dimer itself, but also to the neighboring subunits. In this way, one single kinase domain dimer could potentiate CaM binding to half of the subunits within a 12-meric CaMKII holoenzyme, *i.e.* the dimer pair itself plus its four neighbors. A similar model was proposed previously, but assumed that the neighbors would also be dimers[330]; however, with the observed lower occurrence of dimers, the model would have to be modified to include effects also on non-dimerized neighbors. Indeed, such a model is consistent with the emerging view of CaMKII holoenzyme structure, one that is not constrained by a single defined state, but rather a highly dynamic conformational ensemble characterized by multiple transient low-affinity interactions (see Figure 7).

An intriguing comparison can be made to other systems hallmarked by multivalent low-affinity interactions organized by intrinsically disordered protein domains that are capable of forming biomolecular condensates[361]. We suggest that the unique structural and biophysical properties of the CaMKII holoenzyme structure (*e.g.,* high local concentration of multivalent binding modes) may facilitate the formation of a molecular-

scale condensate, at least from a conceptual point of view. Condensates (*i.e.,* liquid-liquid phase separation or LLPS) have emerged as a novel regulatory mechanism at synapses[362] and the CaMKII interaction with GluN2B has recently been shown to support condensate formation[363]. What is intriguing about this analogy of individual CaMKII holoenzymes to condensates is that the dissolution of biomolecular condensates is highly cooperative[364,365]. Such a model could explain how activation of CaMKII holoenzymes can achieve a higher degree of cooperativity than would be expected based on the extent of kinase domain dimers. Notably, some studies have described Hill coefficients for CaMKII activation by CaM that are even higher than the Hill coefficient of ~1.6 reported here[330,341]. In a model analogous to molecular condensates, each kinase domain would exist in an equilibrium between rapidly exchanging interactions involving multiple neighboring kinase or hub domains, a notion supported by the flexibility of kinase domain positioning with the holoenzymes. The activation of one kinase domain would then disrupt the interaction with multiple neighboring kinase domains, leading to the cooperative collapse or dissolution of the basal-state. While there is currently no direct evidence that a kinase domain dimer (or kinase-hub complex) can affect the positioning of neighboring kinase domains within the holoenzyme, such a proposition appears to be at least more plausible than what can be explained by any single-defined state of CaMKII.

Beyond the 12-mer: Outlook for future studies

The oligomeric state of CaMKII holoenzyme is clearly important for facilitating its physiological roles Ca^{2+}-frequency detection and in regulating LTP and LDP[310–313]. The predominant state of both CaMKIIα and β holoenzymes is the 12-meric assembly (see Figure 2 and Myers, et al 2017[331]). However, both holoenzymes can also support 14-meric assemblies, and here we show that CaMKIIβ can even support a 16-meric assembly. To our knowledge, such a high oligomeric state of the CaMKII hub domain has so far not

been detected in metazoans. Interestingly, bacteria and algae species contain orphan proteins with sequence and structural homology to CaMKII hub domains, that adopt 16- to 20-mers[366]. Crystallographic analysis of the hub-like assembly from *Chlamydomonas reinhardtii* revealed an 18-meric structure with striking similarity to CaMKII hub assemblies, but with increased hydrogen-bonding at the lateral subunit interface. Remarkably, when these hydrogen-bonding residues were incorporated into the CaMKIIα hub domain it assembled as 14- and 16-mers[366]. It is currently unclear if wildtype CaMKIIα holoenzymes support a 16-meric assembly, but if it can it is likely a very minor population as we have found that this state only represents ~0.4% of the population in CaMKIIβ holoenzymes under basal-conditions, and both isoforms lack the hydrogen-bonding potential identified in the algae hub-like assembly.

These observations raise the important question as to what is the functional significance of higher-order oligomeric states of the CaMKII holoenzyme? It has recently been shown that under activating conditions, CaMKII subunits (dimeric pairs) are capable of undergoing exchange between other activated or non-activated holoenzymes[367,368]. While subunit exchange was minimal under basal conditions, it is possible that the small population of 14-mer/16-mers represented high-energy intermediate states involved in the subunit exchange mechanism. Activation of the CaMKII holoenzyme is thought to destabilize the hub complex, through interactions with the regulatory domain[367–369]. Thus, the 14-mer and 16-mer states could also provide a storage mechanism for pools of potentiated subunits to be released under activating conditions. Intriguingly, this subunit-exchange mechanism has been proposed to enable the propagation of CaMKII activation and other neuronal plasticity mechanisms that could play important roles in learning and memory[303,370]. Future studies will be needed to further test these hypotheses, and to shed light on the mechanistic basis for how such regulatory functions are achieved.

Limitations of the study

In addition to the technical and conceptual limitations described above, it should be noted that the observations of structural behavior of CaMKII holoenzymes by EM are made under dilute *in vitro* conditions. While significant effort was made to correlate these behaviors to functional and/or structural phenomena inside cells, there are many factors within a native cellular environment (e.g., temperature, molecular crowding, interactions with cognate binding partners, etc.) that may augment the structural features and/or dynamical properties of CaMKII holoenzymes that are described in this work. Future studies will be targeted at defining how these cellular conditions contribute to the molecular plasticity and functional properties of CaMKII.

ACKNOWLEDGEMENTS

We thank Ms. Janna Mize-Berge for help with mouse colony maintenance as well as Mr. Jonathan Flores and Dr. Janette Myers for help with EM grid preparation and the OHSU Multiscale Microscopy Core for instrumentation access and training. The research was funded by National Institutes of Health grants F32AG066536 (to O.R.B.), P30NS048154 (UCD neuroscience center grant), R01NS081248 and R01NS118786 (to K.U.B.), and R35GM124779 and R01EY030987 (to S.L.R.).

AUTHOR CONTRIBUTIONS

O.R.B., A.P.M., S.J.C., and S.L.R. performed experiments; K.U.B. and S.L.R. conceived this study, with contribution from all authors; K.U.B. and S.L.R. wrote the first draft and all authors contributed to the final manuscript.

DECLARATION OF INTERESTS

Authors declare no competing interests (but wish to disclose that K.U.B. is co-founder and board member of Neurexis Therapeutics).

STAR METHODS

KEY RESOURCES TABLE

REAGENT or RESOURCE	SOURCE	IDENTIFIER
Antibodies		
CaMKII pan	Genetex	GTX127939; RRID: AB_2492051
CaMKIIα	Made in house	CBα2; RRID: AB_2533032
CaMKIIβ	Made in house	CBβ1; RRID: AB_2533045
pT286	Phospho-Solutions	p1005-286; RRID: AB_2492051
Rabbit	GE Healthcare	NA934V; RRID: AB_772206
Mouse	GE Healthcare	NA931V; RRID: AB_772210
Chemicals, peptides, and recombinant proteins		
Glutamate	Sigma	6106-04-3
Papain	Worthington	LS 03126
Lipofectamine 2000	Invitrogen	11668027
B-27 supplement	GIBCO	17504044
complete protease inhibitor cocktail	Roche	1187380001
Microcystin-LR	Calbiochem	475815
Uranyl formate	SPI-Chem	16984-59-1
Sodium hydroxide	Fisher Scientific	1310-73-2,497-19-8
Calmodulin	Made in house	CaM
Ca^{2+}/CaM-dependent kinase II α	Made in house	CaMKIIα
Ca^{2+}/CaM-dependent kinase II β	Made in house	CaMKIIβ
Critical commercial assays		
Pierce BCA protein assay	Thermo Fisher	23225
SuperSignal West Femto	Thermo Fisher	34095
Deposited data		
Raw and analyzed data	This paper	Mendeley Data, V1, doi: 10.17632/35gf4sjxmb.1

Experimental models: organisms/strains		
Rat: Sprague-Dawley	Charles River Laboratory	
Mouse: wild type: C57BL/6	Charles River Laboratory	
Mouse: CaMKIIα KO: C57BL/6	(Coultrap et al., 2014)	
Recombinant DNA		
PSD-95-FingR-GFP	(Gross et al., 2013)	RRID: Addgene_46295
Gephyrin-FingR-GFP	(Gross et al., 2013)	RRID: Addgene_46296
YFP-CaMKIIα	(Bayer et al., 2006; Shen and Meyer, 1999)	N/A
YFP-CaMKIIβ	Made in house	N/A
Software and algorithms		
Slidebook 6.0	Intelligent Imaging Innovations (3i)	RRID:SCR_014300
Prism 7.0	Graphpad	RRID: SCR_002798
AlphaEase FC 4.0	Alpha Innotech	N/A
ImageJ	NIH	RRID:SCR_003070
EMAN2.1	NIH	RRID:SCR_018867
RELION3.0b	MRC (United Kingdom)	RRID:SCR_016274
UCSF Chimera	NIH	RRID:SCR_004097
Python 3	Python Software Foundation	RRID:SCR_008394
Microsoft Excel	Microsoft	RRID:SCR_016137
Other		
400 mesh, 3.0 mm O.D. copper grid	PELCO	1GC400

LEAD CONTACT

Further information and requests for resources and reagents should be directed to and will be fulfilled by the Lead Contact, Steve L. Reichow (reichow@pdx.edu).

MATERIALS AVAILABILITY

This study did not generate new unique reagents.

DATA AND CODE AVAILABILITY

- Raw and analyzed data contributing to this work have been deposited at Mendeley and are publicly available as of the date of publication. The DOI is listed in the key resources table. Microscopy data reported in this paper will be shared by the lead contact upon request.
- This study does not report original code.
- Any additional information required to reanalyze the data reported in this paper is available from the lead contact upon request.

EXPERIMENTAL MODEL AND SUBJECT DETAILS

Hippocampal cultured neurons

Mixed sex pups from homozygous mice (P1-2; on a C57BL/6 background) were used to prepare dissociated hippocampal cultures for live imaging. The CaMKII KO mice were described previously[310]. To prepare primary hippocampal neurons from WT or mutant mice, hippocampi were dissected from mixed sex mouse pups (P1-2), dissociated in papain for 30 min, and plated at 200-300,000 cells/mL for imaging. At DIV 14-15, neurons were transfected with 1 µg total cDNA per well using Lipofectamine 2000 (Invitrogen). At DIV 16-17, neurons were treated and imaged. All animal procedures were approved by the Institutional Animal Care and Use Committee (IACUC) of the University of Colorado Anschutz Medical Campus and were carried out in accordance with NIH best practices for animal use. All animals were housed in ventilated cages on a 12 h light/ 12 h dark cycle and were provided ad libitum access to food and water.

METHOD DETAILS

DNA constructs

CaMKIIα and β constructs are based on a pcDNA3 backbone (Addgene #13033). For imaging studies, the YFP-CaMKII constructs contained N-terminal fusion to an EYFP with its A206 mutated to reduce dimerization of the YFP, as described previously[317,371]. For the biochemical self-association studies with co-expressed isoforms, the YFP tag was removed. All CaMKIIα and β used here were the respective major splice variants in adult mammalian brain of each isoform, i.e. α, not αB; and β, not β', βe, βe', or βM etc.[335]. Expression vectors for the GFP-labeled FingR intrabodies targeting PSD-95 and gephyrin were kindly provided by Dr. Donald Arnold (University of Southern California, Los Angeles, CA, USA) as previously characterized[372,373]. The fluorophore label was exchanged using Gibson Assembly to contain the following tags in place of GFP: PSD-95-FingR-mTurquois and gephyrin-FingR-mCherry.

CaMKII and CaM purification

For biochemistry and electron microscopy, homomeric rodent CaMKIIα and β holoenzymes were expressed in eukaryotic *Sf9* cells via baculovirus and purified using a phosphor-cellulose column followed by a CaM-sepharose column; CaM was purified after expression in BL21 bacteria[374,375]. The heteromeric CaMKII used in Fig. S5 was generated by co-expression in HEK293 cells and purified using the CaM-sepharose step[374].

Electron microscopy

Full length purified CaMKIIβ holoenzymes were prepared for negative stain EM by diluting a freshly thawed aliquot of protein (1:40 vol vol^{-1}) in EM buffer containing 50 mM HEPES (pH 7.4), 120 mM KCl and 0.5 mM EGTA. A 3 µL drop of the diluted specimen (~0.35 µM holoenzyme concentration) was applied to a glow-discharged continuous carbon coated

EM grid (Ted Pella). Excess protein was removed by blotting with filter paper and washing twice with EM buffer. The specimen was then stained with freshly prepared (0.75% wt vol^{-1}) uranyl formate (SPI-Chem), blotted and dried with laminar air flow.

Negatively stained specimens were visualized on a 120kV TEM (Tecnai iCorr, FEI) and digital micrographs were manually collected on a 2K x 2K CCD camera (Eagle, FEI) at a nominal magnification of 49,000 x at the specimen level. Micrographs were collected with a calibrated pixel size of 4.37 Å and defocus of 1.5 – 2.5 µm. A total of 907 micrographs were collected and screened for astigmatism and drift based on Thon rings in the power spectra after determination of contrast transfer function (CTF) parameters in EMAN2.1[246]. 17,347 single particles images were manually picked in EMAN 2.1 and extracted with a box size of 144 x 144 pixels. Boxed images used for single particle analysis were of isolated holoenzymes that were not associated with neighboring holoenzymes (such as the particles examined for clustering). Reference-free 2D classification and variance analysis was conducted in RELION3.0b[376] on CTF-corrected (phase-flipped), using various masking strategies: holoenzyme = 55.0 nm mask, hub domain = 15.0 nm mask, and kinase domains = inner mask 13.5 nm, without applied symmetry. For comparative analysis, the previously acquired negative stain EM dataset of 10,902 untilted CaMKIIα single-particle images[331] was reprocessed in EMAN 2.1 and RELION3.0b, as described above using a box size of 128 x 128 pixels.

Single particle measurements and statistical analysis

Statistical analyses of individual holoenzyme particle dimensions were obtained from particle lengths using the measurement tool in EMAN2.1, as previously described[331]. A radius of extension for individual kinase subunits (*n* = 926 measurements obtained from 95 holoenzymes) was determined by measuring the distance from the center of the pore in the hub domain complex to the center of each peripheral density corresponding to the

kinase domains. For each of these measurements, a distance of 2.25 nm was appended (corresponding to the average radius of the kinase domain) to yield a value that represents the full extension of the kinase domain. Inter-molecular kinase separation was determined by measuring from the center of one peripheral kinase density to the center of the nearest clockwise neighboring kinase density. For the linker extension analysis, the hub average radius (5.5 nm) and the kinase average radius (2.25 nm) was subtracted from the raw hub to kinase radius measurements, as a representative distance of linker extension and comparison to random chain polymer models (traditional random walk model)[337]. The local concentration of kinase domains in the context of a single dodecameric holoenzyme was determined by assuming a spherical volume with the radius corresponding to the average radius extension for each isoform ± 2 x standard deviation appended. To analyze intermolecular clustering of holoenzymes, a random subset of raw micrographs was visually inspected for CaMKIIα (1207 particles) and CaMKIIβ (1255 particles) by counting the total number of holoenzymes and the number of non-clustering holoenzymes (designated as being separated by at least ~1.5 times the particle diameter from a nearest neighbor). For statistical comparisons, an F-test was performed to determine the difference in sample variances, followed by a T-test (two sample assuming unequal variances). All statistical analysis and graphical interpretations were done using libraries in python 3.

Pseudo-atomic modeling of the CaMKII 16-meric hub assembly and back-projection analysis

A pseudo-atomic model of the hexadecameric (16-mer) CaMKII hub assembly was built manually, using the atomic coordinates corresponding to a vertical hub dimer extracted from the previously published dodecameric assembly (PDB 5IG3)[367], with an applied C8 symmetry (overall D8 symmetry) that was adjusted to approximately fit within the

experimental 2D class average density following C8 symmetry averaging (outer diameter of ~13 nm) and to obtain minimal steric overlap between neighboring hub domains. For comparing with 2D class averages, hub models where filtered to 3.0 nm and 2D back projections were generated in RELION[377].

Live imaging of hippocampal cultured neurons

All images were acquired using an Axio Observer microscope (Carl Zeiss) fitted with a 63x Plan-Apo/1.4 numerical aperture objective, using 445, 515, 561, and 647 nm laser excitation and a CSU-XI spinning disk confocal scan head (Yokogawa) coupled to an Evolve 512 EM-CCD camera (Photometrics). During image acquisition, neurons were maintained at 34°C in 10 mM HEPES-buffered neuronal media. After baseline imaging ('pre'), cells were treated with 100 μM glutamate and imaged 5 min later ('post'). Tertiary dendrites from pyramidal spiny neurons were selected from maximum intensity projections of confocal Z stacks. Slidebook 6.0 software (Intelligent Imaging Innovations [3i]) was used to analyze CaMKII-YFP at excitatory (PSD-95) and inhibitory (gephyrin) synapses. Specifically, the mean YFP intensity at PSD-95 or gephyrin threshold masks on a given dendrite was divided by the mean YFP intensity of a line drawn in the adjacent dendritic shaft. ImageJ (National Institute of Health) was used to analyze CaMKII at extra-synaptic sites. Specifically, the thresholded mask for PSD-95 puncta was subtracted from the CaMKII channel and the remaining CaMKII clusters (0.1 μm<cluster<1.0 μm) were quantified as number per 10 μm dendrite.

CaMKII *in vitro* reactions

CaMKII self-associations assays were performed similar to previous work (Vest et al., 2009). Purified CaMKII (0.5 μM or as indicated) was pre-cleared by ultracentrifugation (100,000 x g) at 4 °C for 45 min, then combined with 25 mM PIPES pH 6.4, 20 mM KCl,

10 mM $MgCl_2$, 0.1 mg/mL bovine serum albumin, 0.1% Tween 20, 0.5 mM dithiothreitol, 2 mM $CaCl_2$, 1 μM CaM, and 1 mM ADP. Control samples were instead combined with 25 mM PIPES pH 7.4, 20 mM KCl, 10 mM $MgCl_2$, 0.1 mg/mL bovine serum albumin, 0.1% Tween 20, 0.5 mM dithiothreitol, and 50 mM EGTA. The mixtures were prepared on ice and then incubated for 5 min at room temperature prior to centrifugation (16,000 x g) or ultracentrifugation (100,000 x g) at 4 °C for 30 min. CaMKII in the supernatant and pellet was detected via immunoblot.

For autophosphorylation assays, purified CaMKII (0.1 uM) was pre-cleared by ultracentrifugation (100,000 x g) at 4 °C for 45 min, then combined with 25 mM PIPES pH 7.1, 10 mM $MgCl_2$, 0.1 mg/mL bovine serum albumin, 4 mM $CaCl_2$, 3 μM CaM, and 1 mM ATP. The mixtures were prepared on ice and then incubated at 30 °C for 0 sec, 30 sec, 180 sec, or 15 min. Autophosphorylation at pT286-CaMKIIα and pT287-CaMKIIβ was detected via immunoblot.

For kinase activity assays, purified CaMKII (2.5 nM) was combined with 50 mM PIPES pH 7.1, 10 mM $MgCl_2$, 0.1 mg/mL bovine serum albumin, 1 mM $CaCl_2$, 100 μM [γ-^{32}P] ATP, 75 μM syntide-2 substrate peptide, and 0.6 nM to 6 μM CaM. The mixtures were prepared on ice and then pre-incubated at 30 °C for 5 min. CaMKII was added and the reaction was allowed to progress for 1 min at 30 °C. To stop the reaction, 40 μL of the 50 μL reaction mixture was spotted onto P81 cation exchange chromatography paper (Whatman) squares. After extensive washes with water, phosphorylation of the substrate peptide bound to the P81 paper was measured by liquid scintillation counting. CaMKII activity (Vm; reactions/kinase/min) was quantified as a fraction of maximal activity (Vmax) for each experiment. Data were fitted using a non-linear regression with variable slope.

SDS-PAGE and immunoblot

Protein content was determined using the Pierce BCA protein assay (Thermo Fisher). 4-10 µg of total protein in Laemmli sample buffer was resolved by SDS-PAGE on 9% polyacrylamide gels and transferred to polyvinylidene fluoride (PVDF) membrane at 24 V for 1-2 h at 4°C in transfer buffer containing: 12% MeOH, 25 mM Tris, and 192 mM glycine. All membranes were blocked in 5% nonfat dried milk in TBS-T (20 mM Tris pH 7.4, 150 mM NaCl, 0.1% Tween 20) before primary antibody incubation for 2 h at room temperature or overnight at 4°C. Antibodies and dilutions were as follows: rabbit anti-CaMKII (Genetex; 1:1000), mouse anti-CaMKIIα (in house CBα2; 1:1000), mouse anti- CaMKIIβ (in house CBβ1; 1:1000), and anti-pT286 (Phospho-Solutions; 1:2000). Blots were then washed in TBS-T, incubated in horseradish peroxidase-labeled goat anti-rabbit or goat anti-mouse antibodies (GE Healthcare; 1:10,000) for 1 h at room temperature, and washed again in TBS-T. Immunoreactive signal was visualized by chemiluminescence (Super Signal West Femto, Thermo Fisher) using the Chemi-Imager 4400 system (Alpha-Innotech). Densitometry analysis was performed using ImageJ (National Institute of Health), with all samples normalized to control conditions on the same gel.

QUANTIFICATION AND STATISTICAL ANALYSIS

Structural measurement data are shown as mean ± SEM, with standard deviation or 95% confidence interval were indicated using Microsoft Excel or SciPy. Comparisons between isoforms for kinase radius and separation measurements were done with a f-test to determine sample variance differences, followed by a t-test (two sampled assuming unequal variance). Functional data are shown as mean ± SEM and analyzed using Prism (GraphPad) software. Comparisons between pre- and post-glutamate images in neurons were analyzed using repeated measures two-way ANOVA with Bonferroni's post-hoc test. Self-association assays with purified CaMKII were analyzed using two-way ANOVA with Bonferroni's post-hoc test. Kinase activity assays to assess CaM dose/response were

analyzed using extra-sum-of-squares F-test. Comparisons in WT neurons at inhibitory synapses were analyzed using paired, two-tailed Student's t-test. Statistical significance and sample size (n) are indicated in the figure legends.

SUPPLEMENTAL FIGURES AND LEGENDS

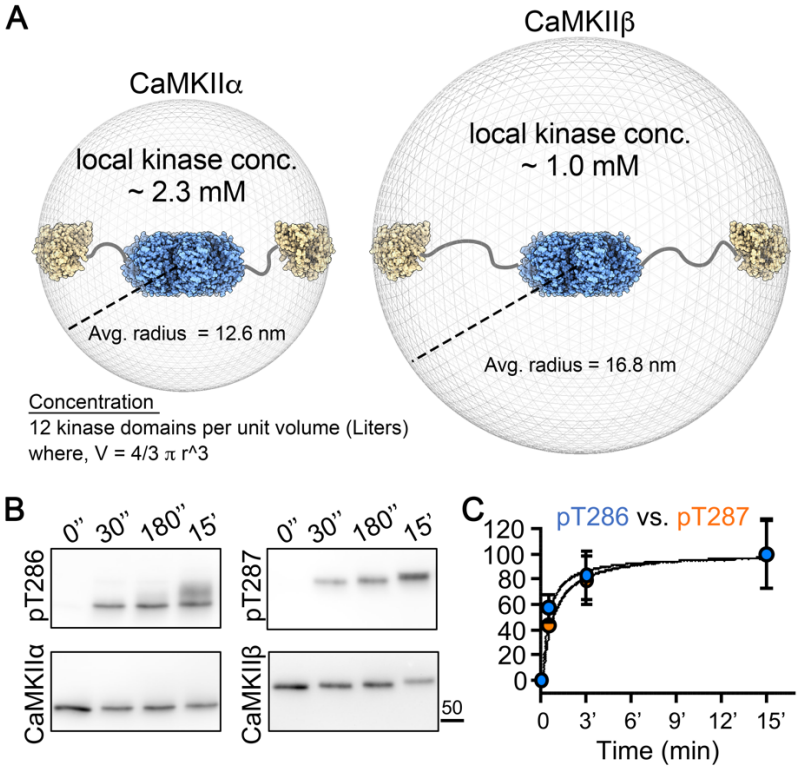

Figure S1: Effect of local kinase domain concentration on pT286-CaMKIIα and pT287-CaMKIIβ in vitro kinetics. Quantifications show mean ± SEM. (A) Estimated local kinase concentration in CaMKIIα (*left*) and CaMKIIβ (*right*) holoenzymes. Calculations assume individual kinase domains (12 per holoenzyme) may occupy a spherical volume that is approximated by the average radius of the holoenzyme complex. (B) Representative immunoblots showing autophosphorylated T286-CaMKIIα (*left*) and T287-CaMKIIβ (*right*) after 0 sec, 30 sec, 180 sec, and 15 min at 30° C. Reactions were performed with 100 nM purified kinase in buffered solution containing 2 mM Ca^{2+}, 3 μM CaM, 10 mM Mg^{2+} and 1 mM ATP. (C) Quantified time-course of normalized pT286-CaMKIIα versus pT287-CaMKIIβ (n=4). Solid lines through the data points represent nonlinear best-fits.

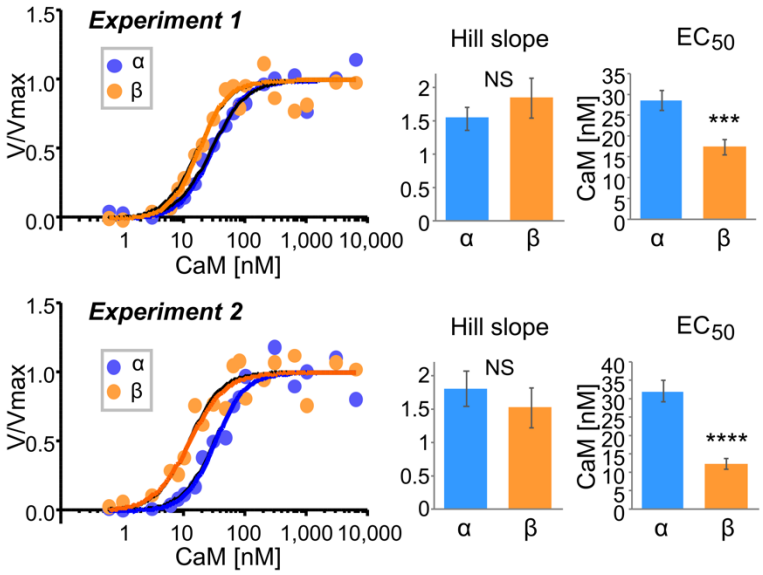

Figure S2: CaMKIIα and CaMKIIβ activation by CaM: individual experiments. Quantifications show mean ± SEM. ***p<0.001, ****p<0.0001. *In vitro* CaMKII activity in response to varying Ca^{2+}/CaM (0.6 nM to 6 μM CaM). The two curve fits shown are based on data from independent reactions: experiment 1 (*top*) and experiment 2 (*bottom*). Both experiments demonstrated a Hill slope >1 for CaMKII, with no differences detected between α and β isoforms (extra-sum-of-squares F-test, p=0.3619 for experiment 1 and p=0.4921 for experiment 2). However, both experiments showed a reduced EC_{50} for CaMKIIβ compared to α (extra-sum-of-squares F-test, ***p=0.006 for experiment 1 and ****p<0.0001 for experiment 2).

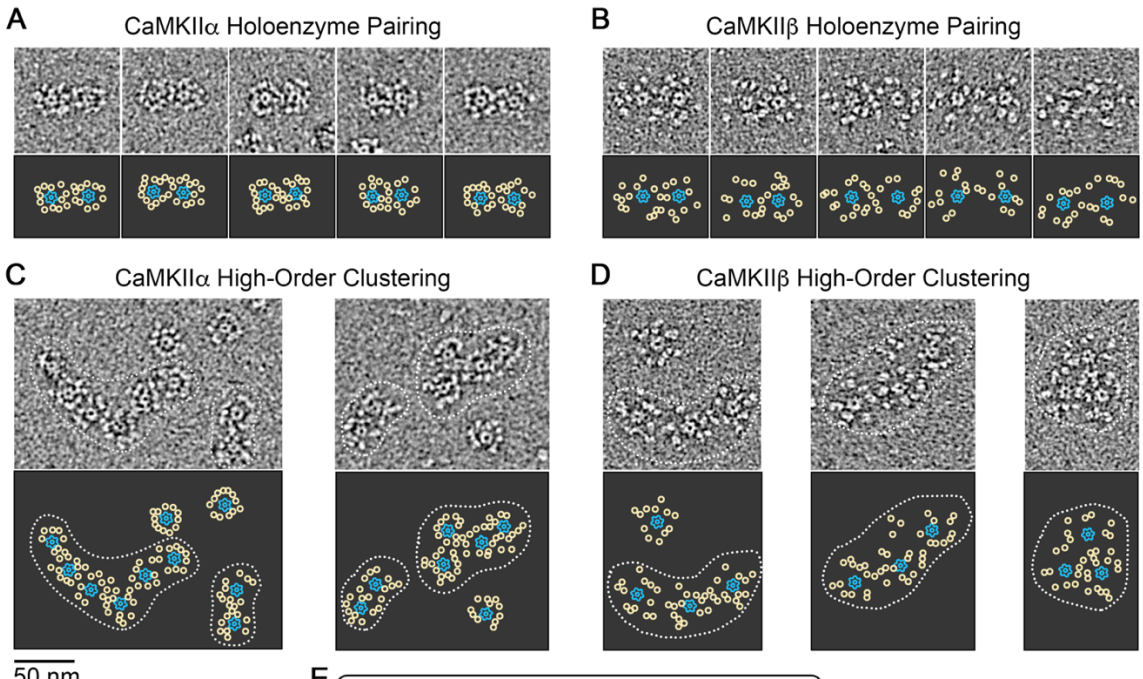

E

	# of particles	paired/clustered
CaMKIIα	1,207	58%
CaMKIIβ	1,255	56%

Figure S3: EM analysis of CaMKII holoenzyme clustering under basal conditions. (A and B) *Top,* representative EM images showing apparent holoenzyme paring for CaMKIIα and CaMKIIβ, respectively. *Bottom*, displays annotated representation of resolved holoenzyme domains, with the hub domain represented as blue outline and kinase domains as yellow circles. (C and D) *Top,* representative EM images showing apparent high-order clustering of holoenzymes (3 or more) for CaMKIIα and CaMKIIβ, respectively (dotted outlines). *Bottom*, annotated representation of resolved holoenzyme domains, as in panels (A) and (B), with holoenzyme clusters indicated by dotted outline. Scale bar = 50 nm in panels (A – D). (E) Percentage of paired/clustered holoenzymes as assigned by visual inspection of micrographs for CaMKIIα and CaMKIIβ image datasets (n=1,207 particles for CaMKIIα and 1,255 particles for CaMKIIβ), indicate an approximately equal propensity for holoenzyme clustering between these two isoforms under basal-state conditions.

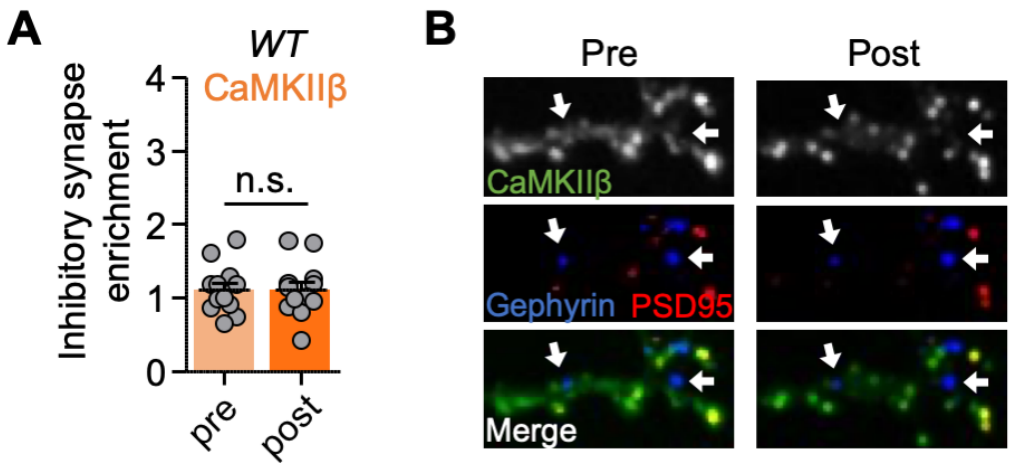

Figure S4: CaMKIIβ does not move to inhibitory synapses following prolonged glutamate. Quantifications show mean ± SEM. (A) Quantification of inhibitory synapse enrichment induced by excitotoxic glutamate (100 μM glutamate, 5 min) in WT cultured hippocampal neurons (paired two-tailed t-test: p=0.4689). (B) Representative confocal images show overexpressed CaMKIIβ, endogenous PSD95 (in red) to mark excitatory synapses, and endogenous gephyrin (in blue) to mark inhibitory synapses.

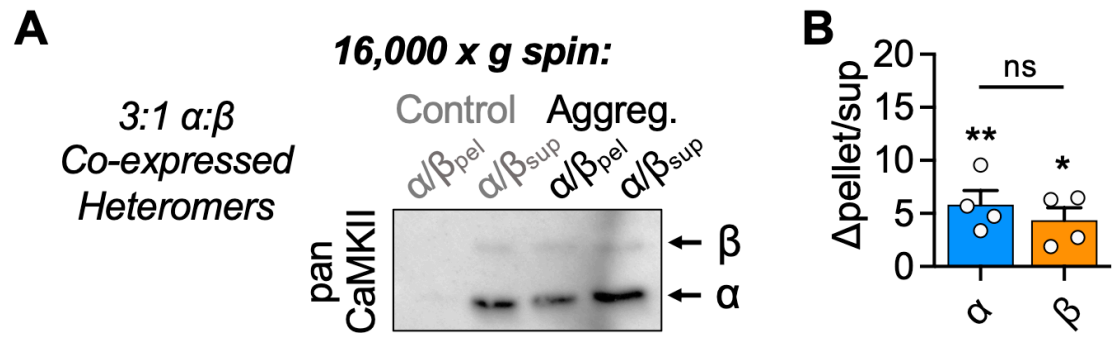

Figure S5: Aggregation in heteromeric CaMKIIα/β holoenzymes. Related to Figure 5. Quantifications show mean ± SEM. ***p<0.001. Aggregation was induced by 2 mM Ca^{2+}, 1 μM CaM, and 1 mM ADP at low pH (6.4) for 5 min at room-temperature. Control samples were incubated in 50 mM EGTA at pH 7.4 and normalized to 1. (A) Representative immunoblot for CaMKIIα/β heteromers. CaMKIIα and CaMKIIβ were co-expressed in HEK-293 cells at 3:1 α:β, then homogenized and purified via CaM-sepharose. Aggregates were detected in 16,000x*g* pellets. (B) Quantification of change in pellet enrichment. Both CaMKIIα and CaMKIIβ showed significant clustering under aggregation conditions in 3:1 co-expressed heteromers, compared to control (two-way ANOVA, Bonferroni's test: **p=0.0047 for CaMKIIα; *p=0.0416 for CaMKIIβ). No significant differences in self-aggregation levels were detected between CaMKIIα and CaMKIIβ (two-way ANOVA, Bonferroni's test, n.s.: p=0.2266).

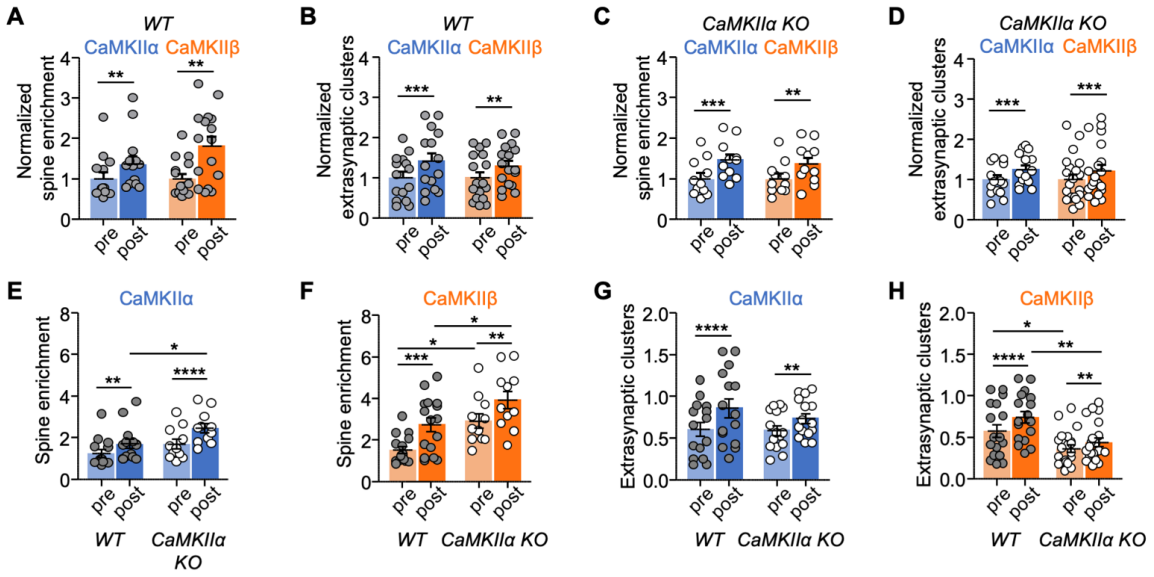

Figure S6: CaMKII movement normalized and compared by genotype. Panels A-D show CaMKIIα vs. CaMKIIβ isoform comparison after normalizing to baseline. Panels E-H show WT vs. CaMKIIα KO genotype comparison. Quantifications show mean ± SEM. *p<0.05, **p<0.01, ***p<0.001, ****p<0.0001. (A) CaMKIIα vs. CaMKIIβ movement to excitatory synapses in WT (two-way repeated-measures ANOVA, Bonferroni's test: **p=0.0012 for pre vs. post in CaMKIIα; **p=0.0017 for pre vs. post in CaMKIIβ). (B) CaMKIIα vs. CaMKIIβ clustering at extra-synaptic cluster sites in WT (two-way repeated-measures ANOVA, Bonferroni's test: ***p=0.0001 for pre vs. post in CaMKIIα; **p=0.0035 for pre vs. post in CaMKIIβ). (C) CaMKIIα vs. CaMKIIβ movement to excitatory synapses in CaMKIIα KO (two-way repeated-measures ANOVA, Bonferroni's test: ***p=0.0001 for pre vs. post in CaMKIIα; **p=0.0017 for pre vs. post in CaMKIIβ). (D) CaMKIIα vs. CaMKIIβ clustering at extra-synaptic cluster sites in CaMKIIα KO (two-way repeated-measures ANOVA, Bonferroni's test: **p=0.0004 for pre vs. post in CaMKIIα; **p=0.0007 for pre vs. post in CaMKIIβ). (E) CaMKIIα movement to excitatory synapses in WT vs. CaMKIIα KO (two-way repeated-measures ANOVA, Bonferroni's test: **p=0.0018 for pre vs. post in WT; ****p<0.0001 for pre vs. post in CaMKIIα KO; *p=0.0344 for post WT vs. post CaMKIIα KO). (F) CaMKIIβ movement to excitatory synapses in WT vs. CaMKIIα KO (two-way repeated-measures ANOVA, Bonferroni's test: ****p<0.0001 for pre vs. post in WT; **p=0.0024 for pre vs. post in CaMKIIα KO; *p=0.0230 for pre WT vs. pre CaMKIIα KO; *p=0.0078 for post WT vs. post CaMKIIα KO). (G) CaMKIIα extra-synaptic clustering in WT vs. CaMKIIα KO (two-way repeated-measures ANOVA, Bonferroni's test: ****p<0.0001 for pre vs. post in WT; *p=0.0179 for pre vs. post in CaMKIIα KO). (H) CaMKIIβ extra-synaptic clustering in WT vs. CaMKIIα KO (two-way repeated-measures ANOVA, Bonferroni's test: ****p<0.0001 for pre vs. post in WT; **p=0.0058 for pre vs. post in CaMKIIα KO; *p=0.0303 for pre WT vs. pre CaMKIIα KO; **p=0.0015 for post WT vs. post CaMKIIα KO).

References

1. Kriehuber, T. *et al*. Independent evolution of the core domain and its flanking sequences in small heat shock proteins. *FASEB J.* **24**, 3633–3642 (2010).
2. Complete Genome Sequence of the Methanogenic Archaeon, Methanococcus jannaschii | Science. https://www.science.org/doi/10.1126/science.273.5278.1058.
3. Waters, E. R. & Vierling, E. Plant small heat shock proteins – evolutionary and functional diversity. *New Phytol*. **227**, 24–37 (2020).
4. Biswas, S., Garg, P., Dutta, S. & Suguna, K. Multiple nanocages of a cyanophage small heat shock protein with icosahedral and octahedral symmetries. *Sci. Rep.* **11**, 21023 (2021).
5. Horwitz, J. a-Crystallin can function as a molecular chaperone. *Proc Natl Acad Sci USA* 5 (1992).
6. Ashburner, M. & Bonner, J. J. The induction of gene activity in drosophila by heat shock. *Cell* **17**, 241–254 (1979).
7. Tissiéres, A., Mitchell, H. K. & Tracy, U. M. Protein synthesis in salivary glands of Drosophila melanogaster: Relation to chromosome puffs. *J. Mol. Biol.* **84**, 389–398 (1974).
8. Haslbeck, M. *et al*. Hsp26: a temperature-regulated chaperone. *EMBO J.* **18**, 6744–6751 (1999).
9. Kim, J. Y., Kim, C. H., Lee, E. Y. & Seo, J. H. Alpha B-Crystallin Overexpression Protects Oligodendrocyte Precursor Cells Against Oxidative Stress-Induced

Apoptosis Through the Akt Pathway. *J. Mol. Neurosci.* (2020) doi:10.1007/s12031-020-01485-z.

10. Fleckenstein, T. *et al.* The Chaperone Activity of the Developmental Small Heat Shock Protein Sip1 Is Regulated by pH-Dependent Conformational Changes. *Mol. Cell* **58**, 1067–1078 (2015).
11. Haslbeck, M., Miess, A., Stromer, T., Walter, S. & Buchner, J. Disassembling protein aggregates in the yeast cytosol. The cooperation of Hsp26 with Ssa1 and Hsp104. *J. Biol. Chem.* **280**, 23861–23868 (2005).
12. Jakob, U., Gaestel, M., Engel, K. & Buchner, J. Small heat shock proteins are molecular chaperones. *J. Biol. Chem.* **268**, 1517–1520 (1993).
13. Bhattacharyya, J. & Das, K. P. α-Crystallin does not require temperature activation for its chaperone-like activity. *IUBMB Life* **46**, 249–258 (1998).
14. Arrigo, A.-P. Human small heat shock proteins: Protein interactomes of homo- and hetero-oligomeric complexes: An update. *FEBS Lett.* **587**, 1959–1969 (2013).
15. Arrigo, A.-P. & Ducasse, C. Expression of the anti-apoptotic protein Hsp27 during both the keratinocyte differentiation and dedifferentiation of HaCat cells: expression linked to changes in intracellular protein organization? *Exp. Gerontol.* **37**, 1247–1255 (2002).
16. Benjamin, I. J., Shelton, J., Garry, D. J. & Richardson, J. A. Temporospatial expression of the small HSP/alpha B-crystallin in cardiac and skeletal muscle

during mouse development. *Dev. Dyn. Off. Publ. Am. Assoc. Anat.* **208**, 75–84 (1997).

17. Kamradt, M. C., Chen, F., Sam, S. & Cryns, V. L. The small heat shock protein alpha B-crystallin negatively regulates apoptosis during myogenic differentiation by inhibiting caspase-3 activation. *J. Biol. Chem.* **277**, 38731–38736 (2002).
18. Lavoie, J. N., Lambert, H., Hickey, E., Weber, L. A. & Landry, J. Modulation of cellular thermoresistance and actin filament stability accompanies phosphorylation-induced changes in the oligomeric structure of heat shock protein 27. *Mol. Cell. Biol.* **15**, 505–516 (1995).
19. Nicholl, I. D. & Quinlan, R. A. Chaperone activity of alpha-crystallins modulates intermediate filament assembly. *EMBO J.* **13**, 945–953 (1994).
20. Park, A.-M. *et al.* Heat Shock Protein 27 Plays a Pivotal Role in Myofibroblast Differentiation and in the Development of Bleomycin-Induced Pulmonary Fibrosis. *PloS One* **11**, e0148998 (2016).
21. Perng, M. D. *et al.* Intermediate filament interactions can be altered by HSP27 and alphaB-crystallin. *J. Cell Sci.* **112 (Pt 13)**, 2099–2112 (1999).
22. Morrow, G. & Tanguay, R. M. Small heat shock protein expression and functions during development. *Int. J. Biochem. Cell Biol.* **44**, 1613–1621 (2012).
23. Adriaenssens, E. *et al.* Small heat shock proteins operate as molecular chaperones in the mitochondrial intermembrane space. *Nat. Cell Biol.* **25**, 467–480 (2023).

24. Kamradt, M. C., Chen, F. & Cryns, V. L. The small heat shock protein alpha B-crystallin negatively regulates cytochrome c- and caspase-8-dependent activation of caspase-3 by inhibiting its autoproteolytic maturation. *J. Biol. Chem.* **276**, 16059–16063 (2001).

25. Tedesco, B., Vendredy, L., Timmerman, V. & Poletti, A. The chaperone-assisted selective autophagy complex dynamics and dysfunctions. *Autophagy* **19**, 1619–1641 (2023).

26. Transcriptional regulation of small heat shock protein genes by heat shock factor 1 (HSF1) in Liriomyza trifolii under heat stress - PubMed. https://pubmed.ncbi.nlm.nih.gov/34337672/.

27. Novel self-regulation strategy of a small heat shock protein for prodigious and rapid expression on demand - PubMed. https://pubmed.ncbi.nlm.nih.gov/33839884/.

28. Mymrikov, E. V. *et al.* Regulation of small heat-shock proteins by hetero-oligomer formation. *J. Biol. Chem.* **295**, 158–169 (2020).

29. Abisambra, J. F. *et al.* Phosphorylation Dynamics Regulate Hsp27-Mediated Rescue of Neuronal Plasticity Deficits in Tau Transgenic Mice. *J. Neurosci.* **30**, 15374–15382 (2010).

30. Ahmad, Md. F., Raman, B., Ramakrishna, T. & Rao, Ch. M. Effect of Phosphorylation on αB-crystallin: Differences in Stability, Subunit Exchange and Chaperone Activity of Homo and Mixed Oligomers of αB-Crystallin and its Phosphorylation-mimicking Mutant. *J. Mol. Biol.* **375**, 1040–1051 (2008).

31. Bakthisaran, R., Akula, K. K., Tangirala, R. & Rao, Ch. M. Phosphorylation of αB-crystallin: Role in stress, aging and patho-physiological conditions. *Biochim. Biophys. Acta BBA - Gen. Subj.* **1860**, 167–182 (2016).

32. Mühlhofer, M. *et al.* Phosphorylation activates the yeast small heat shock protein Hsp26 by weakening domain contacts in the oligomer ensemble. *Nat. Commun.* **12**, 6697 (2021).

33. Phosphorylation-Dependent Ubiquitination of Cyclin D1 by the SCFFBX4-αB Crystallin Complex.

34. Kantorow, M. & Piatigorsky, J. Phosphorylations of hA- and hB-crystallin. *Int. J. Biol. Macromol.* 8 (1998).

35. Mymrikov, E. V., Daake, M., Richter, B., Haslbeck, M. & Buchner, J. The Chaperone Activity and Substrate Spectrum of Human Small Heat Shock Proteins *. *J. Biol. Chem.* **292**, 672–684 (2017).

36. Andley, U. P., Malone, J. P. & Townsend, R. R. In Vivo Substrates of the Lens Molecular Chaperones αA-Crystallin and αB-Crystallin. *PLoS ONE* **9**, e95507 (2014).

37. Basha, E. *et al.* The identity of proteins associated with a small heat shock protein during heat stress in vivo indicates that these chaperones protect a wide range of cellular functions. *J. Biol. Chem.* **279**, 7566–7575 (2004).

38. Lee, G. J., Roseman, A. M., Saibil, H. R. & Vierling, E. A small heat shock protein stably binds heat-denatured model substrates and can maintain a substrate in a folding-competent state. *EMBO J.* **16**, 659–671 (1997).

39. Hsp70 displaces small heat shock proteins from aggregates to initiate protein refolding. https://www.embopress.org/doi/epdf/10.15252/embj.201593378 doi:10.15252/embj.201593378.

40. Ungelenk, S. *et al*. Small heat shock proteins sequester misfolding proteins in near-native conformation for cellular protection and efficient refolding. *Nat. Commun.* **7**, 13673 (2016).

41. Kappé, G. *et al*. The human genome encodes 10 alpha-crystallin-related small heat shock proteins: HspB1-10. *Cell Stress Chaperones* **8**, 53–61 (2003).

42. Haslbeck, M., Peschek, J., Buchner, J. & Weinkauf, S. Structure and function of α-crystallins: Traversing from in vitro to in vivo. *Biochim. Biophys. Acta BBA - Gen. Subj.* **1860**, 149–166 (2016).

43. Sprague-Piercy, M. A., Rocha, M. A., Kwok, A. O. & Martin, R. W. α-Crystallins in the Vertebrate Eye Lens: Complex Oligomers and Molecular Chaperones. *Annu. Rev. Phys. Chem.* **72**, 143–163 (2021).

44. Thorkelsson, A. & Chin, M. T. Role of the Alpha-B-Crystallin Protein in Cardiomyopathic Disease. *Int. J. Mol. Sci.* **25**, 2826 (2024).

45. Srinivas, P. N. B. S., Reddy, P. Y. & Reddy, G. B. Significance of alpha-crystallin heteropolymer with a 3:1 alphaA/alphaB ratio: chaperone-like activity, structure and hydrophobicity. *Biochem. J.* **414**, 453–460 (2008).

46. Braak, H., Tredici, K., Sandmann-Keil, D., Rüb, U. & Schultz, C. Nerve cells expressing heat-shock proteins in Parkinson's disease. *Acta Neuropathol. (Berl.)* **102**, 449–454 (2001).

47. Höhn, A., Tramutola, A. & Cascella, R. Proteostasis Failure in Neurodegenerative Diseases: Focus on Oxidative Stress. *Oxid. Med. Cell. Longev.* **2020**, (2020).

48. WHO | Priority eye diseases. *WHO* http://www.who.int/blindness/causes/priority/en/.

49. Bloemendal, H. *et al.* Ageing and vision: structure, stability and function of lens crystallins. *Prog. Biophys. Mol. Biol.* **86**, 407–485 (2004).

50. Tedesco, B. *et al.* Insights on Human Small Heat Shock Proteins and Their Alterations in Diseases. *Front. Mol. Biosci.* **9**, 842149 (2022).

51. Salinthone, S., Tyagi, M. & Gerthoffer, W. T. Small heat shock proteins in smooth muscle. *Pharmacol. Ther.* **119**, 44–54 (2008).

52. Lutsch, G. *et al.* Abundance and Location of the Small Heat Shock Proteins HSP25 and αB-Crystallin in Rat and Human Heart. *Circulation* **96**, 3466–3476 (1997).

53. Bova, M. P. *et al.* Mutation R120G in B-crystallin, which is linked to a desmin-related myopathy, results in an irregular structure and defective chaperone-like function. *Proc. Natl. Acad. Sci.* **96**, 6137–6142 (1999).

54. Vicart, P. *et al.* A missense mutation in the αB-crystallin chaperone gene causes a desmin-related myopathy. *Nat. Genet.* **20**, 92–95 (1998).

55. Martin, J. L., Mestril, R., Hilal-Dandan, R., Brunton, L. L. & Dillmann, W. H. Small heat shock proteins and protection against ischemic injury in cardiac myocytes. *Circulation* **96**, 4343–4348 (1997).

56. Dimauro, I., Antonioni, A., Mercatelli, N. & Caporossi, D. The role of αB-crystallin in skeletal and cardiac muscle tissues. *Cell Stress Chaperones* **23**, 491–505 (2018).

57. Ray, P. S. *et al*. Transgene overexpression of alphaB crystallin confers simultaneous protection against cardiomyocyte apoptosis and necrosis during myocardial ischemia and reperfusion. *FASEB J. Off. Publ. Fed. Am. Soc. Exp. Biol.* **15**, 393–402 (2001).

58. Fan, G.-C., Chu, G. & Kranias, E. G. Hsp20 and its cardioprotection. *Trends Cardiovasc. Med.* **15**, 138–141 (2005).

59. Miller, D. J. & Fort, P. E. Heat Shock Proteins Regulatory Role in Neurodevelopment. *Front. Neurosci.* **12**, (2018).

60. Abati, E. *et al*. Charcot–Marie–Tooth disease type 2F associated with biallelic HSPB1 mutations. *Ann. Clin. Transl. Neurol.* **8**, 1158–1164 (2021).

61. Baughman, H. E. R., Clouser, A. F., Klevit, R. E. & Nath, A. HspB1 and Hsc70 chaperones engage distinct tau species and have different inhibitory effects on amyloid formation. *J. Biol. Chem.* **293**, 2687–2700 (2018).

62. Hochberg, G. K. A. *et al*. The structured core domain of B-crystallin can prevent amyloid fibrillation and associated toxicity. *Proc. Natl. Acad. Sci.* **111**, E1562–E1570 (2014).

63. Mainz, A. *et al*. The chaperone αB-crystallin uses different interfaces to capture an amorphous and an amyloid client. *Nat. Struct. Mol. Biol.* **22**, 898–905 (2015).

64. Xi, D., Wei, P., Zhang, C. & Lai, L. The minimal α-crystallin domain of Mj Hsp16.5 is functional at non-heat-shock conditions. *Proteins* **82**, 1156–1167 (2014).

65. Baughman, H. E. R., Pham, T.-H. T., Adams, C. S., Nath, A. & Klevit, R. E. Release of a disordered domain enhances HspB1 chaperone activity toward tau. *Proc. Natl. Acad. Sci.* **117**, 2923–2929 (2020).

66. Wyttenbach, A. *et al.* Heat shock protein 27 prevents cellular polyglutamine toxicity and suppresses the increase of reactive oxygen species caused by huntingtin. *Hum. Mol. Genet.* **11**, 1137–1151 (2002).

67. Zourlidou, A., Payne Smith, M. D. & Latchman, D. S. HSP27 but not HSP70 has a potent protective effect against alpha-synuclein-induced cell death in mammalian neuronal cells. *J. Neurochem.* **88**, 1439–1448 (2004).

68. Freilich, R. *et al.* Competing protein-protein interactions regulate binding of Hsp27 to its client protein tau. *Nat. Commun.* **9**, 4563 (2018).

69. Hampton, D. W. *et al.* HspB5 Activates a Neuroprotective Glial Cell Response in Experimental Tauopathy. *Front. Neurosci.* **14**, 574 (2020).

70. Dabir, D. V., Trojanowski, J. Q. & Richter-Landsberg, C. Expression of the Small Heat-Shock Protein ␣B- Crystallin in Tauopathies with Glial Pathology. **164**, 12 (2004).

71. Santana, E., de los Reyes, T. & Casas-Tintó, S. Small heat shock proteins determine synapse number and neuronal activity during development. *PLoS ONE* **15**, e0233231 (2020).

72. de los Reyes, T. & Casas-Tintó, S. Neural functions of small heat shock proteins. *Neural Regen. Res.* **17**, 512–515 (2021).

73. Yang, F. *et al.* Reactive astrocytes secrete the chaperone HSPB1 to mediate neuroprotection. *Sci. Adv.* **10**, eadk9884.

74. Bassnett, S., Shi, Y. & Vrensen, G. F. J. M. Biological glass: structural determinants of eye lens transparency. *Philos. Trans. R. Soc. B Biol. Sci.* **366**, 1250–1264 (2011).

75. Delaye, M. & Tardieu, A. Short-range order of crystallin proteins accounts for eye lens transparency. *Nature* **302**, 415–417 (1983).

76. Siezen, R. J., Bindels, J. G. & Hoenders, H. J. The Quaternary Structure of Bovine alpha-Crystallin. Size and Charge Microheterogeneity: More than 1000 Different Hybrids? *Eur. J. Biochem.* **91**, 387–396 (1978).

77. Rao, P., Q. Huang, Horwitz, J. & Zigler Jr., J. Evidence that alpha-crystallin prevents non-specific protein aggregation in the intact eye lens. *Biochim. Biophys. Acta BBA - Gen. Subj.* **1245**, 439–47 (1995).

78. Thomson, J. A. & Augusteyn, R. C. Ontogeny of human lens crystallins. *Exp. Eye Res.* **40**, 393–410 (1985).

79. Benedek, G. B., Pande, J., Thurston, G. M. & Clark, J. I. Theoretical and experimental basis for the inhibition of cataract. *Prog. Retin. Eye Res.* **18**, 391–402 (1999).

80. Lampi, K. J. *et al*. Age-related Changes in Human Lens Crystallins Identified by Two-dimensional Electrophoresis and Mass Spectrometry. *Exp. Eye Res.* **67**, 31–43 (1998).

81. Philipson, B. T. & Fagerholm, P. P. Human subcapsular cataract — Distribution of protein in relation to opacification. *Exp. Eye Res.* **33**, 621–630 (1981).

82. Wilmarth, P. A. *et al*. Age-Related Changes in Human Crystallins Determined from Comparative Analysis of Post-translational Modifications in Young and Aged Lens: Does Deamidation Contribute to Crystallin Insolubility? *J. Proteome Res.* **5**, 2554–2566 (2006).

83. Pascolini, D. & Mariotti, S. P. Global estimates of visual impairment: 2010. *Br. J. Ophthalmol.* **96**, 614–618 (2012).

84. Kapphahn, R. J., Ethen, C. M., Peters, E. A., Higgins, L. & Ferrington, D. A. Modified alpha A crystallin in the retina: altered expression and truncation with aging. *Biochemistry* **42**, 15310–15325 (2003).

85. Kato, K. *et al*. Tissue distribution and developmental profiles of immunoreactive αB crystallin in the rat determined with a sensitive immunoassay system. *Biochim. Biophys. Acta BBA - Gen. Subj.* **1074**, 201–208 (1991).

86. Shiels, A. & Hejtmancik, J. F. Inherited Cataracts: Genetic Mechanisms and Pathways New and Old. *Exp. Eye Res.* **209**, 108662 (2021).

87. Clark, A. R., Lubsen, N. H. & Slingsby, C. sHSP in the eye lens: Crystallin mutations, cataract and proteostasis. *Int. J. Biochem. Cell Biol.* **44**, 1687–1697 (2012).

88. Shiels, A., Bennett, T. M. & Hejtmancik, J. F. Cat-Map: putting cataract on the map. *Mol. Vis.* **16**, 2007–2015 (2010).

89. Lampros, M., Vlachos, N., Voulgaris, S. & Alexiou, G. A. The Role of Hsp27 in Chemotherapy Resistance. *Biomedicines* **10**, 897 (2022).

90. Malin, D., Petrovic, V., Strekalova, E., Sharma, B. & Cryns, V. L. αB-crystallin: Portrait of a malignant chaperone as a cancer therapeutic target. *Pharmacol. Ther.* **160**, 1–10 (2016).

91. Malin, D. *et al.* αB-crystallin: a Novel Regulator of Breast Cancer Metastasis to the Brain. *Clin. Cancer Res. Off. J. Am. Assoc. Cancer Res.* **20**, 56–67 (2014).

92. Tan, L. *et al.* High α B-crystallin and p53 co-expression is associated with poor prognosis in ovarian cancer. *Biosci. Rep.* **39**, BSR20182407 (2019).

93. Morishita, H. *et al.* Organelle degradation in the lens by PLAAT phospholipases. *Nature* **592**, 634–638 (2021).

94. Disassembly of the lens fiber cell nucleus to create a clear lens: The p27 descent - PubMed. https://pubmed.ncbi.nlm.nih.gov/26946072/.

95. Bassnett, S. On the mechanism of organelle degradation in the vertebrate lens. *Exp. Eye Res.* **88**, 133–139 (2009).

96. Wanko, T. & Gavin, M. A. Electron microscope study of lens fibers. *J. Biophys. Biochem. Cytol.* **6**, 97–102 (1959).

97. Foffi, G. *et al.* Hard sphere-like glass transition in eye lens α-crystallin solutions. *Proc. Natl. Acad. Sci.* **111**, 16748–16753 (2014).

98. Horwitz, J. Alpha-crystallin. *Exp. Eye Res.* **76**, 145–153 (2003).

99. Andley, U. P. Crystallins in the eye: Function and pathology. *Prog. Retin. Eye Res.* **26**, 78–98 (2007).

100. Mathias, R. T., Kistler, J. & Donaldson, P. The lens circulation. *J. Membr. Biol.* **216**, 1–16 (2007).

101. Zhu, Y., Xu, S., Eisenberg, R. S. & Huang, H. A Bidomain Model for Lens Microcirculation. *Biophys. J.* **116**, 1171–1184 (2019).

102. Sue Menko, A. Lens epithelial cell differentiation. *Exp. Eye Res.* **75**, 485–490 (2002).

103. Lynnerup, N., Kjeldsen, H., Heegaard, S., Jacobsen, C. & Heinemeier, J. Radiocarbon dating of the human eye lens crystallines reveal proteins without carbon turnover throughout life. *PloS One* **3**, e1529 (2008).

104. Robertson, L. J. G. *et al.* Susceptibility of Ovine Lens Crystallins to Proteolytic Cleavage during Formation of Hereditary Cataract. *Investig. Opthalmology Vis. Sci.* **49**, 1016 (2008).

105. Lampi, K. J., Wilmarth, P. A., Murray, M. R. & David, L. L. Lens β-crystallins: the role of deamidation and related modifications in aging and cataract. *Prog. Biophys. Mol. Biol.* **115**, 21–31 (2014).

106. Ueda, Y., Duncan, M. K. & David, L. L. Lens Proteomics: The Accumulation of Crystallin Modifications in the Mouse Lens with Age. **43**, 11 (2002).

107. Nandi, S. K., Nahomi, R. B., Rankenberg, J., Glomb, M. & Nagaraj, R. H. Molecular mechanisms for protein crosslinking in human lens: the role of glycation-mediated crosslinking of α-crystallin-client complexes. *Invest. Ophthalmol. Vis. Sci.* **61**, 3476–3476 (2020).

108. Fujii, N. *et al.* Correlation between the loss of the chaperone-like activity and the oxidation, isomerization and racemization of gamma-irradiated alpha-crystallin. *Photochem. Photobiol.* **74**, 477–482 (2001).

109. Roskamp, K. W., Paulson, C. N., Brubaker, W. D. & Martin, R. W. Function and Aggregation in Structural Eye Lens Crystallins. *Acc. Chem. Res.* **53**, 863–874 (2020).

110. Michiel, M. *et al.* Aggregation of deamidated human βB2-crystallin and incomplete rescue by α-crystallin chaperone. *Exp. Eye Res.* **90**, 688–698 (2010).

111. Lampi, K. J., Fox, C. B. & David, L. L. Changes in solvent accessibility of wild-type and deamidated βB2-crystallin following complex formation with αA-crystallin. *Exp. Eye Res.* **104**, 48–58 (2012).

112. Roskamp, K. W. *et al.* Multiple Aggregation Pathways in Human γS-Crystallin and Its Aggregation-Prone G18V Variant. *Invest. Ophthalmol. Vis. Sci.* **58**, 2397–2405 (2017).

113. Sprague-Piercy, M. A. *et al.* Human αB-crystallin discriminates between aggregation-prone and function-preserving variants of a client protein. *Biochim. Biophys. Acta Gen. Subj.* **1864**, 129502 (2020).

114. Norton-Baker, B. *et al.* Deamidation of the human eye lens protein γS-crystallin accelerates oxidative aging. *Struct. Lond. Engl. 1993* **30**, 763-776.e4 (2022).

115. Siezen, R. J., Bindels, J. G. & Hoenders, H. J. The interrelationship between monomeric, oligomeric and polymeric α-crystallin in the calf lens nucleus. *Exp. Eye Res.* **28**, 551–567 (1979).

116. Mörner, C. T. Untersuchung der Proteïnsubstanzen in den leichtbrechenden Medien des Auges I. **18**, 61–106 (1894).

117. Peschek, J. *et al.* The eye lens chaperone -crystallin forms defined globular assemblies. *Proc. Natl. Acad. Sci.* **106**, 13272–13277 (2009).

118. Miller, A. P., O'Neill, S. E., Lampi, K. J. & Reichow, S. L. The α-crystallin Chaperones Undergo a Quasi-ordered Co-aggregation Process in Response to Saturating Client Interaction. *J. Mol. Biol.* **436**, 168499 (2024).

119. Koteiche, H. A. & Mchaourab, H. S. Mechanism of Chaperone Function in Small Heat-shock Proteins: PHOSPHORYLATION-INDUCED ACTIVATION OF TWO-MODE BINDING IN αB-CRYSTALLIN. *J. Biol. Chem.* **278**, 10361–10367 (2003).

120. Mishra, S., Stein, R. A. & Mchaourab, H. S. Cataract-linked γD-crystallin mutants have weak affinity to lens chaperones α-crystallins. *FEBS Lett.* **586**, 330–336 (2012).

121. Augusteyn, R. C. α-crystallin: a review of its structure and function. *Clin. Exp. Optom.* **87**, 356–366 (2004).

122. Boyle, D. L., Takemoto, L., Brady, J. P. & Wawrousek, E. F. Morphological characterization of the AlphaA- and AlphaB-crystallin double knockout mouse lens. *BMC Ophthalmol.* **3**, 3 (2003).

123. Brady, J. P. *et al.* Targeted disruption of the mouse A-crystallin gene induces cataract and cytoplasmic inclusion bodies containing the small heat shock protein B-crystallin. *Proc. Natl. Acad. Sci.* **94**, 884–889 (1997).

124. Aquilina, J. A., Benesch, J. L. P., Bateman, O. A., Slingsby, C. & Robinson, C. V. Polydispersity of a mammalian chaperone: Mass spectrometry reveals the population of oligomers in B-crystallin. *Proc. Natl. Acad. Sci.* **100**, 10611–10616 (2003).

125. Aquilina, J. A. *et al.* Subunit Exchange of Polydisperse Proteins: MASS SPECTROMETRY REVEALS CONSEQUENCES OF αA-CRYSTALLIN TRUNCATION. *J. Biol. Chem.* **280**, 14485–14491 (2005).

126. Fujii, N. *et al.* Comparison of post-translational modifications of alpha A-crystallin from normal and hereditary cataract rats. *Amino Acids* **26**, 147–152 (2004).

127. S R Hanson, Hasan, A., Smith, D. & Smith, J. The major in vivo modifications of the human water-insoluble lens crystallins are disulfide bonds, deamidation, methionine oxidation and backbone cleavage. *Exp Eye Res* **71**, 195–207 (2000).

128. Schmid, P. W. N. *et al.* Imbalances in the eye lens proteome are linked to cataract formation. *Nat. Struct. Mol. Biol.* **28**, 143–151 (2021).

129. Cetinel, S. *et al.* UV-B induced fibrillization of crystallin protein mixtures. *PLoS ONE* **12**, e0177991 (2017).

130. Weinreb, O. & Bloemendal, H. Effect of UV-A Light on the Chaperone-like Properties of Young and Old Lens ␣-Crystallin. **41**, 8 (2000).

131. Serebryany, E. *et al.* Aggregation of Trp > Glu point mutants of human gamma-D crystallin provides a model for hereditary or UV-induced cataract. *Protein Sci. Publ. Protein Soc.* **25**, 1115–1128 (2016).

132. Duot, M. *et al.* Eye Lens Organoids Made Simple: Characterization of a New Three-Dimensional Organoid Model for Lens Development and Pathology. *Cells* **12**, 2478 (2023).

133. Plüss, C. J. & Kustermann, S. A Human Three-Dimensional In Vitro Model of Lens Epithelial Cells as a Model to Study Mechanisms of Drug-Induced Posterior Subcapsular Cataracts. *J. Ocul. Pharmacol. Ther.* **36**, 56–64 (2020).

134. Voorter, C., Leunissen, J. & de Jong, W.W., W. de. Evolution of the alpha-crystallin/small heat-shock protein family. *Mol Biol Evol* **10**, 103–126 (1993).

135. Sluchanko, N. N. *et al.* Structural Basis for the Interaction of a Human Small Heat Shock Protein with the 14-3-3 Universal Signaling Regulator. *Structure* **25**, 305–316 (2017).

136. Bagnéris, C. *et al.* Crystal Structures of α-Crystallin Domain Dimers of αB-Crystallin and Hsp20. *J. Mol. Biol.* **392**, 1242–1252 (2009).

137. van Montfort, R. L. M., Basha, E., Friedrich, K. L., Slingsby, C. & Vierling, E. Crystal structure and assembly of a eukaryotic small heat shock protein. *Nat. Struct. Biol.* **8**, 1025–1030 (2001).

138. Kim, K. K., Kim, R. & Kim, S.-H. Crystal structure of a small heat-shock protein. **394**, (1998).

139. Rajagopal, P. *et al.* A conserved histidine modulates HSPB5 structure to trigger chaperone activity in response to stress-related acidosis. *eLife* **4**, e07304 (2015).

140. Hanazono, Y., Takeda, K., Yohda, M. & Miki, K. Structural Studies on the Oligomeric Transition of a Small Heat Shock Protein, StHsp14.0. *J. Mol. Biol.* **422**, 100–108 (2012).

141. Ghosh, J., Estrada, M. & Clark, J. Interactive domains for chaperone activity in the small heat shock protein, human alphaB crystallin. *Biochemistry* **44**, 14854–69 (2005).

142. Banerjee, P. R., Pande, A., Shekhtman, A. & Pande, J. Molecular mechanism of the chaperone function of mini-α-crystallin, a 19-residue peptide of human α-crystallin. *Biochemistry* **54**, 505–515 (2015).

143. Xi, D., Wei, P., Zhang, C. & Lai, L. The minimal α-crystallin domain of Mj Hsp16.5 is functional at non-heat-shock conditions. *Proteins Struct. Funct. Bioinforma.* **82**, 1156–1167 (2014).

144. Mani, N. *et al.* Multiple oligomeric structures of a bacterial small heat shock protein. *Sci. Rep.* **6**, 24019 (2016).

145. McFarland, R. & Reichow, S. Dynamic fibrillar assembly of αB-crystallin induced by perturbation of the conserved NT-IXI motif resolved by cryo-EM. Preprint at https://doi.org/10.1101/2024.03.22.586355 (2024).

146. Ghosh, J. G., Shenoy, A. K. & Clark, J. I. N- and C-Terminal motifs in human alphaB crystallin play an important role in the recognition, selection, and solubilization of substrates. *Biochemistry* **45**, 13847–13854 (2006).

147. Webster, J. M. *et al.* Hsp22 with an N-Terminal Domain Truncation Mediates a Reduction in Tau Protein Levels. *Int. J. Mol. Sci.* **21**, 5442 (2020).

148. Clouser, A. F., Baughman, H. E. R., Basanta, B., Guttman, M. & Klevit, R. E. Interplay of disordered and ordered regions of a human small heat shock protein yields an ensemble of “quasi-ordered” states. 54.

149. Woods, C. N., Ulmer, L. D., Guttman, M., Bush, M. F. & Klevit, R. E. Disordered region encodes α-crystallin chaperone activity toward lens client γD-crystallin. *Proc. Natl. Acad. Sci.* **120**, e2213765120 (2023).

150. Pasta, S. Y., Raman, B., Ramakrishna, T. & Rao, C. M. Role of the conserved SRLFDQFFG region of alpha-crystallin, a small heat shock protein. Effect on oligomeric size, subunit exchange, and chaperone-like activity. *J. Biol. Chem.* **278**, 51159–51166 (2003).

151. Shatov, V. M., Sluchanko, N. N. & Gusev, N. B. Replacement of Arg in the conserved N-terminal RLFDQxFG motif affects physico-chemical properties and chaperone-like activity of human small heat shock protein HspB8 (Hsp22). *PloS One* **16**, e0253432 (2021).

152. Shatov, V. M., Weeks, S. D., Strelkov, S. V. & Gusev, N. B. The Role of the Arginine in the Conserved N-Terminal Domain RLFDQxFG Motif of Human Small Heat Shock Proteins HspB1, HspB4, HspB5, HspB6, and HspB8. *Int. J. Mol. Sci.* **19**, 2112 (2018).

153. Weeks, S. D. *et al.* Molecular structure and dynamics of the dimeric human small heat shock protein HSPB6. *J. Struct. Biol.* **185**, 342–354 (2014).

154. Clark, A. R. *et al.* Terminal Regions Confer Plasticity to the Tetrameric Assembly of Human HspB2 and HspB3. *J. Mol. Biol.* **430**, 3297–3310 (2018).

155. Shi, X. *et al.* Small heat shock protein AgsA forms dynamic fibrils. *FEBS Lett.* **585**, 3396–3402 (2011).

156. Koteiche, H. A., Chiu, S., Majdoch, R. L., Stewart, P. L. & Mchaourab, H. S. Atomic models by cryo-EM and site-directed spin labeling: application to the N-terminal region of Hsp16.5. *Struct. Lond. Engl. 1993* **13**, 1165–1171 (2005).

157. Strauch, A. *et al.* The permanently chaperone-active small heat shock protein Hsp17 from Caenorhabditis elegans exhibits topological separation of its N-terminal regions. *J. Biol. Chem.* **299**, 102753 (2023).

158. Braun, N. *et al.* Multiple molecular architectures of the eye lens chaperone αB-crystallin elucidated by a triple hybrid approach. *PNAS* **108**, 20491–20496 (2011).

159. Kurre, D. & Suguna, K. Network of Entamoeba histolytica HSP18.5 dimers formed by two overlapping [IV]-X-[IV] motifs. *Proteins* (2021) doi:10.1002/prot.26081.

160. Kaiser, C. J. O. *et al*. The structure and oxidation of the eye lens chaperone αA-crystallin. *Nat. Struct. Mol. Biol.* **26**, 1141–1150 (2019).

161. White, H. E. *et al*. Multiple distinct assemblies reveal conformational flexibility in the small heat shock protein Hsp26. *Struct. Lond. Engl. 1993* **14**, 1197–1204 (2006).

162. Bova, M. P., Ding, L., Horwitz, J. & Fung, B. K.-K. Subunit Exchange of aA-crystallin. *J. Biol. Chem.* **272**, 29511–29517 (1997).

163. Bova, M. P., Mchaourab, H. S., Han, Y. & Fung, B. K.-K. Subunit Exchange of Small Heat Shock Proteins. *J. Biol. Chem.* **275**, 1035–1042 (2000).

164. Bova, M. P., Huang, Q., Ding, L. & Horwitz, J. Subunit Exchange, Conformational Stability, and Chaperone-like Function of the Small Heat Shock Protein 16.5 fromMethanococcus jannaschii. *J. Biol. Chem.* **277**, 38468–38475 (2002).

165. Fu, X. & Chang, Z. Temperature-dependent subunit exchange and chaperone-like activities of Hsp16.3, a small heat shock protein from Mycobacterium tuberculosis. *Biochem. Biophys. Res. Commun.* **316**, 291–299 (2004).

166. Nandi, S. K., Panda, A. K., Chakraborty, A., Ray, S. S. & Biswas, A. Role of Subunit Exchange and Electrostatic Interactions on the Chaperone Activity of Mycobacterium leprae HSP18. *PLoS ONE* **10**, e0129734 (2015).

167. Augusteyn, R. C. Dissociation is not required for α-crystallin's chaperone function. *Exp. Eye Res.* **79**, 781–784 (2004).

168. Johnston, C. L. *et al.* Single-molecule fluorescence-based approach reveals novel mechanistic insights into human small heat shock protein chaperone function. *J. Biol. Chem.* **296**, 100161 (2021).

169. Aquilina, J. A. *et al.* Phosphorylation of αB-Crystallin Alters Chaperone Function through Loss of Dimeric Substructure. *J. Biol. Chem.* **279**, 28675–28680 (2004).

170. Ecroyd, H. *et al.* Mimicking phosphorylation of αB-crystallin affects its chaperone activity. *Biochem. J.* **401**, 129–141 (2007).

171. Ito, H. *et al.* Phosphorylation-induced Change of the Oligomerization State of αB-crystallin. *J. Biol. Chem.* **276**, 5346–5352 (2001).

172. Fürsch, J., Voormann, C., Kammer, K.-M. & Stengel, F. Structural Probing of Hsp26 Activation and Client Binding by Quantitative Cross-Linking Mass Spectrometry. *Anal. Chem.* **93**, 13226–13234 (2021).

173. Baldwin, A. J. *et al.* The Polydispersity of αB-Crystallin Is Rationalized by an Interconverting Polyhedral Architecture. *Structure* **19**, 1855–1863 (2011).

174. Mishra, S. *et al.* Engineering of a Polydisperse Small Heat-Shock Protein Reveals Conserved Motifs of Oligomer Plasticity. *Structure* **26**, 1116-1126.e4 (2018).

175. Shi, J., Koteiche, H. A., McHaourab, H. S. & Stewart, P. L. Cryoelectron microscopy and EPR analysis of engineered symmetric and polydisperse Hsp16.5 assemblies reveals determinants of polydispersity and substrate binding. *J. Biol. Chem.* **281**, 40420–40428 (2006).

176. Yu, C. *et al.* Structural basis of substrate recognition and thermal protection by a small heat shock protein. *Nat. Commun.* **12**, 3007 (2021).

177. Åhrman, E., Lambert, W., Aquilina, J. A., Robinson, C. V. & Emanuelsson, C. S. Chemical cross-linking of the chloroplast localized small heat-shock protein, Hsp21, and the model substrate citrate synthase. *Protein Sci. Publ. Protein Soc.* **16**, 1464–1478 (2007).

178. Cheng, G., Basha, E., Wysocki, V. H. & Vierling, E. Insights into Small Heat Shock Protein and Substrate Structure during Chaperone Action Derived from Hydrogen/Deuterium Exchange and Mass Spectrometry. *J. Biol. Chem.* **283**, 26634–26642 (2008).

179. Żwirowski, S. *et al.* Hsp70 displaces small heat shock proteins from aggregates to initiate protein refolding. *EMBO J.* **36**, 783–796 (2017).

180. Mchaourab, H. S., Dodson, E. K. & Koteiche, H. A. Mechanism of Chaperone Function in Small Heat Shock Proteins: TWO-MODE BINDING OF THE EXCITED STATES OF T4 LYSOZYME MUTANTS BY αA-CRYSTALLIN. *J. Biol. Chem.* **277**, 40557–40566 (2002).

181. Sathish, H. A., Stein, R. A., Yang, G. & Mchaourab, H. S. Mechanism of Chaperone Function in Small Heat-shock Proteins. *J. Biol. Chem.* **278**, 44214–44221 (2003).

182. Shashidharamurthy, R., Koteiche, H. A., Dong, J. & Mchaourab, H. S. Mechanism of Chaperone Function in Small Heat Shock Proteins: DISSOCIATION OF THE HSP27 OLIGOMER IS REQUIRED FOR RECOGNITION

AND BINDING OF DESTABILIZED T4 LYSOZYME*. *J. Biol. Chem.* **280**, 5281–5289 (2005).

183. Shi, J. *et al.* Cryoelectron Microscopy Analysis of Small Heat Shock Protein 16.5 (Hsp16.5) Complexes with T4 Lysozyme Reveals the Structural Basis of Multimode Binding. *J. Biol. Chem.* **288**, 4819–4830 (2013).
184. Stengel, F. *et al.* Quaternary dynamics and plasticity underlie small heat shock protein chaperone function. *Proc. Natl. Acad. Sci.* **107**, 2007–2012 (2010).
185. Stromer, T., Ehrnsperger, M., Gaestel, M. & Buchner, J. Analysis of the Interaction of Small Heat Shock Proteins with Unfolding Proteins*. *J. Biol. Chem.* **278**, 18015–18021 (2003).
186. Stengel, F. *et al.* Dissecting Heterogeneous Molecular Chaperone Complexes Using a Mass Spectrum Deconvolution Approach. *Chem. Biol.* **19**, 599–607 (2012).
187. Rice, L., Marzano, N., Cox, D., Oijen, A. van & Ecroyd, H. Single-molecule observations of human small heat shock proteins in complex with aggregation-prone client proteins. 2024.02.08.579576 Preprint at https://doi.org/10.1101/2024.02.08.579576 (2024).
188. Ungelenk, S. *et al.* Small heat shock proteins sequester misfolding proteins in near-native conformation for cellular protection and efficient refolding. *Nat. Commun.* **7**, 13673 (2016).

189. Iburg, M. *et al.* The noncanonical small heat shock protein HSP-17 from Caenorhabditis elegans is a selective protein aggregase. *J. Biol. Chem.* **295**, 3064–3079 (2020).

190. Morelli, F. F. *et al.* Aberrant Compartment Formation by HSPB2 Mislocalizes Lamin A and Compromises Nuclear Integrity and Function. *Cell Rep.* **20**, 2100–2115 (2017).

191. Joosten, J. *et al.* Dynamics and Composition of Small Heat Shock Protein Condensates and Aggregates. *J. Mol. Biol.* **435**, 168139 (2023).

192. Kedersha, N. L., Gupta, M., Li, W., Miller, I. & Anderson, P. RNA-binding proteins TIA-1 and TIAR link the phosphorylation of eIF-2 alpha to the assembly of mammalian stress granules. *J. Cell Biol.* **147**, 1431–1442 (1999).

193. Protter, D. S. W. & Parker, R. Principles and Properties of Stress granules. *Trends Cell Biol.* **26**, 668–679 (2016).

194. Lee, J., Ryu, B., Kim, T. & Kim, K. K. Cryo-EM structure of a 16.5-kDa small heat-shock protein from Methanocaldococcus jannaschii. *Int. J. Biol. Macromol.* **258**, 128763 (2024).

195. Yasuda, R., Hayashi, Y. & Hell, J. W. CaMKII: a central molecular organizer of synaptic plasticity, learning and memory. *Nat. Rev. Neurosci.* **23**, 666–682 (2022).

196. Buonarati, O. R., Miller, A. P., Coultrap, S. J., Bayer, K. U. & Reichow, S. L. Conserved and divergent features of neuronal CaMKII holoenzyme structure,

function, and high-order assembly. *bioRxiv* 2021.01.21.427643 (2021) doi:10.1101/2021.01.21.427643.

197. Wistow, G. Domain structure and evolution in alpha-crystallins and small heat-shock proteins. *FEBS Lett* **181**, 1–6 (1985).
198. Carra, S. *et al.* Small heat shock proteins: multifaceted proteins with important implications for life. *Cell Stress Chaperones* **24**, 295–308 (2019).
199. Kappe, G. *et al.* The human genome encodes 10 alpha-crystallin-related small heat shock proteins: HspB1-10. *Cell Stress Chaperones* **8**, 53–61 (2003).
200. Slingsby, C. & Wistow, G. J. Functions of crystallins in and out of lens: roles in elongated and post-mitotic cells. *Prog Biophys Mol Biol* **115**, 52–67 (2014).
201. Bakthisaran, R., Tangirala, R. & Rao, Ch. M. Small heat shock proteins: Role in cellular functions and pathology. *Biochim. Biophys. Acta BBA - Proteins Proteomics* **1854**, 291–319 (2015).
202. Ecroyd, H. & Carver, J. A. Crystallin proteins and amyloid fibrils. *Cell Mol Life Sci* **66**, 62–81 (2009).
203. Haslbeck, M., Weinkauf, S. & Buchner, J. Small heat shock proteins: Simplicity meets complexity. *J. Biol. Chem.* **294**, 2121–2132 (2019).
204. Haley, D. A., Bova, M. P., Huang, Q.-L., Mchaourab, H. S. & Stewart, P. L. Small heat-shock protein structures reveal a continuum from symmetric to variable assemblies. *J. Mol. Biol.* **298**, 261–272 (2000).
205. Inoue, R. *et al.* New insight into the dynamical system of αB-crystallin oligomers. *Sci. Rep.* **6**, 29208 (2016).

206. Lambert, H., Charette, S. J., Bernier, A. F., Guimond, A. & Landry, J. HSP27 multimerization mediated by phosphorylation-sensitive intermolecular interactions at the amino terminus. *J Biol Chem* **274**, 9378–85 (1999).

207. Ehrnsperger, M., Lilie, H., Gaestel, M. & Buchner, J. The dynamics of Hsp25 quaternary structure. Structure and function of different oligomeric species. *J Biol Chem* **274**, 14867–74 (1999).

208. Klevit, R. E. Peeking from behind the veil of enigma: emerging insights on small heat shock protein structure and function. *Cell Stress Chaperones* **25**, 573–580 (2020).

209. Jehle, S. *et al.* N-terminal domain of alphaB-crystallin provides a conformational switch for multimerization and structural heterogeneity. *Proc Natl Acad Sci U A* **108**, 6409–14 (2011).

210. Pasta, S. Y., Raman, B., Ramakrishna, T. & Rao, C. M. The IXI/V motif in the C-terminal extension of α-crystallins: alternative interactions and oligomeric assemblies. *Mol. Vis.* 8.

211. Jehle, S. *et al.* Solid-state NMR and SAXS studies provide a structural basis for the activation of αB-crystallin oligomers. *Nat. Struct. Mol. Biol.* **17**, 1037–1042 (2010).

212. Haley, D. A., Horwitz, J. & Stewart, P. L. The small heat-shock protein, αb-crystallin, has a variable quaternary structure. *J. Mol. Biol.* **277**, 27–35 (1998).

213. Bova, M. P., McHaourab, H. S., Han, Y. & Fung, B. K. Subunit exchange of small heat shock proteins. Analysis of oligomer formation of alphaA-crystallin and

Hsp27 by fluorescence resonance energy transfer and site-directed truncations. *J Biol Chem* **275**, 1035–42 (2000).

214. Aquilina, J. A. *et al.* Subunit exchange of polydisperse proteins: mass spectrometry reveals consequences of alphaA-crystallin truncation. *J Biol Chem* **280**, 14485–91 (2005).
215. Delbecq, S. P., Rosenbaum, J. C. & Klevit, R. E. A Mechanism of Subunit Recruitment in Human Small Heat Shock Protein Oligomers. *Biochemistry* **54**, 4276–4284 (2015).
216. Inoue, R. *et al.* Elucidation of the mechanism of subunit exchange in alphaB crystallin oligomers. *Sci Rep* **11**, 2555 (2021).
217. Giese, K. C. & Vierling, E. Changes in oligomerization are essential for the chaperone activity of a small heat shock protein in vivo and in vitro. *J Biol Chem* **277**, 46310–8 (2002).
218. Santhanagopalan, I. *et al.* It takes a dimer to tango: Oligomeric small heat shock proteins dissociate to capture substrate. *J. Biol. Chem.* **293**, 19511–19521 (2018).
219. Ehrnsperger, M., Gräber, S., Gaestel, M. & Buchner, J. Binding of non-native protein to Hsp25 during heat shock creates a reservoir of folding intermediates for reactivation. *EMBO J.* **16**, 221–229 (1997).
220. Goncalves, C. C., Sharon, I., Schmeing, T. M., Ramos, C. H. I. & Young, J. C. The chaperone HSPB1 prepares protein aggregates for resolubilization by HSP70. *Sci Rep* **11**, 17139 (2021).

221. Wang, K. & Spector, A. alpha-crystallin prevents irreversible protein denaturation and acts cooperatively with other heat-shock proteins to renature the stabilized partially denatured protein in an ATP-dependent manner. *Eur J Biochem* **267**, 4705–12 (2000).

222. Cashikar, A. G., Duennwald, M. & Lindquist, S. L. A chaperone pathway in protein disaggregation. Hsp26 alters the nature of protein aggregates to facilitate reactivation by Hsp104. *J Biol Chem* **280**, 23869–75 (2005).

223. Walther, D. M. *et al*. Widespread Proteome Remodeling and Aggregation in Aging C. elegans. *Cell* **161**, 919–32 (2015).

224. Stromer, T., Ehrnsperger, M., Gaestel, M. & Buchner, J. Analysis of the Interaction of Small Heat Shock Proteins with Unfolding Proteins. *J. Biol. Chem.* **278**, 18015–18021 (2003).

225. Vetter, C. J. *et al*. Cumulative deamidations of the major lens protein γS-crystallin increase its aggregation during unfolding and oxidation. *Protein Sci. Publ. Protein Soc.* **29**, 1945–1963 (2020).

226. Siezen, R. J., Bindels, J. G. & Hoenders, H. J. The quaternary structure of bovine alpha-crystallin. Effects of variation in alkaline pH, ionic strength, temperature and calcium ion concentration. *Eur J Biochem* **111**, 435–44 (1980).

227. Selivanova, O. M. & Galzitskaya, O. V. Structural and Functional Peculiarities of α-Crystallin. *Biology* **9**, 85 (2020).

228. Myers, J. B. *et al*. Structure of native lens connexin 46/50 intercellular channels by cryo-EM. *Nature* **564**, 372–377 (2018).

229. Mostofian, B. *et al.* Continuum dynamics and statistical correction of compositional heterogeneity in multivalent IDP oligomers resolved by single-particle EM. *bioRxiv* 2020.06.16.154096 (2021) doi:10.1101/2020.06.16.154096.

230. Schindelin, J. *et al.* Fiji: an open-source platform for biological-image analysis. *Nat. Methods* **9**, 676–682 (2012).

231. Kummer, N. *et al.* Self-Assembly Pathways and Antimicrobial Properties of Lysozyme in Different Aggregation States. *Biomacromolecules* **22**, 4327–4336 (2021).

232. Srinivas, P., Narahari, A., Petrash, J. M., Swamy, M. J. & Reddy, G. B. Importance of eye lens alpha-crystallin heteropolymer with 3:1 alphaA to alphaB ratio: stability, aggregation, and modifications. *IUBMB Life* **62**, 693–702 (2010).

233. Grosas, A. B., Rekas, A., Mata, J. P., Thorn, D. C. & Carver, J. A. The Aggregation of αB-Crystallin under Crowding Conditions Is Prevented by αA-Crystallin: Implications for α-Crystallin Stability and Lens Transparency. *J. Mol. Biol.* **432**, 5593–5613 (2020).

234. Harms, M. J. *et al.* Laser light-scattering evidence for an altered association of beta B1-crystallin deamidated in the connecting peptide. *Protein Sci* **13**, 678–86 (2004).

235. Wright, M. A. *et al.* Analysis of alphaB-crystallin polydispersity in solution through native microfluidic electrophoresis. *Analyst* **144**, 4413–4424 (2019).

236. Tardieu, A. alpha-Crystallin quaternary structure and interactive properties control eye lens transparency. *Int J Biol Macromol* **22**, 211–7 (1998).

237. Bagneris, C. *et al.* Crystal structures of alpha-crystallin domain dimers of alphaB-crystallin and Hsp20. *J Mol Biol* **392**, 1242–52 (2009).

238. Clark, A. R., Naylor, C. E., Bagneris, C., Keep, N. H. & Slingsby, C. Crystal structure of R120G disease mutant of human alphaB-crystallin domain dimer shows closure of a groove. *J Mol Biol* **408**, 118–34 (2011).

239. Laganowsky, A. & Eisenberg, D. Non-3D domain swapped crystal structure of truncated zebrafish alphaA crystallin. *Protein Sci* **19**, 1978–84 (2010).

240. Reddy, G. B., Kumar, P. A. & Kumar, M. S. Chaperone-like activity and hydrophobicity of alpha-crystallin. *IUBMB Life* **58**, 632–41 (2006).

241. Lampi, K. J. *et al.* Decreased heat stability and increased chaperone requirement of modified human βB1-crystallins. *Mol. Vis.* 8 (2002).

242. Harkness, R. W., Ripstein, Z. A., Di Trani, J. M. & Kay, L. E. Flexible Client-Dependent Cages in the Assembly Landscape of the Periplasmic Protease-Chaperone DegP. *J Am Chem Soc* **145**, 13015–13026 (2023).

243. Zwirowski, S. *et al.* Hsp70 displaces small heat shock proteins from aggregates to initiate protein refolding. *EMBO J* **36**, 783–796 (2017).

244. Obuchowski, I., Piróg, A., Stolarska, M., Tomiczek, B. & Liberek, K. Duplicate divergence of two bacterial small heat shock proteins reduces the demand for Hsp70 in refolding of substrates. *PLOS Genet.* **15**, e1008479 (2019).

245. Burgio, M. R., Bennett, P. M. & Koretz, J. F. Heat-induced quaternary transitions in hetero- and homo-polymers of α-crystallin. *Mol. Vis.* 6 (2001).

246. Tang, G. *et al.* EMAN2: an extensible image processing suite for electron microscopy. *J. Struct. Biol.* **157**, 38–46 (2007).

247. Zivanov, J., Nakane, T. & Scheres, S. H. W. A Bayesian approach to beam-induced motion correction in cryo-EM single-particle analysis. *IUCrJ* **6**, 5–17 (2019).

248. Procter, J. B. *et al.* Alignment of Biological Sequences with Jalview. *Methods Mol Biol* **2231**, 203–224 (2021).

249. Webb, B. & Sali, A. Protein Structure Modeling with MODELLER. *Methods Mol Biol* **2199**, 239–255 (2021).

250. Goddard, T. D. *et al.* UCSF ChimeraX: Meeting modern challenges in visualization and analysis. *Protein Sci. Publ. Protein Soc.* **27**, 14–25 (2018).

251. Virtanen, P. *et al.* SciPy 1.0: fundamental algorithms for scientific computing in Python. *Nat. Methods* **17**, 261–272 (2020).

252. de Jong, W. W., Caspers, G. J. & Leunissen, J. A. Genealogy of the alpha-crystallin--small heat-shock protein superfamily. *Int. J. Biol. Macromol.* **22**, 151–162 (1998).

253. Caspers, G.-J., Leunissen, J. A. M. & de Jong, W. W. The expanding small heat-shock protein family, and structure predictions of the conserved "α-crystallin domain". *J. Mol. Evol.* **40**, 238–248 (1995).

254. Landry, J. & Huot, J. Modulation of actin dynamics during stress and physiological stimulation by a signaling pathway involving p38 MAP kinase and heat-shock protein 27. *Biochem. Cell Biol. Biochim. Biol. Cell.* **73**, 703–707 (1995).

255. Jong, W. w. de, Workum, F. P. A. van, Bosman, G. J. C. G., Vooter, C. E. M. & Renkawek, K. Expression of αB-crystallin in Alzheimer's disease. *Acta Neuropathol. (Berl.)* 155–160 (1994).

256. Jehle, S. *et al.* N-terminal domain of αB-crystallin provides a conformational switch for multimerization and structural heterogeneity. 13.

257. Kim, R. *et al.* On the mechanism of chaperone activity of the small heat-shock protein of *Methanococcus jannaschii*. *Proc. Natl. Acad. Sci.* **100**, 8151–8155 (2003).

258. Basha, E., Friedrich, K. L. & Vierling, E. The N-terminal arm of small heat shock proteins is important for both chaperone activity and substrate specificity. *J. Biol. Chem.* **281**, 39943–39952 (2006).

259. Koteiche, H. A., Chiu, S., Majdoch, R. L., Stewart, P. L. & Mchaourab, H. S. Atomic Models by Cryo-EM and Site-Directed Spin Labeling: Application to the N-Terminal Region of Hsp16.5. *Structure* **13**, 1165–1171 (2005).

260. Hanazono, Y., Takeda, K., Yohda, M. & Miki, K. Structural Studies on the Oligomeric Transition of a Small Heat Shock Protein, StHsp14.0. *J. Mol. Biol.* **422**, 100–108 (2012).

261. Hanazono, Y. *et al.* Nonequivalence Observed for the 16-Meric Structure of a Small Heat Shock Protein, SpHsp16.0, from Schizosaccharomyces pombe. *Structure* **21**, 220–228 (2013).

262. Bova, M. P., Huang, Q., Ding, L. & Horwitz, J. Subunit exchange, conformational stability, and chaperone-like function of the small heat shock protein 16.5 from Methanococcus jannaschii. *J. Biol. Chem.* **277**, 38468–38475 (2002).

263. Kim, R., Kim, K. K., Yokota, H. & Kim, S.-H. Small heat shock protein of *Methanococcus jannaschii* , a hyperthermophile. *Proc. Natl. Acad. Sci.* **95**, 9129–9133 (1998).

264. Reddy, G. B. Temperature-dependent Chaperone Activity and Structural Properties of Human ␣A- and ␣B-crystallins. 7.

265. Bult, C. J. *et al.* Complete Genome Sequence of the Methanogenic Archaeon, Methanococcus jannaschii. *Science* **273**, 1058–1073 (1996).

266. Greaves, R. B. & Warwicker, J. Mechanisms for stabilisation and the maintenance of solubility in proteins from thermophiles. *BMC Struct. Biol.* **7**, 18 (2007).

267. Matsue, S., Fujii, T. & Miyawaki, O. Effects of water activity and aqueous solvent ordering on thermal stability of lysozyme, α-chymotrypsinogen A, and alcohol dehydrogenase. *Int. J. Biol. Macromol.* **28**, 343–349 (2001).

268. Lee, G. J. & Vierling, E. A small heat shock protein cooperates with heat shock protein 70 systems to reactivate a heat-denatured protein. *Plant Physiol.* **122**, 189–198 (2000).

269. Rice, L., Marzano, N., Cox, D., Oijen, A. van & Ecroyd, H. Single-molecule observations of human small heat shock proteins in complex with aggregation-prone client proteins. 2024.02.08.579576 Preprint at https://doi.org/10.1101/2024.02.08.579576 (2024).

270. Vendredy, L., Adriaenssens, E. & Timmerman, V. Small heat shock proteins in neurodegenerative diseases. *Cell Stress Chaperones* **25**, 679–699 (2020).

271. Quinlan, R. A. *et al.* Changes in the quaternary structure and function of MjHSP16.5 attributable to deletion of the IXI motif and introduction of the substitution, R107G, in the *α* -crystallin domain. *Philos. Trans. R. Soc. B Biol. Sci.* **368**, 20120327 (2013).

272. Mastronarde, D. N. SerialEM: A Program for Automated Tilt Series Acquisition on Tecnai Microscopes Using Prediction of Specimen Position. *Microsc. Microanal.* **9**, 1182–1183 (2003).

273. Punjani, A., Rubinstein, J. L., Fleet, D. J. & Brubaker, M. A. cryoSPARC: algorithms for rapid unsupervised cryo-EM structure determination. *Nat. Methods* **14**, 290–296 (2017).

274. Punjani, A. & Fleet, D. J. 3D variability analysis: Resolving continuous flexibility and discrete heterogeneity from single particle cryo-EM. *J. Struct. Biol.* **213**, 107702 (2021).

275. Pettersen, E. F. *et al.* UCSF ChimeraX: Structure visualization for researchers, educators, and developers. *Protein Sci. Publ. Protein Soc.* **30**, 70–82 (2021).

276. UCSF ChimeraX: Tools for structure building and analysis - Meng - 2023 - Protein Science - Wiley Online Library. https://onlinelibrary.wiley.com/doi/10.1002/pro.4792.

277. (IUCr) New tools for the analysis and validation of cryo-EM maps and atomic models. https://journals.iucr.org/d/issues/2018/09/00/kw5139/index.html.

278. Afonine, P. V. *et al.* Real-space refinement in PHENIX for cryo-EM and crystallography. *Acta Crystallogr. Sect. Struct. Biol.* **74**, 531–544 (2018).

279. P. Emsley, B. Lohkamp, W.G. Scott, & K. Cowtan. Features and development of COOT. *Acta Crystallogr. Sect. Struct. Biol.* **D66**, 486–501 (2010).

280. Croll, T. I. ISOLDE: a physically realistic environment for model building into low-resolution electron-density maps. *Acta Crystallogr. Sect. Struct. Biol.* **74**, 519–530 (2018).

281. Callaway, E. The revolution will not be crystallized: a new method sweeps through structural biology. *Nature* **525**, 172–174 (2015).

282. Chua, E. Y. D. *et al.* Better, Faster, Cheaper: Recent Advances in Cryo–Electron Microscopy. *Annu. Rev. Biochem.* **91**, 1–32 (2022).

283. Luhrmann, R. & Holger Stark. GraFix: sample preparation for single-particle electron cryomicroscopy. *Nat. Methods* **5**, 53–55 (2008).

284. Terminal Regions Confer Plasticity to the Tetrameric Assembly of Human HspB2 and HspB3 | Elsevier Enhanced Reader. https://reader.elsevier.com/reader/sd/pii/S0022283618307083?token=7D1F4CD24904CFBB7552C2C72A8C0529DA2E534DAC233558A2F0B4AB82CB56826

92FB362CA55BC2D0D196C903C54C26D&originRegion=us-east-1&originCreation=20230312181757 doi:10.1016/j.jmb.2018.06.047.

285. Clouser, A. F. *et al.* Interplay of disordered and ordered regions of a human small heat shock protein yields an ensemble of 'quasi-ordered' states. *eLife* **8**, e50259 (2019).

286. Zhang, P. Advances in cryo-electron tomography and subtomogram averaging and classification. *Curr. Opin. Struct. Biol.* **58**, 249–258 (2019).

287. Andrew J. Baldwin *et al.* Quaternary Dynamics of aB-crystallin as a Direct Consequence of Localised Tertiary Fluctuations in the C-terminus. *JMB* **413**, 310–320 (2011).

288. Augusteyn, R. C. & Koretz, J. F. A possible structure for α-crystallin. *FEBS Lett.* **222**, 1–5 (1987).

289. Callaway, E. The revolution will not be crystallized: a new method sweeps through structural biology. *Nature* **525**, 172–174 (2015).

290. Morris, K. L. *et al.* Cryo-EM of multiple cage architectures reveals a universal mode of clathrin self-assembly. *Nat. Struct. Mol. Biol.* **26**, 890–898 (2019).

291. Shatsky, M., Hall, R. J., Brenner, S. E. & Glaeser, R. M. A Method for the Alignment of Heterogeneous Macromolecules from Electron Microscopy. *J. Struct. Biol.* **166**, 67–78 (2009).

292. Henderson, R. Avoiding the pitfalls of single particle cryo-electron microscopy: Einstein from noise. *Proc. Natl. Acad. Sci.* **110**, 18037–18041 (2013).

293. Zivanov, J. *et al.* A Bayesian approach to single-particle electron cryo-tomography in RELION-4.0. *eLife* **11**, e83724 (2022).

294. Scheres, S. H. W. Single-particle processing in relion-3. 72.

295. Grant, T., Rohou, A. & Grigorieff, N. *cisTEM: User-Friendly Software for Single-Particle Image Processing*. http://biorxiv.org/lookup/doi/10.1101/257618 (2018) doi:10.1101/257618.

296. Kinman, L. F., Powell, B. M., Zhong, E. D., Berger, B. & Davis, J. H. Uncovering structural ensembles from single-particle cryo-EM data using cryoDRGN. *Nat. Protoc.* **18**, 319–339 (2023).

297. Chen, M. & Ludtke, S. J. Deep learning-based mixed-dimensional Gaussian mixture model for characterizing variability in cryo-EM. *Nat. Methods* **18**, 930–936 (2021).

298. Kimanius, D. & Schwab, J. Confronting heterogeneity in cryogenic electron microscopy data: Innovative strategies and future perspectives with data-driven methods. *Curr. Opin. Struct. Biol.* **86**, 102815 (2024).

299. Goettig, P., Koch, N. G. & Budisa, N. Non-Canonical Amino Acids in Analyses of Protease Structure and Function. *Int. J. Mol. Sci.* **24**, 14035 (2023).

300. Adamus, K., Le, S. N., Elmlund, H., Boudes, M. & Elmlund, D. AgarFix: Simple and accessible stabilization of challenging single-particle cryo-EM specimens through crosslinking in a matrix of agar. *J. Struct. Biol.* **207**, 327–331 (2019).

301. Koning, R. I., Koster, A. J. & Sharp, T. H. Advances in cryo-electron tomography for biology and medicine. *Ann. Anat. Anat. Anz. Off. Organ Anat. Ges.* **217**, 82–96 (2018).

302. Powell, B. M. & Davis, J. H. Learning structural heterogeneity from cryo-electron sub-tomograms with tomoDRGN. *Nat. Methods* 1–12 (2024) doi:10.1038/s41592-024-02210-z.

303. Bayer, K. U. & Schulman, H. CaM Kinase: Still Inspiring at 40. *Neuron* **103**, 380–394 (2019).

304. Hell, J. W. CaMKII: claiming center stage in postsynaptic function and organization. *Neuron* **81**, 249–65 (2014).

305. Lisman, J., Yasuda, R. & Raghavachari, S. Mechanisms of CaMKII action in long-term potentiation. *Nat Rev Neurosci* **13**, 169–82 (2012).

306. Coultrap, S. J., Vest, R. S., Ashpole, N. M., Hudmon, A. & Bayer, K. U. CaMKII in cerebral ischemia. *Acta Pharmacol Sin* **32**, 861–72 (2011).

307. Deng, G. *et al.* Autonomous CaMKII Activity as a Drug Target for Histological and Functional Neuroprotection after Resuscitation from Cardiac Arrest. *Cell Rep* **18**, 1109–1117 (2017).

308. Vest, R. S., O'Leary, H., Coultrap, S. J., Kindy, M. S. & Bayer, K. U. Effective post-insult neuroprotection by a novel Ca(2+)/ calmodulin-dependent protein kinase II (CaMKII) inhibitor. *J Biol Chem* **285**, 20675–82 (2010).

309. Cook, S. G., Buonarati, O. R., Coultrap, S. J. & Bayer, K. U. CaMKII holoenzyme mechanisms that govern the LTP versus LTD decision. *Sci Adv* **7**, (2021).

310. Coultrap, S. J. *et al.* Autonomous CaMKII mediates both LTP and LTD using a mechanism for differential substrate site selection. *Cell Rep.* **6**, 431–437 (2014).

311. Giese, K. P., Fedorov, N. B., Filipkowski, R. K. & Silva, A. J. Autophosphorylation at Thr286 of the alpha calcium-calmodulin kinase II in LTP and learning. *Science* **279**, 870–3 (1998).

312. Hanson, P. I., Meyer, T., Stryer, L. & Schulman, H. Dual role of calmodulin in autophosphorylation of multifunctional CaM kinase may underlie decoding of calcium signals. *Neuron* **12**, 943–56 (1994).

313. De Koninck, P. & Schulman, H. Sensitivity of CaM kinase II to the frequency of Ca2+ oscillations. *Science* **279**, 227–30 (1998).

314. Barria, A. & Malinow, R. NMDA receptor subunit composition controls synaptic plasticity by regulating binding to CaMKII. *Neuron* **48**, 289–301 (2005).

315. Buonarati, O. R. *et al.* CaMKII versus DAPK1 binding to GluN2B in ischemic neuronal cell death after resuscitation from cardiac arrest. *Cell Rep* **30**, 1–8 (2020).

316. Halt, A. R. *et al.* CaMKII binding to GluN2B is critical during memory consolidation. *EMBO J* **31**, 1203–16 (2012).

317. Bayer, K. U. *et al.* Transition from reversible to persistent binding of CaMKII to postsynaptic sites and NR2B. *J Neurosci* **26**, 1164–74 (2006).

318. Strack, S., McNeill, R. B. & Colbran, R. J. Mechanism and regulation of calcium/calmodulin-dependent protein kinase II targeting to the NR2B subunit of the N-methyl-D-aspartate receptor. *J Biol Chem* **275**, 23798–806 (2000).

319. Bayer, K. U., De Koninck, P., Leonard, A. S., Hell, J. W. & Schulman, H. Interaction with the NMDA receptor locks CaMKII in an active conformation. *Nature* **411**, 801–5 (2001).

320. Miller, S. G. & Kennedy, M. B. Regulation of brain type II Ca2+/calmodulin-dependent protein kinase by autophosphorylation: a Ca2+-triggered molecular switch. *Cell* **44**, 861–70 (1986).

321. Hudmon, A., Aronowski, J., Kolb, S. J. & Waxham, M. N. Inactivation and self-association of Ca2+/calmodulin-dependent protein kinase II during autophosphorylation. *J Biol Chem* **271**, 8800–8 (1996).

322. Dosemeci, A., Reese, T. S., Petersen, J. & Tao-Cheng, J. H. A novel particulate form of Ca(2+)/calmodulin-dependent [correction of Ca(2+)/CaMKII-dependent] protein kinase II in neurons. *J Neurosci* **20**, 3076–84 (2000).

323. Hudmon, A., Kim, S. A., Kolb, S. J., Stoops, J. K. & Waxham, M. N. Light scattering and transmission electron microscopy studies reveal a mechanism for calcium/calmodulin-dependent protein kinase II self-association. *J Neurochem* **76**, 1364–75 (2001).

324. Vest, R. S., O'Leary, H. & Bayer, K. U. Differential regulation by ATP versus ADP further links CaMKII aggregation to ischemic conditions. *FEBS Lett* **583**, 3577–81 (2009).

325. Hudmon, A. *et al.* A mechanism for Ca2+/calmodulin-dependent protein kinase II clustering at synaptic and nonsynaptic sites based on self-association. *J Neurosci* **25**, 6971–83 (2005).

326. Coultrap, S. J. & Bayer, K. U. CaMKII regulation in information processing and storage. *Trends Neurosci* **35**, 607–618 (2012).

327. Rossetti, T. *et al.* Memory Erasure Experiments Indicate a Critical Role of CaMKII in Memory Storage. *Neuron* **96**, 207-216 e2 (2017).

328. Kanaseki, T., Ikeuchi, Y., Sugiura, H. & Yamauchi, T. Structural features of Ca2+/calmodulin-dependent protein kinase II revealed by electron microscopy. *J Cell Biol* **115**, 1049–60 (1991).

329. Woodgett, J. R., Davison, M. T. & Cohen, P. The calmodulin-dependent glycogen synthase kinase from rabbit skeletal muscle. Purification, subunit structure and substrate specificity. *Eur J Biochem* **136**, 481–7 (1983).

330. Chao, L. H. *et al.* A mechanism for tunable autoinhibition in the structure of a human Ca2+/calmodulin- dependent kinase II holoenzyme. *Cell* **146**, 732–45 (2011).

331. Myers, J. B. *et al.* The CaMKII holoenzyme structure in activation-competent conformations. *Nat. Commun.* **8**, 15742 (2017).

332. Sloutsky, R. *et al.* Heterogeneity in human hippocampal CaMKII transcripts reveals allosteric hub-dependent regulation. *Sci Signal* **13**, (2020).

333. Bayer, K. U., Lohler, J., Schulman, H. & Harbers, K. Developmental expression of the CaM kinase II isoforms: ubiquitous gamma- and delta-CaM kinase II are

the early isoforms and most abundant in the developing nervous system. *Brain Res Mol Brain Res* **70**, 147–54 (1999).

334. Bennett, M. K. & Kennedy, M. B. Deduced primary structure of the beta subunit of brain type II Ca2+/calmodulin-dependent protein kinase determined by molecular cloning. *Proc Natl Acad Sci U A* **84**, 1794–8 (1987).
335. Cook, S. G. *et al.* Analysis of the CaMKIIalpha and beta splice-variant distribution among brain regions reveals isoform-specific differences in holoenzyme formation. *Sci Rep* **8**, 5448 (2018).
336. Tombes, R. M., Faison, M. O. & Turbeville, J. M. Organization and evolution of multifunctional Ca(2+)/CaM-dependent protein kinase genes. *Gene* **322**, 17–31 (2003).
337. Flory, P. J. Spatial configuration of macromolecular chains. *Science* **188**, 1268–76 (1975).
338. Bradshaw, J. M., Hudmon, A. & Schulman, H. Chemical quenched flow kinetic studies indicate an intraholoenzyme autophosphorylation mechanism for Ca2+/calmodulin-dependent protein kinase II. *J Biol Chem* **277**, 20991–8 (2002).
339. Rich, R. C. & Schulman, H. Substrate-directed function of calmodulin in autophosphorylation of Ca2+/calmodulin-dependent protein kinase II. *J Biol Chem* **273**, 28424–9 (1998).

340. Hoelz, A., Nairn, A. C. & Kuriyan, J. Crystal structure of a tetradecameric assembly of the association domain of Ca2+/calmodulin-dependent kinase II. *Mol Cell* **11**, 1241–51 (2003).

341. Rosenberg, O. S., Deindl, S., Sung, R. J., Nairn, A. C. & Kuriyan, J. Structure of the autoinhibited kinase domain of CaMKII and SAXS analysis of the holoenzyme. *Cell* **123**, 849–60 (2005).

342. Thaler, C., Koushik, S. V., Puhl, H. L., Blank, P. S. & Vogel, S. S. Structural rearrangement of CaMKIIalpha catalytic domains encodes activation. *Proc Natl Acad Sci U A* **106**, 6369–74 (2009).

343. Coultrap, S. J. & Bayer, K. U. Improving a natural CaMKII inhibitor by random and rational design. *PLoS One* **6**, e25245 (2011).

344. Coultrap, S. J., Buard, I., Kulbe, J. R., Dell'Acqua, M. L. & Bayer, K. U. CaMKII autonomy is substrate-dependent and further stimulated by Ca2+/calmodulin. *J Biol Chem* **285**, 17930–7 (2010).

345. Brocke, L., Chiang, L. W., Wagner, P. D. & Schulman, H. Functional implications of the subunit composition of neuronal CaM kinase II. *J Biol Chem* **274**, 22713–22 (1999).

346. Cook, S. G., Goodell, D. J., Restrepo, S., Arnold, D. B. & Bayer, K. U. Simultaneous live-imaging of multiple endogenous proteins reveals a mechanism for Alzheimer's-related plasticity impairment. *Cell Rep* **27**, 658–665 (2019).

347. Fink, C. C. *et al.* Selective regulation of neurite extension and synapse formation by the beta but not the alpha isoform of CaMKII. *Neuron* **39**, 283–97 (2003).

348. Khan, S., Conte, I., Carter, T., Bayer, K. U. & Molloy, J. E. Multiple CaMKII Binding Modes to the Actin Cytoskeleton Revealed by Single-Molecule Imaging. *Biophys J* **111**, 395–408 (2016).

349. O'Leary, H., Lasda, E. & Bayer, K. U. CaMKIIbeta association with the actin cytoskeleton is regulated by alternative splicing. *Mol Biol Cell* **17**, 4656–65 (2006).

350. Okamoto, K., Narayanan, R., Lee, S. H., Murata, K. & Hayashi, Y. The role of CaMKII as an F-actin-bundling protein crucial for maintenance of dendritic spine structure. *Proc Natl Acad Sci U A* **104**, 6418–23 (2007).

351. Dyla, M. & Kjaergaard, M. Intrinsically disordered linkers control tethered kinases via effective concentration. *Proc Natl Acad Sci U A* **117**, 21413–21419 (2020).

352. Bhattacharyya, M. *et al.* Flexible linkers in CaMKII control the balance between activating and inhibitory autophosphorylation. *Elife* **9**, (2020).

353. Colbran, R. J. Inactivation of Ca2+/calmodulin-dependent protein kinase II by basal autophosphorylation. *J Biol Chem* **268**, 7163–70 (1993).

354. Barcomb, K., Hell, J. W., Benke, T. A. & Bayer, K. U. The CaMKII/GluN2B Protein Interaction Maintains Synaptic Strength. *J Biol Chem* **291**, 16082–9 (2016).

355. Incontro, S. *et al.* The CaMKII/NMDA receptor complex controls hippocampal synaptic transmission by kinase-dependent and independent mechanisms. *Nat Commun* **9**, 2069 (2018).

356. Sanhueza, M. *et al.* Role of the CaMKII/NMDA receptor complex in the maintenance of synaptic strength. *J Neurosci* **31**, 9170–8 (2011).

357. Aronowski, J., Grotta, J. C. & Waxham, M. N. Ischemia-induced translocation of Ca2+/calmodulin-dependent protein kinase II: potential role in neuronal damage. *J Neurochem* **58**, 1743–53 (1992).

358. Nguyen, T. A. *et al.* Covert Changes in CaMKII Holoenzyme Structure Identified for Activation and Subsequent Interactions. *Biophys J* **108**, 2158–70 (2015).

359. Nguyen, T. A., Sarkar, P., Veetil, J. V., Koushik, S. V. & Vogel, S. S. Fluorescence polarization and fluctuation analysis monitors subunit proximity, stoichiometry, and protein complex hydrodynamics. *PLoS One* **7**, e38209 (2012).

360. Rellos, P. *et al.* Structure of the CaMKIIdelta/calmodulin complex reveals the molecular mechanism of CaMKII kinase activation. *PLoS Biol* **8**, e1000426 (2010).

361. Brangwynne, C. P. *et al.* Germline P granules are liquid droplets that localize by controlled dissolution/condensation. *Science* **324**, 1729–32 (2009).

362. Chen, X., Wu, X., Wu, H. & Zhang, M. Phase separation at the synapse. *Nat Neurosci* **23**, 301–310 (2020).

363. Hosokawa, T. *et al.* CaMKII activation triggers persistent formation and segregation of postsynaptic liquid phase. *bioRxiv* 2020.11.25.397091 (2020) doi:10.1101/2020.11.25.397091.

364. Banani, S. F., Lee, H. O., Hyman, A. A. & Rosen, M. K. Biomolecular condensates: organizers of cellular biochemistry. *Nat Rev Mol Cell Biol* **18**, 285–298 (2017).

365. Li, P. *et al.* Phase transitions in the assembly of multivalent signalling proteins. *Nature* **483**, 336–40 (2012).

366. McSpadden, E. D. *et al.* Variation in assembly stoichiometry in non-metazoan homologs of the hub domain of Ca(2+) /calmodulin-dependent protein kinase II. *Protein Sci* **28**, 1071–1082 (2019).

367. Bhattacharyya, M. *et al.* Molecular mechanism of activation-triggered subunit exchange in Ca(2+)/calmodulin-dependent protein kinase II. *Elife* **5**, (2016).

368. Stratton, M. *et al.* Activation-triggered subunit exchange between CaMKII holoenzymes facilitates the spread of kinase activity. *Elife* **3**, e01610 (2014).

369. Karandur, D. *et al.* Breakage of the oligomeric CaMKII hub by the regulatory segment of the kinase. *Elife* **9**, (2020).

370. Bhattacharyya, M., Karandur, D. & Kuriyan, J. Structural Insights into the Regulation of Ca(2+)/Calmodulin-Dependent Protein Kinase II (CaMKII). *Cold Spring Harb Perspect Biol* **12**, (2020).

371. Zacharias, D. A., Violin, J. D., Newton, A. C. & Tsien, R. Y. Partitioning of lipid-modified monomeric GFPs into membrane microdomains of live cells. *Science* **296**, 913–6 (2002).

372. Gross, G. G. *et al.* Recombinant probes for visualizing endogenous synaptic proteins in living neurons. *Neuron* **78**, 971–85 (2013).

373. Mora, R. J., Roberts, R. W. & Arnold, D. B. Recombinant probes reveal dynamic localization of CaMKIIalpha within somata of cortical neurons. *J Neurosci* **33**, 14579–90 (2013).

374. Coultrap, S. J. & Bayer, K. U. Ca^{2+}/Calmodulin-Dependent Protein Kinase II (CaMKII). in *Neuromethods: Protein Kinase Technologies* (ed. Mukai, H.) 49–72 (Springer, 2012).

375. Singla, S. I., Hudmon, A., Goldberg, J. M., Smith, J. L. & Schulman, H. Molecular characterization of calmodulin trapping by calcium/calmodulin-dependent protein kinase II. *J Biol Chem* **276**, 29353–60 (2001).

376. Zivanov, J. *et al.* New tools for automated high-resolution cryo-EM structure determination in RELION-3. *Elife* **7**, (2018).

377. Scheres, S. H. RELION: implementation of a Bayesian approach to cryo-EM structure determination. *J Struct Biol* **180**, 519–30 (2012).